Design And Development of New Controllers for Grid Tied PV Systems

A Thesis Submitted to the
Delhi Technological University
For the Award of Doctor of Philosophy
In
Electrical Engineering

Submitted By:

ANKITA ARORA
(2K17/PhD/EE/14)

Under the Supervision of

Dr. Alka Singh
Professor

DEPARTMENT OF ELECTRICAL ENGINEERING
DELHI TECHNOLOGICAL UNIVERSITY
(Formerly Delhi College of Engineering)
DELHI-110042, INDIA
February, 2023

DECLARATION

I Ankita Arora a student of Ph.D. hereby declare that the thesis titled **Design And Development of New Controllers for Grid Tied PV Systems** which is submitted by me to the Department of Electrical Engineering, Delhi Technological University, Delhi in partial fulfillment of the requirement for the award of the degree of Doctor of Philosophy has not previously formed the basis for the award of any Degree, Diploma Associate ship, fellowship or other similar title or recognition.

Place: Delhi **(Ankita Arora)**

Date: 14/02/2023

CERTIFICATE

On the basis of the declaration submitted by Ms. Ankita Arora, student of Ph.D., I hereby certify that the thesis titled **Design And Development of New Controllers for Grid Tied PV Systems** which is submitted to the Department of Electrical Engineering, Delhi Technological University, Delhi in partial fulfilment of the requirement for the award of the degree of Doctor of Philosophy is an original contribution with existing knowledge and faithful record of research carried out by her under my guidance and supervision.

To the best of my knowledge this work has not been submitted in part or full for any Degree or Diploma to this University or elsewhere.

Date: 14/02/2023

(Prof. Alka Singh)

Supervisor
Department of Electrical Engineering

Delhi Technological University

Delhi, India

ACKNOWLEDGEMENT

I would like to express my deep and sincere gratitude to my supervisor Prof. Alka Singh for her valuable guidance and continuous monitoring of my research work. It was great honor for me to pursue my research work under her supervision. Prof. Alka Singh has been the main motivating and inspiring factor behind my research work. It's her vigor and hunger to perform in adverse situation, which has inspired me to thrive for excellence and nothing less.

I would also like to convey my sincere gratitude to Prof. Madhusudan Singh, DTU, whose continuous monitoring, valuable guidance and input has always been a driving force to complete my research work. I would like to thank the SRC members mainly Prof. Prerna Gaur, who have given me valuable guidance and advice to improve quality of my research work. I am extremely thankful to staff members of Power System Lab, DTU, Delhi for providing me immense facility and assistance to carry out my research work. I would like to thank other office staff, Central library and Computer Centre staff, for their valuable co-operation and support.

I would like my sincere thanks to Dr. Prakash Chittora, who has guided me to develop hardware at initial level of research work. His research publications have guided me during all time of my research work. I am extremely grateful to my research group and friends Amarendra Pandey, Kanchan Bala Rai and Sudhanshu Mittal for their valuable assistance, co-operation and great source of learning.

If I get any success today for my research work, the entire credit should go to my family and my Late grandfather Shri Joginder Singh Arora.

I thank to almighty, the father of all for his blessing to accomplish my research work

successfully.

Place: Delhi **(Ankita Arora)**

Date: 14/02/2023

TABLE OF CONTENTS

LIST OF FIGURES

LIST OF TABLES

LIST OF SYMBOLS AND ABBREVIATION

List of Symbols

Z_s	Source Impedance
R_s	Source Resistance
L_s	Source Inductance
L_f	Interfacing inductor
R_c	Ripple Filter
V_{rms}	RMS Grid Voltage
V_{dc}	DC link Voltage
C_{dc}	DC Link Capacitance
K_1	Constant
V_{dc1}	Calculated minimum level of DC link Voltage
I_{ph}	Phase Current
a	Overloading Factor
f_s	Switching Frequency
I_{crpp}	Ripple in Current
m	Modulation Index
I_m	Current Maximum Level
R_{in}	Input Side Resistance
I_{in}	Input Current
V_{in}	Input Voltage

P_m	Minimum Wattage Power
P_{mp}	PV Maximum Power
V_{oc}	Open Circuit Voltage
I_{sc}	Short Circuit Current
V_{mp}	Peak Amplitude Grid voltage
I_{mp}	Maximum Current
(%/°C)	Temperature Coefficient
L_b	Boost Converter Inductor
D	Duty Cycle
C_b	Boost Converter Capacitor
P_{pv}	PV Power
v_{mpp}	Voltage at Maximum Power
I_{out}	Output current of Boost Converter
V_{out}	Output voltage of Boost Converter
ΔV_{out}	Ripple in output voltage of Boost Converter
V_b	Battery Voltage
ΔI_{pv}	Ripple in Inductor Current of Boost Converter
∂P/∂V	Change in Power with respect to Voltage
V_{dc}^*	Reference DC link Voltage
ΔI_L	Ripple in Charging Current of Battery
$v_{de}(n)$	Error Difference in DC Link voltage and Reference DC Link Voltage

K_p	Proportionality Gain Constant
k_i	Integral Constant
$i_{Loss}(n)$	Switching Loss
i_{pnet}	Total Fundamental Component of Grid Current
$\mathrm{i}_{\mathrm{pvff}}$	PV Feed Forward Component
P_{pv}	PV Power
V_m	Peak Amplitude Grid Voltage
$v_{s\alpha}$	In-phase component of Grid Voltage
$v_{s\beta}$	Quadrature component of Grid Voltage
u_p	Unit in-Phase Template
i_s^*	Reference Source Current
u_{pa}, u_{pb}, u_{pc}	Three phase Unit Templates
$i_{sa}^*, i_{sb}^*, i_{sc}^*$	Three Phase Reference Source Currents
i_{sa}, i_{sb}, i_{sc}	Three Phase Source Currents
v_s	Source Voltage
i_s	Source Current
i_L	Load Current
$i_{L\alpha}$	In-phase component of Load Current
$i_{L\beta}$	Quadrature component of Load Current
i_{Ld}	Fundament Active component of Load Current
i_{Lq}	Fundamental Reactive component of Load Current
$\overline{i_{Ld}}$	Filtered Fundamental Active component of Load Current

$\widetilde{i_{Ld}}$	Harmonic Active Component of Load Current
$\overline{i_{Lq}}$	Filtered Fundamental Reactive component of Load Current
$\widetilde{i_{Lq}}$	Harmonic Reactive Power Component of Load Current
i_{LD}^{*}	Total Fundamental Active Power Component of Load Current
i_{Lq}^{*}	Total Fundamental Reactive Power Component of Load Current
i_{Lest}	Estimated Fundamental Component of Load Current
K	Gain constant in SOGI
t_s	Sampling Time
ω	Sampling frequency
$w(n)$	Weight components
f(.)	Non-linear Functional Expansion of Input Vector
T	Transpose of the Matrix
e	Error
P	Order of the matrix
i_f	Compensator Current
sinωt	Unit in phase template
cosωt	Quadrature Template
P_s, Q_s	Source Active Power, Source Reactive Power
P_L, Q_L	Load Active Power, Load Reactive Power
P_f, Q_f	Compensator Active power, Compensator Reactive Power,
$G(I_{rr})$	Irradiation level

i_{L0}, i_{L1}, i_{L2}	Load current expansion components
i_{LA}, i_{LB} and i_{LC}	Three phase Load Currents
v_{sa}, v_{sb} and v_{sc}	Three phase Grid Voltages
v_{sabc}	Three phase Grid Voltage
i_{sabc}	Three phase Grid Current
i_{Labc}	Three phase Load Current
i_{fabc}	Three Phase Compensator Current
P_{sabc}, Q_{sabc}	Three Phase source Active and Reactive Power
P_{Labc}, Q_{Labc}	Three Phase Load Active and Reactive Power
P_{fabc}, Q_{fabc}	Three Phase Compensator Active and Reactive Power
B	Beizer Constant
q	Knot point
J	Cost Function
$v_{s\alpha}$	Phase component of Grid Voltage
$v_{s\beta}$	Quadrature component of Grid Voltage
v_{sd}	Active component of Grid Voltage
v_{sq}	Reactive component of Grid Voltage
$v_{sq(est)}$	Estimated Quadrature Voltage
$B_{m,k}(t)$	Bernstein Coefficient
μ	Learning Parameter
E	Expected Mean Error
ω	Angular Frequency

$\Delta\omega$	Error in Angular Frequency
ω_r^*	Natural Frequency
ω_{est}	Estimated Frequency
θ_{est}	Estimated grid voltage angle
$V_{magnitude}$	Grid Terminal Voltage
i_{BattFF}	Battery Feed Forward Component
V_{mL}	PCC Peak Voltage
v_L^*	PCC Reference Voltage
i_{vsc}^*	VSC Reference Current
v_{eL}	Difference in PCC voltage Error
θ_s	Grid Phase Angle
θ_g	Load Phase Angle
f_s	Grid Frequency
f_L	PCC Frequency

List of Abbreviations

SAPF	Shunt Active Power Filter
VSC	Voltage Source Converter
SRFT	Synchronous Reference Frame Theory
SOGI	Second Order Generalized Integrator
TFLNN	Trigonometric Functional Link Neural Network
LFNN	Legendre Functional Neural Network

DSOGI	Dual Second Order Generalised Integrator
AVSF	Adaptive Volterra Second Order Filter
CS-FEBAF	Cubic Spline Functional Expansion Based Adaptive Filter
QB-FBNN	Quadratic Bernstein Functional Blending Neural Network
FD-NSLI	Fractional Delay Newton Langrangian Interpolation
GSS	Grid Sequence Separator Control
PQ	Power quality
SMPS	switch mode power supply
PCC	point of common coupling
HCC	Hysteresis Current Controller
UPQC	.Unified Power Quality Conditioner
DVR	Dynamic Voltage Restorer
PLL	Phase Locked loops
PV	photovoltaic
MPPT	Maximum Power Point Tracking
ANN	Artificial Neural Network
FLC	Fuzzy Logic Controllers
ANFIS	Adaptive Neuro Fuzzy Inference System
LMS	Least Mean Square
LMF	Least Mean Fourth Algorithm
SCCR	Short Circuit Capacity Ratio
DDSRF	Decoupled Double Synchronous Reference Frame
CGI	Cascaded Generalised Integrator
SOGI-FLL	Second Order Generalized Integrator Fuzzy Logic Controller
MTOGI	Mixed Second and Third-Order Generalized Integrator

STS	Static Transfer Switch
BJT	Bipolar Junction Transistor
MOSFET	Metal-Oxide-Semiconductor Field-Effect Transistor
GTO	Gate Turn-Off Thyristor
IEEE	Institute of Electrical and Electronics Engineers
IEC	International Electro Technical Commission
THD	Total Harmonic Distortion
IRPT	Instantaneous Reactive Power Theory
PBT	Power Balance Theory
PI	Proportional Integrator
PNKLMS	Power Normalized Kernel Least Mean Square
LQR	Linear Quadratic Regulator
ANOVA	Analysis of Variance
GI	Generalized Integrator
LTI-EPLL	Linear Time Invariant-Improved Enhanced Phase Lock Loop
PWM	Pulse Width Modulation
PN-KLMF	Power Normalized Kernel Least Mean Fourth Algorithm based neural network (NN)
MGI	Multiple Generalized Integral
ILST	Improved Linear Sinusoidal Tracer
FOGI-FLL	Fuzzy logic based fourth order generalized integrator (FOGI) Frequency Locked Loop
CDSC	Cascaded Delay Signal Cancellation
MAF	Moving Average Filter
DER	Distributed Energy Resources

ARSNS	Advanced Robust Shrinkage Normalized Sign
LQ	Learning Quantization
AFLL	Adaptive Frequency Locked Loop
FOCV	Fractional Open Circuit Voltage
P&O	Perturb and Observe
DSO	Digital Storage Oscilloscope
IGBT	Insulated Gate Bipolar Transistors
ADC	Analog to Digital Conversion
FLANN	Functional Link Adaptive Neural Network
SPV	Solar Photovoltaic
RES	Renewable Energy Sources
BES	Battery Energy Storage System

ABSTRACT

Modern power distribution systems face twin challenges of increased use of power electronic based loads and integration of renewable energy systems. These power electronic devices cause current based power quality problems in distribution systems. Prominent power quality problems include poor power factor, load unbalancing, harmonics in supply current, voltage regulation etc. The Shunt Active Power Filter (SAPF) is employed to mitigate current based power quality problems. Several controllers are designed to achieve this task. The synchronizing signals are sinusoidal in shape in case of normal grid and can be extracted with the help of unit in phase template method. But under weak grid conditions there are problems of voltage sag, swell, distortion and DC offset. Thus, there is a need of effective Phase Locked Loop (PLL) methods employed for estimation of synchronizing template signals under distorted grid conditions.

Several controllers are designed to achieve the task of mitigation of power quality problems. The SAPF can be configured for single phase as well as three phase systems. Two-Leg Voltage Source Converter (VSC) configurations have been used in single-phase system. These are H-bridge for single phase system and three-phase three-leg configuration for three-phase system.

SAPF working is based on the fundamental load current for generation of reference signals. The fundamental component of load current is extracted with the help of several algorithms. Various type of control algorithms has been proposed in this work. Time domain conventional techniques along with adaptive and Functional Link Neural Network and Fractional Delay algorithms are proposed.

The entire thesis work has been split in to six chapters. The first two chapters deal with the introduction and literature review related to problems and mitigation techniques of shunt compensation, PLL and battery energy storage systems. The third chapter deals with the design and analysis of PV integrated grid connected systems. The configuration of SAPF in single-phase and three-phase PV integrated grid connected and battery energy storage systems are discussed. The fourth chapter discusses the shunt compensation in single-phase grid connected systems. The control algorithms considered for compensation are Synchronous Reference Frame Theory (SRFT), Second Order Generalized Integrator (SOGI), Trigonometric Functional Link Neural Network (TFLNN) and Legendre Functional Neural Network (LFNN). These algorithms are studied under varying load conditions i.e., linear, non-linear and mixed loading conditions using Matlab Simulink models. The algorithms have also been tested in the Simulink environment as well as hardware developed in the laboratory with and without PV interfaced systems.

The fifth chapter deals with the shunt compensation in three-phase grid connected systems. It studies some conventional and few algorithms such as Synchronous Reference Frame Theory (SRFT), Second Order Generalized Integrator (SOGI), Adaptive Volterra Second Order Filter (AVSF) and Cubic Bezier Functional Expansion Based Adaptive Filter (CB-FEBAF) under varying load conditions such as linear, non-linear and mixed loading conditions. Their efficiency has been tested in the Simulink as well as on the hardware developed in the laboratory with and without PV interfaced systems.

The sixth chapter studies the voltage-based power quality problems that arises in weak grid conditions such as voltage sag, swell, distortion, phase change and frequency change. PLL has been used to generate the synchronizing template for

reference waveform generation. Some conventional PLLs have been studied such as Synchronous Reference Frame Theory (SRFT), Second Order Generalised Integrator (SOGI) and some new PLLs such as Quadratic Bernstein Functional Blending Neural Network (QB-FBNN) and Fractional Delay Newton Structure for (FD-NSLI) Lagrangian Interpolation method have been proposed. Extensive Simulation and experimental results have been taken for PLL testing.

Chapter 7 studies the battery integrated system where the voltage control mode and current control mode both are studied. This system considers a battery integrated PV systems under grid connected and islanding mode. Control algorithms such as Synchronous Reference Frame Theory (SRFT) and Grid Sequence Separator (GSS) based control have been developed and tested using MATLAB Based models.

CHAPTER-1

INTRODUCTION

1.1 General

Power quality (PQ) is defined as maintaining high-quality electrical power at all power levels such as generation, transmission and distribution. Power quality is described in terms of voltage, current and frequency deviation. The difference in the prescribed levels of above parameters leads to poor power quality. Power quality problems can be natural or man-made. Natural Power quality problems include faults, lightning which lead to variation in prescribed current and voltage levels. Man-made power quality problems are mainly due to the increased use of non-linear loads in distribution systems. Non-linear loads and solid-state power electronic devices such as switch mode power supply (SMPS), power converters and variable speed drives etc. worsen power quality problems. Excessive use of power electronic devices due to their compact size and less maintenance and ease of control by using semiconductor-based switches in industries and commercial applications further aggravate the problems. Poor power quality leads to maloperation and failure of electrical machines affects the customer equipment's and leads to increased losses in the distribution system.

The power quality problems can be differentiated on the basis of transient or steady state events, problem occurring at load end or on supply system side where variation in voltage, current and frequency take place for several reasons. Transient events include voltage flicker or short duration current or voltage disturbances. Steady state events include long duration voltage and harmonic current disturbances. The supply systems have voltage-based power quality problems and different types of loads

cause current based power quality problems as well as voltage-based power quality problems in weak grids.

Power quality has become a challenging and important area of exploration for the mitigation of PQ problems nowadays. This has evolved as the new research area for engineers working in the area of power electronics, electric drives, renewable energy resources, power systems etc. Voltage-based PQ problems occurring at point of common coupling (PCC) in weak grid are voltage sag, voltage swell, DC offset, frequency change, phase change and voltage distortions. The current based power quality problems are poor power factor, harmonics in source currents, load unbalancing and reactive power unbalance.

Various types of active and passive filters have been designed to enhance the power quality of the power system. The passive filters use energy absorbing and delivering reactive elements such as inductor and capacitors to compensate power quality problems such as power factor improvement, load balancing, power balancing, voltage regulation etc. Theses filters are not preferred due to bulky component size and possibility of resonance with the supply. The active filters include custom power devices such as Shunt Active Power Filter (SAPF). It is used for the mitigation of current based power quality problems. Dynamic Voltage Restorer is active series filter and inject the voltage in series with the supply to achieve compensation in all voltage-based power quality problems. Unified power quality conditioner (UPQC) is a combination of Shunt Active Power Filter and Dynamic Voltage Restorer (DVR). SAPF removes current harmonics and provides load and power balancing and DVR maintains flat voltage profile. Thus, it is used for mitigating both types of current and voltage-based power quality problems.

Out of the above-mentioned custom power devices, SAPF is highly preferred for mitigating current based power quality problems. Hybrid combination of passive filters and SAPF are also used. Further Phase Locked loops (PLL) control algorithms are required for mitigating voltage-based power quality problems along with SAPF. This is particularly required when the grid is weak.

The SAPF is developed and controlled using simulink models in PV integrated single phase and three phase distribution systems. The performance is analyzed under both balanced and unbalanced loads. Two configurations are classified viz off-grid standalone PV systems and PV integrated systems. PV integrated grid connected systems are best preferred solution for feeding consumer load. In off-grid mode when the fault in grid occurs or the grid voltage and current signals cross predefined limits, islanding control mode is implemented. In grid connected mode, the PV and the grid feed the load as well as charge the battery. The battery is connected through the bidirectional buck boost converter to the DC link voltage. In islanding operation mode, the battery discharges to feed the load till the grid supply is restored. The SAPF performs shunt compensation and maintains power quality.

The performance of the SAPF depends on the control algorithm employed. Controller extracts the fundamental component of load current and generate the reference current for switching pulses.

1.2 PQ Problems due to Different Load Types

Several electrical loads draw non-sinusoidal current from the supply mains. Problems due to non-linear loads include harmonics and reactive power component, saturation in magnetic circuits, resonance with the energy storage elements such as inductors and capacitors. The first category consists of solid-state devices based non-

linear loads. They use diode or thyristor-based converters such as cycloconverters, AC voltage controllers, computers, televisions etc. The other category consists of non-solid state based non-linear load such as electrical machines having saturation in magnetic circuits, arc furnaces, fluorescent lightning etc. These non-linear loads draw increased current from the supply mains in addition to the fundamental load current.

Mixed Loads are a combination of non-linear and linear loads. They consist of combination of current fed type and voltage fed type of loads. They consist of non-linear loads having solid state converter and examples are AC DC converters with LC filters. Here the converters are connected in parallel with the linear loads. Both types of loads are present in power distribution systems and need to be studied extensively

1.3 Power Quality Problems in Source Current due to Loads in Distribution Systems

Non-linear loads connected in distribution systems draw harmonics from the supply mains which deteriorate the power factor of supply current. The harmonics injected to the supply current from the non-linear load cause losses and increase the rms value of source current leading to low efficiency. These harmonics present in addition to fundamental component of source current further causes maloperation of protective equipment such as circuit breakers, relays, failure of capacitor banks, heating and derating of the equipment's in distribution systems. They also cause distortion in voltage waveform at the point of common coupling which further causes disturbance to nearby consumers.

1.4 Power Quality Problems in Grid Voltage

Several voltage-based power quality problems occurring in grid voltage due to loading

in distribution systems are voltage sag, swell, DC offset, frequency change, phase change and harmonic distortions. Voltage sag is defined when the supply voltage decreases from 0.1 pu to 0.9 pu of the normal rated rms voltage at power frequency from 0.5 cycles to 1 min. It may be caused by heavy machine loads or faults on the power line or the starting of electric motors. When the supply voltage increases from 1.1 pu to 1.8 pu of the normal rated rms voltage at power frequency, voltage swell results. It may be caused by shutting down of heavy loads, loss of generation, switching of capacitor banks. The existence of DC component of voltage or current in ac power system manifests in the form of DC offset. It occurs due to magnetic circuits in transformer and switching mismatches with the natural zero of the supply voltage. Power frequency may deviate from acceptable frequency range of 50 Hz. If there is more load demand then the frequency falls down and vice-versa. Phase change takes place due to sudden load change, switching of current and voltage. Further there is possibility of harmonic contamination in power distribution systems. Harmonics are defined as integral multiples of the fundamental frequency. They lead to distortion of voltage and current waveform, higher losses and reduced efficiency.

1.5 State of the Art

Power quality problems discussed above have become a major cause of concern in distribution systems. Non-linear load injects harmonics in to the supply due to which supply suffers from voltage based and current based power quality problems. The current based power quality problems cause load unbalancing and reactive power unbalance, voltage regulation and power factor deterioration etc [1-8]. Voltage-based power quality problems lead to voltage sag, swell, frequency, DC offset and other interruptions in grid [9-13]. The passive and active filters are used to improve the power

quality of the distribution system. Passive filters consist of LCL filters which are bulkier in size and causes resonance with the supply [14-17]. Other filters are active filters which are used for mitigating power quality problems. They are classified based on the topology as active series [18-27], active shunt [28-32] and hybrid active power filters [33-36]. Shunt Active Power Filter (SAPF) plays an important role in improving current based power quality problems in distribution systems with/without PV integration [28-32]. Fast depletion of conventional energy resources, increased price of fossil fuels and increased global warning and pollution has led to high popularity of renewable energy resources [37-39]. Among several renewable energy resources available today, photovoltaic (PV) source is pre-dominant source of renewable energy as compared to wind energy and hydro energy. It needs less area, simple maintenance, has no rotating parts and is clean pollution free energy [40-44]. PV output depends on environmental conditions such as changing solar irradiation conditions and temperature, yet being a clean source makes it suitable for integration with grid or battery storage systems.

PV based VSC converter in grid connected systems plays a crucial role and serves dual purpose of bidirectional active power transfer to the grid and load and grid currents balancing, harmonic reduction, reactive power balance and improves the power factor to unity. The VSC can be directly connected to the PV source through DC link called Single Stage Topology or can be integrated through DC-DC boost converter called Double Stage Topology. In this work, double stage topology is used. It offers various advantages of additional degree of freedom, though the device count is less in single stage. It has an increased operation region and more flexibility due to independent Maximum Power Point Tracking and VSC control algorithm used [45-49]. The non-linear nature of PV voltage with current depends on the environmental

conditions and hence requires the use of Maximum Power Point Tracking algorithms. Various MPPT algorithms are discussed in literature such as Perturb & Observe, Incremental Conductance [50-56] which help to extract maximum power from the PV array.

The interfacing of PV source with the grid connected system takes place at the PCC with the help of VSC. Non-Linear loads are also connected at PCC. These power electronic based loads are increasing day by day and are preferred due to their compactness and efficiency. They inject the harmonics in to the grid, draw reactive power which deteriorate the power quality and increase the losses. To overcome the above problems SAPF is used which does power factor correction, reactive power compensation and harmonic mitigation. Various IEEE IEC based international standards are recommended to improve the quality of power in distribution systems [57-66]. Harmonic mitigation in grid currents should follow IEEE-519 standard. It is measured in terms of Total Harmonic Distortion Factor (THD) in grid current which should be less than 5% as per IEEE-519 standard [57]. Moreover IEEE-1547 standard discusses the harmonic content in grid connected PV systems and recommends that the oscillations in PCC voltage during integration of Distributed Energy Systems is less than 5% [60-61].

The SAPF is developed using simulink environment of MATLAB in single phase and three phase distribution systems. The performance is analyzed under both balanced and unbalanced loads. In single phase SAPF, two leg topology or H bridge configuration is used where as in three phase distribution systems, a three phase, three-leg conventional topology is used. Three phase three-leg topology is the accepted topology as it is compact, less bulky and minimizes the switching losses. It does not require bulkier transformer [67-70]. The gate pulses are generated by indirect current

control technique by comparing the generated reference with the actual supply current signals [71-76]. Hysteresis current controller (HCC) scheme is used for generation of pulses for the VSC. The switching frequency does not remain constant in this scheme and the controller works in such a manner that the current remains within a fixed hysteresis band which can be selected appropriately [77-80].

The performance of the SAPF is dependent on the various control algorithms used to extract the harmonics from the non-linear load current and estimate the fundamental load current component. Different conventional and adaptive algorithms are discussed in the literature [81-159]. The performance evaluation of any control algorithm is dependent on various important aspects such as computational complexity, degree of filter, oscillations, overshoot, settling time, mean square error, PLL requirement, memory required, THD obtained fundamental current convergence under steady state and dynamic conditions.

Various conventional control algorithms are discussed in the literature [81-92] such as Synchronous Reference Frame Theory (SRFT), Instantaneous Reactive Power Theory (IRPT), Second Order Generalized Integrator (SOGI) etc. These are time based conventional algorithms. These time-based algorithms are not adaptive to load conditions and other parameter variations. Therefore, intelligent neural network-based control algorithms are discussed such as Artificial Neural Network (ANN), Fuzzy Logic Controllers (FLCs), Adaptive Neuro Fuzzy Inference System (ANFIS) [93-102] which respond well under varied conditions automatically. The comparison of the time-based conventional algorithm is made with the intelligent control algorithms.

Several real time adaptive based algorithms [103-116] are developed in literature which can be trained online by Gradient Descent Algorithms such as Least Mean

Square (LMS) algorithm, Leaky LMS, Variable LMS, Least Mean Fourth (LMF) Algorithm, Leaky Least Mean Fourth Algorithm, LMS-LMF, Normalised Least Mean Fourth, Weiner Filter, Adaptive Neuro Fuzzy Inference system based LMS. The use of various algorithms in solving power quality problems in single-phase grid connected systems is discussed in [117-137] and for three-phase grid connected systems, several algorithms are discussed in [138-159].

Synchronization of power electronic converters with the grid is essential for proper control. Indian grids are weak and suffer from voltage-based power quality problems [160-163]. The voltage signals used for synchronization suffer from problems such as voltage sag, swell, harmonics, phase angle jump, frequency change, DC offset [164-166]. These voltage-based power quality problems can be resolved with the help of both open loop and closed loop synchronization algorithms. Some of the popular synchronization techniques involve the use of phase locked loops (PLL). The phase locked loop method must detect the phase angle and frequency of the grid rapidly and precisely. The synchronization with the grid affects the stability and accuracy of the control system [167-170]. Incorrect estimation of PLL information may lead to grid crash down. The robustness of any grid is defined by Short Circuit Capacity Ratio (SCCR) [168]. It ranges from 1 (weak grid) to 3 (strong grid). The harmonics present in the load directly aggravate the problems in weak grid and disturb the voltage profile [169-172].

Various PLLs are discussed in the literature [173-187] such as Synchronous Reference Frame Theory (SRFT) PLL. This PLL is commonly used and works well under normal conditions. However, this PLL suffers from frequency and phase angle tracking in distorted grid conditions. It is necessary to overcome the disadvantage of SRFT PLL hence Decoupled Double Synchronous Reference Frame (DDSRF-PLL) is

proposed. It uses double decoupled SRFT PLL which obtains the positive and negative sequence from grid voltage but introduces time delays which causes sluggish dynamic response. Other PLLs discussed in literature are Second Order Generalized Integrator (SOGI), Cascaded Generalised Integrator (CGI) PLL, Second Order Generalized Integrator Fuzzy Logic Controller (SOGI-FLL), Mixed Second-and Third-Order Generalized Integrator (MTOGI), Discrete Fourier Transform, Notch Filter and Kalman Filtering, Enhanced Third-Order Generalized Integrator PLL, Modified SOGI-FLL and zero-crossing detector, Adaptive spline-based PLL, Digital Phase-Locked Loop and Gradient Descent Least Squares Regression Based NN have been discussed in recent years [172-186]. Appropriate PLL should be searched which overcome the issues of the weak grid and which can be implemented easily in real time.

The integration of PV integrated grid connected system with the battery energy storage system forms the microgrid. The connection of battery with the PV based system ensures the continuity of supply to the consumer loads due to varying nature of PV and also in case of interruption of grid or fault on the grid side [188-190]. The paper [191] discusses the PV interfaced system in islanded mode when battery is not connected at the DC Link. The battery cannot be directly connected at the DC link as the battery is subjected to second harmonic components, which degrades the life of the battery. The DC-DC buck boost converter is used to connect the battery at the DC link. The converter controls the dynamics and charging and discharging of the battery-controlled system [192-193]. The double stage topology of PV system is preferred as it reduces the DC link voltage fluctuations and allows the panel voltage to adjust according to MPP with the help of boost converter [194-196]. The VSC controls the frequency and voltage of the microgrid. This requires the smooth transfer from grid connected to islanded mode without disturbing the consumer load demand [195-196].

The smooth transfer should be free from voltage and current transients and be fast to respond during/after faults. This increases the robustness of the microgrid. The static transfer switch is used to ensure the transient free switching between both the modes. The instantaneous disruption in load demand leads to failure of equipment's, data loss and accidents [197-204] and must be avoided.

1.6 Objectives of Present Work

Based on the comprehensive literature review done on the power quality problems and its mitigation techniques, it has been found that the new control algorithms need to be explored for shunt active power compensation in distribution systems. Theses control algorithms must also be tested for compensating power quality problems in PV integrated grid connected systems under varying linear, non-linear and mixed loading conditions. Performance analysis of control algorithms on both single phase and three-phase grid connected systems needs detailed studies. In single phase grid connected systems, two-leg SAPF topology is used where as in three-phase distribution systems three-phase three-wire topology is used and both these are conventional and proven in the past

In this thesis, both voltage-based power quality problems and current-based power quality problems are studied. The voltage-based power quality problems consist of weak grid conditions such as voltage sag, swell, phase change, frequency change and harmonics. These problems are addressed using conventional and new phase locked loop techniques.

The current-based power quality problems consist of poor power factor, harmonics in source current, load unbalancing and reactive power unbalance. These are addressed by control techniques designed for Shunt Active Power Filter. The PV

integrated battery energy storage systems are also discussed which meet the load demand in case of varying nature of PV and during load perturbations. Performance of all these systems is discussed in detail with extensive results including experimental tests also.

1.6.1 Development of New Control Algorithms for Shunt Compensation

Real time online training-based control algorithms are discussed in single-phase and three-phase grid connected systems. Adaptive Volterra Second Order Filter (AVSF) has been discussed and developed. These algorithms use weight parameters updated by LMS algorithm.

The new area of Functional Link Neural Network based controllers is exploited in this thesis. The functional expansion of different polynomials such as Trigonometric Functional Link Neural Network (TFLNN), Legendre Functional Neural Network (LFNN) and Spline polynomials, is used to extract the fundamental component of the load current. The Bernstein Spline-based algorithm exploits the Spline properties. These have been used in signal processing [205-220] but never exploited for shunt compensation in PV integrated grid connected systems. These algorithms do not face the challenges of selection of neurons and number of hidden layers and therefore their implementation is simpler and less complex. These algorithms have been designed and developed for shunt compensation with the help of online real time training adaptive LMS algorithm and shown effective results.

1.6.2 PV Interfaced Grid Systems for Single-Phase and Three-Phase Systems

The depletion of fossil fuels and increasing environmental pollution have led to the increasing interest towards renewable energy sources such as wind, PV etc. PV is the abundant source of renewable energy with less maintenance, less area and no

moving parts. The double stage topology consisting of MPPT and boost converter is used to integrate to the grid. PV integration to both single-phase and three-phase systems is discussed in this work.

The boost converter regulates the Maximum Power Point Tracker to operate at Maximum Power Point and ensures the maximum power to be delivered to the grid. The PV based VSC ensures the bidirectional flow of active power to the grid as well as load and also performs shunt compensation of mitigating power quality problems.

1.6.3 Development of New Synchronization Techniques in Grid Tied Systems.

It is important to overcome voltage-based power quality problems such as voltage sag, swell, phase change and frequency change using well designed PLL techniques for synchronizing power electronic converters to the grid connected systems. Conventional PLL techniques developed include SRFT PLL, SOGI PLL and Adaptive PLL techniques. New synchronization techniques such as Quadratic Bernstein Functional Blending Neural Network (QB-FBNN) PLL and Functional Link Neural Network PLL have been developed in this work.

1.6.4 Performance Analysis of PV Interfaced Battery Grid Connected Systems

PV interfaced battery connected systems in grid connected and islanding mode are also discussed in this thesis. The grid mode operation is discussed in current control mode and islanding operation is discussed in voltage control mode. The SRFT and Grid Sequence Separator (GSS PLL) based control are discussed in detail for both the modes. Adequate performance results have been presented under steady state and dynamic load changes of different types.

1.7 Outline of the Thesis

The content of thesis has been divided in to following chapters:

Chapter 1 discusses various types of mixed and non-linear loading in grid connected PV distribution systems. These loads inject current and voltage harmonics in grid voltage and grid current respectively. The mitigation of both voltage and current harmonics is essential and beneficial for both supply and consumer load services. This chapter gives an overview of the thesis work in the form of state of art techniques and proposed objectives of the work.

Chapter 2 provides an extensive literature review on current based power quality problems in single-phase and three-phase grid connected systems. The literature review on the configuration of SAPF, control algorithms associated with Shunt Compensator and Phase locked Loop techniques for synchronization through conventional, Neural Network, adaptive control algorithms are discussed in detail in this chapter. It also discusses papers related to PV-integrated battery-connected systems in grid connected and islanding mode. Based on the study done, the research gaps are identified at the end of chapter.

Chapter 3 It presents the design and analysis of PV integrated grid connected systems. The configuration of SAPF in single-phase and three-phase grid connected and PV integrated grid connected battery energy storage systems is discussed. It studies the selection criterion of the calculation of DC Link voltage, DC Link capacitance and interfacing inductors in single-phase and three-phase grid connected systems. The design of PV array, inductor and capacitor of boost converter for double stage topology and design specifications of battery are discussed. The development of rating of SAPF, sensor circuits, amplifier circuits is discussed in detail.

Chapter 4 discusses the development and analysis of control algorithms for mitigation of power quality problems in single-phase grid connected PV systems using SAPF. It discusses the mathematical control of the conventional and adaptive algorithms such as Synchronous Reference Frame Theory (SRFT), Second Order Generalised Integrator (SOGI), Trigonometric Functional Link Neural Network (TFLNN), Legendre Functional Neural Network (LFNN). The performance analysis of the algorithms is discussed using simulation and hardware under varying loading conditions. A suitable comparison of the algorithms is also considered.

Chapter 5 discusses the implementation of algorithms for control of three-phase three-leg SAPF for mitigation of power quality problems in three-phase grid connected systems. The mathematical design analysis of three-phase SRFT, Dual-SOGI and Cubic Bezier-Functional expansion based Adaptive Filter (CB-FEBAF) is discussed in detail. The performance analysis of different algorithms is discussed using simulation and hardware studies. The chapter concludes by analysing in detail the different aspects of these techniques in terms of performance.

Chapter 6 This chapter presents the weak grid connected systems suffering from voltage sag, swell, harmonics, DC offset in grid connected systems. Various PLL are developed for synchronization and tested under single-phase non-ideal and weak grids. The Phase Locked Loop (PLL) Techniques such as Synchronous Reference Frame Theory (SRFT-PLL), SOGI-PLL, Fractional Delay Newton Structure for Lagrangian Interpolation (FD-NSLI) PLL, Quadratic Bernstein Functional Blending Neural Network (QB-FBNN) PLL are discussed. The performance analysis of the proposed PLL is studied in MATLAB Simulink and through hardware prototype developed in the laboratory under varying grid conditions. The steady state and

dynamic performance analysis for detecting the phase angle accurately and generating sinusoidal unit template under weak grid conditions are discussed in detail.

Chapter 7 In this chapter, the simulation, design and performance analysis of PV interfaced battery connected system in grid connected and islanding mode is discussed. The grid mode operation is discussed in current control mode and islanding operation is discussed in voltage control mode. The SRFT and Grid Sequence Separator (GSS) PLL control are discussed in detail in both the modes. Simulation results have been shown for the improvement of PQ of PV interfaced battery system.

Chapter 8 discusses the future scope of work and conclusion of the thesis.

CHAPTER 2

LITERATURE SURVEY

2.0 General

PQ issues have caused major problems in power distribution systems. Non-linear loads inject harmonics in the grid which deteriorate both grid voltage and grid current. The grid current related problems can be solved by Shunt Active Power Filter (SAPF). The SAPF is designed to improve power factor, harmonics in source current, performs load balancing and reactive power balance. The grid voltage related issues such as voltage sag, swell, DC offset, harmonics are addressed by the Phase Locked Loop techniques. They generate the sinusoidal unit in phase template even under weak grid conditions for generation of reference current signals. Phase Locked Loop Techniques are needed for synchronizing the power electronic equipment with the grid. PLLs track the phase angle and the grid voltage while synchronizing. New and adaptive neural network controllers are used for mitigation of power quality problems for SAPF in single-phase and three-phase grid connected systems. The adaptive PLL techniques are designed for mitigating grid voltage problems. A three-leg SAPF is realized in three-phase and two-leg H-bridge based VSC is realized in single-phase grid connected systems. The SAPF is realized by connecting VSC in parallel with the DC Link capacitor. The integration of PV and battery connected systems is studied in grid connected and islanding mode. The Static Transfer Switch (STS) is used for smooth transfer between both the modes. The battery dynamics are controlled by bidirectional DC-DC converter.

2.1 Literature Survey

Current based and voltage-based power quality problems are discussed in this section. There are various voltage and current based power quality problems. The voltage-based power quality problems in grid include voltage sag, swell, harmonics, voltage flicker, DC offset, phase angle change, frequency change, fluctuations and notches. The current based power quality problems are poor power factor, reactive power burden, harmonics current, unbalanced currents. The power quality problems and solutions are discussed as follows.

2.1.1 Power Quality Problems and Solutions

Power distribution systems feed a variety of loads-linear loads, mixed loads and non-linear loads. Non-linear loads consist of solid-state devices. They use cycloconverters, AC voltage controllers, computers, televisions etc. [1-4]. The solid-state devices have many benefits of lower cost, reduced maintenance and less wear and tear. Moreover, the non-linear loads inject harmonics in to the system [5-8]. Power quality problems related to current drawn from the AC mains are poor power factor, reactive power burden, harmonics current, unbalanced currents. They cause voltage harmonics, spikes, notches, voltage dip, voltage swell at the point of common coupling [9].

The voltage-based power quality problems in grid such as voltage sag, swell, voltage sag, swell, harmonics, voltage flickering, DC offset, phase angle change, frequency change, fluctuation and notches [10-11]. The paper [12] discusses the voltage sag and swells. Voltage sag [12] is defined as decrease in the supply voltage from 0.1 pu to 0.9 pu of the normal rated voltage. Voltage swell [12] is defined as increase in supply voltage from 1.1 pu to 1.8 pu of the normal rated rms voltage at power frequency. The paper [13] discusses the voltage harmonics, voltage flicker, fluctuations and transients in current.

Active and passive filters are suitable and designed for mitigating power quality problems. Passive filters use inductors and capacitors to compensate power quality problems but they are bulky in size and causes resonance with the supply [14-15]. Passive Filters are used for suppressing voltage and current harmonics in the supply system. Theses filters are classified as tuned filters, damped filters and combination of both filters based on topology. They can be further classified as shunt filter, series filter and combination of both based on connection. The combination of shunt and series filter is called Hybrid Passive Filter [16-17]. Active Filters are classified based on the basis of configuration of power converters. They are used to mitigate power quality problems [18-21]. These topologies are generally classified as active shunt, series or combination of both.

Active Series filters are used to eliminate voltage-based power quality problems such as sag, swell, harmonics. It is connected in series with the AC supply system to inject the required voltage to safeguard the sensitive loads [22-24]. Dynamic Voltage Restorer may also be used for damping out harmonics caused by resonance of passive filters with the supply [25-27].

Active shunt filter is used for mitigating current based power quality problems. They perform power factor correction, reactive power compensation, harmonic mitigation and load balancing [28-29]. The semiconductor device for using SAPFs is Insulated Gate Bipolar Transistor (IGBT). Initially Bipolar Junction Transistor (BJTs), Metal-Oxide Semiconductor Field-Effect Transistor (MOSFET), Gate Turn off Transistor (GTOs) were used to design SAPF but the development of IGBTs has revolutionized the area of power electronics. The advancement in sensor technology such as Hall effect voltage and current sensors has further improved the performance

of SAPF. Moreover, the enormous development in Digital Signal Processing (DSP) technology helps to implement VSC based complex control algorithms fast [30-34].

The combination of active shunt and active series filter improves both voltage related and current related power quality problems. Unified Power Quality Conditioner (UPQC) improves both voltage based and current based PQ problems. The shunt compensator part is equivalent to SAPF and it compensates current based PQ problems while the series compensator part equivalent to a DVR compensates voltage-based power quality problems [35-36].

2.1.2 Integration of Renewable Energy Resources to the Grid

These days integration of renewable energy resources with the grid is increasing due to the increased price of fossil fuels, increased global warming and pollution. However, photovoltaic sources have gained importance compared to other renewable energy resources due to availability of solar energy in abundance. In PV based VSC the efficiency of the SAPF is increased as it performs dual function of bidirectional flow transfer and as well as shunt compensation. Therefore, VSC does not remain idle but performs all the time [37-41]. The PV feedforward term is added to mitigate DC link voltage fluctuations during integration of renewable energy resources [42-43]. The VSC may be directly connected to the PV source through DC link referred to as Single Stage Topology or can be integrated through DC-DC boost converter based Double Stage Topology. In this thesis, Double Stage Topology is used. It offers various advantages of reducing the control complexity though the device count is less in single stage, it has an increased operation region and more flexibility due to independent Maximum power point tracking techniques. The solar PV power being non-linear in nature uses maximum power techniques which vary the duty cycle of boost converter array to attain maximum power from the PV [44-49]. The papers [50-56] discusses the

comparison of various MPPT techniques such as Fractional Open-Circuit Voltage (FOCV), Perturb and Observe, Incremental and Conductance [49], Fuzzy Logic Technique, Artificial Neural Network. The paper [50] discusses the Takagi-Sugeno Fuzzy logic Method. Fast current based MPPT technique based sliding control method is discussed in [51]. These Maximum Power Point algorithms and VSC control algorithm are used and further increase the stability of the system.

2.1.3 Power Quality Standards

The international standards related to power quality has been developed by various organizations such as Institute of Electrical and Electronics Engineers (IEEE) and International Electro Technical Commission (IEC). These standards are developed, updated and imposed to maintain the power quality level [57-58].

IEEE-519 [59] standard recommends that the THD of supply voltage and current in distribution systems in presence of non-linear loads be less than 5%. IEEE 1547 standard recommends the procedure for interconnecting distributed energy resources [60-61]. IEEE 1100 standard regulates the electric power and grounding maintenance practices, their design and installation [62]. IEEE-1159 [63] standards monitor the electric power characteristics in single-phase and polyphase system. IEEE 1459 standard is recommended for measurement of electric power quantities such as active power, reactive power, apparent power, power factor and Total Harmonic Distortion (THD) Factor [64].

Several other IEC standards are there such as IEEE 61000-4-15 which recommends the design specification of Flicker Meter [65]. IEC 61000-3-2 recommends the limits on Harmonic Current Emissions [66]. All the above standards ensure the proper operation of power system distribution systems.

2.1.4 Configuration of SAPF System

In single-phase SAPF two-leg topology is used where as in three-phase distribution systems three-phase three-wire topology is used. Three-phase Three-wire topology is the accepted topology as it is compact, less bulky, minimizes the switching losses. It does not use bulkier transformer [67-70]. The generation of reference current methods is by direct and indirect control technique [71-76]. It is found that the direct control technique is better than indirect control technique. The comparison between the Hysteresis Current controller and Dead-Beat current controller for SAPF is done. HCC performs better than Dead Beat Controller [77-80].

2.1.5 SAPF Control Algorithms

SAPF are used for improving PQ problems in distribution system. The effective implementation of control algorithm enhances the performance of the SAPF

2.1.5.1 Conventional Control Algorithms

Many time domain conventional control algorithms are discussed in the literature [81-92]. This includes Synchronous Reference Frame theory [81-82], Instantaneous Reactive Power Theory [83], Power Balance Theory [84-85], I-cosϕ algorithm in [86] through three-phase three-wire system. The comparison between these algorithms for power quality improvement is described in [87]. They require the tuning of PI controllers. Algorithms such as SRFT, IRPT-O, IRPT-R to improve power quality for three-phase four-wire distribution system is discussed in [88-90]. A four-leg VSI configuration is used to get improved results in unbalanced systems and also the current in the neutral wire is controlled to its acceptable levels but TPFW system is more complex than TPTW system due to extra neutral wire. Hence, three-phase three-wire distribution system is preferred and is used in this thesis [91-92].

2.1.5.2 Neural Network Based Control Algorithms

An artificial neural network is made up of several layers, including an input layer, a hidden layer, and an output layer. The hidden layer consists of number of neurons having fixed activation function [93-94]. These layers are trained in offline mode. These neurons of the hidden layers are updated by adjustable weights to pass signals forward to other neurons. The neural network face challenges in selection of neurons and hidden layers. Artificial neural network for shunt compensation is shown in [95-97], Fuzzy Logic Controller in [98], Adaptive Neuro Fuzzy Inference system in [99-102]. These NN are trained offline using training data which may be cumbersome and difficult. Therefore, various gradient methods are introduced which perform real time training of Neural Networks (NN) for PQ improvement [103-104].

2.1.5.3 Adaptive Control Algorithms

Adaptive Control Algorithms work on the real time training of algorithm using several techniques such as Levenberg Marquardt Algorithm [104-105]. The adaptive techniques respond fast to changing environment and load conditions online. Unlike the neural network they are not trained offline. LMS algorithms are developed [106], Several variations include Leaky LMS in [107], Variable LMS [108-109], Least Mean Fourth Algorithm in [110-111], Leaky Least Mean Fourth Algorithm in [112], LMS-LMF in [113], Normalized Least Mean Fourth in [114], Weiner Filter in [115], Adaptive Neuro Fuzzy Inference system based LMS in [116] discussed in literature.

2.2 SAPF Applications to Single-Phase Grid Connected System

The single-phase grid connected systems feed linear and non-linear loads. The non-linear loads inject harmonics in to the supply system. Therefore, algorithms are developed which mitigate power quality problems in single-phase grid connected

systems. Adaptive linear combiner filter-based control scheme is developed in [117], Multilayer Fifth order generalized Integrator in [118], PNKLMS based algorithm in [119], Lyapunov Function in [120-121], LQR control in [122], Godzel Algorithm in [123], Adaptive Neuron Detection in [124], Single-phase inverter system with non-linear inductor consideration in [125], predictive controller in [126], Linear Quadratic Regulator in [127], Adaptive proportional resonant controller in [128], ANOVA Kernel Kalman Filter in [129], adaptive backstepping control technique in [130], Backstepping Controller with Dual Self-Tuning Filter in [131], Adaptive Neural Filtering in [132], GI-Based Control Scheme in [133], Optimal control scheme in [134], Two PWM techniques using direct current control strategy in [135] , LTI-EPLL based control algorithm in [136], Frequency Adaptive Notch Filter for Power Quality Improvement in [137]. Theses above algorithms are implemented in single-phase grid connected systems.

2.3 SAPF Applications to Three-Phase Grid Connected Systems

Three-phase grid connected systems face power quality problems such as harmonics in supply current injected due to load, poor power factor, load unbalancing etc. Various control techniques [138-159] techniques are developed in literature such as Nishant et. al presented PNKLMF based technique for power quality improvement [138], Kalman filter in [139-140], Extended Kalman Filter in [141], P. Shah [142] discussed FOGI-FLL, Badoni et. al [143] discussed Euclidian based control technique, Chittora et. al [144] discussed Chebyshev technique, B. Singh et. al discussed Laplacian Regression Technique [145], MGI control in [146], ILST control algorithm in [147], Recursive Digital Filter in [148], QNBP NN-based I cos ϕ in [149], Jain et al discussed HTF-Based Higher-Order Adaptive Control [150], Predictive model control in [151],

Rahamani et.al discussed Lyapunov control in [152], Naive Back Propagation based I-cosϕ in [153], Learning based Anti-Hebbian in [154], Variable Forgetting Factor Recursive Least Square Control Algorithm in [155], Conductance based fryze in [156], Fast Zero Attracting Normalized Least Mean Fourth Based Adaptive Control in [157] and JAYA Optimization based control algorithm in [158], Leaky Least Logarithmic Absolute Difference based control in [159]. These above algorithms are implemented in single-phase grid connected systems.

2.4 PLL Control Algorithms

The grid voltage related issues such as voltage sag, swell, DC offset, harmonics are addressed by the Phase Locked Loop techniques [160-165]. They generate the sinusoidal unit in phase template under weak grid conditions for generation of reference current signals. The Phase Locked Loop Techniques are used for synchronizing the power electronic equipment's with the grid. PLLs track the phase angle and the grid voltage while synchronizing [166-172]. The accurate estimation improves the performance of the power electronic converters. Various PLLs are described in the literature [173-187]. SRFT PLL is discussed in [173-174]. SOGI PLL works well under accurate phase tracking but do not work well under DC offset [175-176]. Delay Based PLL structure has been used however they suffer from double frequency estimation [177]. To overcome various modified SOGI versions have been introduced such as Cascaded Delayed Generalized Integrator (CGI) PLL [175], mixed third order generalized integrator (MTOGI) [176] and SOGI FLL [184] have been introduced. In MTOGI extra integrator is added, CGI PLL has two SOGI transfer function in series, SOGI FLL has fuzzy logic concept added making is more complex. The modification in SOGI has made its dynamic response becomes slow due to increase in order of SOGI

function. Cascaded Delayed Signal Cancellation (CDSC) PLL and Moving Average Filter (MAF) PLL have also been proposed but they donot work well under frequency change [178-179]. To overcome the problems faced in synchronization various PLL has been introduced such as Discrete Fourier Transform [180], Notch Filter [181] and Kalman Filtering [182] have been discussed in recent years, Enhanced Third-Order Generalized Integrator PLL in [183], modified SOGI-FLL and zero-crossing detector [184], Adaptive spline-based PLL in [185], Digital Phase-Locked Loop in [186] and Gradient Descent Least Squares Regression Based NN in [187].

2.5 PV Battery Interfaced Control Algorithms

PV interfaced battery connected systems in both grid connected and islanded mode have also been discussed in literature. The current control mode is used in grid connected mode and voltage control is used in islanding condition [188-190]. Current control mode is developed to improve power quality problem and voltage control mode provides synchronization in the absence of utility grid [191-194]. Various algorithms for PV based Battery interfaced systems are available in the literature. These include unified control management scheme in [195], Improved Frequency Regulation in an Islanded Mixed Source Microgrid through coordinated operation of Distributed Energy Resources (DERs) and Smart Loads [196], Frequency Adaptive Multistage Harmonic Oscillator in [197]. Normalized Gradient Adaptive Regularization Factor Neural Filter [198], Advanced robust shrinkage normalized sign (ARSNS)-based control algorithm in [199], Multivariance Generalized Adaptive controller [200], Varying phase angle control in isolated bidirectional DC–DC converter in [201], Control of Battery in fixed and variable power mode in [202], Learning Quantization (LQ) based current control in

[203], Adaptive frequency locked loop (FLL) with comb filtering is described in [204]. The above PLLs are tested under both grid connected and islanded modes.

2.6 Identified Research Areas

Based on the extensive literature review, following research gaps are identified:

1. Intelligent control algorithms such as Fuzzy and Neural Network etc. involve the challenging task of selection of hidden layers and its training with the standard data to get precise results. This increases the computational processing time. Therefore, algorithms based on single-layer neural network or simplified versions may be exploited used for extraction of harmonics from distorted load current. These techniques have not been extended for controller development.

2. Multifunctional Capabilities of inverter have not been exploited much such as PQ improvement, Voltage regulation, MPPT Techniques, PQ compensation etc.

3. Advanced control techniques for single-phase and three-phase grid connected PV system for improvement in power quality are required to be tested and developed. Some advanced techniques have been studied for shunt compensators (DSTATCOM); however, these can be modified in the presence of PV source requires thorough study, investigation, and performance analysis.

4. Modification of control techniques considering polluted grid, weak grid needs to be addressed. Also, a fair comparison of these is required based on both simulation and experimental studies.

2.7 Objectives of Current Research

1. Simulation and Development of new control algorithms for shunt compensation.

2. Design and Control for PV interfaced grid systems and study its performance analysis of single-phase and three-phase systems.

3. To analyze the impact of voltage distortion, sag, swell, harmonics in grid tied PV systems.

4. Simulation, design and performance analysis of PV interfaced system with additional resource such as battery and developing modified controllers for the same.

2.8 Conclusions

Exhaustive research work has been done in the area of mitigating power quality problems in grid connected distribution systems. Current based power quality problems are mitigated by shunt compensator. Voltage-based power quality problems are mitigated by Phase Locked Loop Techniques. Battery interfaced PV systems are also developed and controlled in grid connected and islanding mode. It has been observed after extensive literature study that there exists a scope to develop algorithms for shunt compensation and Phase Locked Loop techniques which are less complex, fast, accurate and has less computational burden. Algorithms based on LMS based adaptive techniques are quite prevalent in the literature; however, the use of functional NN based controllers is a new area. The study of such functional NN [205-220] based on Legendre, Trignometric, Cubic-Beizer, Quadratic Bernstein and Lagrangian polynomial [205-220] and others is new and requires in depth performance evaluations with respect to conventional techniques. They have been used in digital signal processing applications but not exploited in shunt compensation and Phase Locked Loop Techniques. PV based battery interfaced systems in both grid connected and islanding mode need to be explored and tested using new algorithms.

CHAPTER 3

DESIGN AND ANALYSIS OF PV INTEGRATED GRID CONNECTED SYSTEMS

3.0 General

In this chapter, Shunt Active Power Filter (SAPF) is designed for performance analysis of single-phase and three-phase grid connected PV systems. New Controllers are developed using adaptive control techniques and tested rigorously on the prototype/hardware developed under different system conditions. The configuration of the grid connected system comprises grid supply, voltage and current sensors, SAPF, linear and non-linear loads, diode bridge rectifier, interfacing inductor and the DC link capacitance. This chapter discusses the SAPF configuration for single-phase and three-phase power distribution systems and the important design parameters involved.

3.1 System Configuration of SAPF in Grid Connected System

This section discusses the conventional H-bridge and three phase three-leg voltage source converter topology used in single phase and three phase systems respectively.

3.1.1 System Configuration of SAPF in Single-Phase Grid Connected System

The proposed system consists of a PV integrated grid connected distribution systems feeding linear and non-linear loads connected at the PCC. Non-Linear load is modelled using diode bridge rectifier with series R-L load. Fig. 3.1 shows the system diagram with source impedance Z_s (source resistance R_s and inductance L_s), interfacing inductor L_f, ripple filter R_c, diode bridge rectifier, VSC with DC link capacitance all collectively connected at PCC. The conventional H-bridge configuration is selected for the VSC with four IGBT and antiparallel diodes. SAPF with the help of suitable control

algorithm sends the compensating current to mitigate harmonics in grid currents injected by non-linear load. It also improves power factor to nearly unity, makes grid

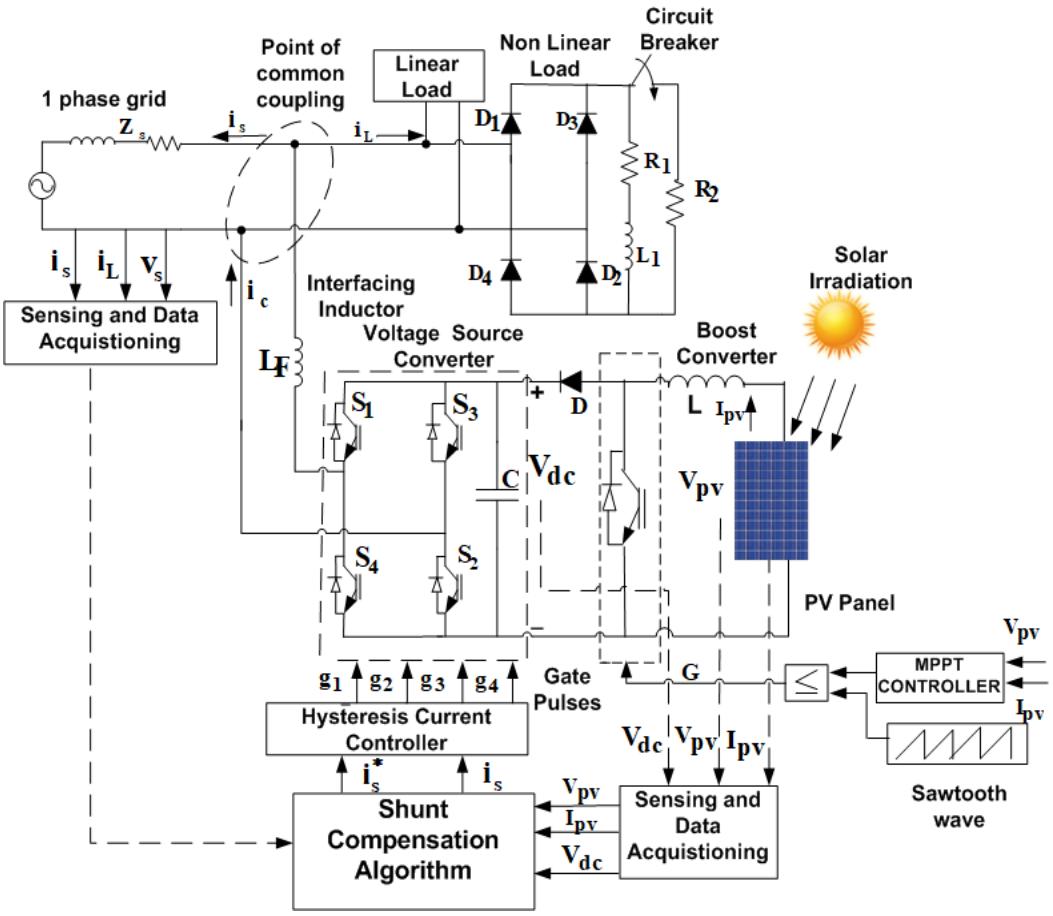

Fig. 3.1. Schematic block diagram of single-phase grid connected PV system

current sinusoidal and provides reactive power compensation. A PV array capacity of 750 W is connected at the DC link of the VSC through boost converter. The Perturb and Observe (P&O) MPPT algorithm regulates the duty cycle of the DC-DC boost converter to extract the maximum power from the PV array. The H-bridge VSC performs dual function of active power transfer to the grid as well as shunt compensation. The DC link voltage is regulated using a tuned PI controller. The interfacing inductor are used to minimize ripples in the compensating current. The simulation and experimental parameters are listed in Appendix I.

3.1.2 System Configuration of SAPF in Three-Phase Grid Connected System

The configuration of the PV integrated three-phase grid connected system is shown in Fig. 3.2. It consists of three-phase grid, VSC converter connected in parallel to the system and loads. The three-phase, three-leg configuration comprising six IGBT switches with antiparallel diodes is selected for VSC. The VSC is coupled to DC Link capacitor is referred to as Shunt Active Power Filter. Further, the specification of interfacing inductors, boost converter and PV array are determined and connected. The boost converter with the help of MPPT P&O algorithm helps in extracting the maximum power from the PV array. The interfacing inductor is used to minimize the

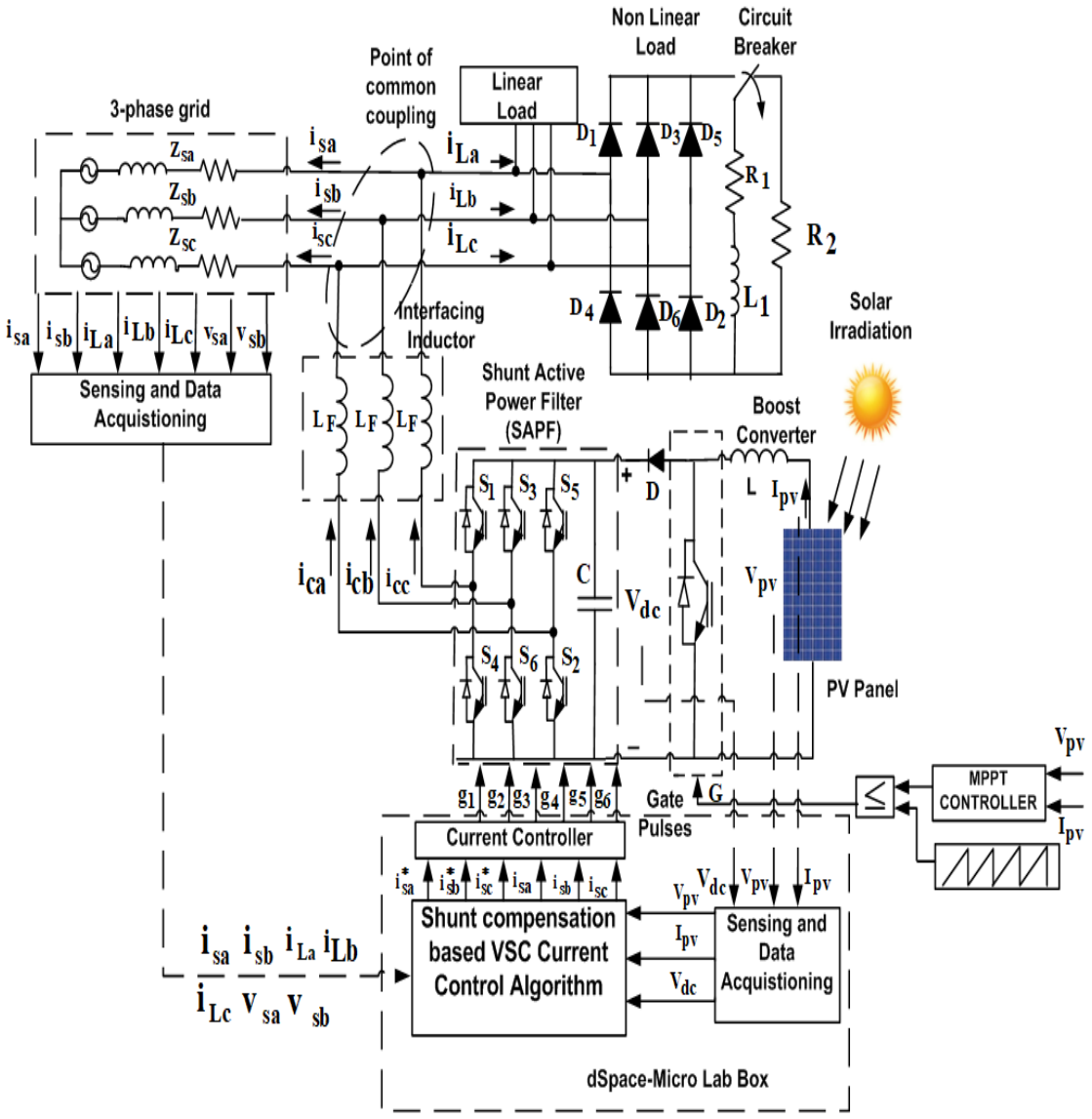

Fig. 3.2. Schematic block diagram of three-phase grid connected PV system

ripples in the compensating current. The SAPF is used in mitigating power quality problems with the help of suitable control algorithms and this is discussed in successive chapters. The DC link voltage is controlled with the help of PI controller. The simulation and experimental parameters are listed in Appendix II.

For the experimental verification, the single-phase and three-phase three wire grid connected systems are developed in the laboratory. The grid supply is varied through autotransformer. The load, compensator are connected at the point of common coupling (PCC). The compensator is realized in the form of H-bridge configuration for single-phase system, while a three-phase, three leg configuration is selected for three-phase system. SAPF comprises a VSC with DC link capacitance connected in parallel. The interfacing inductors are suitably designed to minimize switching ripples in the SAPF connected at PCC. The voltages and current are sensed and measured with the help of Hall effect sensors viz. LEM LA25 and LV25 current and voltage sensors respectively. The sensed voltage and current signals are processed and necessary computations are carried out inside the Microlab Box which produces the six gating signals for the SAPF. The performance of steady state and dynamic waveforms are recorded using Digital Storage Oscilloscope (DSO).

3.1.3 System Configuration of PV interfaced Grid connected Battery Energy Storage system (PV-BES System)

The schematic diagram of PV-BES system is shown in Fig. 3.3. It consists of PV array, MPPT control algorithm, Boost Converter, Battery Energy Storage System, Bidirectional Buck Boost Converter, non-linear loads. The MPPT algorithm is used to extract the maximum power from the PV array by regulating the duty cycle of DC-DC boost converter. The PV array is connected to the battery at DC link through Bidirectional Buck Boost converter. The Bidirectional converter operates by working

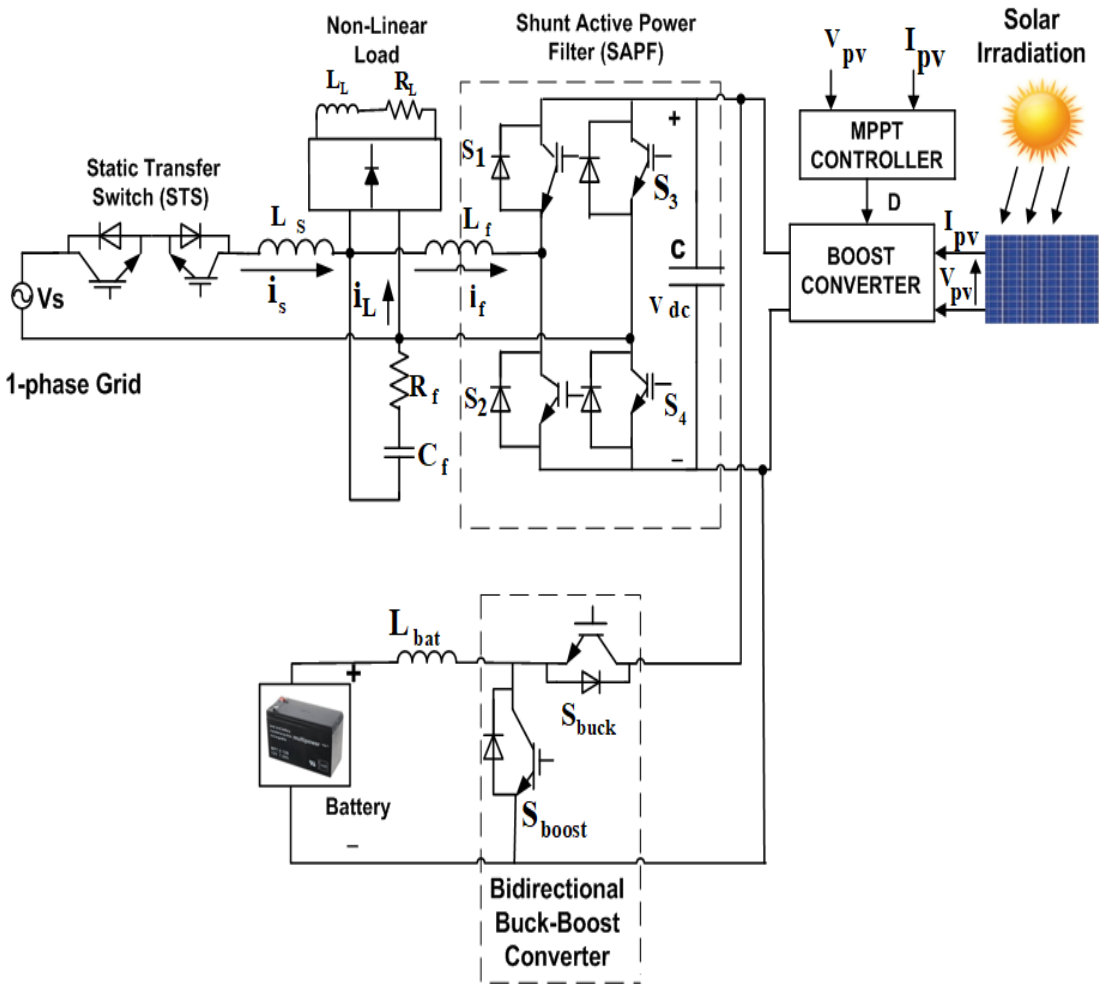

Fig. 3.3. Schematic block diagram of battery interfaced PV integrated grid connected system

in the two modes viz charging and discharging mode in buck and boost mode respectively. A static transfer switch (STS) is connected for bidirectional power flow and smooth transfer between both the grid connected and islanded modes. In grid connected mode, current control mode is used to control VSC for harmonic compensation and supply of active power. In islanded mode of operation, voltage control mode is used to control VSC.

3.2 Design Aspects of Shunt Compensator System

The design details of various parameters of SAPF integrated systems are discussed below. This Section includes calculations for DC link voltage, DC link capacitance

and interfacing inductor. Design is discussed for both single phase and three phase systems.

3.2.1 Design of Single-Phase systems [1]

The selection criterion of the above parameters in single-phase system are presented here

3.2.1.1 Calculation of DC Link Voltage

$$V_{dc} = \sqrt{2}V_{rms} = \sqrt{2} * 110 = 155.56\,V \quad (3.1)$$

The DC link voltage should be higher than the peak of single-phase grid voltage. Hence, the DC Link voltage is chosen as 200 V

3.2.1.2 DC Link Capacitance

Using the energy stored in the DC link capacitor (C_{dc}) we get

$$\frac{1}{2}C_{dc}(V_{dc}^2 - V_{dc1}^2) = K_1 V_{rms} aIt$$

$$C_{dc} = \frac{2*K_1 V_{rms} aIt}{(V_{dc}^2 - V_{dc1}^2)} \quad (3.2)$$

where C_{dc} is the DC Link Capacitance. V_{dc} is the DC link voltage equal to reference DC link voltage and V_{dc1} is the calculated minimum level of DC link voltage, V_{rms} is the rms grid voltage, I is the phase current, a is the overloading factor. K_1 is the constant. Putting the values $K_1 = 0.5$, $V_a = 110V$, $I_{ph} = 20A$, t=0.02s, $V_{dc} = 200V$, $V_{dc1} = 155.56V$, $a = 1.2$. We get $C_{dc} = 3341\mu F$. Therefore, the chosen value of $C_{dc} = 3000\mu F$

3.2.1.3 Interfacing Inductor

The interfacing inductor is used for calculation of minimizing ripples in the

compensating current. It depends on the switching frequency f_s, ripple in current I_{crpp} and DC link voltage V_{dc} .

$$L_f = \frac{m*V_{dc}}{4*a*f_s I_{crpp}} = \frac{1*200}{4*1.2*10*10^3*1.5} = 2.77\ mH = 3mH \quad (3.3)$$

where 'm' is the modulation index, a is the overloading factor. The chosen value of L_r is 3 mH.

3.2.2 Design of Three-Phase systems [1]

The formulae calculation in three-phase system are listed

3.2.2.1 Calculation of DC Link voltage

The minimum DC voltage should be greater than the calculated voltage. It is computed as

$$V_{dc} = \frac{2\sqrt{2}V_{LL}}{\sqrt{3}\,m} \quad (3.4)$$

$$= \frac{2\sqrt{2}*110}{\sqrt{3}*1} = 179.60\ \text{V}$$

where V_{dc} is the DC Link Voltage, V_{LL} is the grid line rms voltage, m is the modulation index. The voltage is chosen as 200 V.

3.2.2.2 DC Link Capacitance

The principle of energy transformation in the DC link capacitor is applied as

$$\frac{1}{2}C_{dc}(V_{dc}^2 - V_{dc1}^2) = K_1 3V_{ph}\ aIt$$

$$C_{dc} = \frac{2*K_1 3V_{ph}\ aIt}{(V_{dc}^2 - V_{dc1}^2)} \quad (3.5)$$

Putting the values $K_1 = 0.05, V_{ph} = 89.5V, I_{ph} = 25\ A$, t=0.02s, $V_{dc} = 200V, V_{dc1} = 179.60V$, $a = 1.2$. We get $C_{dc} = 2081\mu F$. Therefore, the chosen value of $C_{dc} = 3000\mu F$

where C_{dc} is the DC Link Capacitance. V_{dc} is the DC link voltage equal to reference DC link voltage and V_{dc1} is the calculated minimum level of DC link voltage, V_{ph} is the rms three phase grid voltage, I is the phase current, a is the overloading factor, K_1 is the constant.

3.2.2.3 Selection of an Interfacing Inductor

The interfacing inductor used for calculation of minimizing ripples in the compensating current depends on the switching frequency f_s, ripple in current I_{crpp} and DC link voltage V_{dc} .

$$L_f = \frac{\sqrt{3}*m*V_{dc}}{12\ af_s I_{crpp}} \tag{3.6}$$

$$=\frac{\sqrt{3}*1*200}{12*1.2*10*10^3*2.5} = 0.962 \text{ mH} = 1\text{mH}$$

where $V_{dc} = 200V$ is the reference DC link voltage, $f_s = 10kHz$ is the switching frequency, $I_{crpp} = 2.5A$ is the current ripple.

3.2.3 Rating of switches of SAPF

The Insulated Gate Bipolar Transistors (IGBT) switch is being used for design of Shunt Active Power Filter (SAPF). The rating of these IGBT switches selected depend on the switching frequency (f_s) and current maximum level (I_m) to be attained. Considering the f_s to be 10 kHz and I_m to be attained is 25 A, the IGBT module selected is SKM150GB12V. Fig. 3.4 shows the internal connection diagram of IGBT switches used. Two such modules are used for single-phase SAPF and three such modules are

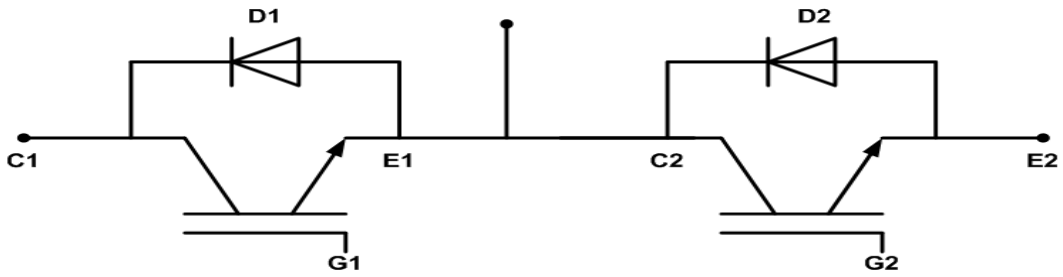

Fig. 3.4. Internal connection diagram of IGBT module

used for three-phase SAPF. The internal connection diagram of IGBT module is shown in Fig. 3.4.

3.2.4 Design of sensor circuits, amplifier circuit

LV-25 P voltage has an input voltage range of 0-500 V. The maximum primary input nominal current cannot exceed the 10 mA. To measure the input voltage of 110 V, the input side resistance is chosen as

$$R_{in} = \frac{V_{in}}{I_{in}} = \frac{110}{10*10^{-3}} = 11k\Omega \quad (3.7)$$

The minimum wattage of input side resistance should be

$$P_m = V_{in} * I_{in} = 110 * 10 * 10^{-3} = 1.1W \quad (3.8)$$

For DC link voltage 200 V

$$R_{in} = \frac{V_{in}}{I_{in}} = \frac{200}{10*10^{-3}} = 20\ k\Omega \quad (3.9)$$

The minimum wattage of input side resistance is selected to be 2W. Using

$$P_m = V_{in} * I_{in} = 200 * 10 * 10^{-3} = 2W \quad (3.10)$$

From above, the values of input resistor have been optimized for a supply voltage of 110V and DC Link voltage of 200V at 47kΩ. The power rating of resistance of input voltage is 110V is taken as 2W and for 200V is taken as 5W respectively. The output signals from theses sensors are fed to the dSpace 1104 through ADC port. The output voltage from the dSpace 1104 is 5V. This is amplified to 15V with the help of voltage amplifier circuit and given to the gating signal of SAPF. The inverting amplifier of IC 7406 is used to nullify the effect of 180^ophase shift.

3.2.5 Linear and Non-Linear Loads

In single-phase and three-phase systems the linear loads of rating $250V, 24A$

are connected. Non-Linear loads are connected through diode bridge rectifier. The DC side of the diode bridge rectifier has a load of variable resistor (20-120Ω) and fixed inductor of 80mH.

3.2.6 Design of PV array

PV module of Kyocera Solar KD320GX-LPB available in the Simulink library has been used with the below specifications. PV panel specifications: Kyocera Solar KD250GX-LFB2,

Maximum power P_{mp} = 250.022W
Open circuit voltage V_{oc} = 36.9V
Short circuit current I_{sc} = 9.09A
Maximum voltage, V_{mp} = 29.8V
Maximum current I_{mp} = 8.39A
Series connected module per string = 3
cells per module = 60
parallel solar strings = 1
temperature coefficient of voltage (%/°C) = −0.32
temperature coefficient of current (%/°C) = 0.06
For hardware we have selected
Chroma PV Simulator: PV panel Specifications: EN50530,
Solar Irradiation: 1000 W/m^2
P_{mp}=300W
Temperature Coefficient of Voltage (%/℃)=-0.38.

3.2.7 Design of inductor and Capacitor of Boost Converter [110]

$$L_b = \frac{D*V_{mp}}{\Delta I_{PV}*f_{sw}} = \frac{0.5*40.1}{0.81*10*10^3} = 4.95mH \quad (3.11)$$

L_b is calculated as 4.95mH and taken as 5mH, where D is the duty cycle, V_{mp} is the voltage at maximum power, ΔI_{PV} is the ripple in inductor current, f_{sw} is the switching frequency of IGBT

$$C_b = \frac{D*I_{out}}{\Delta V_{out}*f_{sw}} = \frac{0.5*10}{10*5*10^3} = 100\mu F \quad (3.12)$$

C_b is the calculated as 100μF and taken as 150μF, where D is the duty cycle, I_{out} is

the output current, ΔV_{out} is ripple in boost output voltage i.e 10% of the output voltage V_{out}, V_{out} is 100V.

3.2.8 Design specifications of Battery [192]

The design specifications for battery integrated system shown in Fig. 3.3 are described. Here the Lead Acid Battery of 120V,20Ah is taken as the battery capacity, Initial state of charge=90%, Battery response time=0.1s.

A bidirectional converter operation is designed. In buck mode, the inductor filter design is carried out as

$$D = \frac{V_b}{V_{dc}} = \frac{120}{200} = 0.6 \quad (3.13)$$

$$L_b = \frac{D(V_{dc}-V_b)}{\Delta I_L * f_{sw}} = \frac{0.6*(200-120)}{5*10^3*0.1*7} = 1.37mH \quad (3.14)$$

In boost mode,

$$D = \frac{V_{dc}-V_b}{V_{dc}} = \frac{200-120}{200} = 0.66 \quad (3.15)$$

$$L_b = \frac{V_b\, D}{\Delta I_L * f_{sw}} = \frac{120*0.66}{5*10^3*0.1*7} = 2.26\text{mH} \quad (3.16)$$

Therefore, the required value of inductor chosen is 3mH. Here V_b is the battery voltage, V_{DC} is the DC Link voltage and ΔI_L is the charging current which is considered as 20% of f_{sw} where f_{sw} is the frequency of switching which is considered as 5kHz.

3.3 Mathematical Analysis of Control Strategy of SAPF

Mathematical control strategy operation of PV- SAPF involves two operations (i) MPPT Control (ii) VSC switching control. MPPT control is used to extract the maximum power from the PV array. VSC switching control involves estimation of fundamental load component, DC link voltage regulation and switching losses, PV-feedforward component, estimation of unit templates and reference current generation.

Different controllers have been designed and discussed in the subsequent sections and chapters

3.3.1 MPPT Algorithm [47]

P&O algorithm is used to extract the maximum power from the PV array by regulating the duty cycle of the boost converter. It is the simplest method which senses the PV operating voltage. It operates by disturbing the PV voltage and comparing the PV power with the previous power illustrated in Fig. 3.5 and its flow chart is shown in Fig. 3.6. If the power increases due to disturbance, then the step size ΔD is added to the duty cycle and the disturbance will continue in the same direction. If the power decreases, the step size ΔD is subtracted from the duty cycle and the direction of disturbance will be reversed. The above process of disturbing the PV voltage and comparing the power continues until it reaches MPP (Maximum Power Point) i.e. Maximum power is obtained. P&O has the advantage that it simple to implement and robust in nature. However, it suffers from oscillations around MPP when fast change in irradiation is there.

$\partial P/\partial V>0$ for $V<V_{mp}$ i.e. Left Side of MPP

$\partial P/\partial V= 0$ for $V=V_{mp}$ i.e. at MPP (3.17)

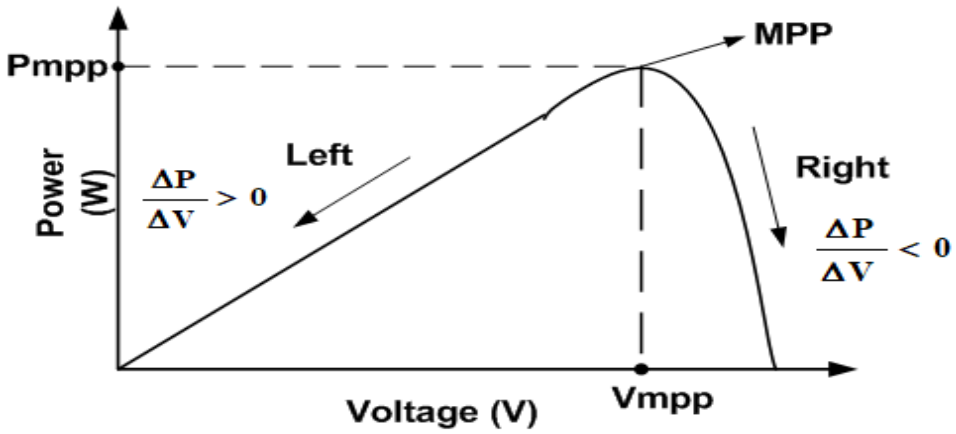

Fig. 3.5. Characteristic curve of P&O algorithm

$\partial P/\partial V<0$ for $V>V_{mp}$ i.e Right side of MPP

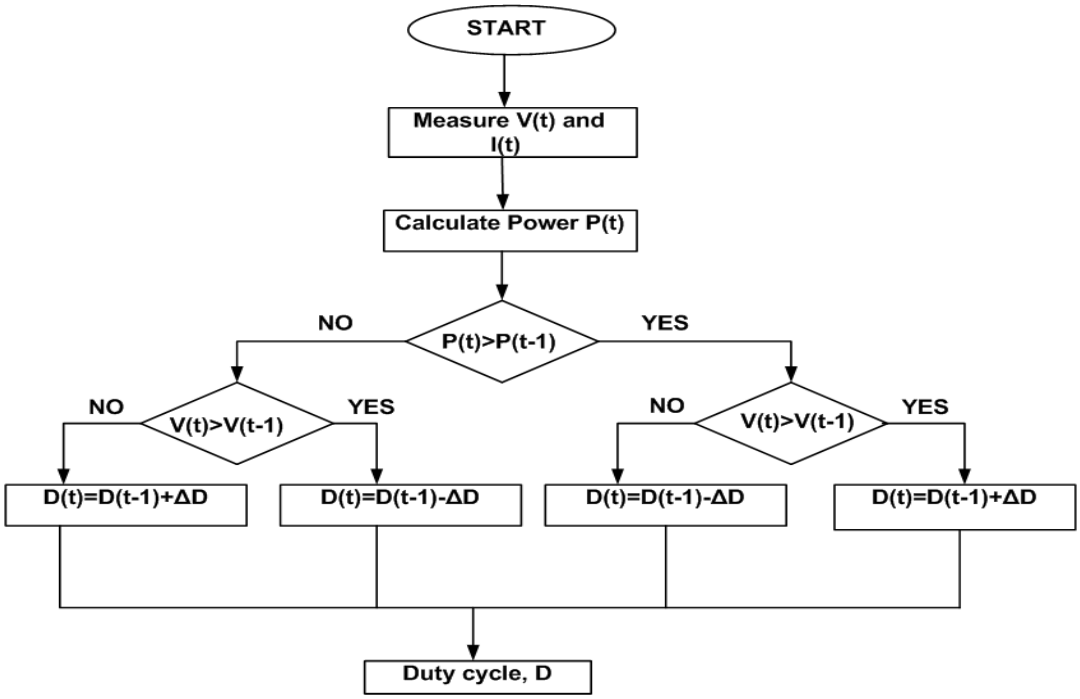

Fig. 3.6. Flow chart of P&O Algorithm

3.3.2 VSC Switching Algorithm

The design of algorithms varies depending on single phase or three-phase systems. Four or six switching pulses are generated in single-phase and three-phase system respectively. In general, the controller design in both the systems involves the following common steps:

(i) Estimation of Fundamental Load current

The algorithm is designed to extract the fundamental component of load current which is distorted. The algorithms discussed for single-phase are Synchronous Reference Frame Theory (SRFT), Second Order Generalised Integrator (SOGI), Trignometric Functional Link Neural Network (TFLNN) and Legendre Functional Neural Network (LFNN) extract the fundamental component of the load current.

(ii) DC Link Voltage Regulation and Estimation of Switching Losses

The DC Link voltage needs to be regulated for SAPF operation. The DC Link voltage is regulated using PI controller. The difference between the sensed DC link voltage (V_{dc}^{*}) and the reference DC link voltage (V_{dc}) is taken as error and is fed to the PI controller. The difference gives the i_{Loss} component taken from the grid to maintain the DC Link voltage and compensate for switching losses taking place in the SAPF.

$$v_{de}(n) = V_{dc}^{*} - V_{dc} \tag{3.18}$$

$$i_{Loss}(n) = i_{pdc}(n-1) + K_p\{v_{de}(n) - v_{de}(n-1)\} + k_i v_{de}(n) \tag{3.19}$$

The i_{Loss} is added to the i_{Lest} and subtracted from i_{pvff} to estimate the total fundamental component active component of current required from the grid

$$i_{pnet} = i_{Loss} + i_{Lest} - \mathrm{i_{pvff}} \tag{3.20}$$

3.3.2.1 Mathematical Analysis of Control in Single-Phase Grid Connected System

The calculation of PV feedforward component and generation of reference source current in single-phase grid connected systems is discussed below:

(i) Calculation of PV Feedforward Component

The PV feedforward component is to account for the contribution from PV array and incorporated to minimize the oscillations in grid voltage and currents due to change in PV insolation. The feedforward component is taken as

$$i_{PVff} = \frac{2P_{pv}}{V_t} \tag{3.21}$$

where P_{pv} is the maximum power, V_t is the peak amplitude of grid voltage.

(ii) Estimation of Unit Templates for Single-Phase Systems

The sensed PCC voltage ($v_{s\alpha}$) and its quadrature voltage ($v_{s\beta}$) is used for estimating the unit-in phase template for synchronizing the signal.

$$v_{s\alpha} = V_m sin\omega t \tag{3.22}$$

$$v_{s\beta} = V_m \sin(\omega t + \frac{\pi}{2}) \tag{3.23}$$

The terminal voltage (V_t) or peak amplitude of the grid voltage is calculated as

$$V_t = \sqrt{v_{sp}^2 + v_{sq}^2} = V_m \tag{3.24}$$

The unit in-phase template (u_p) are obtained as

$$u_p = \frac{V_{sp}}{V_m} = sin\theta \tag{3.25}$$

(iii) Generation of Reference Source Current

The reference source current ($i_{ref} = i_s^*$) is generated by multiplying it with the unit-in phase templates (u_{pa})

$$i_{ref} = i_s^* = i_{Total} u_{pa} \tag{3.26}$$

The generated reference source current (i_s^*) is compared with the actual source current (i_s) to generate the switching pulses for the SAPF.

3.3.2.2 Mathematical Analysis of Control in Three-Phase Grid Connected System

The calculation of PV feedforward component and generation of reference source current in three-phase grid connected systems

(i) Estimation of PV Feedforward Component

To minimize the oscillations due to PV insolation, feedforward component is computed as

$$i_{PVff} = \frac{2P_{pv}}{3V_t} \tag{3.27}$$

where P_{pv} is the maximum power, V_t is the peak amplitude of grid voltage.

(ii) Estimation of Unit Templates for Three-Phase systems

Three phase supply voltages (v_{sa}, v_{sb}, v_{sc}) are sensed at PCC and their magnitude (V_t) is calculated for the generation of three phase reference currents

$$V_t = \sqrt{\frac{2}{3}(v_{sa}^2 + v_{sb}^2 + v_{sc}^2)} \tag{3.28}$$

Three phase unit templates (u_{pa}, u_{pb}, u_{pc}) are calculated as

$$u_{pa} = \frac{v_{sa}}{V_t}, u_{pb} = \frac{v_{sb}}{V_t}, u_{pc} = \frac{v_{sc}}{V_t} \tag{3.29}$$

(iii) Generation of Reference Source Currents

The generated reference source current is compared with the actual source current to generate the switching pulses for the SAPF

$$i_{sa}^* = u_{pa} i_{pnet},\ i_{sb}^* = u_{pb} i_{pnet},\ i_{sc}^* = u_{pc} i_{pnet} \tag{3.30}$$

where i_{pnet} is the net current drawn from the supply

This template method cannot be used reliably under distorted grid conditions. Under non-ideal, polluted grid conditions Phase Locked Loop (PLL) Techniques are preferred for prefiltering. These techniques are discussed in detail in Chapter 6.

The reference source currents ($i_{sa}^*, i_{sb}^*, i_{sc}^*$) are generated and compared with the actual source currents (i_{sa}, i_{sb}, i_{sc}) and errors are passed through the hysteresis current controller to produce the requisite gate pulses for the VSC.

Table 3.1 shows the design values of different parameters in single-phase and three-phase grid connected systems

Table 3.1. Design Values of different Parameters in single-phase and three-phase Grid connected systems for simulation and hardware

Parameters	Single-phase System	Three-phase System
$\boldsymbol{V_s}$	110 V (rms)	110 V (rms)
$\boldsymbol{L_f}$	$L_f = \frac{m * V_{dc}}{4\ af_s I_{crpp}}$ =3 mH	$L_f = \frac{\sqrt{3} * m * V_{dc}}{12\ af_s I_{crpp}}$ =1 mH
$\boldsymbol{C_{dc}}$	$C_{dc} = \frac{2 * K_1 V_{rms} aIt}{(V_{dc}^2 - V_{dc1}^2)}$ =3334 $\mu F \approx 3000 \mu F$	$C_{dc} = \frac{2 * K_1 3V_{ph}\ aIt}{(V_{dc}^2 - V_{dc1}^2)}$ =20810 $\mu F \approx 3000 \mu F$
$\boldsymbol{V_{dcref}}$	$V_{DC} = \sqrt{2} V_{\text{rms}} = 155.56$ V $\approx 200\ V$	$V_{DC} = \frac{2\sqrt{2} V_{LL}}{\sqrt{3}\ m} = 179.60\ V \approx 200\ V$
Load	Variable (20-120 Ω), 80 mH	Variable (20-120 Ω), 80 mH
Configuration	H-bridge	3 phase 3 leg
Gating Pulses	4	6

3.4 Conclusions

This chapter discusses the design aspects of SAPF connected in single-phase and three -phase systems. Detailed designs of both system configurations are shown in this chapter. Further, details of PV array, SAPF, loads and battery design are shown. General control aspects of SAPF control in single-phase and three-phase systems are also discussed. The controller design helps to achieve the desired gating pattern for fulfilling the objectives of mitigation of PQ problems in power distribution systems.

Chapter 4

DESIGN AND ANALYSIS OF CONTROL ALGORITHMS FOR MITIGATION OF POWER QUALITY PROBLEMS IN SINGLE PHASE GRID CONNECTED PV SYSTEM

4.0 General

This chapter discusses the PV integrated single-phase grid connected systems for compensating current based power quality issues such as harmonic mitigation, power factor improvement and reactive power compensation. The schematic diagram of the proposed system is shown in Fig. 4.1. A PV array capacity of 750W is connected at the DC link of the VSC through boost converter. Various control techniques for mitigating power quality problems are developed and simulated in MATLAB Simulink environment and also verified experimentally. The performance of the PV integrated

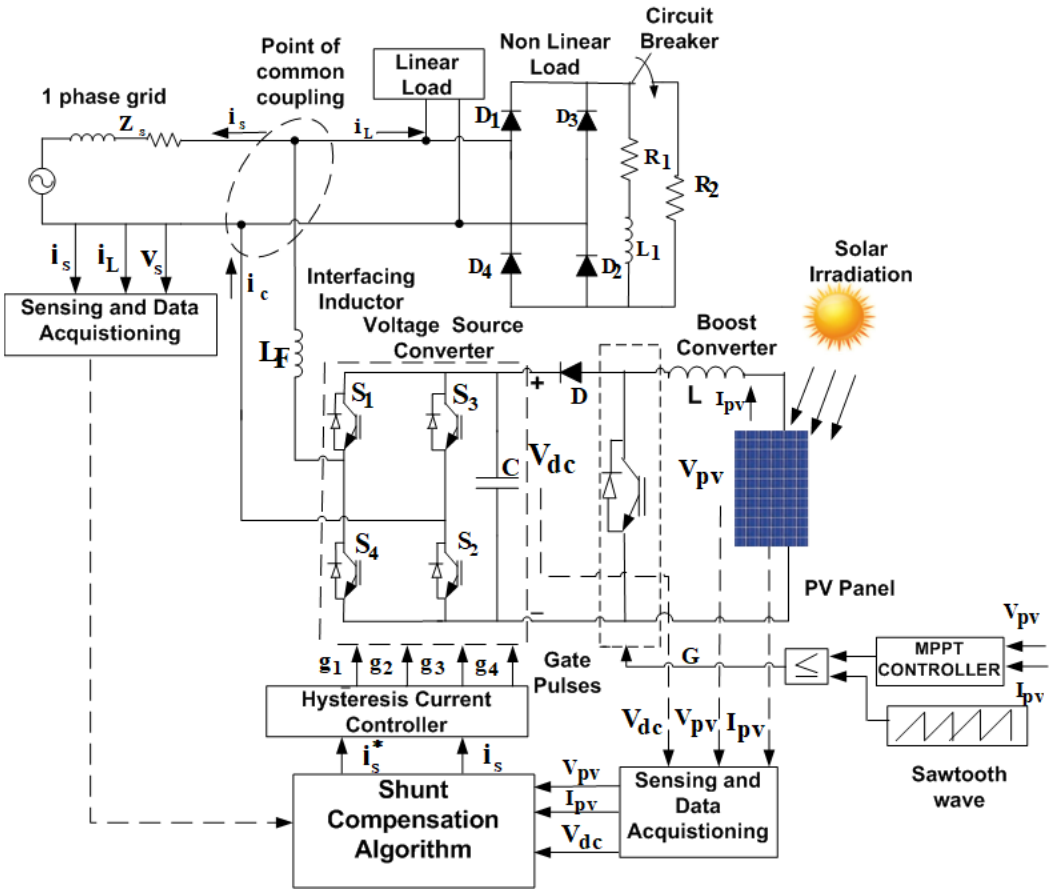

Fig. 4.1. Schematic Diagram of PV interfaced single-phase grid connected system

distribution system in steady state and dynamic state conditions under changing solar irradiation and different loading conditions such as linear load, non-linear load and mixed loading conditions are discussed in detail. The following control algorithms have been studied in this chapter viz Synchronous Reference Frame Theory (SRFT), Second Order Generalized Integrator (SOGI), Trigonometric Functional Link Neural Network (TFLNN), Legendre Functional Neural Network (LFNN).

4.1 Mathematical Analysis of Control Algorithms for Control of Single-Phase SAPF

The mathematical analysis of control algorithms for generation of sinusoidal reference currents for control of SAPF in mitigating power quality problems in single-phase PV integrated grid connected systems are discussed below. The first controller is designed on the basis of Synchronous Reference Frame Theory (SRFT) which is a conventional technique.

4.1.1 Synchronous Reference Frame Theory (SRFT)

The SRFT controller is realized using source voltage (v_s), source current (i_s) load current (i_L) and DC link voltage (V_{dc}) as input signals. The SRFT controller requires the voltage and current signals of single-phase system to be converted to d-q components. The schematic block diagram of control algorithm is shown in Fig. 4.2. Hence, first conversion to $\alpha\beta$ frame of reference is performed. A second pseudo phase is created by giving $90°$ lag to the original signal. Therefore, the sensed grid connected current and voltage are taken in α frame. The signals in β frame is generated by shifting the corresponding signal by $90°$. Using the above approach, the load current in $\alpha\beta$ frame is represented by

$$\begin{bmatrix} i_{L\alpha} \\ i_{L\beta} \end{bmatrix} = \begin{bmatrix} i_L(\omega t + \varphi) \\ i_L(\omega t + \varphi + \frac{\pi}{2} \end{bmatrix} \quad (4.1)$$

The stationary frame $i_{L\alpha}$ and $i_{L\beta}$ is transformed to synchronously rotating frame i_{Ld} and i_{Lq} by Park transformation matrix

$$\begin{bmatrix} i_{Ld} \\ i_{Lq} \end{bmatrix} = \begin{bmatrix} \sin \omega t & -cos\omega t \\ cos\omega t & sin\omega t \end{bmatrix} \begin{bmatrix} i_{L\alpha} \\ i_{L\beta} \end{bmatrix} = \begin{bmatrix} i_{L\alpha.}(sin\omega t) - i_{L\beta}.(cos\omega t) \\ i_{L\alpha.}(cos\omega t) + i_{L\beta.}(sin\omega t) \end{bmatrix} \quad (4.2)$$

SRFT PLL is used to synchronize the signals and generate the unit-in phase ($\sin \omega t$) and unit-in quadrature ($\cos \omega t$) templates.

The obtained currents (i_{Ld} , i_{Lq}) show sufficient harmonics which need to be eliminated. The $\overline{i_{Ld}}$ is the filtered fundamental component of load current. The current i_{Ld} is decomposed into fundamental and harmonic active component of load current and i_{Lq} is decomposed in to fundamental reactive and harmonic component.

$$i_{Ld} = \overline{i_{Ld}} + \widetilde{i_{Ld}} \ , \ i_{Lq} = \overline{i_{Lq}} + \widetilde{i_{Lq}} \quad (4.3)$$

The AC components and DC components are extracted using High Pass and Low Pass Filters respectively. The controller is designed such that source current contains only the fundamental estimated active component of load current ($\overline{i_{Ld}} = i_{Lest}$) and the load harmonics and the reactive component of current are supplied by Shunt Active Power Filter hence i_{Lq}^* component can be equated to zero.

$$\begin{bmatrix} i_{LD}^* \\ i_{Lq}^* \end{bmatrix} = \begin{bmatrix} \overline{i_{Ld}} + 0 \\ 0 + 0 \end{bmatrix} \quad (4.4)$$

The reference source current is produced by taking the inverse Park Transformation. The inverse Park transformation is shown in equation (4.7). To generate the reference source current the total fundamental active component ($i_{LD}^* =$

i_{pnet}) of current is required from the grid. The loss component (i_{Loss}) obtained from the PI controller of DC link voltage is added to the $\overline{i_{Ld}}$ and subtracted from PV feed forward component i_{PVFF} computed as $\frac{2P_{pv}}{V_t}$ to estimate the total fundamental active component (i_{LD}^*) of current required from the grid shown in equation (4.5).

$$i_{LD}^* = i_{pnet} = i_{Loss} + i_{Lest} - \mathrm{i_{PVFF}} \tag{4.5}$$

$$\begin{bmatrix} i_{s\alpha}^* \\ i_{s\beta}^* \end{bmatrix} = \begin{bmatrix} \sin\omega t & -cos\omega t \\ cos\omega t & sin\omega t \end{bmatrix}^{-1} \begin{bmatrix} i_{LD}^* \\ i_{Lq}^* \end{bmatrix} \tag{4.6}$$

Here i_{LD}^* is given by equation (4.5) and $i_{Lq}^* = 0$ as grid must not supply any reactive component of current

$$\begin{bmatrix} i_{s\alpha}^* \\ i_{s\beta}^* \end{bmatrix} = \begin{bmatrix} \sin\omega t & cos\omega t \\ -cos\omega t & sin\omega t \end{bmatrix} \begin{bmatrix} i_{LD}^* \\ 0 \end{bmatrix} \tag{4.7}$$

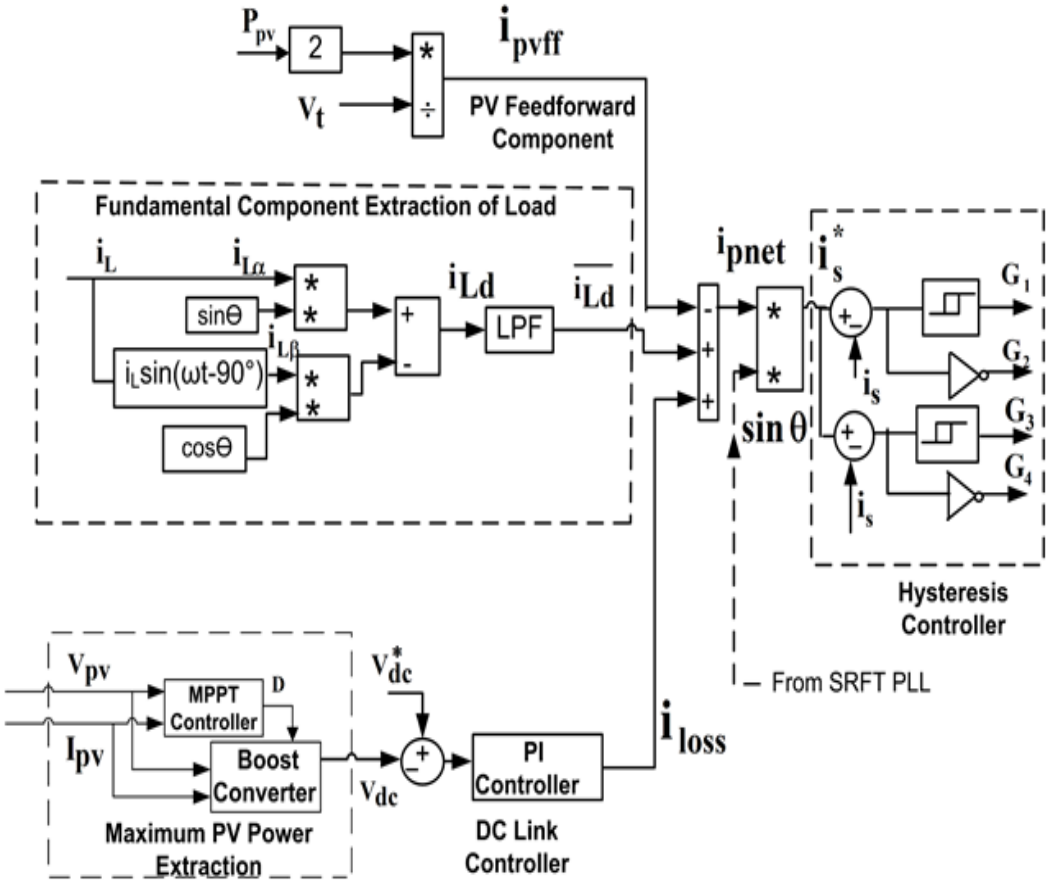

Fig. 4.2. Control algorithm based on SRFT control

$$i_s^* = i_{s\alpha}^* = \sin \omega t \; i_{LD}^* = \sin\omega t(i_{Loss} + i_{Lest} - \mathrm{i_{pvff}}) \quad (4.8)$$

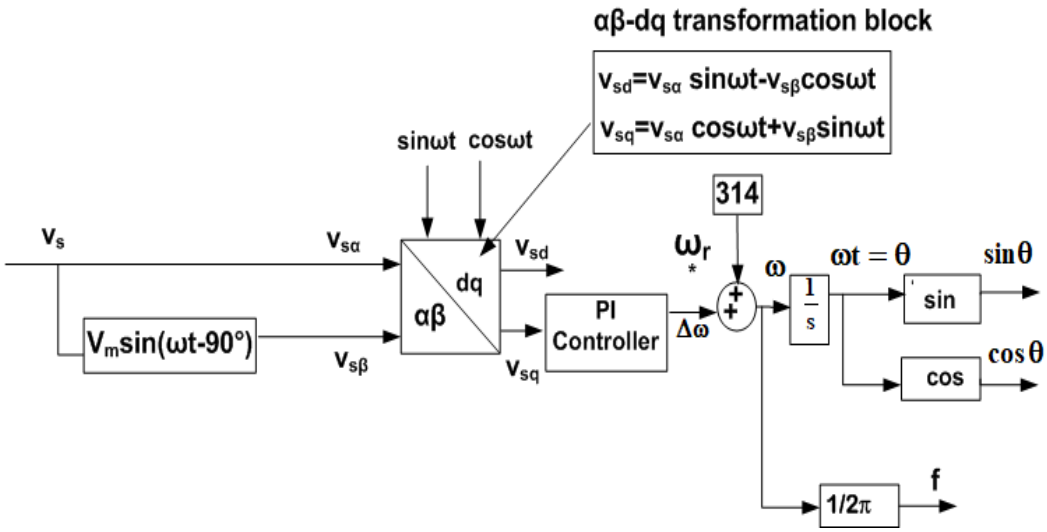

Fig. 4.3. Control algorithm for generation of unit template for SRFT controller

The total estimated fundamental component is used to generate reference source currents for SAPF discussed.

4.1.2 Second Order Generalized Integrator (SOGI)

SOGI is a very popular and convenient technique for fundamental component extraction as well as used as a PLL. SOGI is used to generate the filtered in-phase load current i_L' and quadrature phase output current qi_L' from the input load current. Fig. 4.4 shows the control diagram for fundamental extraction of load current using SOGI controller. The transfer functions for SOGI filters are shown in equations (4.9) and (4.10). Lower value of 'K' leads to narrower bandwidth and better filtering capability. Higher value of 'K' leads to wider bandwidth hence slow response and degrades the filtering capability. The outputs produced by SOGI are related to the input load current by two transfer functions. $i_{L\alpha}(s)$ has the characteristic of low pass filter and $i_{L\beta}(s)$ has the characteristic of band pass filter.

$$i_{L\alpha}(s) = \frac{i_L'}{i_L} = \frac{K\omega s}{s^2 + K\omega s + \omega^2} \quad (4.9)$$

$$i_{L\beta}(s)=\frac{qi_L}{i_L}=\frac{K\omega^2}{s^2+K\omega s+\omega^2} \quad (4.10)$$

where ω is selected as 314 rad/s corresponding to 50 Hz fundamental component.

The outputs $i_{L\alpha}$ and $i_{L\beta}$ are used to compute the fundamental estimated active component of load current (i_{Lest}). The control diagram is shown in Fig. 4.4.

$$i_{Lest}=\sqrt{i_{L\alpha}^2+i_{L\beta}^2} \quad (4.11)$$

The estimated fundamental component is used to generate reference source currents for SAPF discussed in Section 3.3.

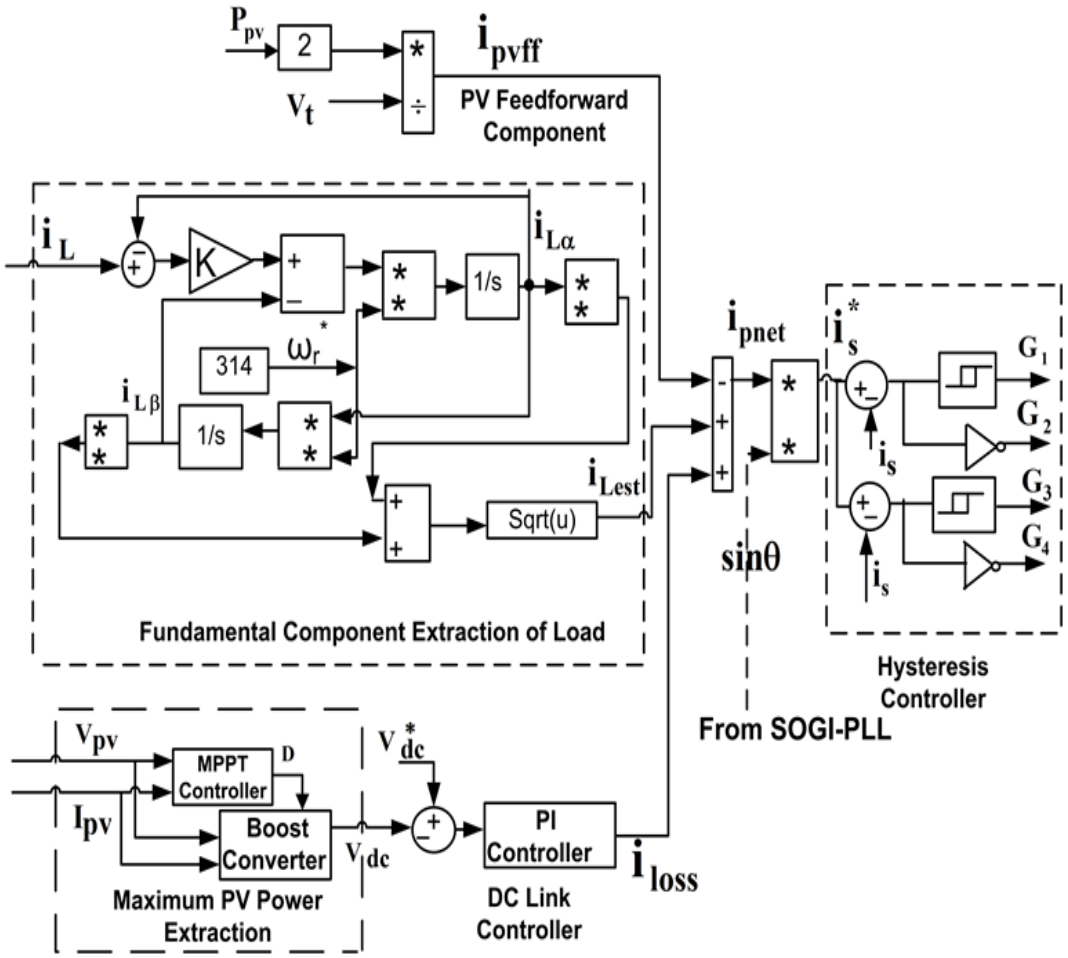

Fig. 4.4. Control algorithm based on SOGI controller for SAPF operation

The central frequency (ω) of SOGI is called resonant frequency and it should correspond to the fundamental input supply frequency (50 Hz or 314 rad/sec) to get the equal amplitude of in-phase ($i_{L\alpha}$) and quadrature component ($i_{L\beta}$) of load current.

The bandwidth of both the filters (Band-pass and Low pass Filter) are controlled by gain 'K' which is related to the settling time t_s and can be determined by

$$K = \frac{9.2}{t_s * \omega} \tag{4.12}$$

The value of 'K' is chosen to be 1.414 to have good compromise between the steady state and dynamic speed. The SOGI PLL can also be designed to synchronize the signals and generate the unit-in phase ($\sin \omega t$) and unit-in quadrature ($\cos \omega t$) templates. This is shown in Fig. 4.5, as SOGI-PLL. The reference source current is generated by multiplying it with the unit-in phase ($\sin \omega t$) template. Once the fundamental current i_{pnet} and PV feedforward term along with i_{Loss} term for regulating the DC link voltage is accounted, the gating control can be designed. Fig. 4.4 shows the detailed SOGI controller block which uses a SOGI-PLL shown in Fig.4.5.

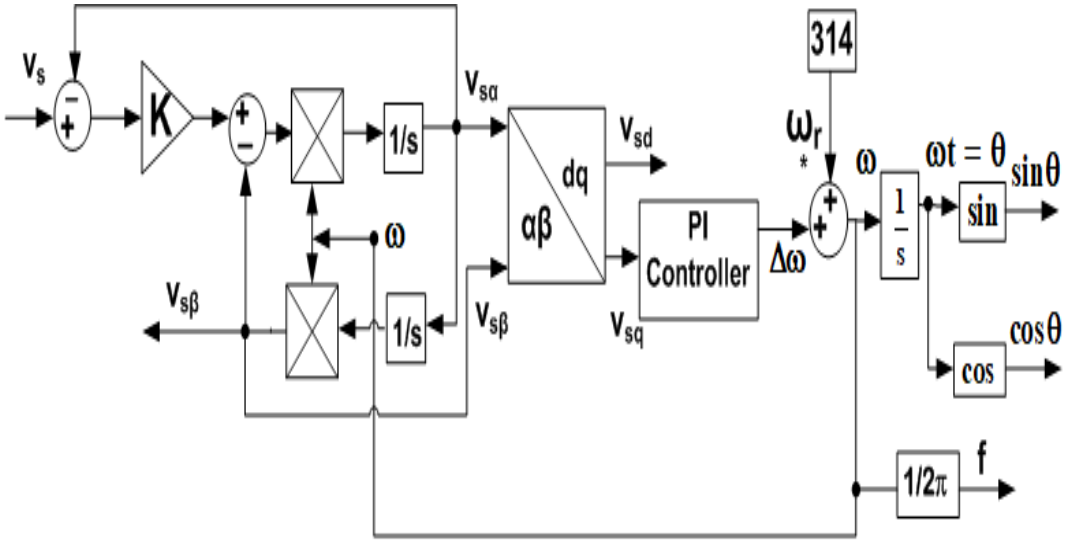

Fig. 4.5. Control algorithm for generation of unit template for SOGI control

4.1.3 Trignometric Functional Link Neural Network (TFLNN)

Functional Link Artificial Neural Network (FLANN) represents a higher order neural network using functional expansion of the input mapping the corresponding non-linearity with the output [198-200]. The control structure of FLANN is shown in Fig. 4.6. The input vector comprising 'k' elements is expanded by trigonometric expansion to 'm' elements and linearly combined with weight vectors to generate the output. The updation of weights is performed online to train the FLANN.

FLANN filter belongs to the family of non-recursive filters whose output depends linearly on the filter coefficients and satisfy time shift property. The transfer function of the FLANN Filter is described by input output relationship as

$$i_{Lest} = \sum_{i=1}^{m} w_i \, i_L \tag{4.13}$$

where i_{Lest} indicates the output of the FLANN filter, w indicates the weight and i_L denotes the expansion of the input vector of length N

$$i_L = [i_L(n), i_L(n-1), \ldots\ldots i_L(n-N)]^T \tag{4.14}$$

$$i_L = f(i_{Lr}(n)) \tag{4.15}$$

$$i_{Lf(n)} = f\big(i_{Lr}(n)\big), 1 \le i \le M, 1 \le k \le N \tag{4.16}$$

and f(.) represents the non-linear functional expansion of input vector $i_L[.]^T$. 'T' denotes the transpose of a matrix. In vector form, it can be written as

$$i_{Lf(n)} = [f(i_{Lr}(n) \;\; f(i_{Lr}(n-1) \;\; f(i_{Lr}(n-N+1)]^T \tag{4.17}$$

The weights are represented as

$$\text{w} = [w_1, w_2, w_3, w_4, \ldots\ldots w_M]^T \tag{4.18}$$

The cross terms i.e., the product of delayed input sample with the trigonometric term are

introduced to capture the non-linearity of the load current well and extract the fundamental component of load current. The trigonometric expansion with cross-terms is called extended Trigonometric expansion terms.

$$i_{LF(n)=}i_{Lr}(n) \tag{4.19}$$

$$i_{LF12(n)=}\sin\left[\pi i_{Lr(n)}\right] \tag{4.20}$$

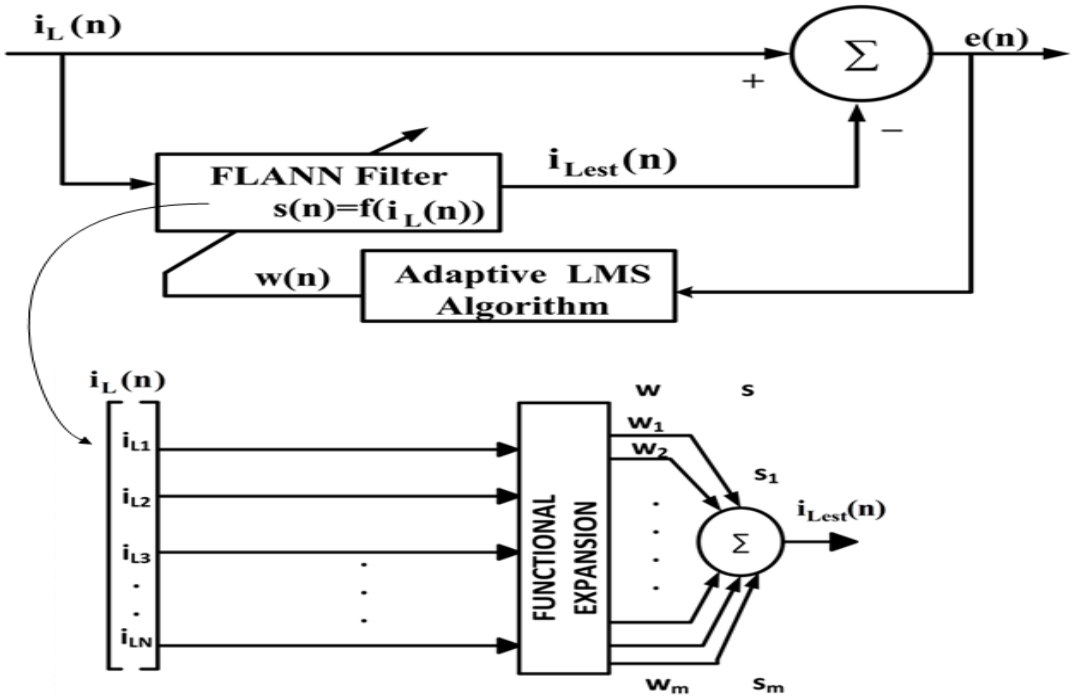

Fig. 4.6. FLANN Algorithm (a) Principle of shunt active power compensator using FLANN Filter (b) Schematic structure of FLANN

$$i_{LF13(n)=}\cos\left[\pi i_{Lr(n)}\right] \tag{4.21}$$

$$i_{LF21(n)} = i_{Lr}(n-1)\sin\left[\pi i_{Lr(n)}\right] \tag{4.22}$$

$$i_{LF22(n)} = i_{Lr}(n-1)\cos\left[\pi i_{Lr(n)}\right] \tag{4.23}$$

From above the generalized expressions can be written as

$$i_{LF(N-1)(2P+1)}(n) = i_{Lr}(\mathrm{n}-\mathrm{N}+1)\sin[P\pi i_{Lr}(n-N+2)] \tag{4.24}$$

$$i_{LFN(2P+1)}(n) = x(n-N+1)\cos\left[P\pi i_{Lr}(n-N+2)\right] \tag{4.25}$$

where P denotes the order of the trigonometric expansion and N denotes the expansion of the input vector of length N.

In both simulation and hardware five terms have been considered for order P=1 and N=2,i.e. $i_L(n), \sin[\pi i_{L(n)}], \cos[\pi i_{L(n)}], i_L(n-1)\sin[\pi i_{L(n)}],\ i_L(n-1)\cos[\pi i_{L(n)}]$ The trigonometric functional expansion is shown in Fig. 4.7.

The i_{Lest} is obtained by the summation of the multiplication of the weight vector 'w' and the functional expansion components.

$$i_{Lest} = wi_L + w\sin(\pi i_L) + w\cos(\pi i_L) + w\, i_L(n-1)\sin[\pi i_{L(n)}] + i_L(n-1)\cos[\pi i_{L(n)}] \quad (4.26)$$

This estimated fundamental current component (i_{Lest}) is used to generate reference source currents for SAPF discussed in Section 3.3.

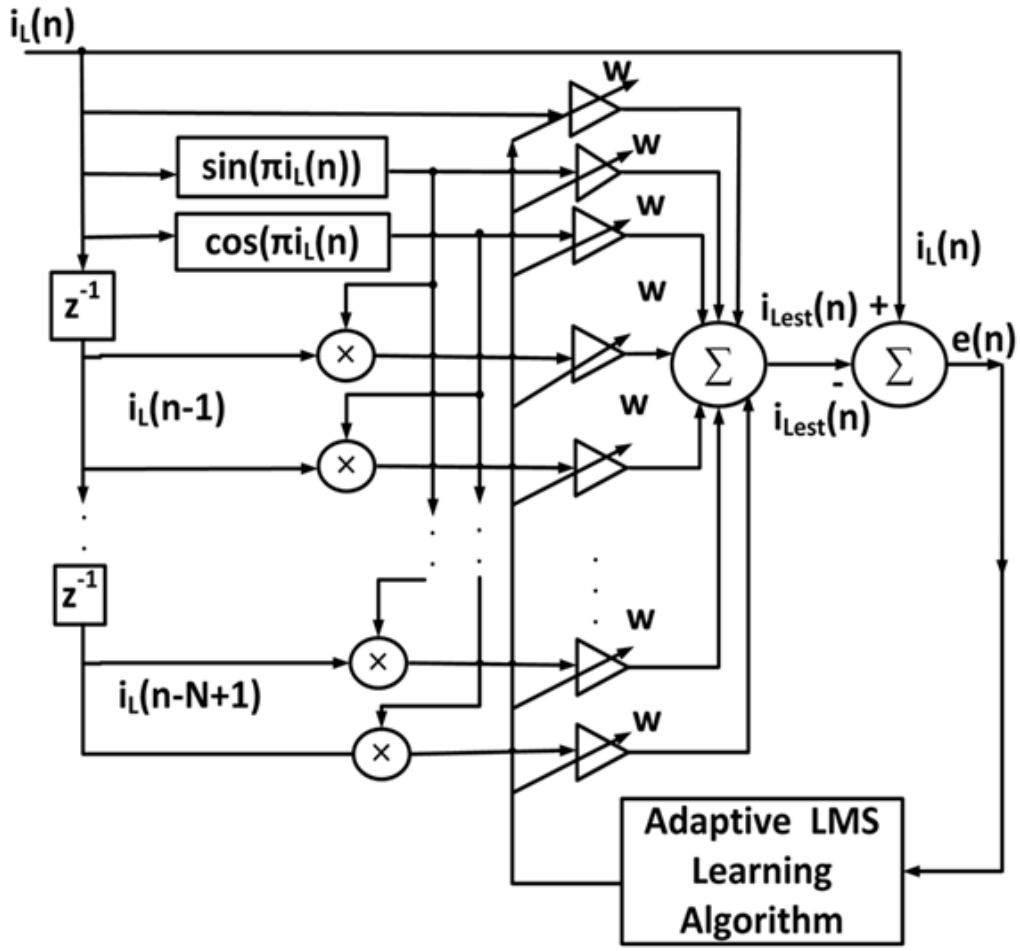

Fig. 4.7. Schematic Diagram of TFLNN based control

Further, the algorithm is made adaptive by online weight updation algorithm through error minimization called LMS algorithm. The error between the actual load current and the estimated load current is given by

$$e(n) = i_L - i_{est}.(sin\theta) \tag{4.27}$$

The weight updation is done online to instantly respond under changing environmental and loading conditions. The functional block diagram of the algorithm is shown in Fig. 4.8 to estimate the fundamental component of load current and minimize the error correspondingly.

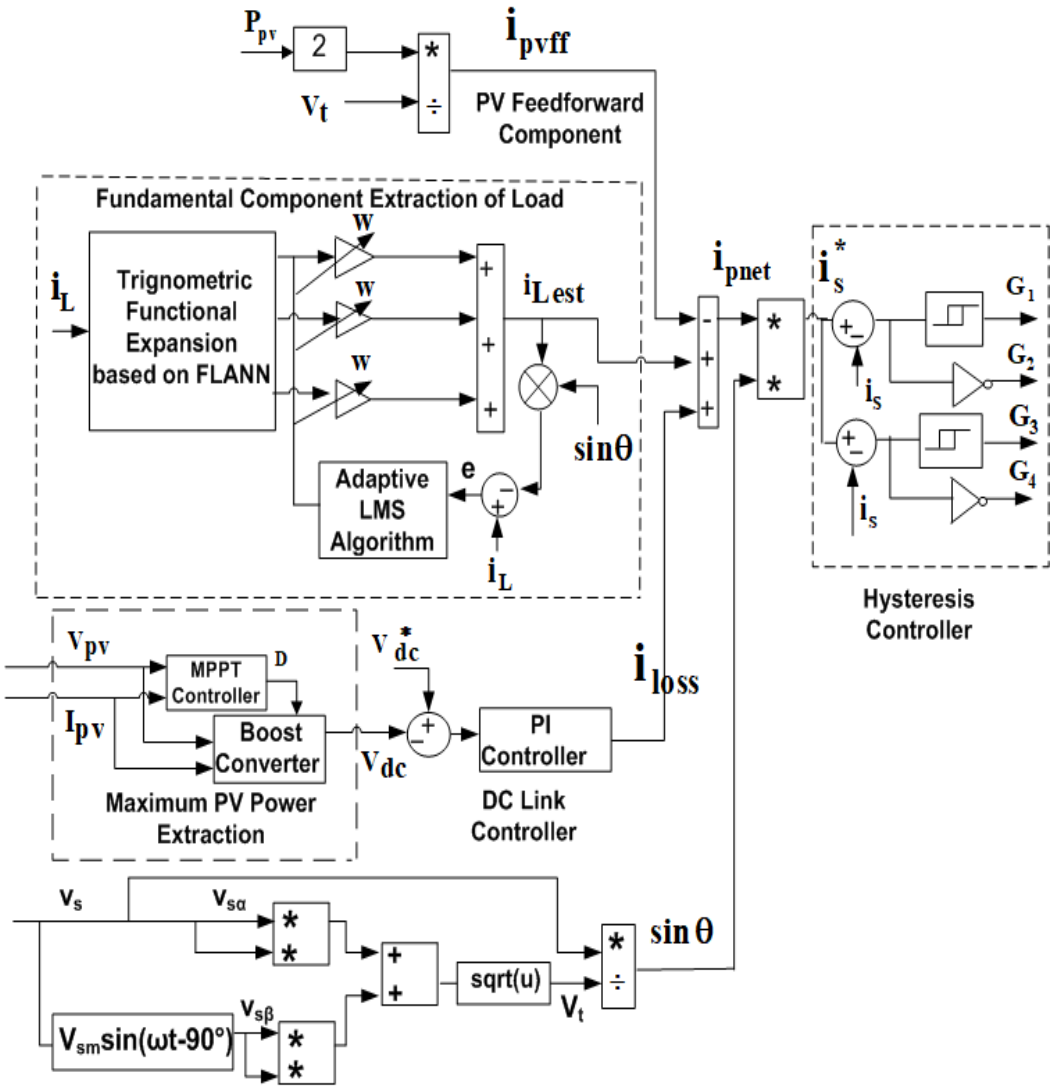

Fig. 4.8. Control diagram of TFLNN controller

$$w(n+1) = w(n) + \mu e sin\theta \tag{4.28}$$

Once i_s^* is computed, four gating pulses are computed with the usual manner.

4.1.4 Legendre Functional Neural Network (LFNN)

The Legendre Series Functional Expansion was first studied by French Mathematician Adrein Marie Legendre [201-204]. The expansion exhibits the orthogonal properties. The LFNN expansion components are fed as inputs to generate a corresponding set of output vectors. It is trained online by adjusting weight using the LMS algorithm. The LFNN series expansion is defined by the differential equation as

$$\left(1 - {i_L}^2\right)\frac{d^2y}{dx^2} - i_L\frac{dy}{dx} + n(n+1)i_{Lest} = 0 \tag{4.29}$$

where n denotes the order of Legendre Polynomial. The functional expansion is used for estimating the fundamental load current (i_{Lest}) which converges for the input load current between the interval for -1<i_L<1. The solution of Legendre differential equation is defined by:

$$i_{LF} = \sum_{k=0}^{\infty} c_k\, i_L^k \tag{4.30}$$

where c_k denotes the general coefficient terms.

After differentiating equation (4.30) and substituting in equation (4.29) gives

$$\left(1 - {i_L}^2\right)\sum_{k=0}^{\infty} k(k-1)\, c_k {i_L}^{k-2} - 2i_L\sum_{k=0}^{\infty} c_k\, k {i_L}^{k-1} + n(n+1)\sum_{k=0}^{\infty} c_k\, {i_L}^k = 0 \tag{4.31}$$

Rearranging equation (4.31) and readjusting the limits we obtained

$$\sum_{k=0}^{\infty}(k+2)(k+1)\, c_{k+2} i_L^k - \sum_{k=0}^{\infty} k(k-1) c_k\, i_L^k - 2\sum_{k=0}^{\infty} c_k\, i_L^k + n(n+1)\sum_{k=0}^{\infty} c_k\, i_L^k = 0 \tag{4.32}$$

Equating the coefficient of i_L^k to zero we get

$$(k+2)(k+1)c_{k+2} - \big(k(k+1) - n(n+1)\big)c_k = 0 \tag{4.33}$$

$$c_{k+2} = \frac{k(k+1)-n(n+1)}{(k+2)(k+1)} c_k \tag{4.34}$$

The coefficient terms are obtained from equation (4.34) for k=0,1,2,3 as

$$c_2 = \frac{-n(n+1)}{2!} c_0$$

$$c_3 = \frac{-(n-1)(n+2)}{3!} c_1$$

$$c_4 = \frac{-(n-2)(n+3)}{4.3} c_2 = \frac{(n-2)(n)(n+1)(n+3)}{4!} c_0$$

$$c_5 = \frac{-(n-3)(n+4)}{5.4} = \frac{(n-3)(n-1)(n+2)(n+4)}{5!} c_1$$

Inserting the above value of the coefficients in equation (4.32) we obtained

$$i_{LF} = c_0 \left[1 - \frac{n(n+1)}{2!} i_L^2 + \frac{(n-2)(n)(n+1)(n+3)}{4!} i_L^4 - \cdots .\right] + c_1 [\, x - \frac{(n-1)(n+2)}{3!} i_L^3 + \frac{(n-3)(n-1)(n+2)(n+4)}{5!} i_L^5 - \cdots] \tag{4.35}$$

$$i_{LF} = c_0 i_{Lest1} + c_1 i_{Lest2} \tag{4.36}$$

where the series i_{Lest1} constitute even powers of i_L while the series i_{Lest2} constitutes odd powers of i_L and i_{Lest1} and i_{Lest2} are linearly independent solutions. The polynomial solutions with c_0 and c_1 are so chosen that the value of the polynomial becomes 1, is called Legendre polynomial of order n. It is denoted by $P_n(i_L)$.

Choosing c_0 *and* c_1 to be

$$c_0 = \frac{(-1)^{n/2}\ 1.3.5....(n-1)}{2.4.6....n}, c_1 = \frac{(-1)^{n-1/2}\ 1.3.5.....n}{2.4.6.....n-1}$$

and substituting in Equation (4.35) gives

$$P_n(i_L) = \frac{(-1)^{n/2}\ 1.3.5....(n-1)}{2.4.6....n} \left[1 - \frac{n(n+1)}{2!} i_L^2 + \frac{(n-2)(n)(n+1)(n+3)}{4!} i_L^4 + \cdots ...\right] + \frac{(-1)^{n-1/2}\ 1.3.5.....n}{2.4.6.....n-1} [i_L - \frac{(n-1)(n+2)}{3!} i_L^3 + \frac{(n-3)(n-1)(n+2)(n+4)}{5!} i_L^5 - \cdots]. \tag{4.37}$$

The simplified expression for $P_n(i_L)$is based on Rodrigue's Formulae [204]

$$P_n(i_L) = \frac{1}{2^n n!} \frac{d^n}{dx^n} (i_L^2 - 1)^n \tag{4.38}$$

Using Rodrigues Formulae and putting n= 1,2,3,4 in equation (4.38) the expansion terms with input load current vector i_L are obtained as

$i_{L0}(x)=1$, $i_{L1}(x)= i_L$, $i_{L2}(x)= \frac{1}{2}[1 - 3i_L^2]$, $i_{L3}(x) = \left(\frac{1}{2}\right)[5i_L^2 - 3i_L]$ (4.39)

The estimated load current in vector form is expressed as

$i_{LF} = [i_{L0}\ i_{L1}\ i_{L2}\ i_{L3}]$

$i_{Lest} = i_{LF}^T\, w = w^T i_{LF}$ (4.40)

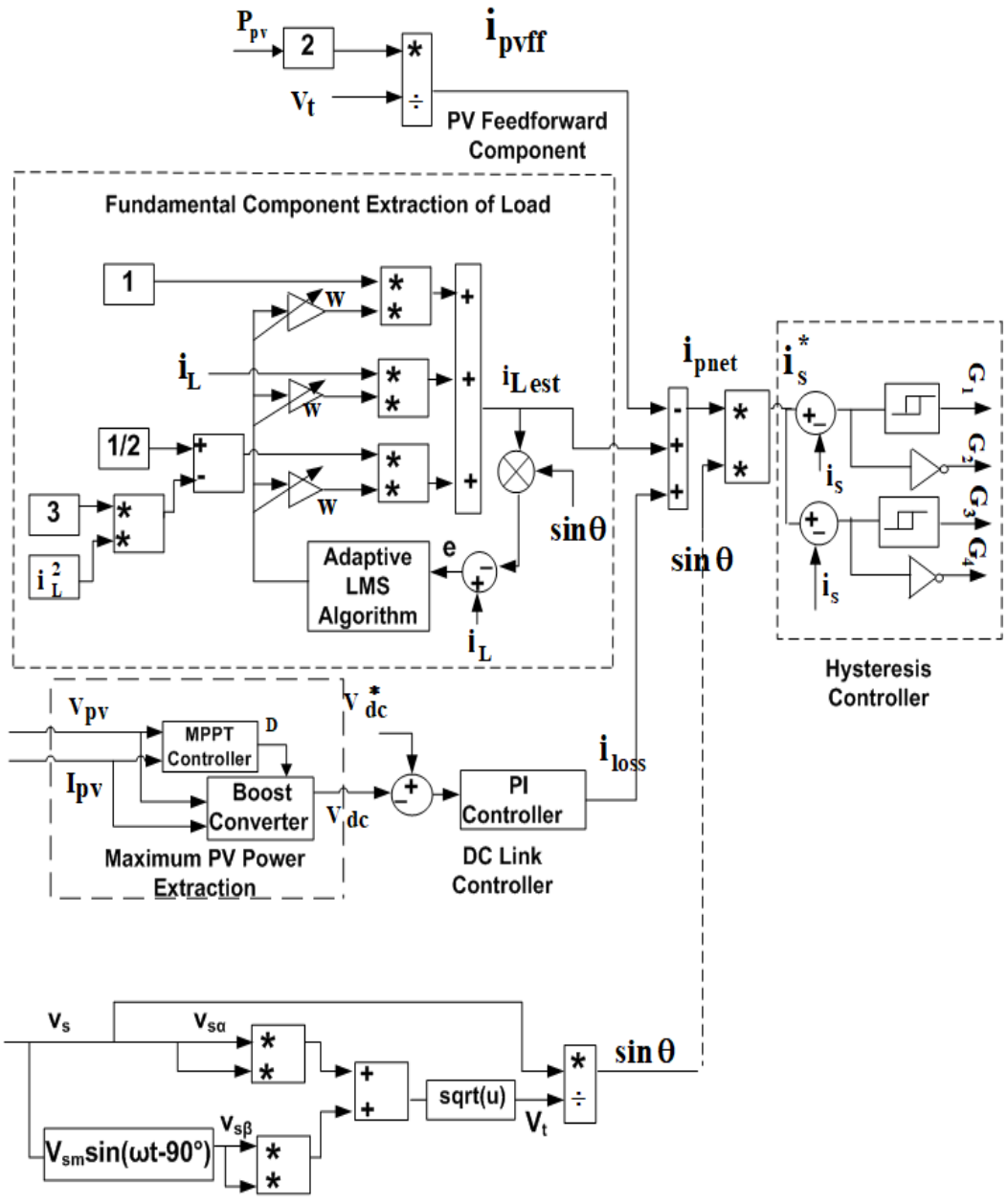

Fig. 4.9. Control diagram of LFNN controller

This estimated fundamental component (i_{Lest}) is used to generate reference source currents for SAPF discussed in Section 3.3

The error between the actual load current and the estimated load current is given by

$$e = i_L - i_{Lest}\ sin\theta \tag{4.41}$$

This error is minimized by updating the weights regularly by LMS algorithm. This is done online to deal with the variations in load current and other environmental conditions such as solar insolation's and estimate the fundamental component of the load current accurately. The schematic block diagram of LFNN based controller for single-phase PV integrated system is shown in Fig. 4.9.

$$w(n+1) = w(n) + \ \mu\ e\ sin\theta \tag{4.42}$$

Once the weights are updated, the Legendre polynomial NN estimated the fundamental current component properly. Hence i_s^* is computed as shown in Fig. 4.9. The comparison of i_s^* with the actual supply current (i_s) generates the gating pulses. The simulation results with all the algorithms are now discussed.

4.2 Simulation Results

This section discusses the performance aspects of SRFT, SOGI, TFLNN, and LFNN based controllers for SAPF in single-phase grid connected with out and with PV interfaced systems. The PV array with a capacity of 750W is simulated using three Kyocera solar 320GX-LPB connected at the DC link of SAPF. The performance analysis under different linear, non-linear, mixed loading conditions for checking the effectiveness of these control algorithms are discussed in detail.

4.2.1 Performance analysis with SRFT Controller

The SRFT based control scheme is modelled and simulated in MATLAB under different loading and changing solar irradiation conditions.

4.2.1.1 Performance under changing load conditions

Fig. 4.10 shows the waveforms of source voltage (v_s), source current (i_s), load current (i_L), compensator current (i_f)and DC link voltage (V_{dc}) under varying load conditions. The load current is quite distorted due to connection of non-linear loads. It has been observed that till 0.1s, under non-linear load conditions, the source current of 15A is used to meet the load demand. The source current is sinusoidal and in phase with the voltage. The THD of source current under non-linear loading conditions is found to be 2.18% when i_L has 29.16 % THD as shown in Fig. 4.11. From 0.1s to 0.2s, additional linear load is put in parallel to the existing non-linear load and mixed loading conditions are created. It is observed that the source current increases to 20A to meet the increased

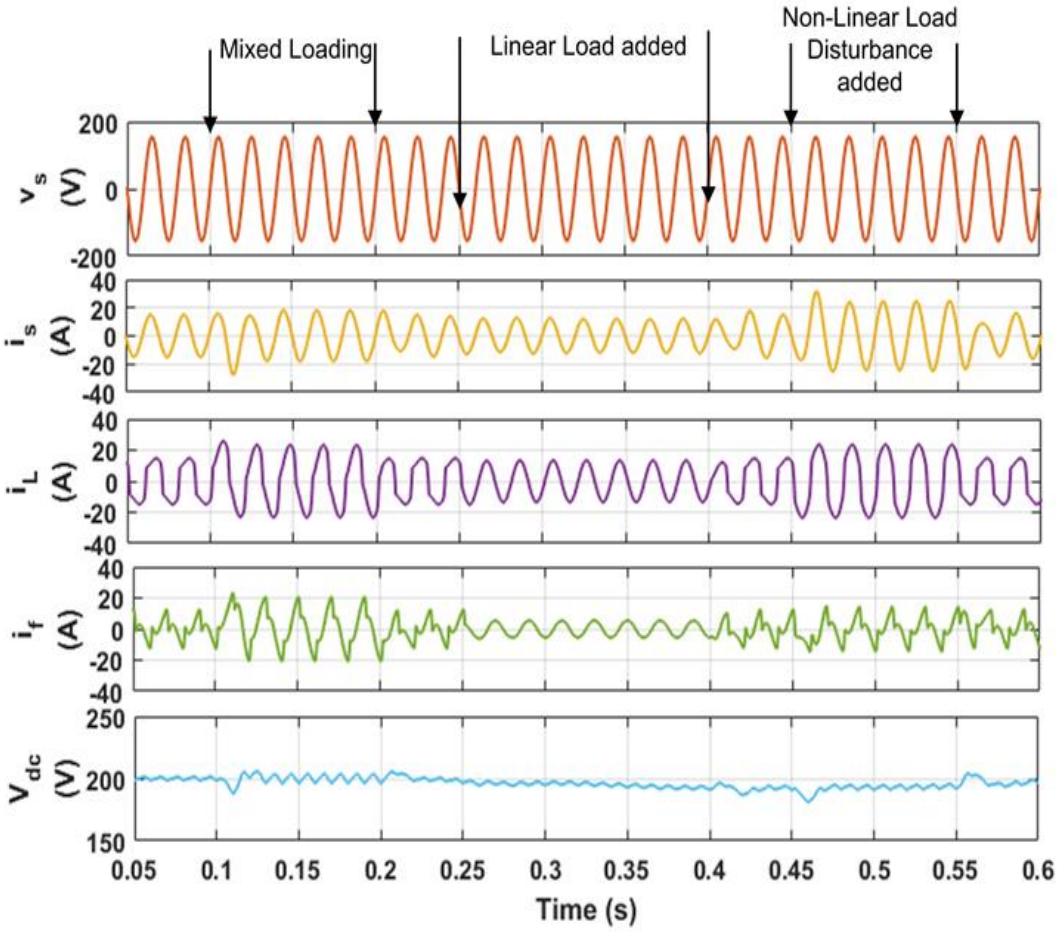

Fig. 4.10. Steady State waveforms under changing load conditions with SRFT controller in simulink

load current demand. The source current is in phase with the grid voltage and is sinusoidal in shape. The THD of source current under mixed loading conditions is found to be 3.49% when i_L has 18.45% THD shown in Fig. 4.12. When the mixed loading conditions are removed, the source current regains its original magnitude of 15A but remains in phase and sinusoidal in shape.

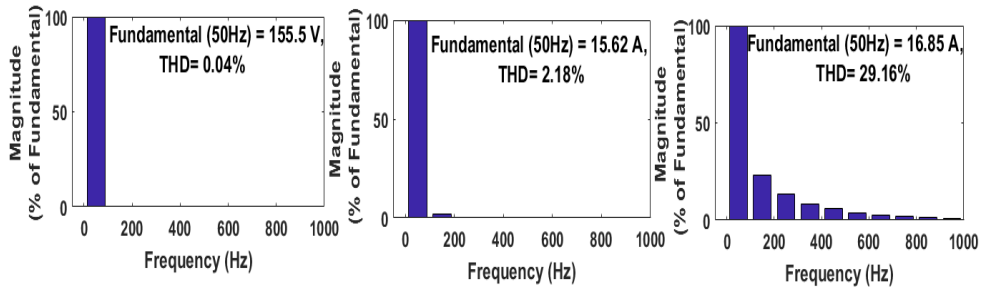

(a) (b) (c)

Fig. 4.11. THD of SRFT controller for (a) source voltage (v_s) (b) source current (i_s) and (c) load current (i_L) under non-linear load conditions in simulink

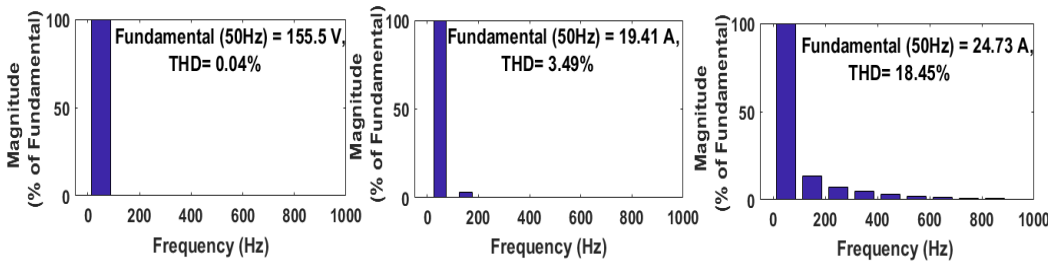

(a) (b) (c)

Fig. 4.12. THD of SRFT controller for (a) source voltage (v_s) (b) source current (i_s) and (c) load current (i_L) under mixed loading conditions in simulink

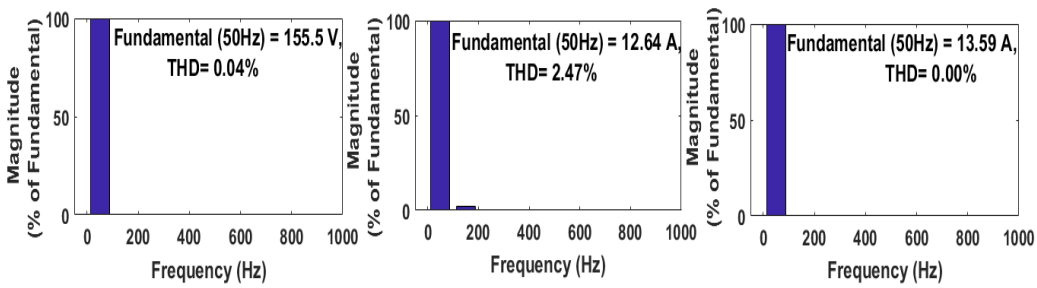

(a) (b) (c)

Fig. 4.13. THD of SRFT algorithm for (a) source voltage (v_s), (b) source current (i_s) and (c) load current (i_L) under linear loading conditions in simulink

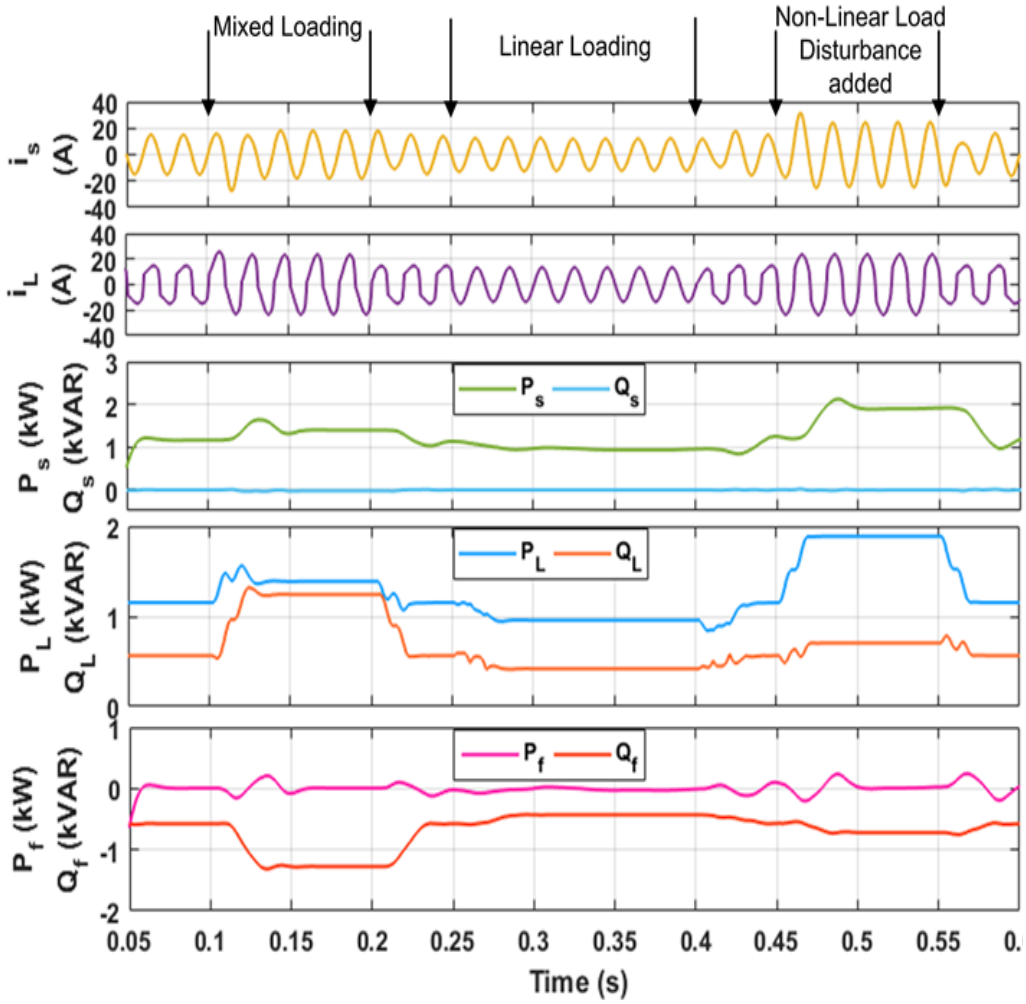

Fig. 4.14. Steady state power waveforms under changing load conditions for SRFT controller in simulink

At 0.25s, under linear load conditions, source current and load current both are sinusoidal and the source current of 12A is used to meet the load demand. The THD of source current under linear load conditions is found to be 2.47% as shown in Fig. 4.13.

At 0.45s, the non-linear load addition is there the source current increases to 24 A to meet the load demand. The grid current and grid voltage both are sinusoidal and in phase with each other. It is observed that the DC link voltage is well regulated to reference value of 200V under above varied loading conditions.

Fig. 4.14 shows the waveform of steady state power (P_s, Q_s), load power (P_L, Q_L) and compensator power (P_f, Q_f). Under non-linear load conditions till 0.1s, the

source active power of 1.2kW is used to meet the load active power of 1.2kW. The reactive power of load is 0.5kVAR which is met by the compensator.

Under mixed loading conditions from 0.1s to 0.2s, the source active power is increased to 1.5kW to meet the load demand. The reactive power of load has been increased to 1.2kVAR which is again met by the compensator.

Under linear loading conditions the source active power of 1kW is used to meet the load demand of 1kW. The reactive power of 0.45kVAR is met by the compensator.

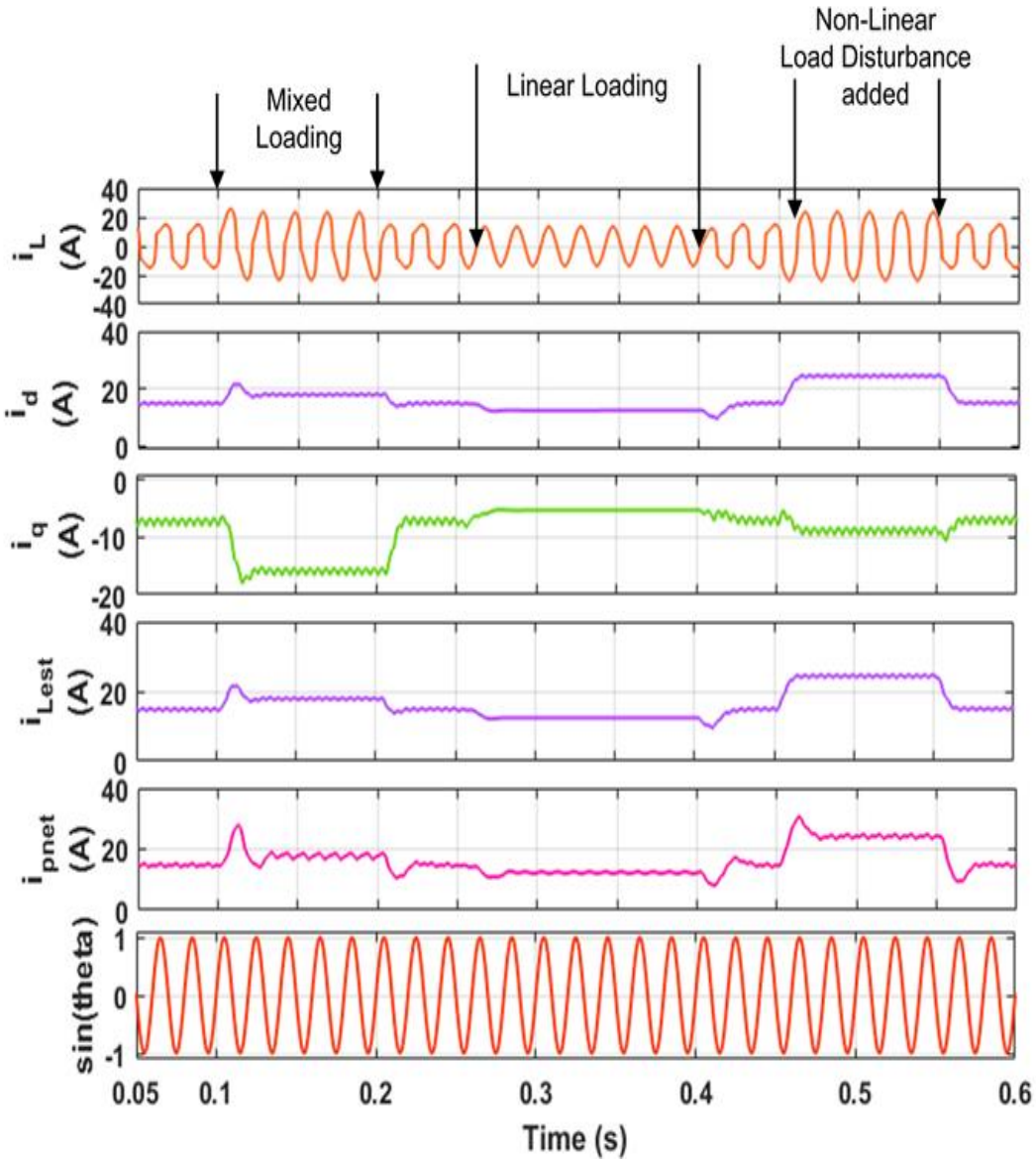

Fig. 4.15. Steady state intermediates waveforms under changing load conditions with SRFT controller in simulink

Under non-linear load disturbance the source active power increases to meet the load demand of 2kW and the reactive power of 1.2kVAR is met by the compensator.

Fig. 4.15 shows the intermediate results of the SRFT algorithm and plots showing i_L, i_d , i_q , i_{Lest} and i_{pnet} and unit in phase template $sin\theta$. It has been observed that i_d the active component of load current called i_{Lest} increases correspondingly under changing load conditions to meet the increased load demand. i_q corresponds to reactive power of load current. i_{pnet} is the summation of fundamental load component i_{Lest} and the DC link voltage current controller output i_{loss}.The i_{loss} component is used to meet the losses occurring in the switching of VSC. $sin\theta$ corresponds to the unit in phase template required for synchronization and reference current generation. Table 4.1 shows the THD values obtained in simulink using SRFT algorithm under various loading conditions i.e., non-linear load, linear load and mixed loading conditions with normal grid conditions.

Table 4.1. THD values obtained in simulink using SRFT algorithm under various loading conditions

Loading Conditions	Synchronous Reference Frame Theory (SRFT)		
	i_L(THD)	i_S(THD)	v_s(THD)
Non-Linear Load	29.16%	2.18%	0.04%
Mixed Load	18.45%	3.49%	0.04%
Linear Load	0.00%	2.47%	0.04%

4.2.1.2. Performance under changing solar irradiation

Fig. 4.16, Fig. 4.17 and Fig. 4.18 show the waveforms of irradiation level $G(I_{rr})$, source voltage (v_s), supply current (i_s), load current (i_L), compensator current (i_f), DC link voltage (V_{dc}), THD of v_s, i_s, i_L,source power (P_s, Q_s), load power (P_L, Q_L),compensator power (P_f, Q_f) under changing solar irradiation of 1000W/m2 from 0.13s to 0.25s and

400W/m^2 from 0.3s to 0.5s. It has been found that with zero solar irradiation till 0.13s the source current is 15A and it is amounting to 1.21kW. This power is used to meet the load's active power demand and the reactive power demand of 0.5kVAR is met by the compensator. The three Kyocera 250W PV array panels connected in series produce maximum power capacity of 750W at 1000W/m^2. However, after losses PV panels deliver power of 660W at the DC link of inverter. When the solar irradiation intensity

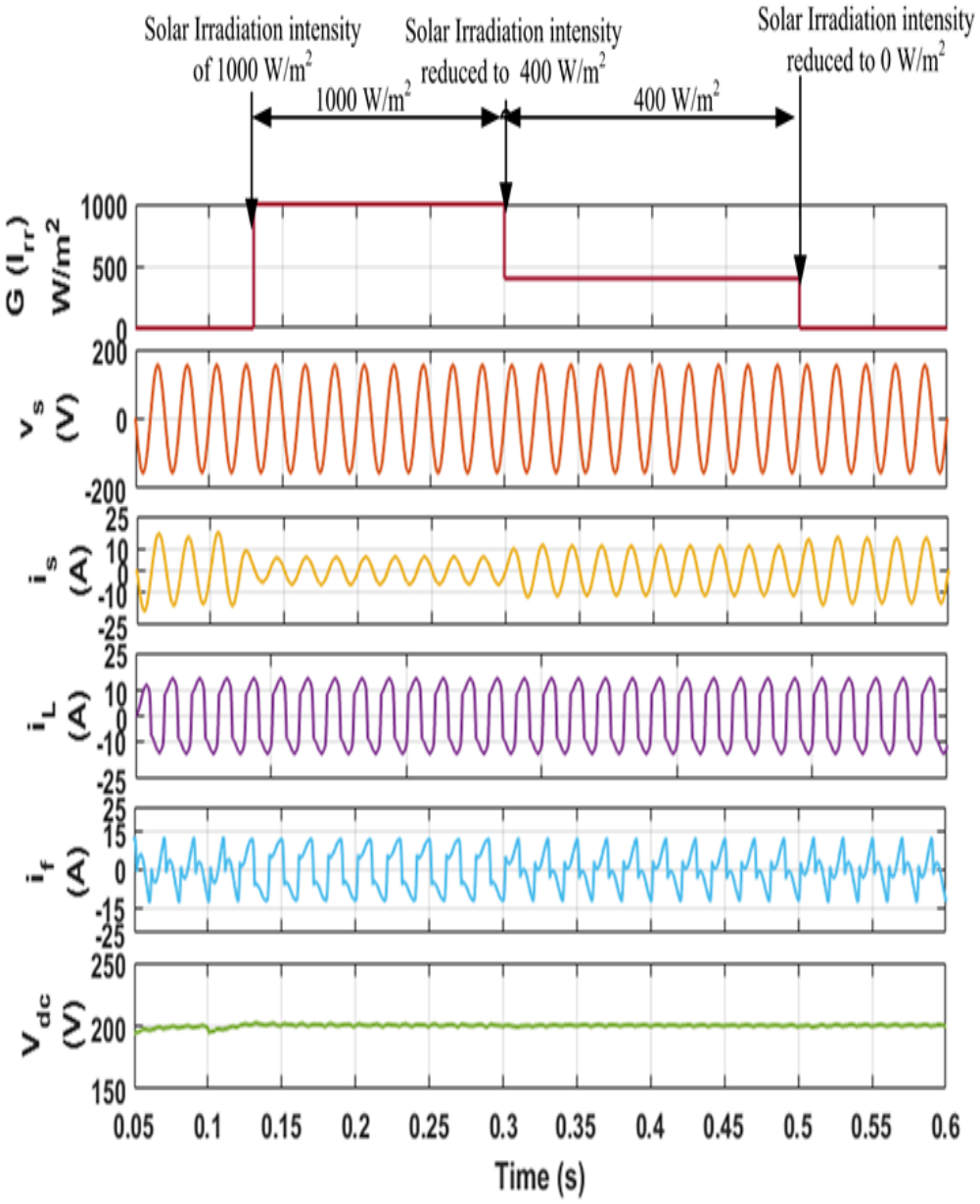

Fig. 4.16. Steady state waveforms under changing irradiation conditions with constant non-linear load conditions with SRFT controller in simulink

of 1000W/m^2 is simulated the source current decreases to 7A as the load power of 1.21kW is shared by both PV power of 0.66 kW and the grid power of 0.55kW. The THD of source current is 3.70% under non-linear load THD of 29.16% shown in Fig. 4.18.

At 0.3s, the solar irradiation intensity has been reduced from 1000 W/m^2 to 400 W/m^2 as the result the grid power increases to 0.94kW and the PV power reduces to 0.27kW to meet the load demand of 1.21kW. Thus, the PV power correspondingly reduces in accordance with the varying irradiance conditions.

When the solar irradiation of 0W/m^2 is considered, it refers to SAPF operation alone without PV integration. During this night time condition, PV doesn't supply active power hence the grid current again increases to 15A and the grid power increases to meet the whole load demand of 1.21kW. The SAPF mitigates PQ problems only and no active power transfer takes place during this duration meet the whole load demand of 1.21kW.

The SAPF mitigates PQ problems only and no active power transfer takes place during this duration.

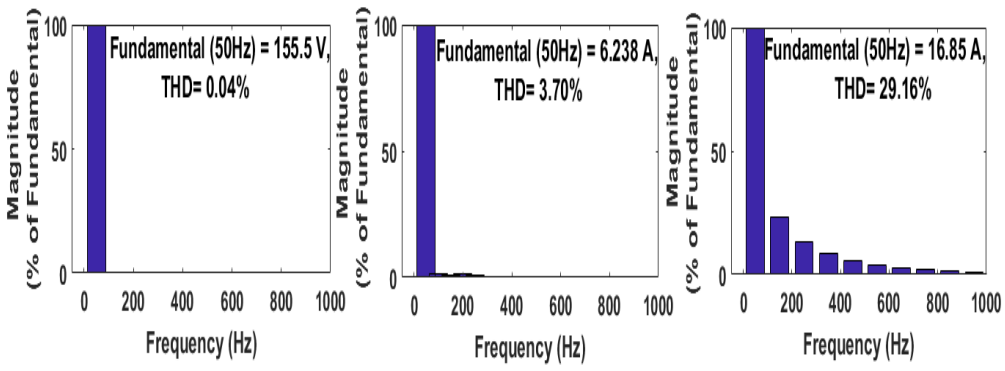

(a) (b) (c)

Fig. 4.17. THD of SRFT controller for source voltage (v_s), source current (i_s) and load current (i_L) under changing solar irradiation conditions for constant non-linear load in simulink

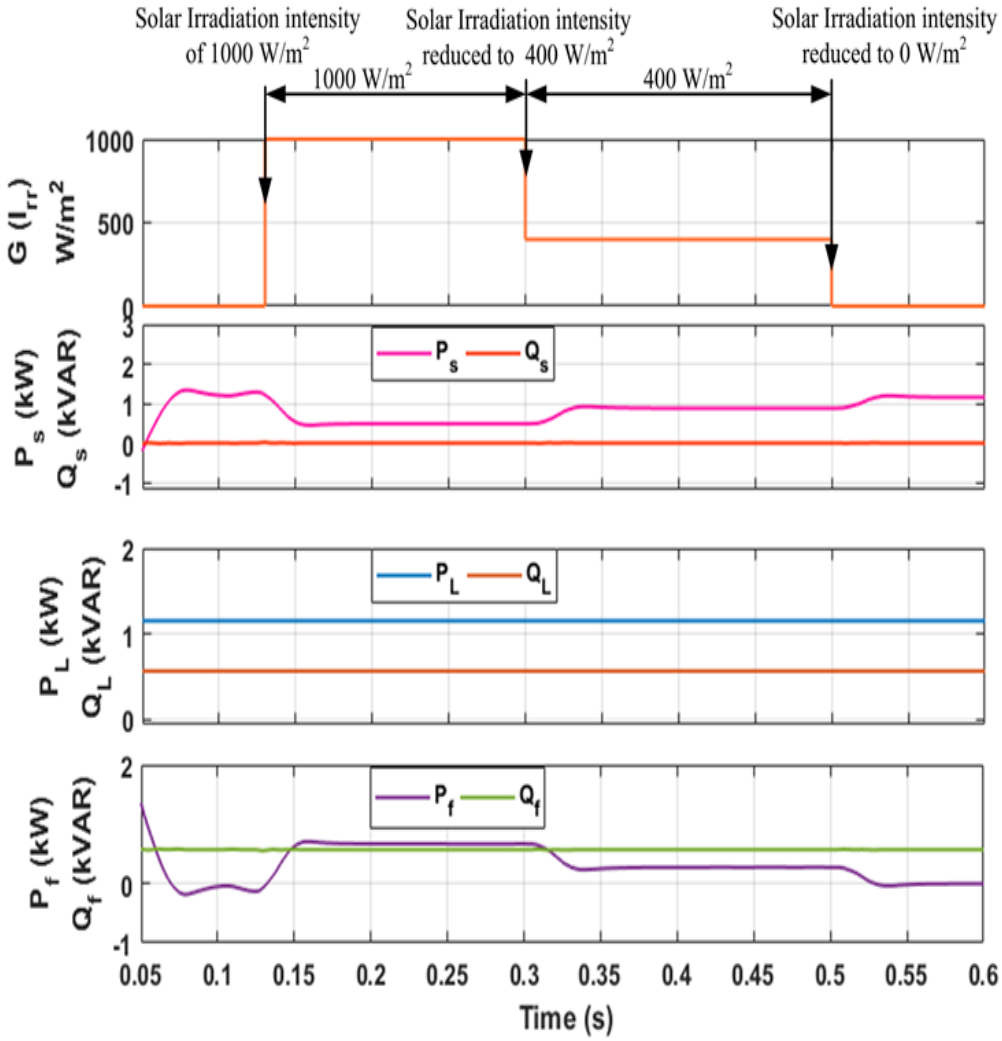

Fig. 4.18. Steady state power waveforms under changing irradiation conditions under non-linear load with SRFT controller in simulink

4.2.2 Performance analysis with SOGI Controller

The SOGI based control scheme is now modelled and simulated in MATLAB environment. Its performance is tested under different loading and changing solar irradiation conditions.

4.2.2.1 Performance under changing load conditions

Fig. 4.19 shows the waveforms of supply voltage (v_s), source current (i_s), load current (i_L), compensator current (i_f) and DC Link voltage (V_{dc}) under varying load conditions. It has been observed that till 0.1s that source current of 15 A is used to

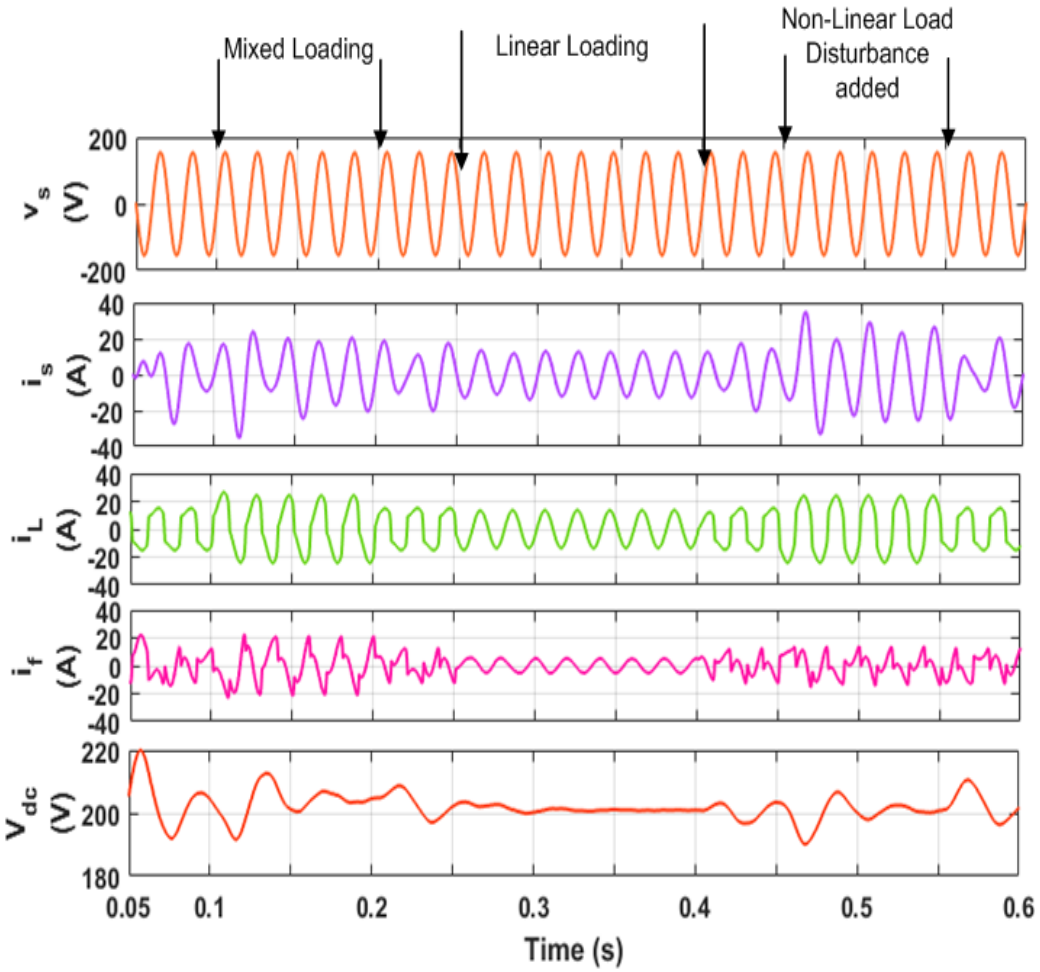

Fig. 4.19. Steady State waveforms of under changing load conditions with SOGI controller in simulink

meet the load demand. The source current THD has been improved to 1.79% under non-linear load THD of 29.9% shown in Fig. 4.20. From 0.1s to 0.15s, the mixed loading conditions are simulated and it is found that the source current increases to 19 A to meet the required load demand. The THD of source current is observed to be 2.53% under load current THD of 18.45% under mixed loading conditions as illustrated through Fig. 4.21.

From 0.25s to 0.4s, the linear loading has been observed and it has been found that the source current of 12A is used to meet the load demand 12A. The THD of source current is observed to be 2.33% under linear loading conditions shown in Fig. 4.22.

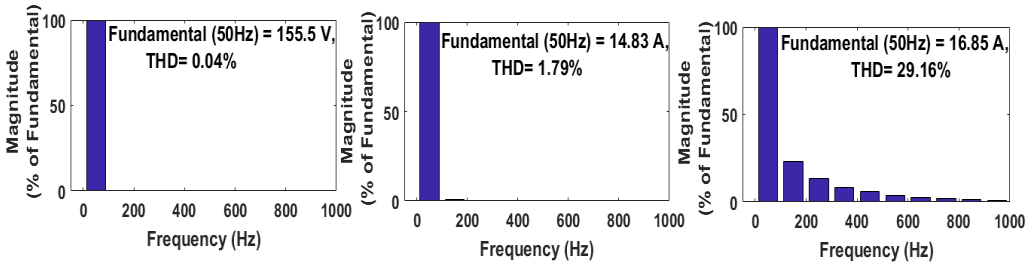

(a) (b) (c)

Fig. 4.20. THD of SOGI controller for (a) source voltage (v_s) (b) source current (i_s) and (c) load current (i_L) under non-linear load conditions in simulink

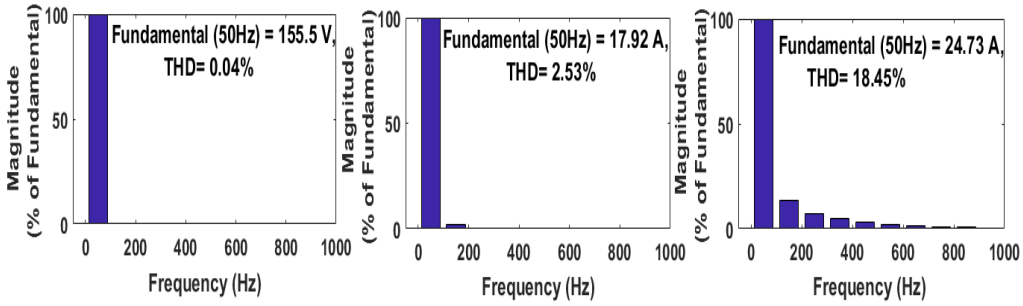

(a) (b) (c)

Fig. 4.21. THD of SOGI controller for (a) source voltage (v_s) (b) source current (i_s) and (c) load current (i_L) under mixed loading conditions in simulink

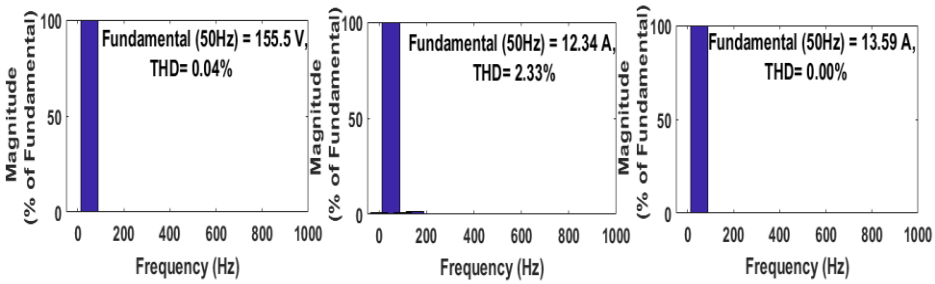

(a) (b) (c)

Fig. 4.22. THD of SOGI controller for (a) source voltage (v_s) (b) source current (i_s) and (c) load current (i_L) under linear loading conditions in simulink

From Fig. 4.19. it has been observed that source current shows slow dynamic response under changing load conditions and takes larger time to settle down to steady state. The DC link voltage shows continuous transient perturbations before settling down to steady state.

Under non-linear load disturbances from 0.45s to 0.55s, the source current increases to 24A to meet the load demand. The source current is found to be sinusoidal

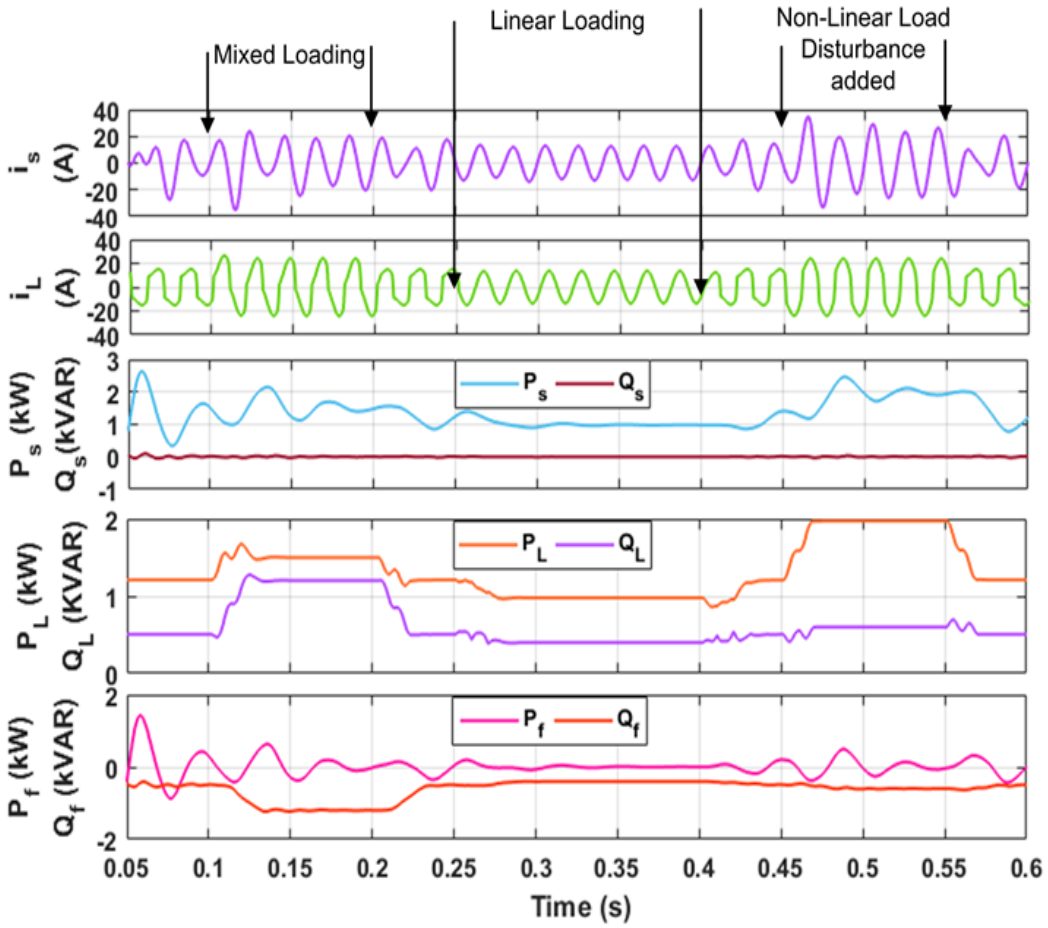

Fig. 4.23. Steady state power waveforms under changing load conditions with SOGI controller in simulink

and in phase with the voltage.

Fig. 4.23 shows the power balance waveforms (P_s, Q_s), load power (P_L, Q_L) and compensator power (P_f, Q_f) under all loading conditions. It has been found that under non-linear load conditions till 0.1s, the load power of 1.2kW is met by the source power of 1.2kW and reactive load of 0.5kVAR is met by the compensator.

From 0.1s to 0.2s, the mixed loading conditions have been simulated and it has been observed that the active load of 1.5kW is met by the source and reactive load of 1.2 kVAR is met by the compensator.

Under linear loading conditions from 0.25s to 0.4s, the active power of 1.5 kW of

load is met by the source. The compensator meets the reactive power demand of the load.

From 0.45s to 0.55s the non-linear load disturbance takes place and the load power of 2kW is met by the source power of 2kW. The reactive power of 1.2kVAR is met by the SAPF of 1.2kVAR.

Fig. 4.24 shows the intermediate waveforms of i_L i_{Lalpha},i_{Lbeta} ,i_{Lest} ,i_{pnet} and unit in phase templates $sin\theta$ under varying load conditions. It has been found that the i_{Lalpha} is in phase with the source voltage and i_{Lbeta} is 90° out of phase with the voltage. The i_{Lest} is the active component of load current is obtained by taking the square of the magnitude of the i_{Lalpha} and i_{Lbeta}. The i_{pnet} is obtained by adding the i_{Lest} with the i_{Loss} component obtained from DC link voltage controller. The

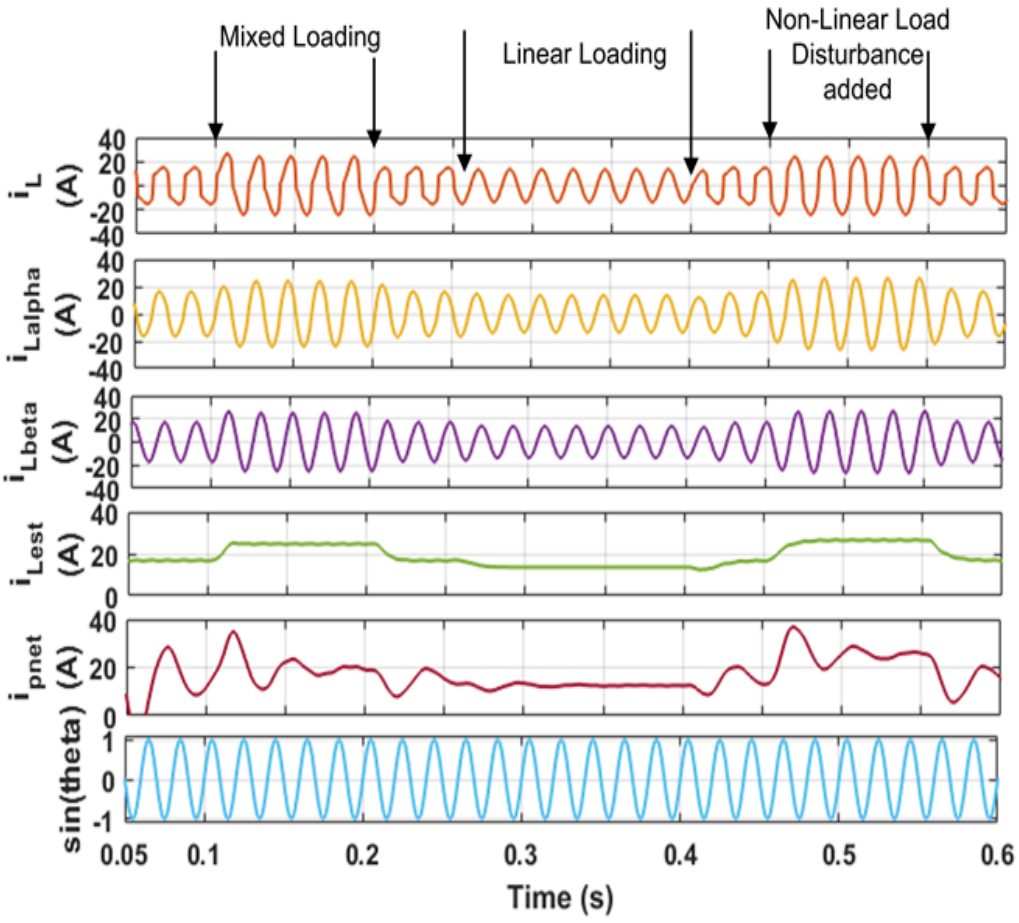

Fig. 4.24. Steady state intermediate waveforms under changing load conditions with SOGI controller in simulink

i_{pnet} is multiplied by $sin\theta$ given by the SOGI PLL. The unit in phase template is to obtain the reference source current for generating the gate pulses for the VSC.

Table 4.2 shows THD values obtained in simulink using SOGI algorithm under various loading conditions i.e., non-linear load, linear load and mixed loading Conditions

Table 4.2. THD values obtained in simulink using SOGI algorithm under various loading conditions

Loading Conditions	Second Order Generalised Integrator (SOGI)		
	i_L(THD)	i_S(THD)	v_s(THD)
Non-Linear Load Conditions	29.16%	1.79%	0.04%
Mixed Load Conditions	18.45%	2.53%	0.04%
Linear Load Conditions	0.04 %	2.33%	0.04%

4.2.2.2 Performance under changing solar irradiation

Fig. 4.25 shows the waveforms of $G(I_{rr})$, v_s, i_s, i_L, i_f, V_{dc} under changing solar irradiation of 1000W/m^2 from 0.13s to 0.25s and 400W/m^2 from 0.3s to 0.5s. It has been found that without solar irradiation till 0.13s the source current of 15A is used to meet the load demand. The source current is found to be sinusoidal and in phase with the voltage. The three Kyocera 250W PV array panels connected in series produce maximum power capacity of 750W at 1000W/m^2. However, after losses PV panels deliver power of 660W at the DC link of inverter. When the solar irradiation intensity of 1000W/m^2 is put the source current decreases to 7A as the load current is now partially shared by both PV and source. The THD of source current is 3.20% under non-linear load THD of 29.16% shown in Fig. 4.26.

At 0.3s the solar irradiation intensity has been reduced to 400W/m^2, now the source current increases to 10A as the contribution from PV has decreased due to reduced irradiation intensity.

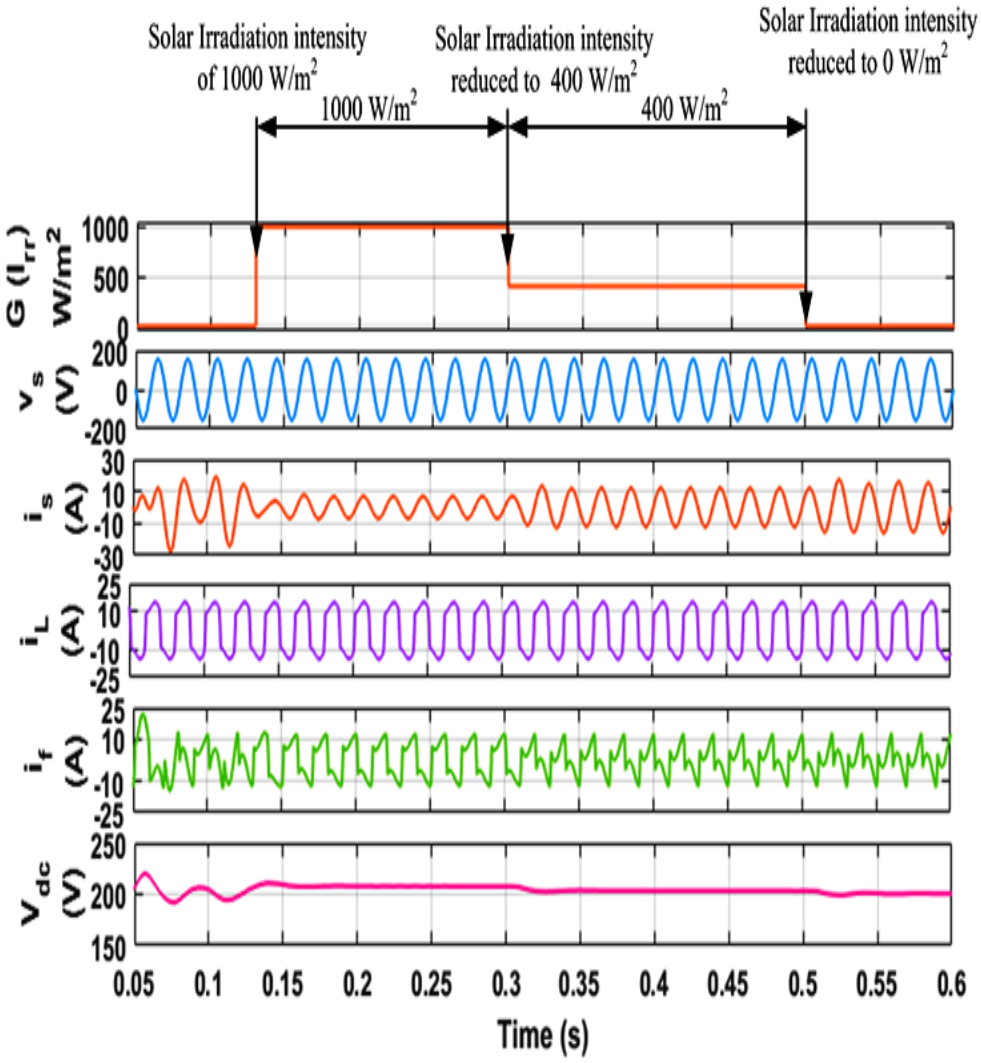

Fig. 4.25. Steady state waveforms under changing irradiation conditions with constant non-linear load conditions with SOGI controller in simulink

After 0.3s, the PV has been disconnected and the whole load current of 15A is again met by the source. The DC link voltage shows a little dip and rise when solar irradiation intensity has been changed but settles down to its reference value of 200V.

Fig. 4.27 shows the steady state power waveforms of G(W/m^2), (P_s, Q_s), (P_L, Q_L),(P_f, Q_f) under changing solar irradiation conditions of 1000W/m^2 from 0.13s to 0.25s and 400W/m^2 from 0.3s to 0.5s. It has been found that till 0.13s, under normal grid conditions without PV irradiation, the source power 1.21kW is used to meet the load demand and the reactive kVAR of 0.5 is met by the compensator.

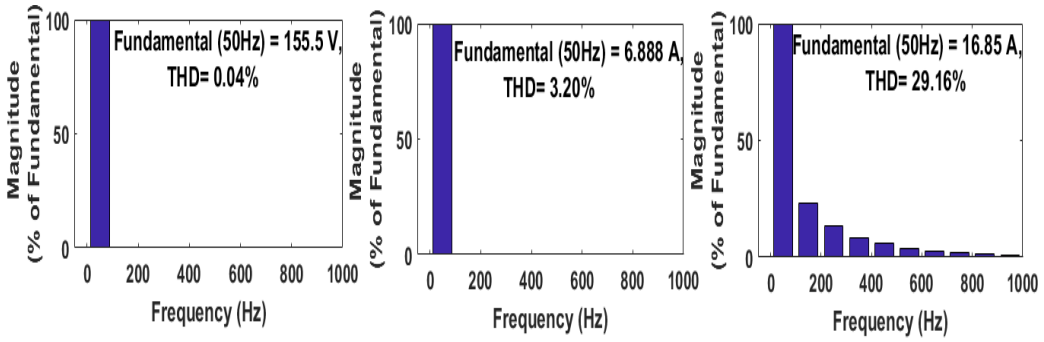

(a) (b) (c)

Fig. 4.26. THD of SOGI controller for (a) source voltage (v_s) (b) source current (i_s) and (c) load current (i_L) under changing solar irradiation conditions with constant non-linear load in simulink

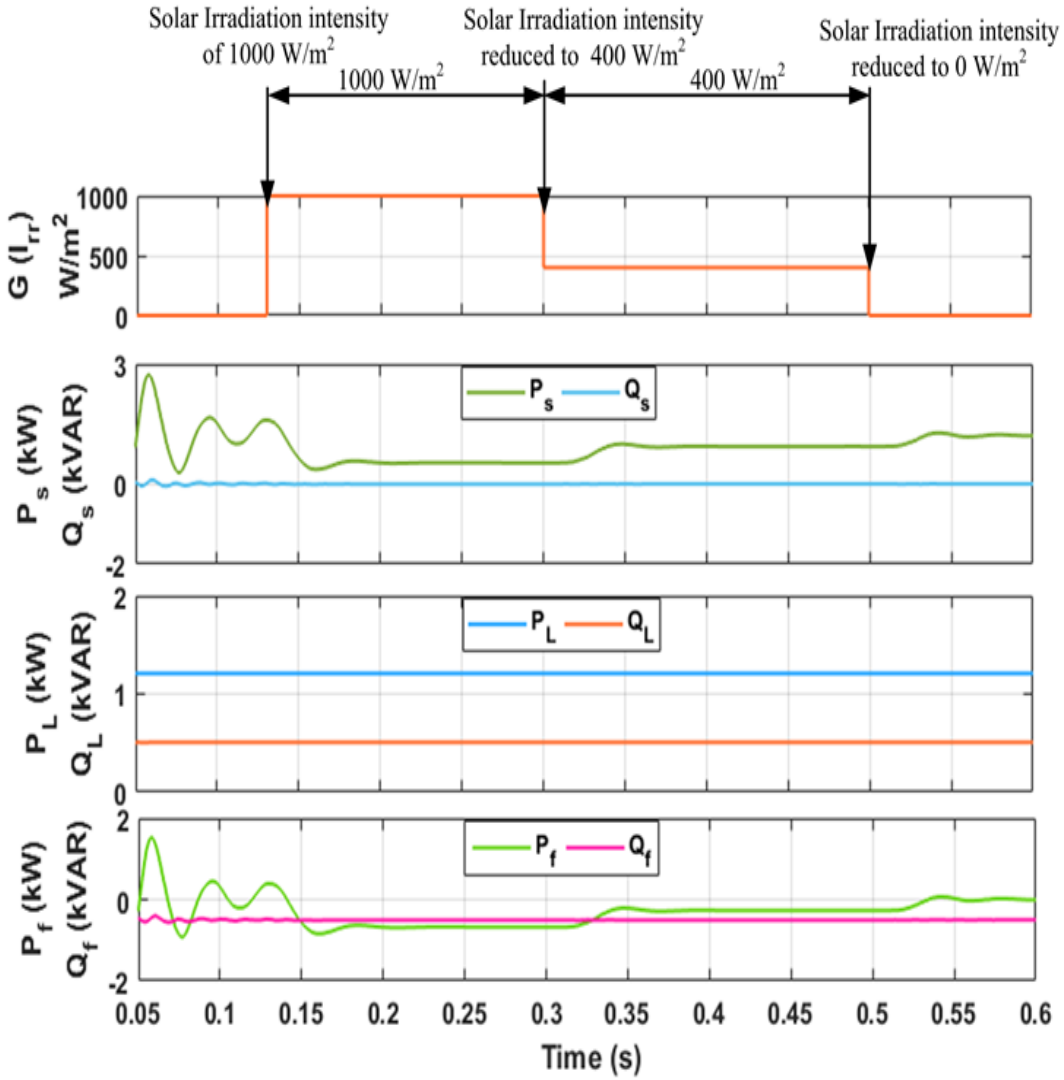

Fig. 4.27. Steady state power curves for supply, load and PV source with SOGI based controller in simulink

When the solar irradiation intensity of 1000W/m^2 is simulated, the load power of 1.21 kW is shared by both PV power of 0.66kW and the grid power of 0.55kW. At 0.3s the solar irradiation intensity has been reduced to 400W/m^2 as the result the grid power increases to 0.94kW and the PV power reduces to 0.27kW to meet the load demand of 1.21kW. When the solar irradiation is made zero from t= 0.5s onwards, the grid power increases correspondingly to meet the total load demand of 1.21kW. The load reactive power of 0.5kVAR is completely met by the compensator.

4.2.3 Performance Analysis with TFLNN Controller

The performance of the Trigonometric Functional Link Neural Network based control scheme is designed and modelled under changing load conditions and changing solar irradiation conditions.

4.2.3.1 Performance under changing load conditions

The waveforms of v_s,i_s ,i_L ,i_f and V_{dc} are shown in Fig. 4.28 under different loading conditions. It has been observed that till 0.1s, under non-linear load conditions the grid current of 15A is used to meet the load demand. The source current is sinusoidal and in phase with grid voltage. The THD under non-linear load conditions is 1.96% shown in Fig. 4.29. It has been found that at 0.1s, the linear load is put additionally along with non-linear load and mixed loading conditions are created. The source current is sinusoidal and in phase with grid voltage.

Under mixed loading conditions, the source current increases to 20A to meet the load demand. It remains sinusoidal and in phase with the voltage. The THD of source current under mixed loading conditions is 3.27% with load current THD of 18.47% as shown in Fig. 4.30.

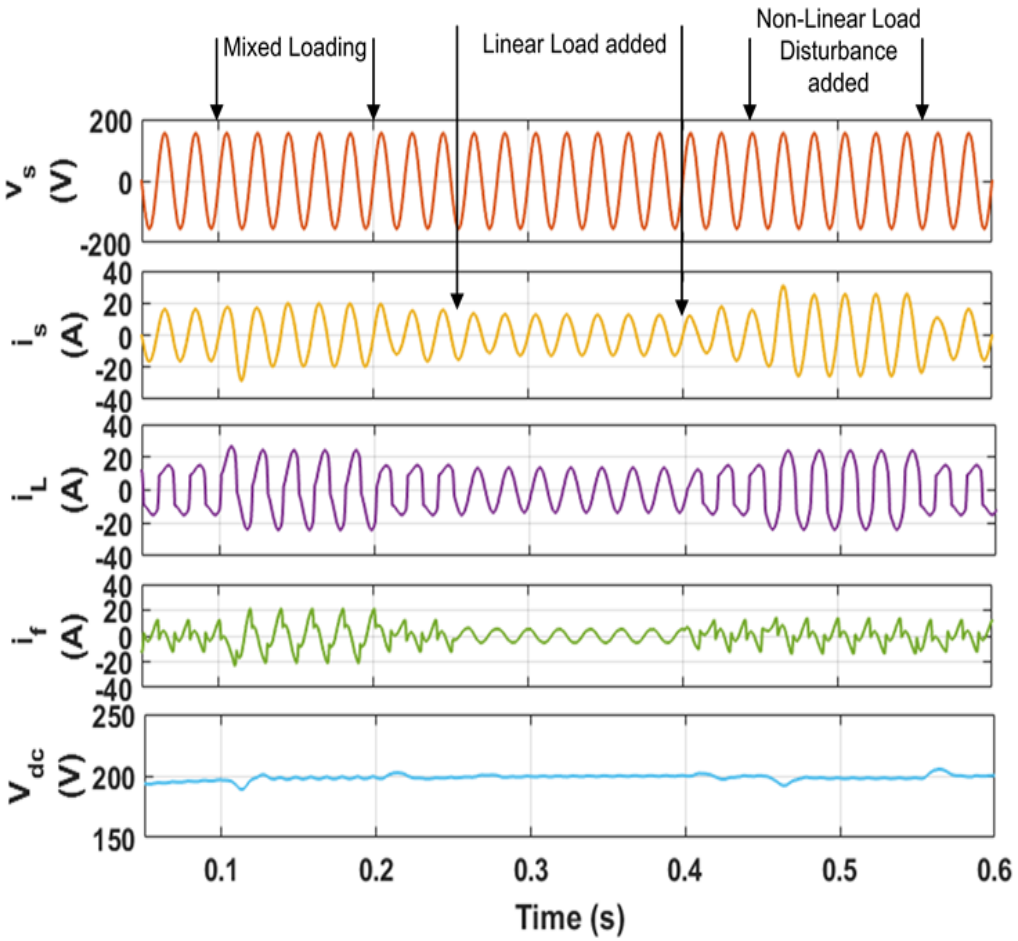

Fig. 4.28. Steady state waveforms under changing load conditions with TFLNN controller in simulink

At 0.25s, under linear load conditions, the source current and load current are sinusoidal meeting the demand of magnitude 12A. The THD of supply current with TFLNN controller under linear load conditions is 2.37% as shown in Fig. 4.31.

Under non-linear load disturbances the source current increases to 24A to meet the load demand. The source current is sinusoidal and in phase with the voltage.

A little dip in DC link voltage is observed when the load is added or removed but it soon settles down to its reference value of 200V due to PI controller action.

Fig. 4.32 shows the steady state power sharing between source, load and compensator under different loading conditions. It has been found that under non-linear

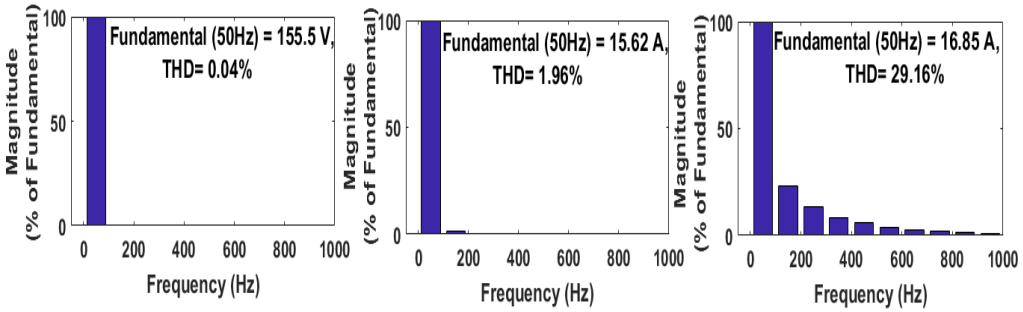

(a) (b) (c)

Fig. 4.29. THD of TFLNN controller for (a) source voltage (v_s) (b) source current (i_s) and (c) load current (i_L) under non-linear load conditions in simulink

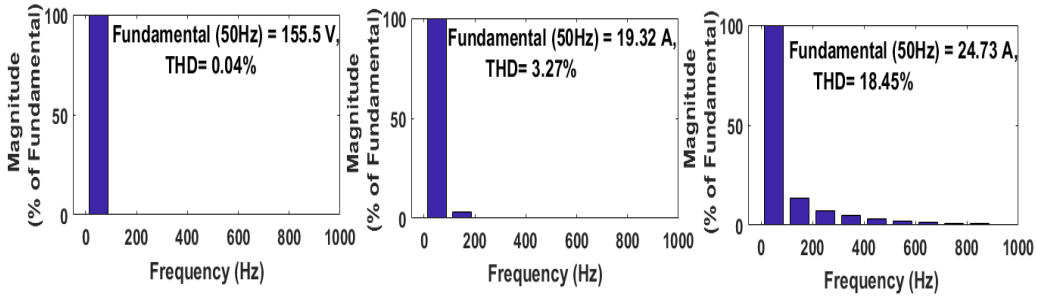

(a) (b) (c)

Fig. 4.30. THD of TFLNN controller for (a) source voltage (v_s) (b) source current (i_s) and (c) load current (i_L) under mixed loading conditions in simulink

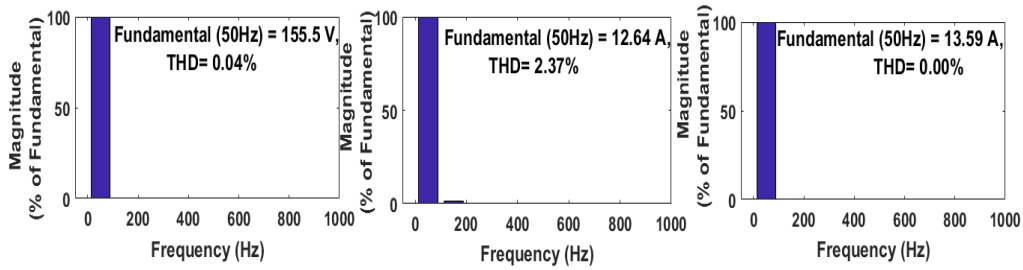

(a) (b) (c)

Fig. 4.31. THD of TFLNN controller for (a) source voltage (v_s) (b) source current (i_s) and (c) load current (i_L) under linear loading conditions in simulink

load conditions the load active power is met by the source power of 1.21kW and the reactive load of 0.5kVAR is met by the compensator. Under non-linear load disturbance the load active and reactive power demand has been increased to 2kW and 1.2kVAR.

Under mixed loading conditions the load demand of 1.5kW is met by the source and reactive power of load is met by the compensator power of 1.2kVAR.

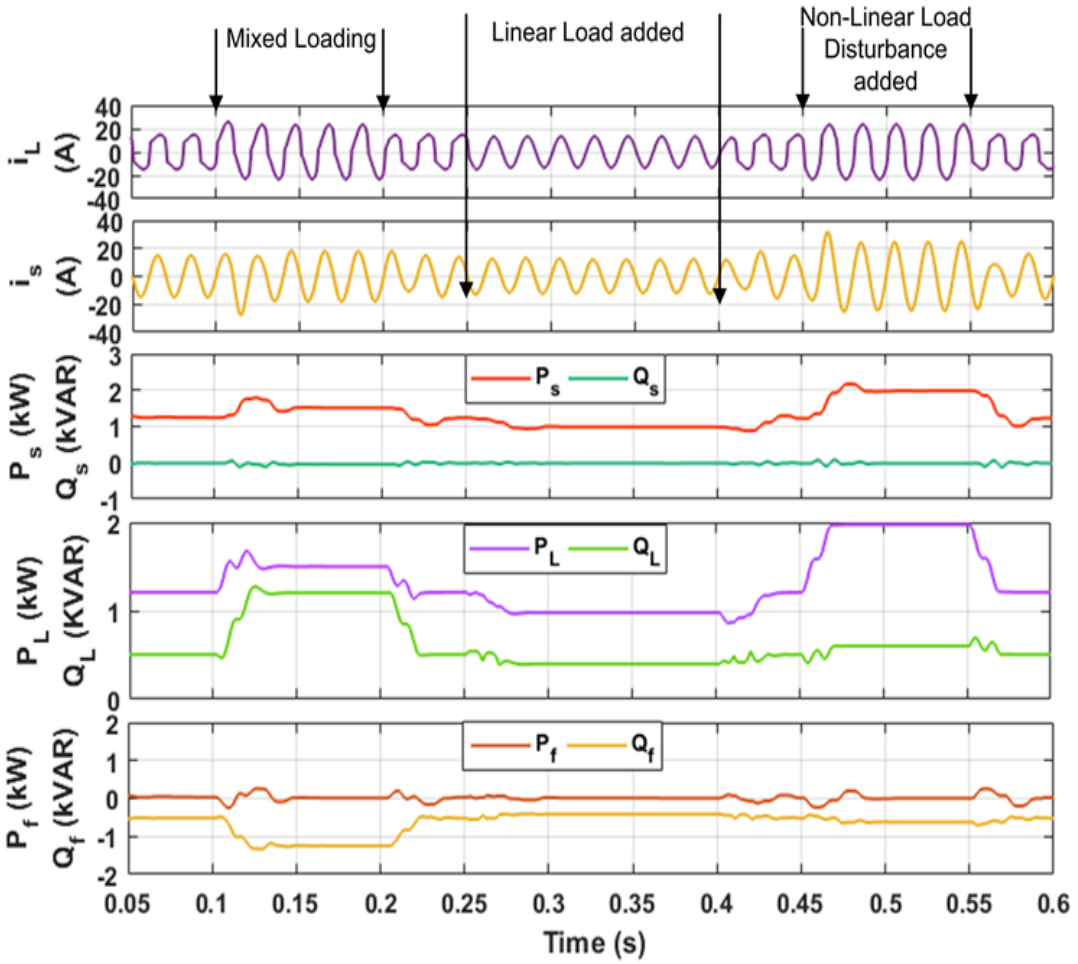

Fig. 4.32. Steady state power waveforms under changing load conditions with TFLNN controller in simulink

Under linear load conditions the active power demand of 1kW is met by the corresponding source power and the reactive VAR of load is met by the compensator of 0.5kVAR.

Fig. 4.33 shows the intermediate results of the algorithm such as i_{Lest}, w_{sin}, w_{cos}, w, e, i_{pnet} and $sin\theta$. When the linear or non-linear load increases, the active power and hence the estimated load component of current i_{Lest} and i_{pnet} increases. The individual expansion components w_{sin} increases with the loading conditions and the w_{cos} decreases with the loading conditions. These expansion components are updated online by the coefficient w of the LMS algorithm. The error 'e' generated between the actual

load current and the estimated load current updates the coefficient 'w' of the LMS algorithm, which in turn updates the expansion component of the Trigonometric algorithm. The term i_{pnet} is the gross active current needed from the source to support the load. It is obtained by the addition of estimated component of load current i_{Lest} and switching loss component of VSC i_{Loss}. The $sin\theta$ is the unit in template generated which when multiplied with the i_{pnet} gives the sinusoidal reference current.

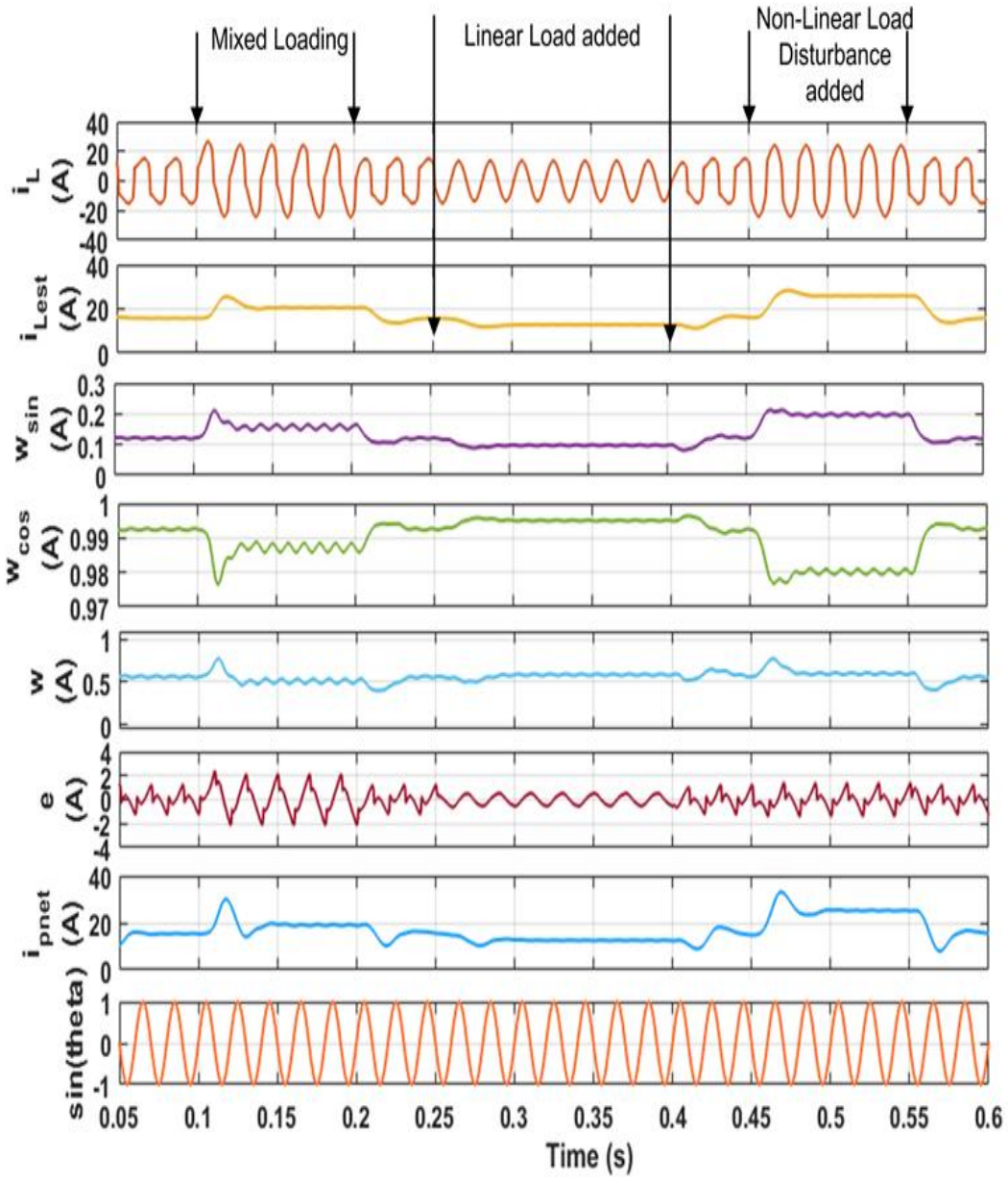

Fig. 4.33. Steady state intermediate waveforms under changing load conditions with TFLNN controller in simulink

Table 4.3 shows the values of THD obtained in simulink using TFLNN controller under various loading conditions i.e., non-linear load, linear load and mixed loading conditions

Table 4.3. THD values obtained in simulink using TFLNN under various loading conditions

Loading Conditions	Trigonometric Functional Link Neural Network (TFLNN)		
	i_L(THD)	i_S(THD)	v_s(THD)
Non-Linear Load Conditions	29.16%	1.96%	0.04%
Mixed Load Conditions	18.45 %	3.27%	0.04%
Linear Load Conditions	0.00 %	2.37%	0.04%

4.2.3.2. Performance under changing solar irradiation conditions

The waveforms of $G(I_{rr})$, v_s,i_s, i_L, i_f and V_{dc} are shown in Fig. 4.34 below. It has been found that till 0.13s, the solar irradiation is zero and under grid connected non-linear load conditions, the source current of 15A is used to meet the load demand. It is sinusoidal and in phase with voltage. The load current is clearly non sinusoidal as connected load is non-linear in nature.

The PV array panel has a maximum power capacity of 750W at 1000W/m^2. However, after losses panels deliver power of 660W at the DC link of inverter after meeting switching losses in double stage configuration. When the solar irradiation of 1000W/m^2 is there the source current decreases to 7.07A as the load demand is shared by both PV and the grid. The THD of source current is 2.04% under non-linear load THD of 29.19% shown in Fig. 4.35. When the solar irradiation is reduced to 400W/m^2 the grid current increases and the PV current decreases to meet the load demand of 12A.

Fig. 4.36 shows the steady state power sharing between source, load and compensator. It is found that till 0.13s the total load power demand is shared by the grid

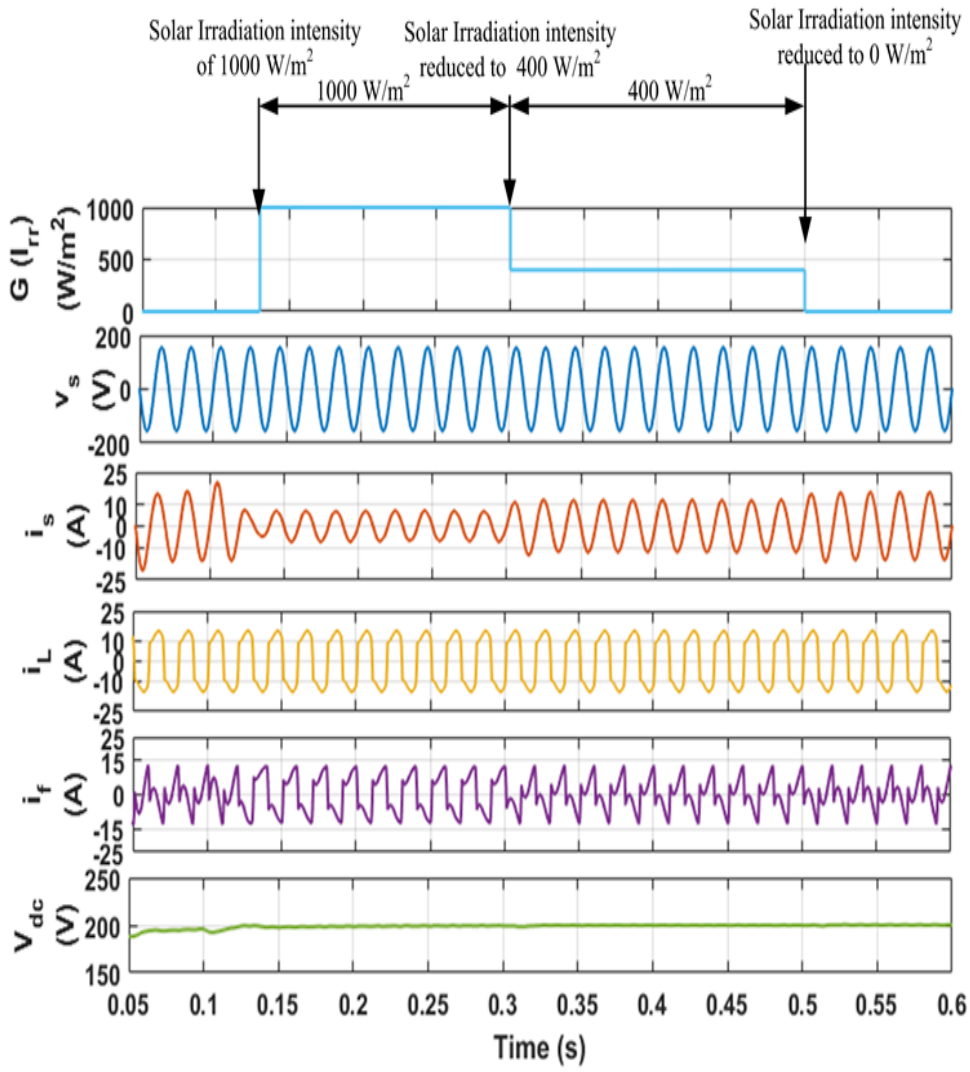

Fig. 4.34. Steady state waveforms under changing irradiation conditions with constant non-linear load conditions with TFLNN controller in simulink

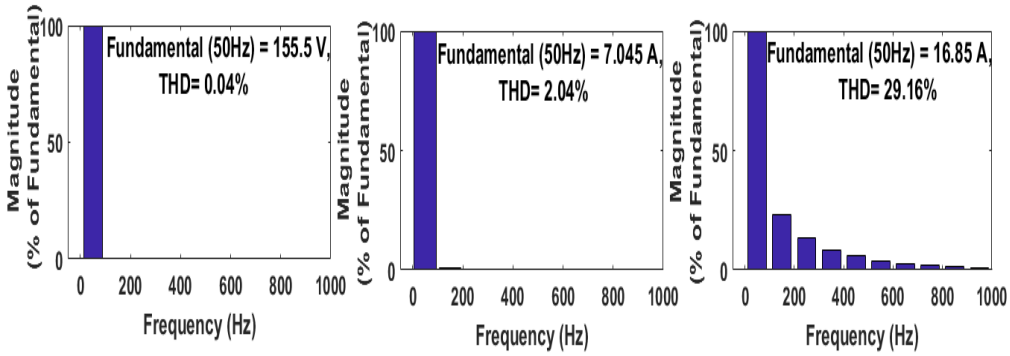

Fig. 4.35. THD of TFLNN controller for (a) source voltage (v_s) (b) source current (i_s) and (c) load current (i_L) under changing solar irradiation conditions with constant non-linear load in simulink

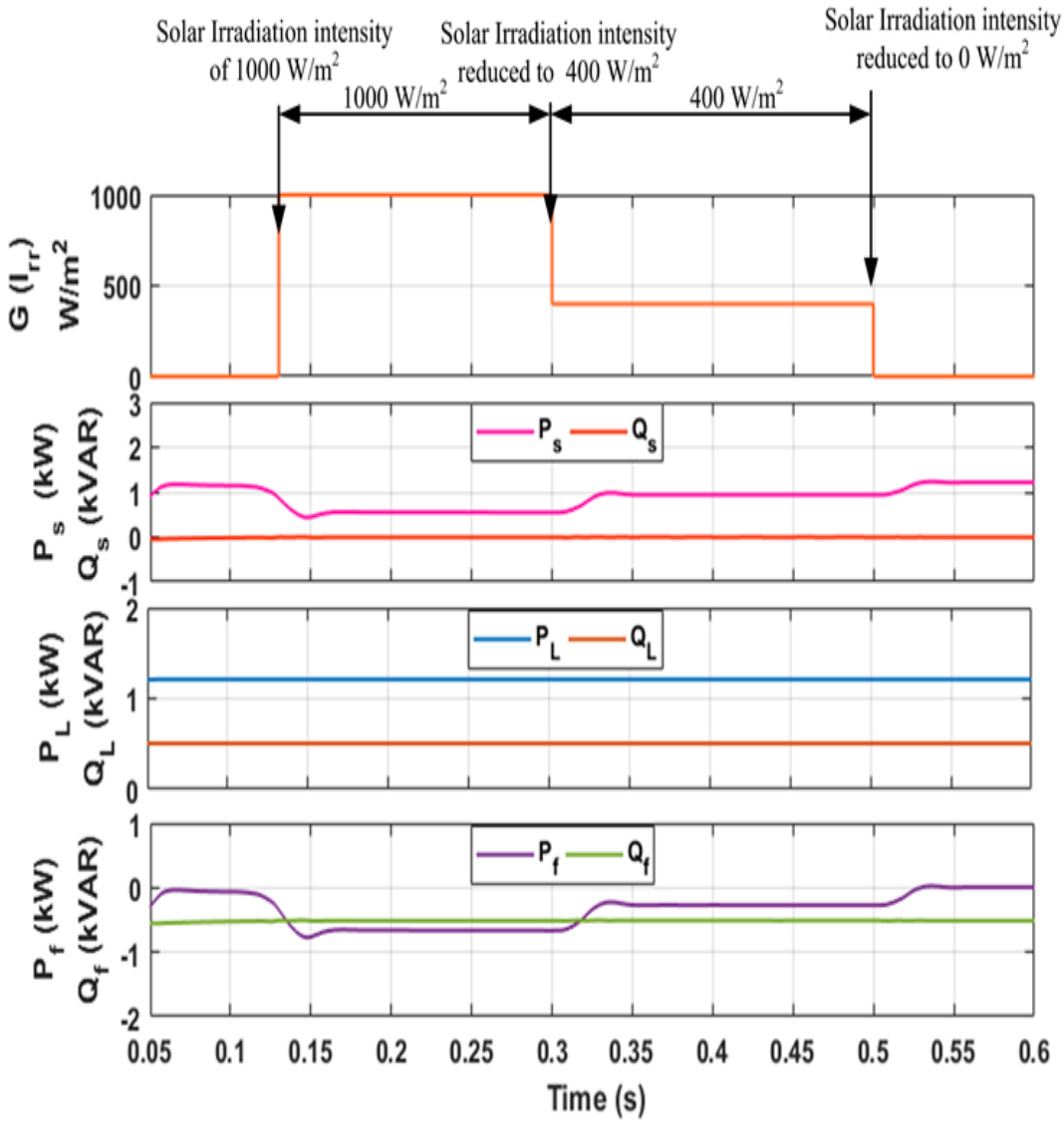

Fig. 4.36. Steady state power waveforms under changing irradiation conditions with constant non-linear load with TFLNN controller in simulink

After 0.13s under solar irradiation intensity of 1000W/m^2 till 0.3s, the load power of 1.2kW is shared by the source power of 0.55kW and the PV power of 0.66 kW.

After 0.3s till 0.5s, the solar irradiation intensity has been reduced to 400W/m^2, it has been found that the source power increased to 0.94kW and the PV power decreased to 0.27kW under lower irradiance levels. After 0.5s the solar irradiation is reduced to 0 W/m^2, the source power again increases to 1.2kW to meet the complete load power.

4.2.4 Performance Analysis with LFNN Controller

The performance of the Legendre Functional Neural Network based control scheme is designed and modelled under changing load conditions and changing solar irradiation condition.

4.2.4.1 Performance under changing load conditions

The dynamic performance under grid connected systems under changing load conditions is analyzed using the waveforms v_s, i_s,i_L, i_f, V_{dc} which are shown in Fig. 4.37 below. Under non-linear load conditions up to 0.1s, the source current is sinusoidal and in phase with the voltage. The load current of 15A is met by the source current of 15A.

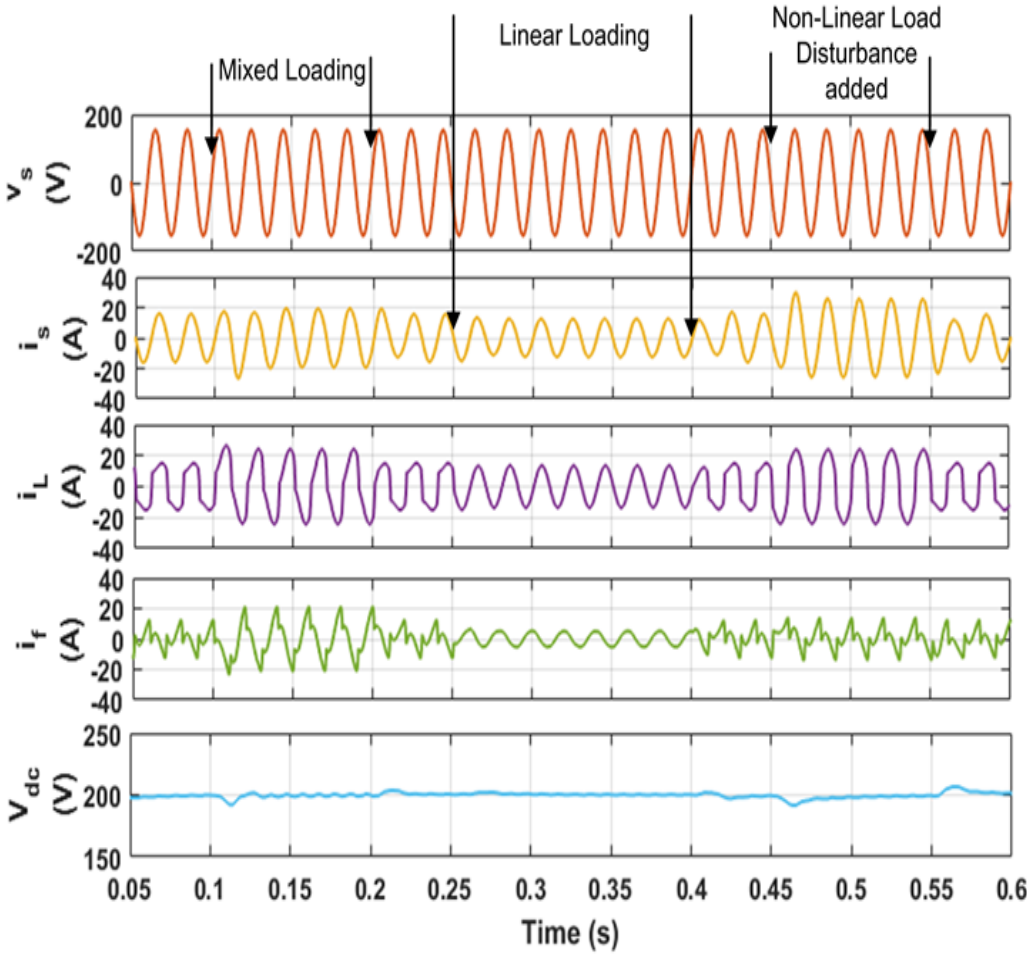

Fig. 4.37. Steady state waveforms under changing load conditions with LFNN controller in simulink

From 0.1s to 0.2s, the linear load is put and mixed loading conditions are simulated. The source current is sinusoidal and in phase with the voltage. The source current is increased to 20A to meet the load demand.

From 0.25s to 0.35s the linear load is there, the load current of 12A is met by the source current of 12A. The load current as well as source current both are sinusoidal and in phase with each other.

From 0.45s to 0.55s, the non-linear load disturbance is there and it is found that the source current is sinusoidal and in phase with the voltage The source current of 24A is met by the source current of 24A.The THD of source current under non-linear load conditions is found to be 1.42% for load current THD of 29.16% shown in Fig. 4.38 and under mixed loading conditions source current THD is found to be 3.63% for load current THD of 16.51% shown in Fig. 4.39 and under linear load conditions it is found to be 1.78% under load current THD of 0.00% shown in Fig. 4.40.

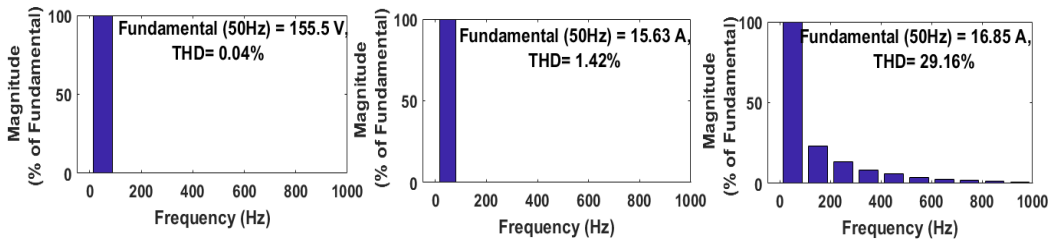

Fig. 4.38. THD of LFNN controller for (a) source voltage (v_s) (b) source current (i_s) and (c) load current (i_L) under non-linear load conditions in simulink

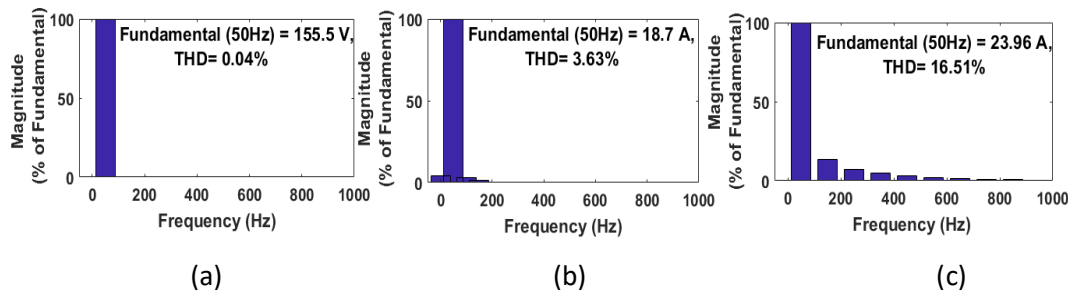

Fig. 4.39. THD of LFNN controller for (a) source voltage (v_s) (b) source current (i_s) and (c) load current (i_L) under mixed loading conditions in simulink

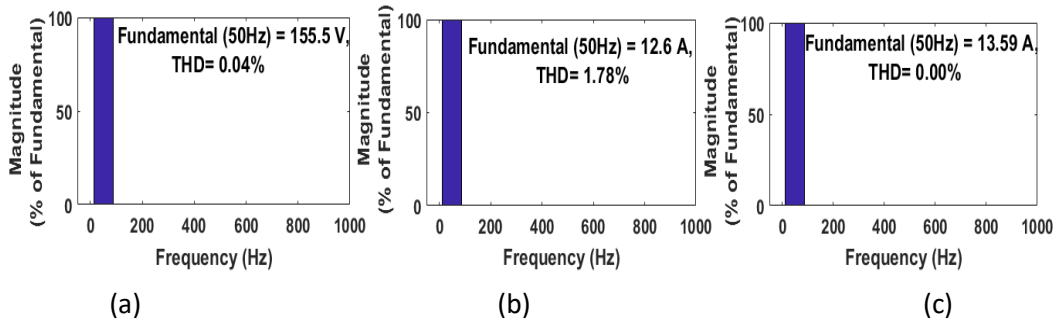

Fig. 4.40. THD of LFNN controller for (a) source voltage (v_s) (b) source current (i_s) and (c) load current (i_L) under linear loading conditions in simulink

Fig. 4.41 shows that under non-linear load up to 0.1s, the load power of 1.2kW is met by the source power of 1.21kW. The reactive power of 0.5kVAR is met by the SAPF of 0.5kVAR.

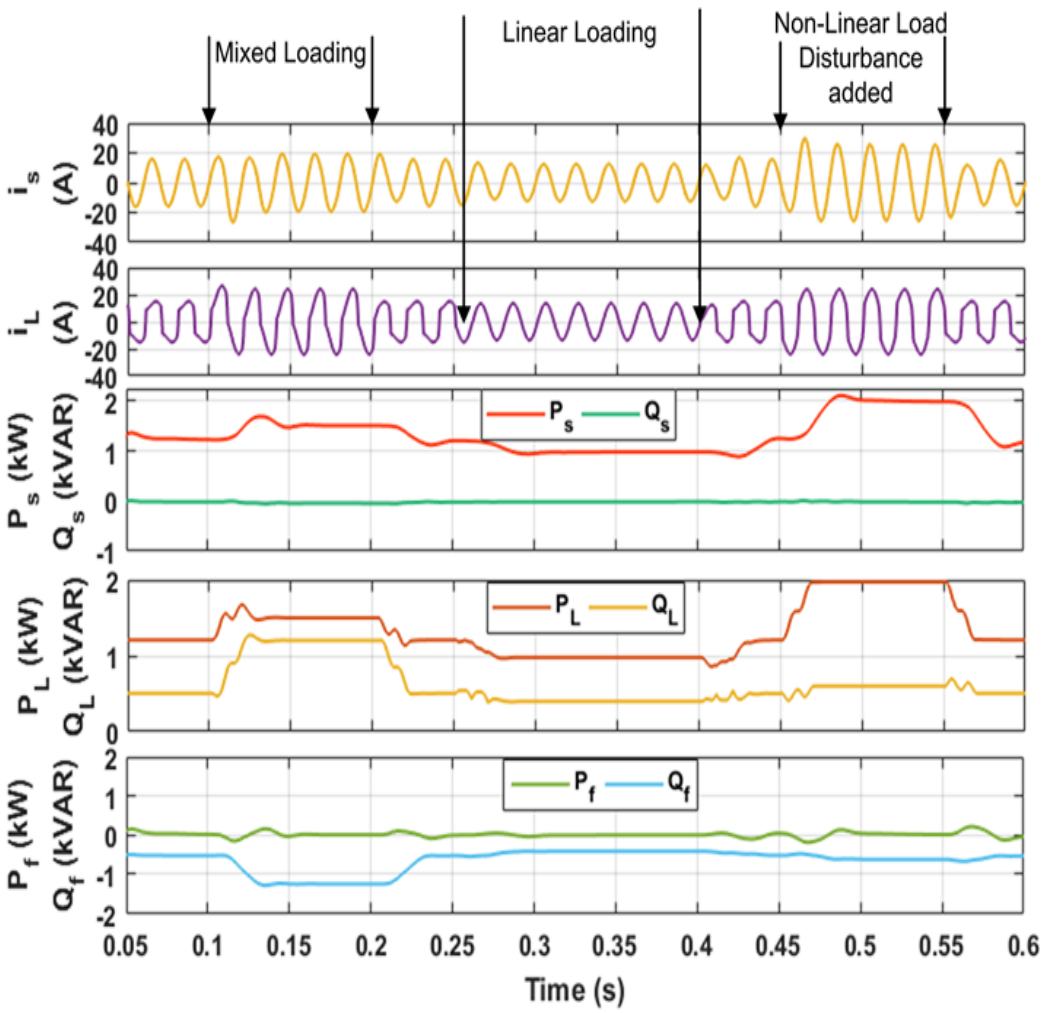

Fig. 4.41. Steady state power waveform under changing loading conditions with LFNN controller in simulink

Under mixed loading conditions, the load power of 1.5kW is met by the source power of 1.5kW. Under linear loading conditions from 0.25s to 0.4s, the load power of 1kW met by the source power of 1kW. From 0.45s to 0.55s the non-linear load disturbance takes place and the load power of 2kW is met by the source power of 2kW. The reactive power of 1.2kVAR is met by the SAPF of 1.2kVAR.

Fig. 4.42 shows the intermediate results of the LFNN algorithm consisting of load current i_L, load current expansion components i_{L0}, i_{L1}, i_{L2},estimated load current, i_{Lest} and error 'e'. It has been observed that the load expansion components sum up to i_{LTotal} which further estimates the load current. The weight vectors are regulated between 0 and 1.

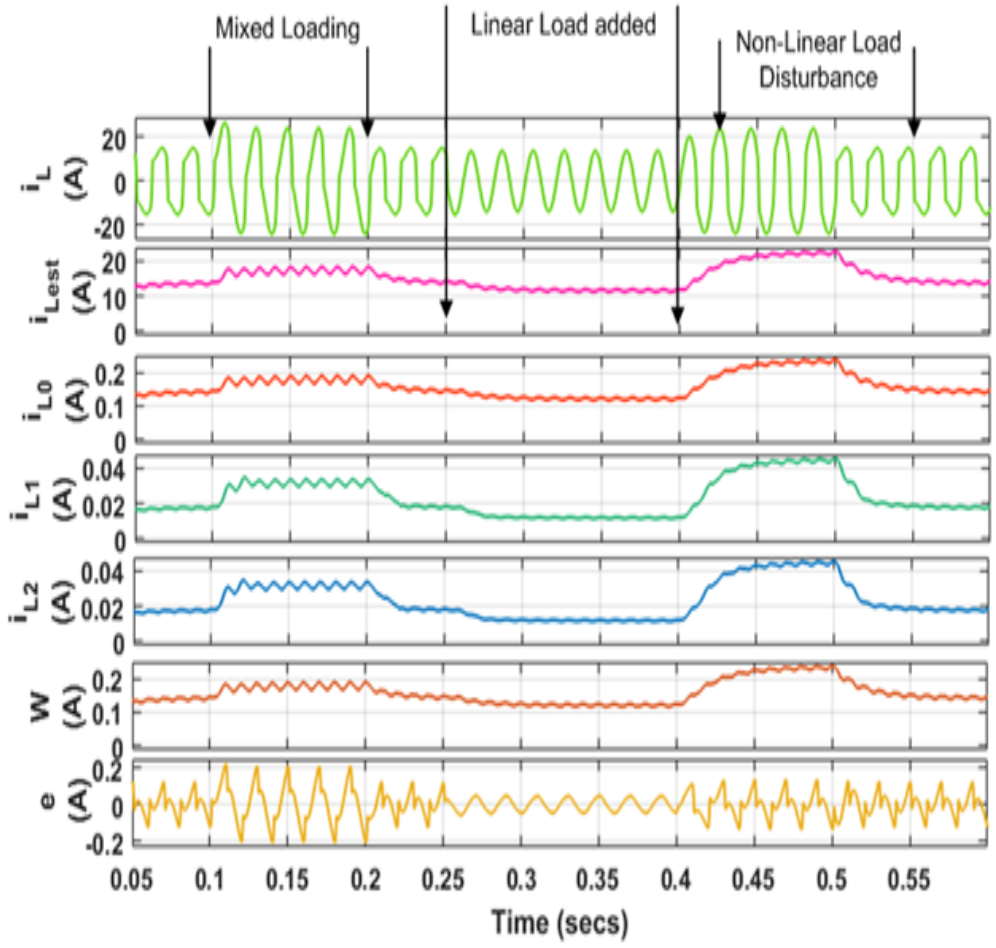

Fig. 4.42. Steady state intermediate waveforms under changing loading conditions with LFNN controller in simulink

Table 4.4 shows the THD values obtained in simulink using LFNN algorithm under various loading conditions

Table 4.4. THD values obtained in simulink using LFNN algorithm under various loading conditions

Loading Conditions	Legendre Functional Neural Network (LFNN)		
	i_L(THD)	i_S(THD)	v_s(THD)
Non-Linear Load	29.16%	1.42%	0.04%
Mixed Load	18.45 %	3.63%	0.04%
Linear Load	0.00%	1.78%	0.04%

4.2.4.2 Performance under changing irradiation conditions

The dynamic performance of the system under PV integrated grid connected systems is shown in Fig. 4.43 below. The waveforms of $G(I_{rr})$, v_s,i_s, i_L, i_f are shown below. Till 0.1s there is non-linear load conditions. The source current of 15A is used to meet the load current. The three Kyocera 250W PV array panels connected in series produce maximum power capacity of 750W at 1000 W/m^2. However, after losses panels deliver power of 660W at the DC link of inverter.

At 0.13s, the solar irradiation of 1000W/m^2 is used. It has been found that the grid current has been decreased to 7A as the load current is shared by both PV current and grid current.

After 0.3s, the solar irradiation intensity is of 400W/m^2, as the PV irradiation intensity has decreased, the source current increases to 12A to meet the load demand.

After 0.5s, the solar irradiation intensity is reduced to zero, the source current again regains its value to 15A to meet the load demand of 15A. The THD in source current under changing solar irradiation conditions is 2.04% shown in Fig. 4.44 and within IEEE-1547 limits with PV system.

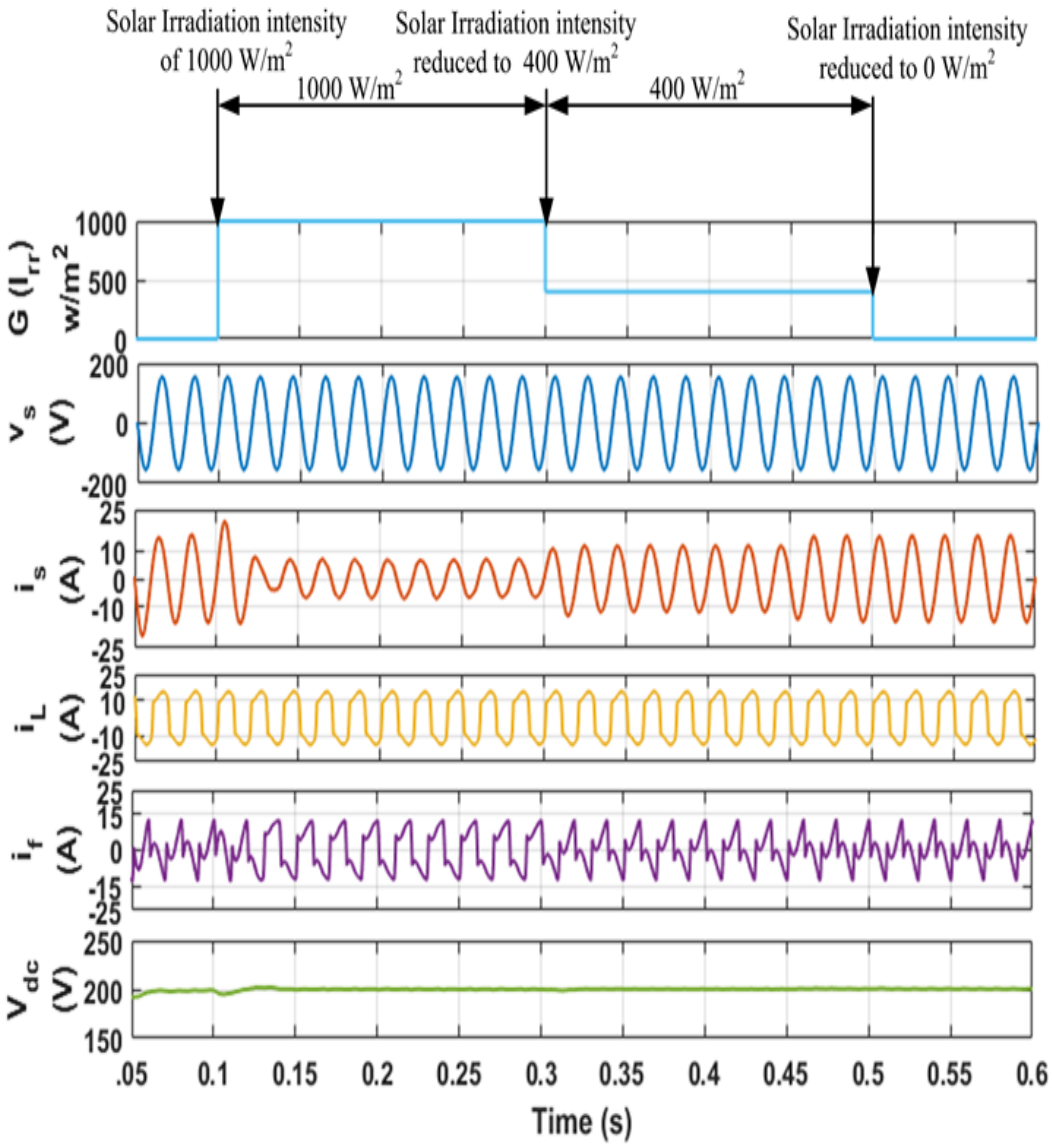

Fig. 4.43. Steady state waveforms under changing irradiation conditions with constant non-linear load with LFNN controller in simulink

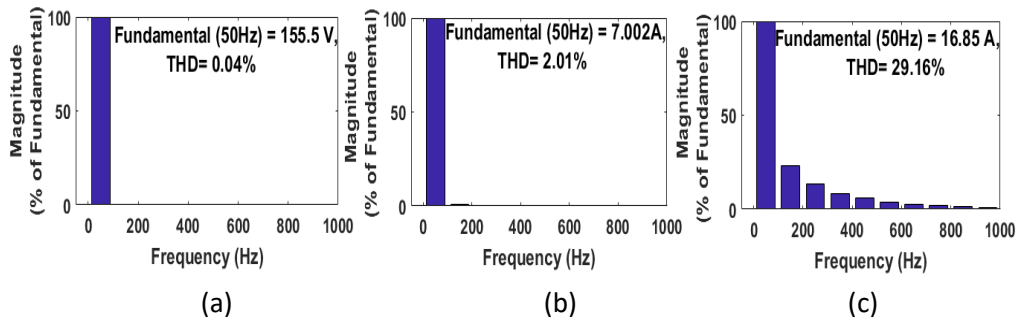

Fig. 4.44. THD of LFNN controller for (a) source voltage (v_s) (b) source current (i_s) and (c) load current (i_L) under changing irradiation conditions with constant non-linear loading conditions in simulink

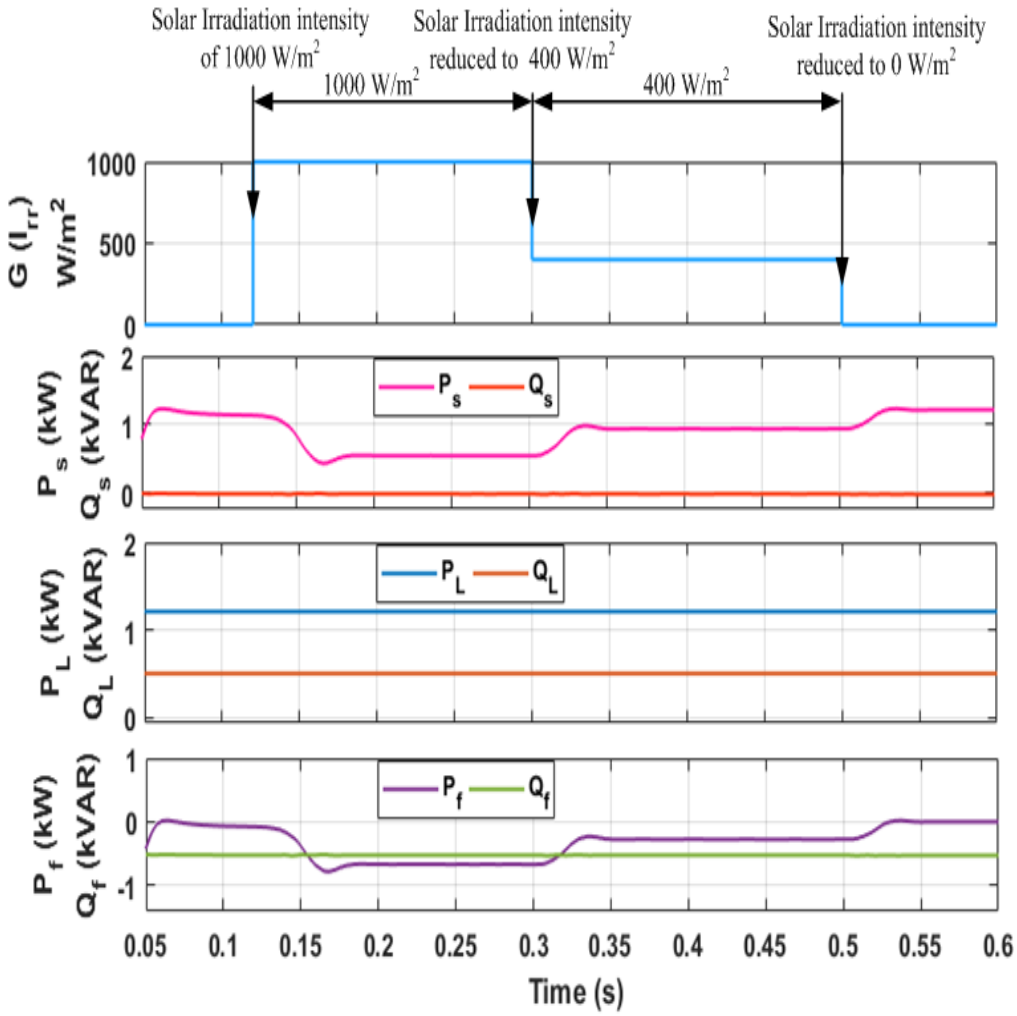

Fig. 4.45. Steady state power waveforms under changing irradiation conditions with constant non-linear load with LFNN controller in simulink

The steady state sharing of power waveform is shown in Fig. 4.45. Up to non-linear load conditions up to 0.1s the load power of 1.21kW is met by the source power of 1.21kW. Under solar irradiation intensity of 1000W/m^2, the load power of 1.21kW is met by the source power of 0.55kW and the PV power of 0.66kW. The reactive power of 0.5kVAR needed by the load is met by the SAPF.

Under solar irradiation intensity of 400W/m^2, 1.21kW is met by the source of 0.94kW and PV of 0.27kW. After 0.5s, the PV irradiation is reduced to zero, hence the 1.21kW load demand is met by the source power of 1.21kW.

4.3 Hardware Results

This section discusses the experimental results of the developed system with Synchronous Reference Frame Theory (SRFT), Second Order Generalized Integrator (SOGI), Trigonometric Functional Link Neural Network (TFLNN) and Legendre Functional Neural Network (LFNN) based controller for SAPF on hardware prototype of single-phase grid connected non-linear load system developed in the laboratory using dSPACE 1104 with and with-out PV interfaced systems. The Chroma EN50530 Sandia PV array of maximum power capacity of 300W is interfaced at the DC link of inverter. The hardware results are taken on power analyzer and DSO. The performance analysis is done under different linear, non-linear, and mixed loading conditions to check the effectiveness of these control algorithms.

4.3.1 Performance analysis with SRFT Controller

The SRFT based control scheme is modelled in dSpace 1104 on hardware prototype developed on single-phase grid connected systems.

4.3.1.1 Performance under non-linear loading conditions

Fig. 4.46 shows the hardware operation of SAPF on single-phase grid connected systems. The SAPF operation is performed at 110V, 50Hz supply feeding non-linear load. The steady-state performance voltage and current waveform results for SAPF integrated grid-connected systems are shown in Fig. 4.46. Figs. 4.46 (a-f) shows the source voltage waveform (v_s), load current waveform (i_L), compensator current waveform (i_f), source voltage THD, source current THD (i_s) and load current THD. The source current is observed to be sinusoidal and in phase with the voltage. The source current THD with SRFT controller is found to be 4.5% under non-linear load conditions having a THD of 30.3%. The THD in supply voltage is 0.8%.

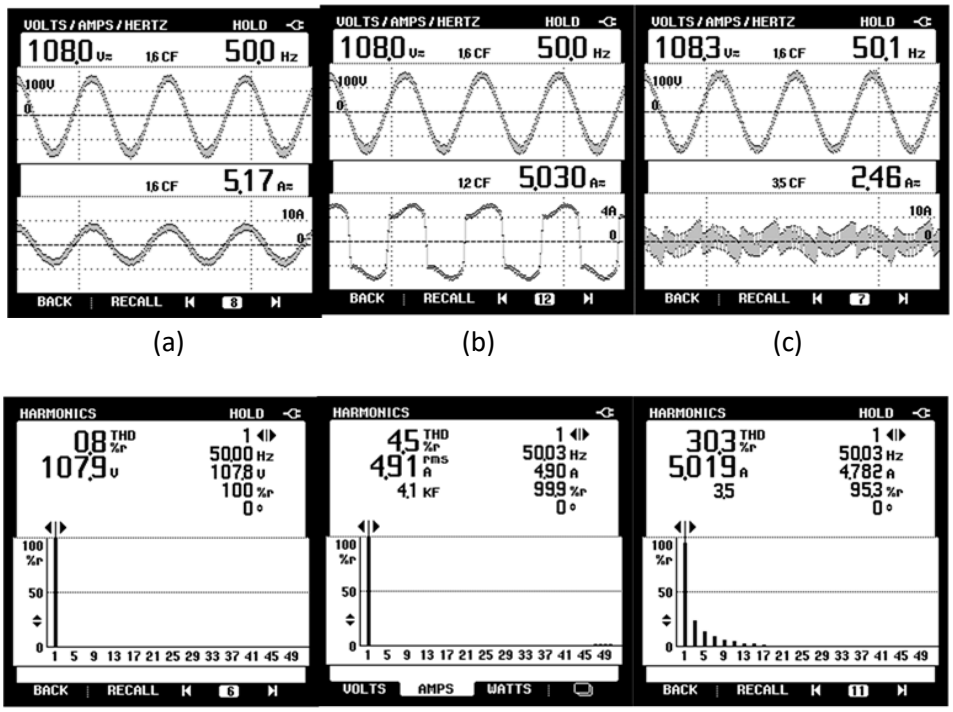

Fig. 4.46. Steady state experimental performance analysis of SRFT controller under non-linear load conditions (a) source voltage waveform (v_s) (b) load current waveform (i_L) (c) compensator current waveform (i_f) (d) source voltage THD (e) source current THD and (f) load current THD

4.3.1.2. Performance under Mixed loading conditions

Figs. 4.47 (a-d) show the source voltage waveform (v_s), load current waveform (i_L), compensator current waveform (i_f), source voltage THD, source current THD (i_s) and load current THD under mixed loading conditions. The source current is observed

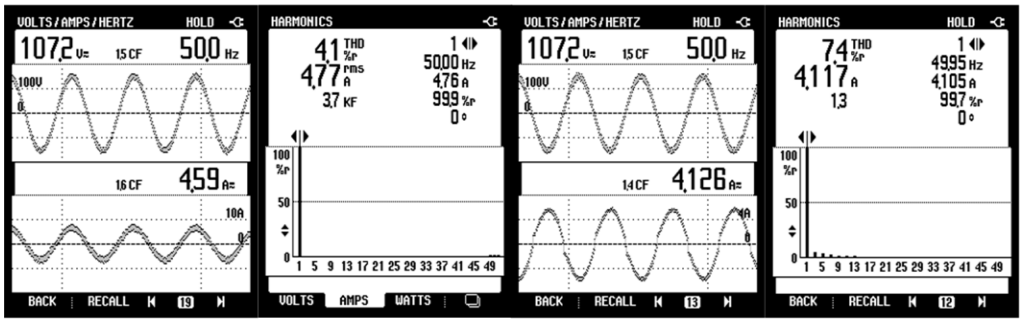

Fig. 4.47. Steady state experimental performance analysis of SRFT controller under mixed loading conditions (a) source voltage (v_s) (b) source current THD (i_s) and (c) load current (i_L) waveform (d) load current THD

to be sinusoidal and in phase with the voltage. The source current THD with SRFT controller is found to be 4.1% under mixed load conditions of 7.4%.

4.3.1.3 Performance under linear loading conditions

Figs. 4.48 (a-d) show the source voltage waveform (v_s), load current waveform (i_L), compensator current waveform (i_f), source voltage THD, source current THD (i_s) and load current THD under linear loading conditions. The source current is observed to be sinusoidal and in phase with the voltage. The source current THD is found to be 4.5% with SRFT controller under linear load THD of 0.4% since the VSC injects the harmonics. Table 4.5 shows the THD values obtained experimentally with SRFT

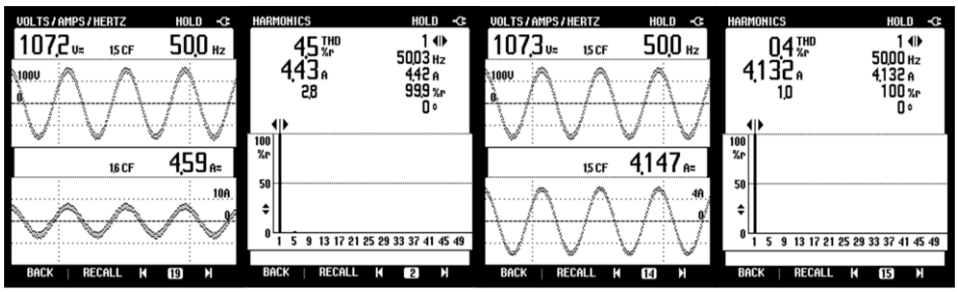

Fig. 4.48. Steady state experimental performance analysis of SRFT controller under linear loading conditions (a) source voltage (v_s) waveform (b) source current THD (i_s) and (c) load current (i_L) waveform (d) load current THD

algorithm under various loading conditions.

Table 4.5. THD values obtained experimentally with SRFT algorithm under various loading conditions

Loading Conditions	Synchronous Reference Frame Theory (SRFT)		
	i_L(THD)	i_S(THD)	v_s(THD)
Non-Linear Load Conditions	29.9%	4.5%	0.5%
Mixed Load Conditions	7.4%	4.1%	0.5%
Linear Load Conditions	0.4%	4.5%	0.5%

4.3.1.4 Steady State Power flow under non-linear load conditions

The steady state power transfer between the non-linear load, SAPF and grid is shown in Fig. 4.49. The load active power of 470W is met by the source active power of 510 W. The source also meets extra switching losses of 40W. The reactive power of the load of 110VAR is met completely by the compensator. The reactive power of 120VAR is generated by SAPF as shown in Fig. 4.49.

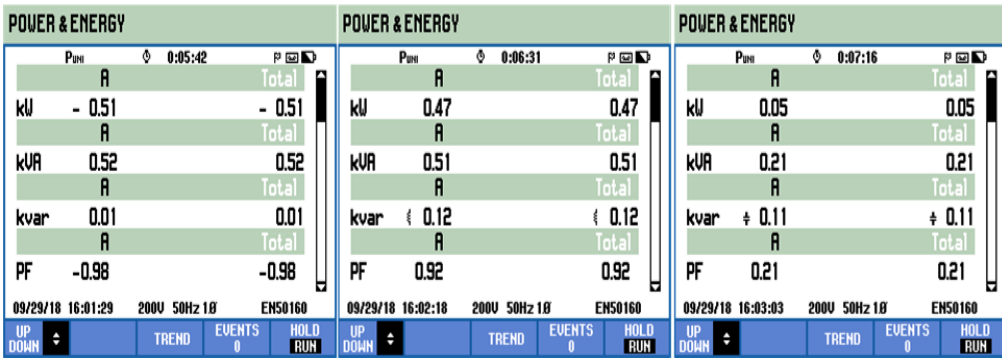

(a) (b) (c)

Fig. 4.49. Steady state experimental power analysis of SRFT controller under non-linear load conditions (a) source power (P_s) (b) load power (P_L) and (c) compensator power (P_f)

4.3.1.5 Dynamic Results with SRFT Controller

Fig. 4.50 shows the dynamic results of SRFT algorithm under changing load conditions. Fig. 4.50 (a) shows the waveform of load current (i_L), fundamental load component (i_{Ld}), quadrature component (i_{Lq}) and unit template ($\sin\theta$) under load increase. The fundamental load component (i_{Ld}) increases as the load increases. Fig. 4.50(b) shows the waveform of load current (i_L), fundamental load component (i_{Ld}), quadrature component (i_{Lq}) and unit template ($\sin\theta$) under load decrease. The fundamental load components are expected to vary with the loading conditions while the $\sin\theta$ is not expected to change. This is observed in the dynamic results with SRFT algorithm.

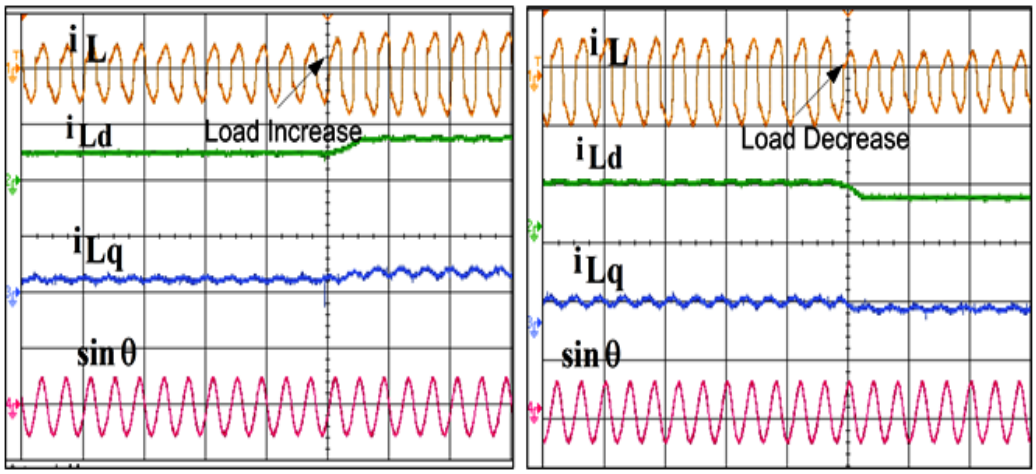

(a) (b)

Fig. 4.50. Dynamic waveforms of SRFT observed on oscilloscope (a) i_L, i_{LD}, i_{Lq}, $sin\theta$ under load increase (b) i_L, i_{LD}, i_{Lq}, $sin\theta$ under load decrease

4.3.1.6 Performance analysis with SRFT Controller for PV grid tied system

Fig. 4.51 shows the hardware operation of SAPF for single-phase grid connected systems when PV is interfaced. PV integration results are taken for 45V, 50Hz supply feeding non-linear loads. Fig. 4.51 shows the steady state performance voltage and current waveform results under SAPF integrated grid connected systems. Figs. 4.51 (a-f) shows the source voltage waveform (v_s), load current waveform (i_L), compensator current waveform (i_f), source voltage THD, source current THD (i_s) and load current THD. The source current is observed to be sinusoidal and in phase with the voltage. The source current THD is found to be 6.09% under highly non-linear load conditions having THD of 32.46% with SRFT algorithm.

Since the load demand is low, PV injects power in to the grid which is seen by phase reversal in $\boldsymbol{v_s}$ and $\boldsymbol{i_s}$ plots.

The steady state power transfer between the non-linear load, SAPF and grid under solar irradiation conditions are shown in Fig. 4.52. The Chroma EN50530 Sandia PV array of capacity 300W is taken. The PV array is interfaced at the DC link of inverter

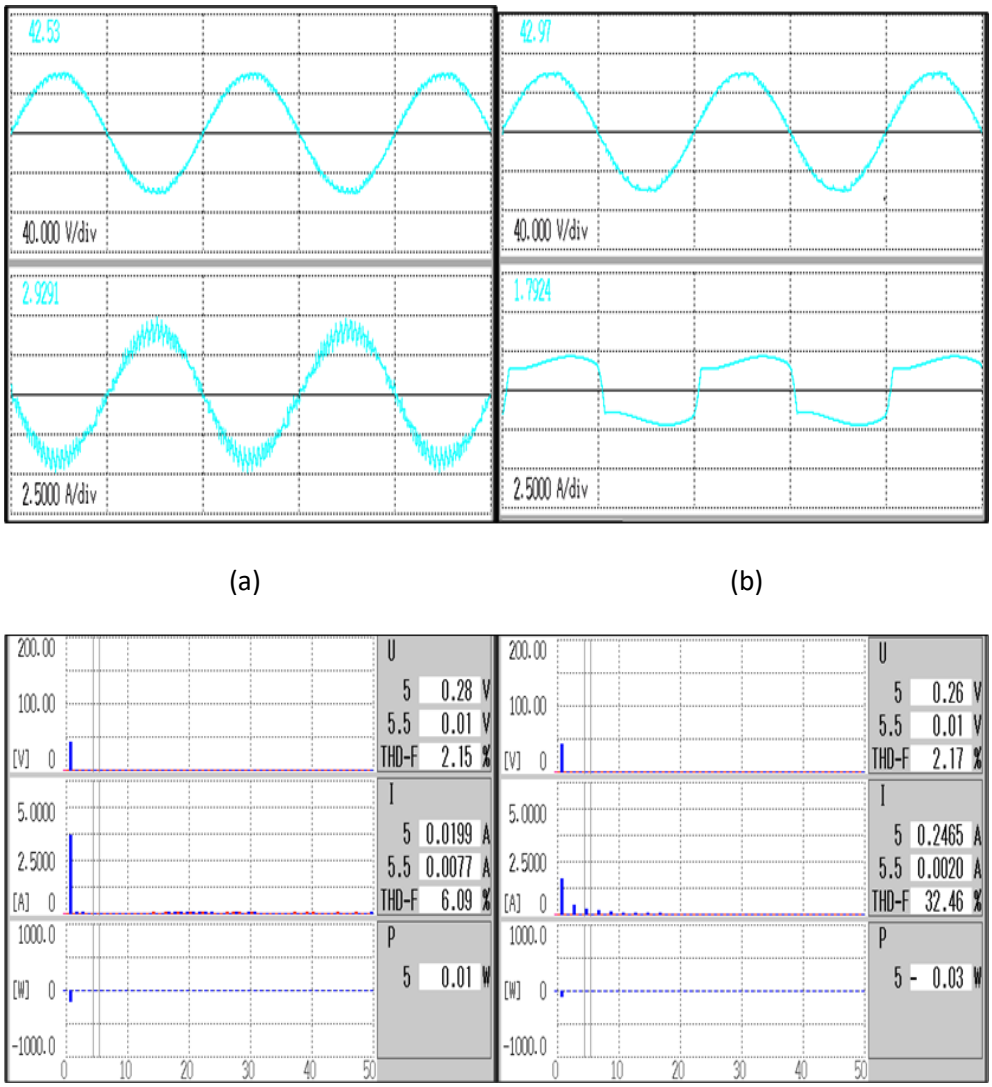

Fig. 4.51. Steady state experimental performance analysis of SRFT controller under non-linear load conditions with PV grid tied systems (a) source current waveform (b) load current waveform (c) source current THD and (d) load current THD

called compensator is now delivering active power of 228W. Out of which 157W is absorbed by the source and 71W by the load.

4.3.2 Performance analysis with SOGI Controller

The SOGI based control scheme is modelled in dSPACE 1104 on hardware prototype developed in single-phase grid connected system. Results without/with PV integration are discussed in detail.

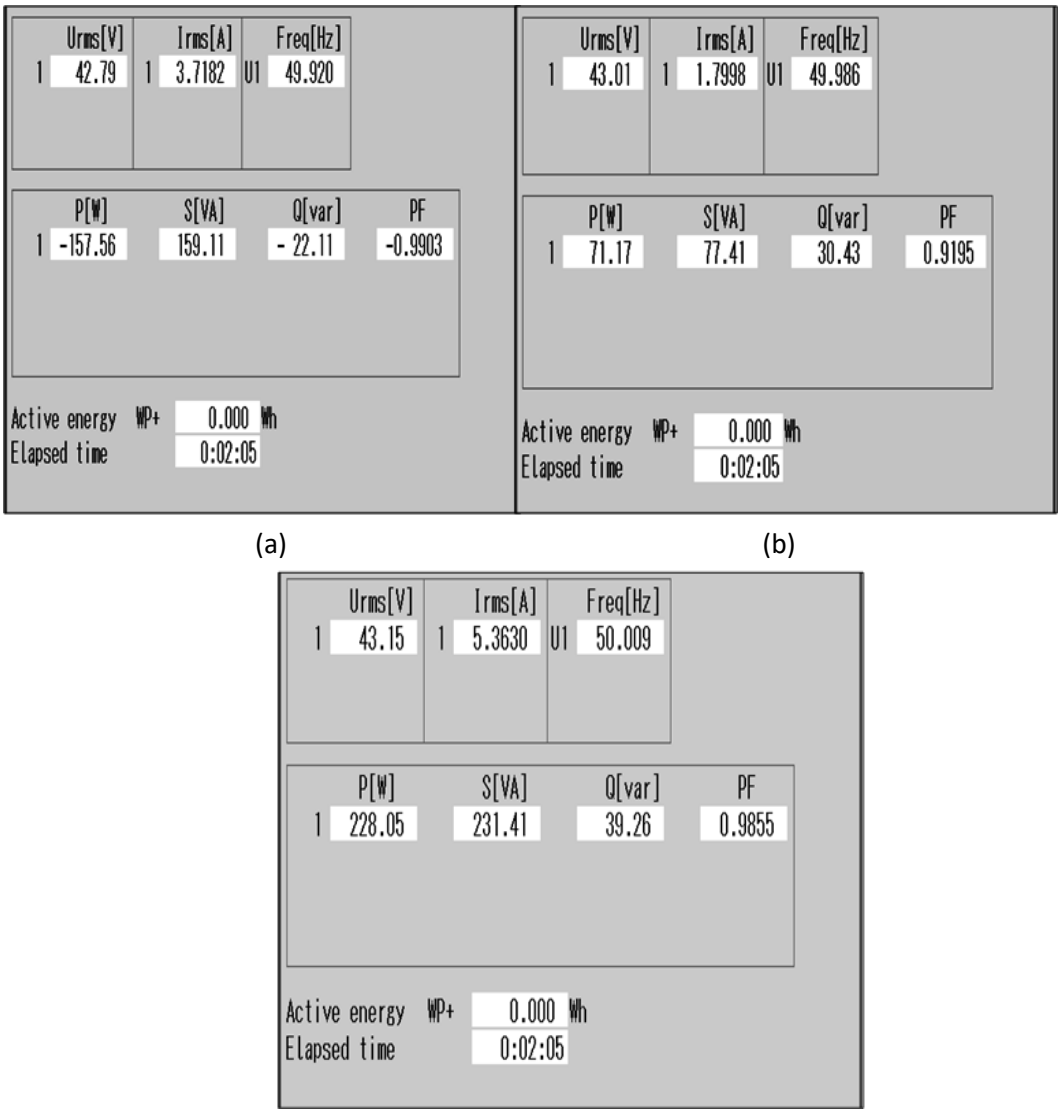

Fig. 4.52. Steady state experimental power analysis of SRFT controller under non-linear load with PV grid tied systems (a) source power (P_s) (b) load power (P_L) and (c) compensator power (P_f)

4.3.2.1 Performance under non-linear load conditions

Fig. 4.53 shows the hardware operation of SOGI controller on single-phase grid connected systems. The SAPF operation is performed at 110V, 50Hz supply feeding non-linear load. Figs. 4.53 (a-f) show the source voltage waveform ($\boldsymbol{v_s}$), load current waveform $\boldsymbol{(i_L)}$, compensator current waveform ($\boldsymbol{i_f}$), source voltage THD, source current THD ($\boldsymbol{i_s}$) and load current THD. The source current is observed to be sinusoidal and in

phase with the voltage. The source current THD is found to be 4.1% with SOGI controller under non-linear load conditions of 29.6%.

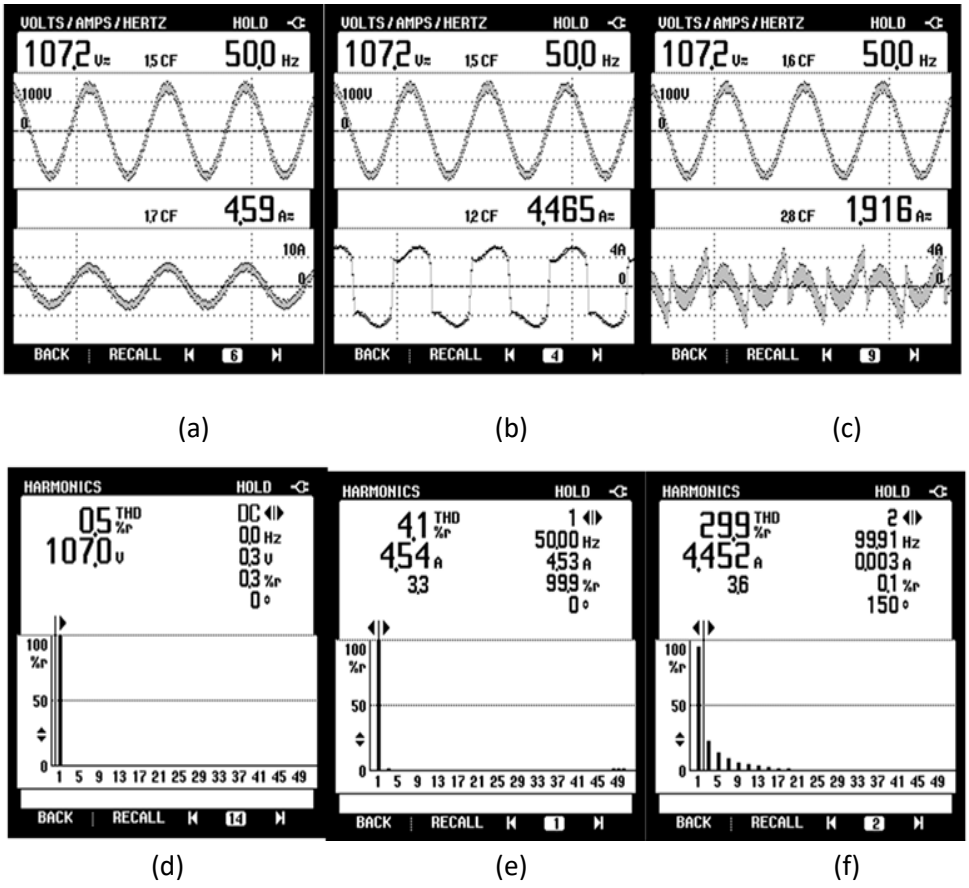

Fig. 4.53. Steady state experimental performance analysis of SOGI controller under non-linear load conditions (a) source voltage waveform (v_s) (b) load current waveform (i_L) (c) compensator current waveform (i_f) (d) source voltage THD (e) source current THD and (f) load current THD

4.3.2.2. Performance under Mixed load conditions

Figs. 4.54 (a-d) show the source voltage waveform (v_s), load current waveform (i_L), compensator current waveform (i_f), source voltage THD, source current THD (i_s) and load current THD under mixed loading conditions. The source current is observed to be sinusoidal and in phase with the voltage. The source current THD is found to be 4.1% under mixed load conditions of 7.4% with SOGI algorithm. This loading conditions comprises a high proportion of linear load and low proportion of non-linear load.

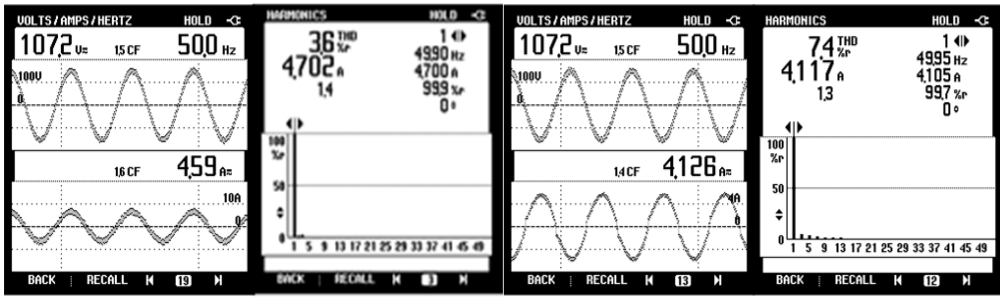

(a) (b) (c) (d)

Fig. 4.54. Steady state experimental performance analysis of SOGI controller under mixed loading conditions (a) source voltage (v_s) (b) source current THD (i_s) and (c) load current (i_L) waveform (d) load current THD

4.3.2.3 Performance under Linear load conditions

Figs. 4.55 (a-d) show the source voltage waveform (v_s), load current waveform (i_L), compensator current waveform (i_f), source voltage THD, source current THD (i_s) and load current THD under mixed loading conditions. The source current is observed to be sinusoidal and in phase with the voltage. The source current THD is found to be 4.0%

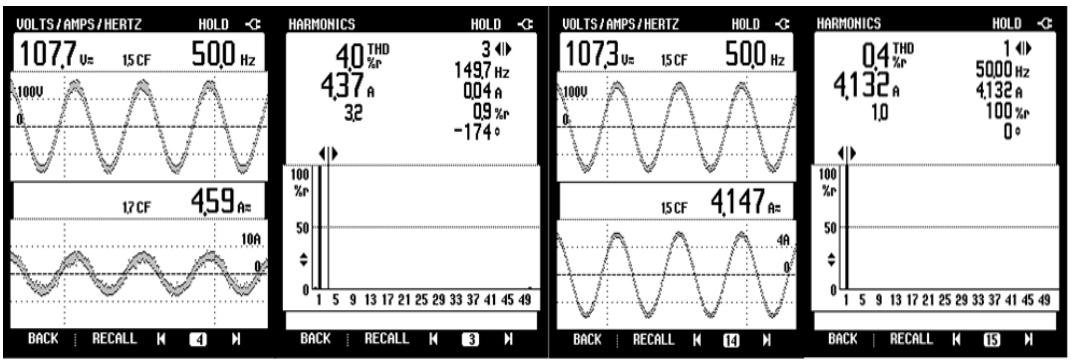

(a) (b) (c) (d)

Fig. 4.55. Steady state performance analysis of SOGI controller under linear loading conditions (a) source voltage (v_s) (b) source current THD (i_s) and (c) load current (i_L) waveform (d) load current THD

under linear load. The THD of linear load is 0.4% but the VSC injects the harmonics when SAPF is switched on.

Table 4.6 shows the THD values obtained experimentally with SOGI algorithm under various loading conditions

Table 4.6. THD values obtained experimentally with SOGI algorithm under various loading conditions

Loading Conditions	Second Order Generalised Integrator (SOGI)		
	i_L(THD)	i_S(THD)	v_s(THD)
Non-Linear Load Conditions	30.16%	3.8%	0.8%
Mixed Load Conditions	7.4%	3.6%	0.8%
Linear Load Conditions	0.04%	4.0%	0.8%

4.3.2.4 Dynamic Results with SOGI controller

Fig. 4.56 shows the dynamic results of SOGI algorithm under changing load conditions. It has been found that the i_{Lalpha} is in phase with the source voltage and i_{Lbeta} is 90° out of phase with the voltage. The i_{Lest} , the active component of load current is obtained by taking the square of the magnitude of the i_{Lalpha} and i_{Lbeta}. As the load decreases/increases in Fig. 4.56a and Fig. 4.56b respectively, the estimated load component correspondingly changes. These observations are in agreement with the simulation results.

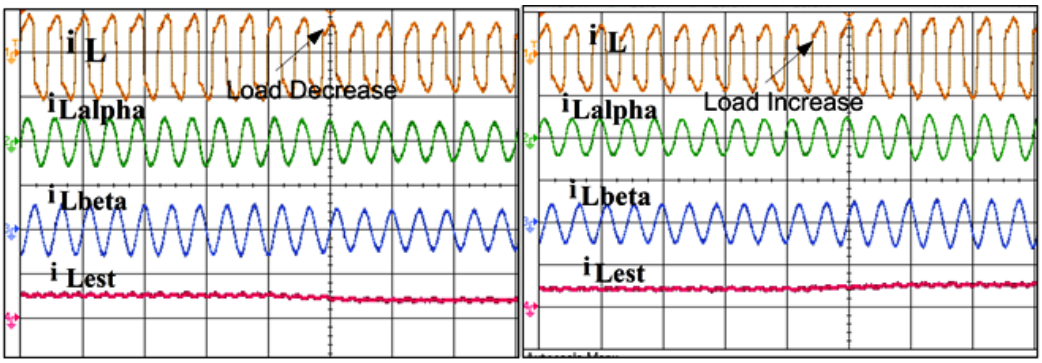

(a) (b)

Fig. 4.56. Dynamic waveforms of SOGI observed on oscilloscope (a) $i_L(10\,A/div), i_{Lalpha}(20\,A/div), i_{Lbeta}\,(20\,A/div)$ $i_{Lest}\,(20\,A/div)$ under load increase (b) $i_L(10\,A/div)$, $i_{Lalpha}(20\,A/div)$ $i_{Lbeta}\,(20\,A/div)\,i_{Lest}\,(20\,A/div)$ under load decrease

4.3.2.5 Steady State power flow under non-load conditions

The steady state power transfer between the non-linear load, SAPF and grid is shown in Fig. 4.57. The load active power of 480W is met by the source active power of 530W which includes switching loss also. The reactive power of load of 110VAR is met by the compensator reactive power of 120VAR. This shows the controller is well designed and meets the objective of supplying entire reactive power demand of load.

4.3.2.6 Performance analysis with SOGI controller for PV grid tied systems

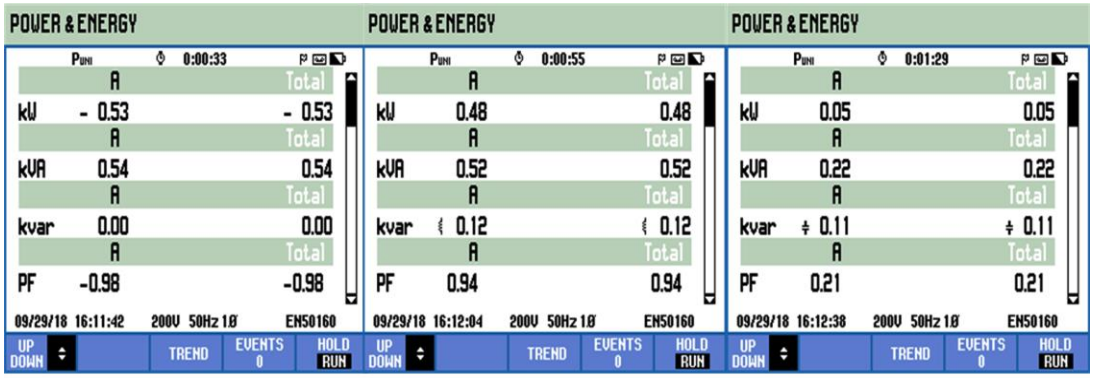

(a) (b) (c)

Fig. 4.57. Steady state experimental power analysis of SOGI controller under non-linear load conditions (a) source power (P_s) (b) load power (P_L) and (c) compensator power (P_f)

Fig. 4.58 shows the hardware operation of SAPF for single-phase grid connected systems when PV is interfaced. PV integration results are taken for 45V, 50Hz supply feeding non-linear load. Fig. 4.58 shows the steady state performance voltage and current waveform results under SAPF integrated grid connected systems. Figs. 4.58 (a-f) show the source voltage waveform ($\boldsymbol{v_s}$), load current waveform ($\boldsymbol{i_L}$), compensator current waveform ($\boldsymbol{i_f}$), source voltage THD, source current THD ($\boldsymbol{i_s}$) and load current THD. The source current is observed to be sinusoidal and in phase with the voltage.

The source current THD is found to be 5.75% under non-linear load conditions having a THD of 32.46% with SOGI algorithm.

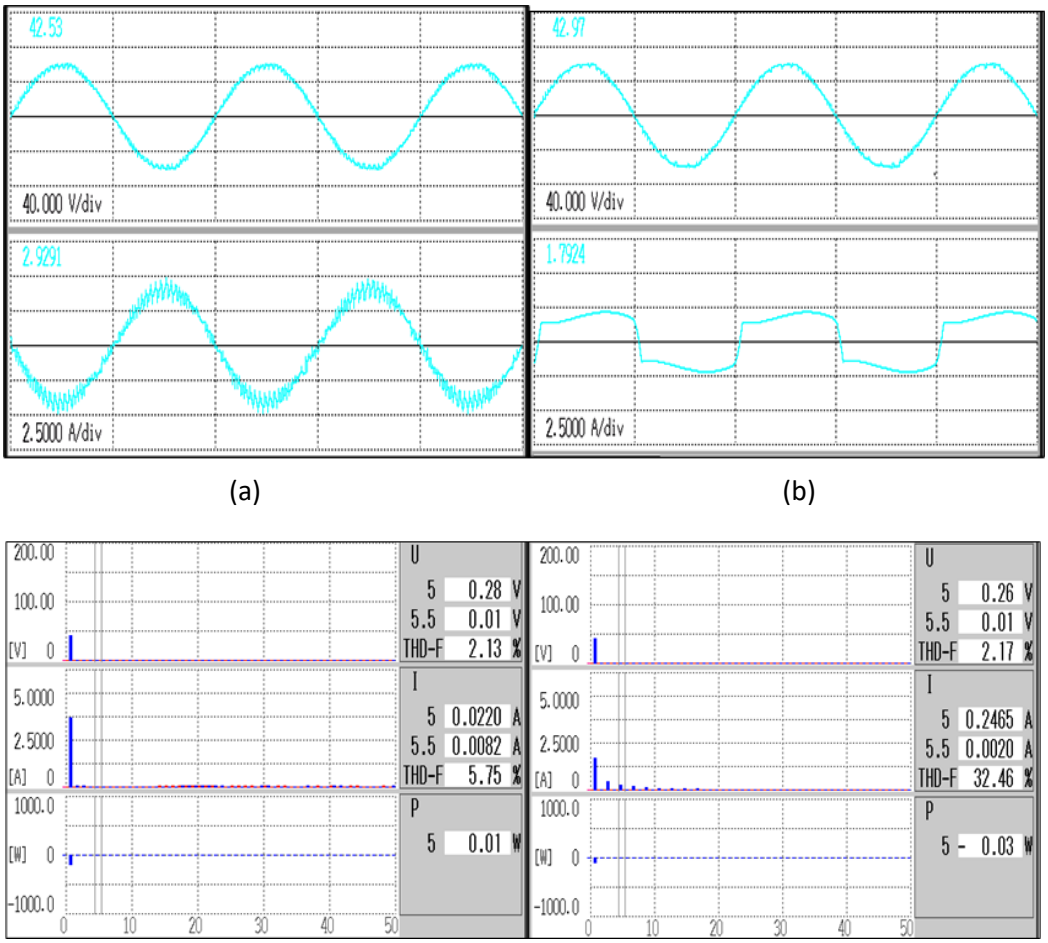

Fig. 4.58. Steady state experimental performance analysis of SOGI controller under non-linear load conditions with PV grid tied systems (a) source current waveform (b) load current waveform (c) source current THD and (d) load current THD

Since the load demand is low, PV injects power in to the grid which is seen by phase reversal in $\boldsymbol{v_s}$ and $\boldsymbol{i_s}$ plots.

The steady state power transfer between the non-linear load, SAPF and grid is shown in Fig. 4.59. The Chroma EN50530 Sandia PV array of capacity 300 W is taken. The PV array is interfaced at the DC link of inverter is delivering active power of 228W after switching losses. The load active power of 71.20W is met by the compensator of power of 221W. The reactive power of load of 30.31VAR is met by the compensator reactive power of 39VAR.

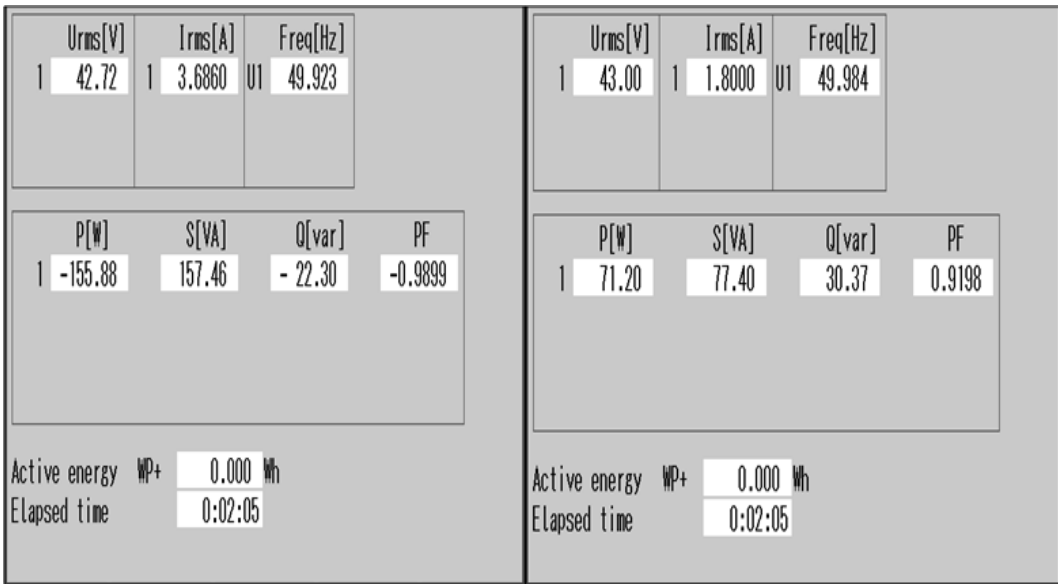

(a) (b)

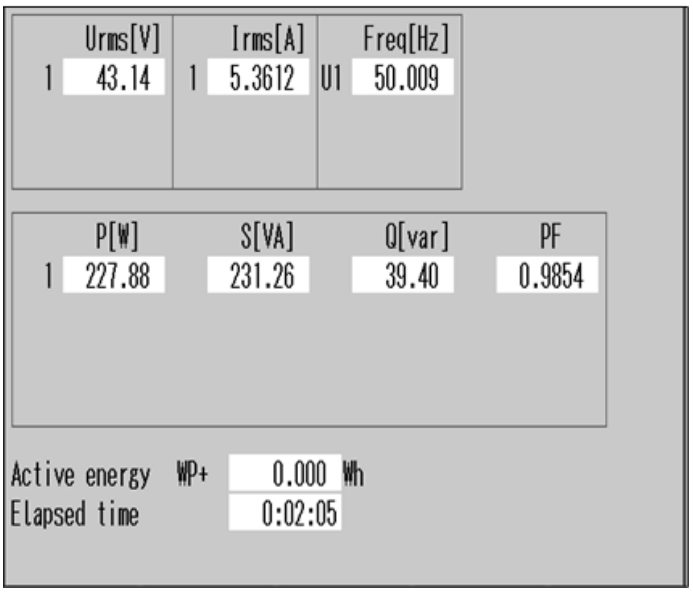

(c)

Fig. 4.59. Steady state experimental power analysis of SOGI controller under non-linear load conditions with grid tied PV systems (a) source power (P_s) (b) load power (P_L) and (c) compensator power (P_f)

4.3.3 Performance analysis with TFLNN Controller

The TFLNN based control scheme is modelled in dSPACE 1104 on hardware prototype developed on single-phase grid connected system.

4.3.3.1 Performance under non-linear load conditions

Fig. 4.60 shows the hardware operation of TFLNN on single-phase grid connected systems. The SAPF operation is performed at 110V, 50Hz supply feeding non-linear load. Fig. 4.60 shows the steady state voltage and current waveform results under SAPF integrated grid connected systems. Figs. 4.60 (a-f) show the source voltage waveform ($\boldsymbol{v_s}$), load current waveform ($\boldsymbol{i_L}$), compensator current waveform ($\boldsymbol{i_f}$), source voltage THD, source current THD ($\boldsymbol{i_s}$) and load current THD. The source current is observed to be sinusoidal and in phase with the voltage. The source current THD is found to be 3.1% with TFLNN algorithm under non-linear load conditions of 30.1%.

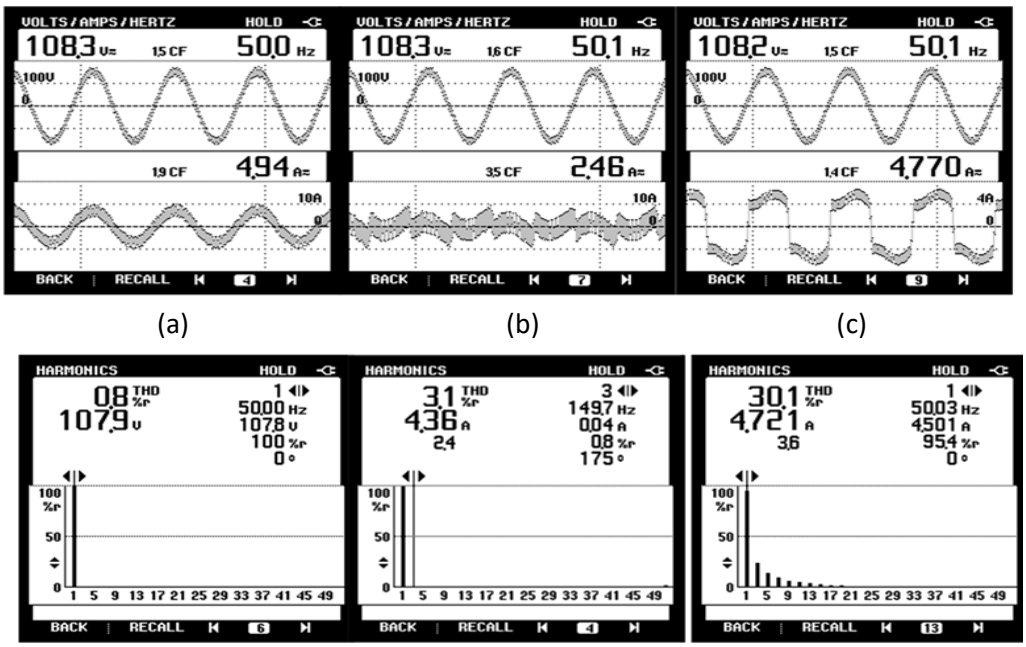

Fig. 4.60. Steady state experimental performance analysis of TFLNN controller under non-linear load conditions (a) source voltage waveform (v_s) (b) load current waveform (i_L) (c) compensator current waveform (i_f) (d) source voltage THD (e) source current THD and (f) load current THD

4.3.3.2 Performance under Mixed Load Conditions

Figs. 4.61 (a-d) show the source voltage waveform (v_s), load current waveform (i_L), compensator current waveform (i_f), source voltage THD, source current THD (i_s)

and load current THD under mixed loading conditions. The source current is observed to be sinusoidal and in phase with the voltage. The source current THD is found to be

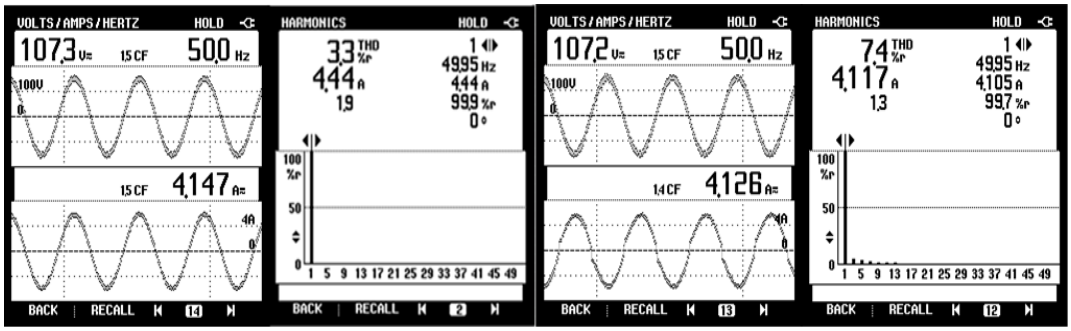

(a) (b) (c) (d)

Fig. 4.61. Steady state experimental performance analysis of TFLNN controller under mixed loading conditions (a) source voltage (v_s) (b) source current THD (i_s) and (c) load current (i_L) waveform (d) load current THD

3.3% when the load current shows THD of 7.4%.

4.3.3.3 Performance under linear load conditions

Figs. 4.62 (a-d) show the source voltage waveform (v_s), load current waveform

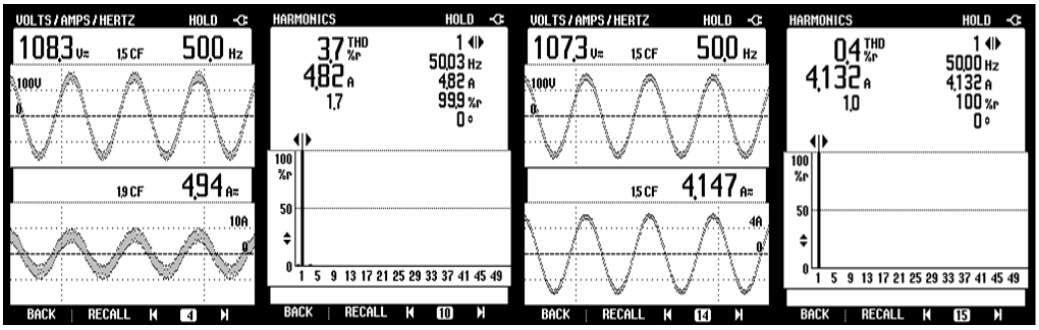

(a) (b) (c) (d)

Fig. 4.62. Steady state experimental performance analysis of TFLNN controller under linear loading conditions (a) source voltage (v_s) (b) source current THD (i_s) and (c) load current (i_L) waveform (d) load current THD

(i_L), compensator current waveform (i_f), source voltage THD, source current THD (i_s) and load current THD under mixed loading conditions. The source current is observed to be sinusoidal and in phase with the voltage. The source current THD of TFLNN controller is found to be 3.7% under linear load conditions. The THD of linear load is

0.4% but the VSC injects the harmonics. Table 4.7 shows the THD values obtained experimentally with TFLNN algorithm under various loading conditions

Table 4.7.THD values obtained experimentally with TFLNN algorithm under various loading conditions

Loading Conditions	Trignometric Functional Link Neural Network (TFLNN)		
	i_L(THD)	i_S(THD)	v_s(THD)
Non-Linear Load Conditions	30.1%	3.1%	0.04%
Mixed Load Conditions	7.4%	3.3%	0.04%
Linear Load Conditions	0.4%	3.7%	0.04%

4.3.3.4 Steady State power flow under Non-Linear load condition

The steady state power transfer between source power, load power and compensator power of non-linear load is shown in Fig. 4.63. The load active power of 500W is met by the source active power of 540W. The reactive power of load of 130VAR is met by the compensator reactive power of 140VAR.

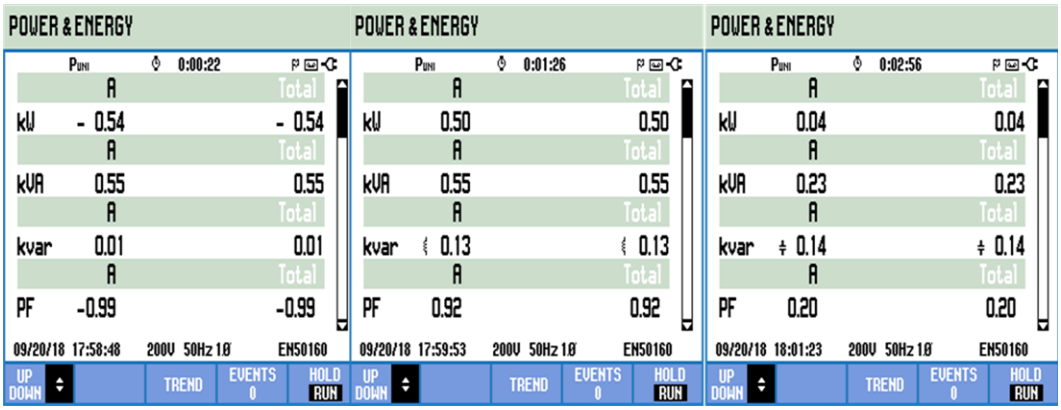

(a) (b) (c)

Fig. 4.63. Steady state experimental power analysis of TFLNN controller under non-linear load conditions (a) source power (P_s) (b) load Power (P_L) and (c) compensator Power (P_f)

4.3.3.5 Dynamic Results with TFLNN Controller

Fig. 4.64. shows the intermediate results of the algorithm such as $\boldsymbol{i_L}$, $\boldsymbol{i_{Lest}}$, $\boldsymbol{w_{sin}}, \boldsymbol{w_{cos}}$ $\boldsymbol{w}$, e. Fig. 4.64 (a) shows the results of $\boldsymbol{i_L}$, $\boldsymbol{i_{Lest}}$, $\boldsymbol{w_{sin}}, \boldsymbol{w_{cos}}$ when non-linear load is increased. It has been found that the estimated load component of current $\boldsymbol{i_{Lest}}$ increases with the load current. The individual expansion component terms such as $\boldsymbol{w_{sin}}$ increase with the loading conditions and the $\boldsymbol{w_{cos}}$ term decreases by very small amount with the loading conditions. Fig. 4.64 (b) shows the results of $\boldsymbol{i_L}$, $\boldsymbol{i_{Lest}}$, $\boldsymbol{w_{sin}}$, $\boldsymbol{w_{cos}}$ when non linear load is decreased. It has been found that the estimated load component of current $\boldsymbol{i_{Lest}}$ decreases with the decrease in load current. The individual expansion components $\boldsymbol{w_{sin}}$ decreases with the loading conditions and the $\boldsymbol{w_{cos}}$ decreases by a very small amount with the loading conditions. Figs. 4.64 (c-d) show the

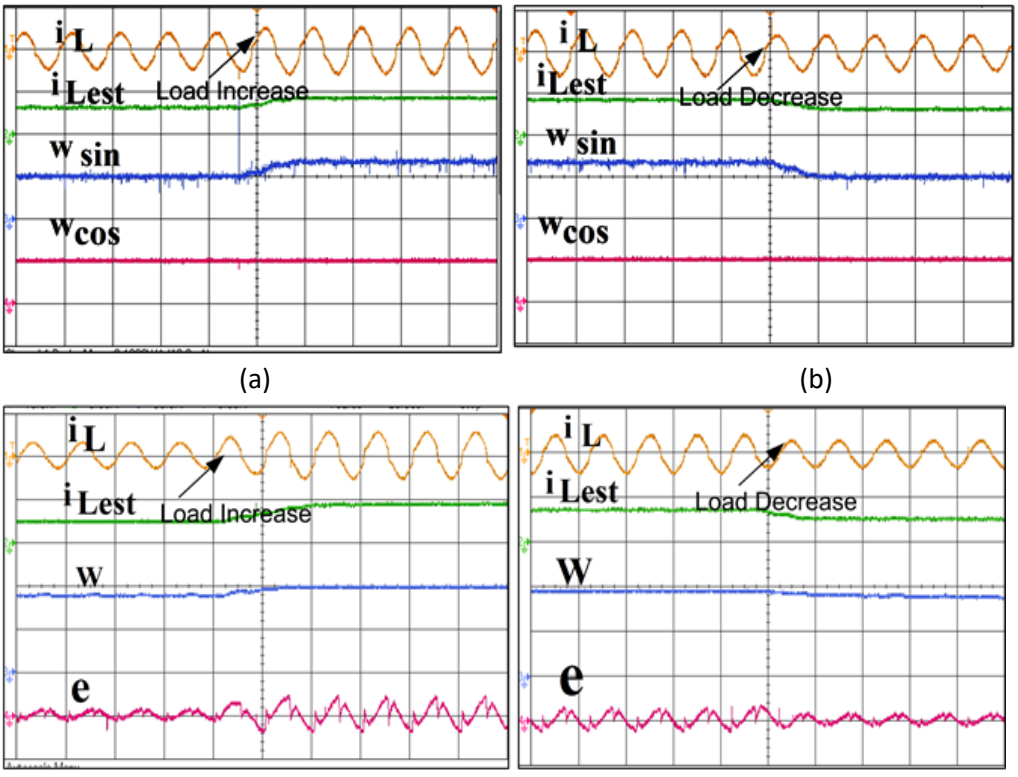

Fig. 4.64. Dynamic waveforms of TFLNN observed on oscilloscope (a) $i_L(10A/div)$, i_{Lest} $(5\ A/div)$ w_{sin} $(50\ A/div)$ $w_{cos}(5\ A/div)$ under load increase (b) $i_L(10\ A/div)$, i_{Lest} $(5\ A/div)$ $w_{\sin}$ $(50\ A/div)$, $w_{cos}(5A/div)$ under load increase (c) $i_L(10A/div)$, i_{Lest} $(5A/div)$, $w(50A/div)$, $e(19\ A/div)$ under load increase (d) $i_L(10A/div)$, i_{Lest} $(5A/div)$, $w(50A/div)$, $e(19\ A/div)$ under load decrease

results of i_L, i_{Lest}, w, e. The weight coefficient 'w' is updated by the error 'e' generated between the actual load current and the estimated load current which in turn updates the expansion component of the Trignometric Controller.

4.3.3.6. Performance analysis with TFLNN controller for PV grid tied systems

Fig. 4.65 shows the hardware operation of SAPF on single-phase grid connected systems when PV is interfaced. PV integration results are taken for 45V, 50Hz supply

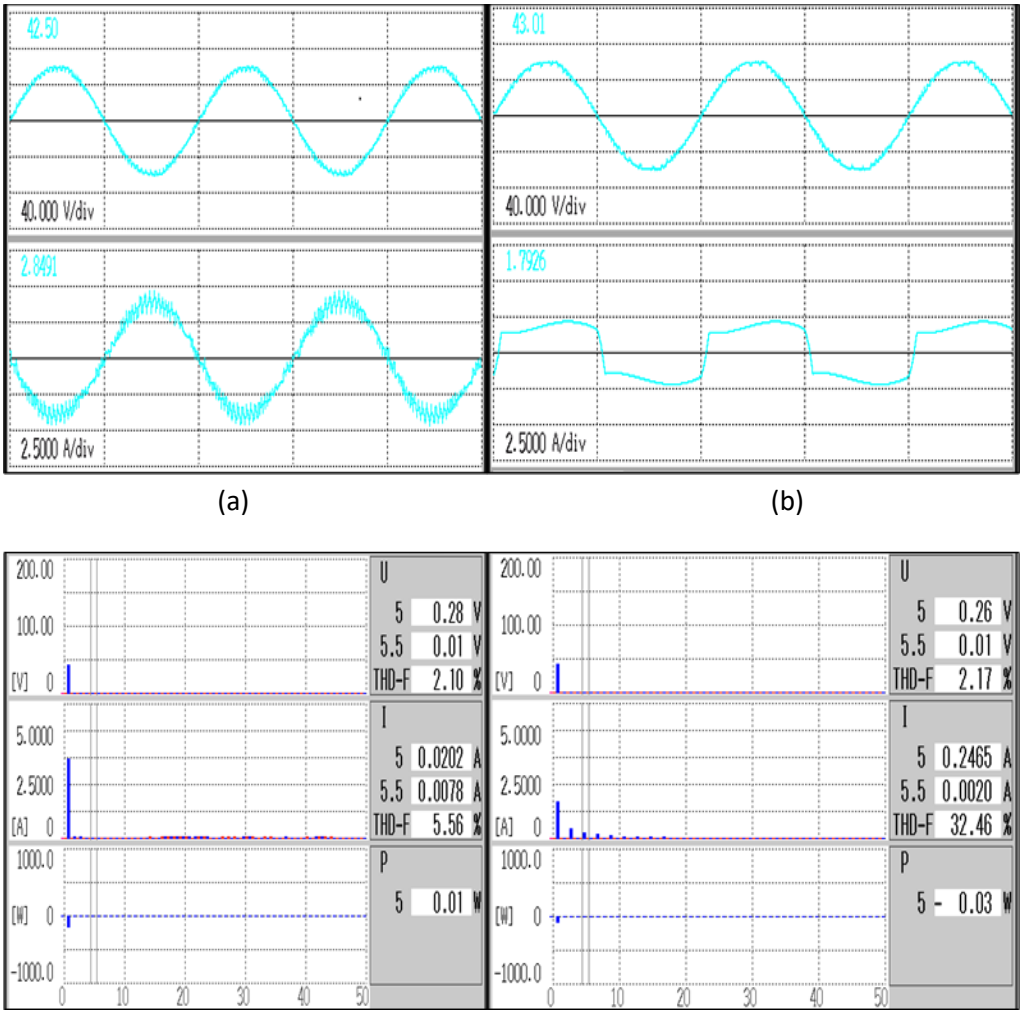

Fig. 4.65. Steady state experimental power analysis of TFLNN controller under non-linear load conditions with grid tied PV systems (a) source current waveform (b) load current waveform (c) source current THD and (d) load current THD

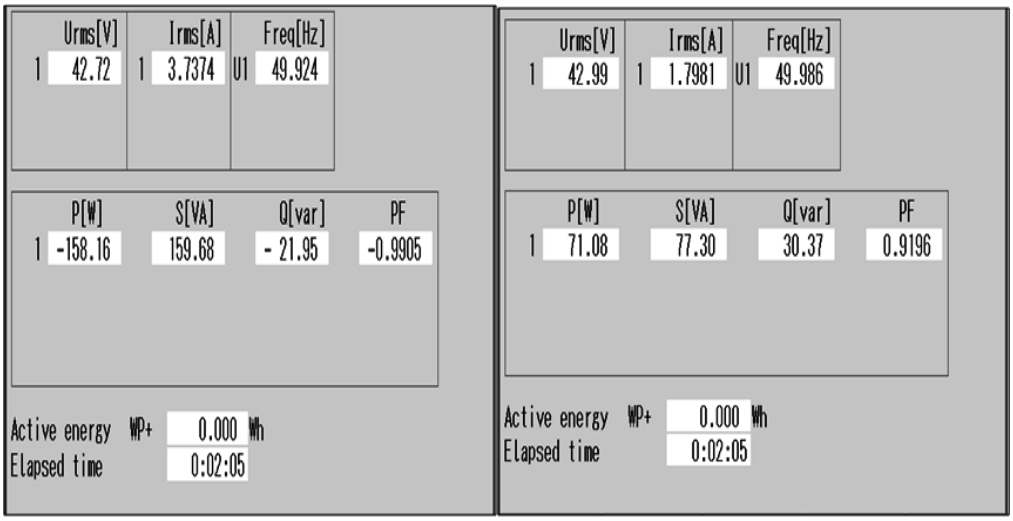

(a) (b)

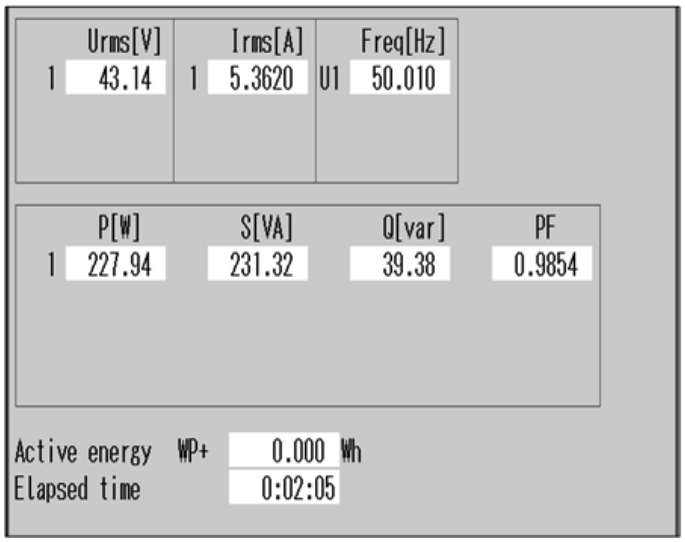

(c)

Fig. 4.66. Steady state experimental power analysis of TFLNN controller under non-linear load with grid tied PV systems (a) source power (P_s) (b) load power (P_L) and (c) compensator power (P_f)

feeding non-linear loads. Fig. 4.65 shows the steady state performance results of voltage and current waveform under SAPF integrated grid connected systems. Figs. 4.65 (a-d) show the source voltage waveform ($\boldsymbol{v_s}$), load current waveform ($\boldsymbol{i_L}$), compensator current waveform ($\boldsymbol{i_f}$), source voltage THD, source current THD ($\boldsymbol{i_s}$) and load current THD. The source current is observed to be sinusoidal and in phase with the voltage.

The source current THD is found to be 5.56% under non-linear load conditions having a THD of 32.46% with TFLNN algorithm.

Since the load demand is low, PV injects power in to the grid which is seen by phase reversal in $\boldsymbol{v_s}$ and $\boldsymbol{i_s}$ plots.

The steady state power transfer between the non-linear load, SAPF and grid is shown in Fig. 4.66. The Chroma EN50530 Sandia PV array of capacity 300W is taken. The PV array is interfaced at the DC link of inverter called compensator is delivering active power of 228W after switching losses. The load active power of 71.08W is met by the compensator.

4.3.4. Performance analysis with LFNN Controller

The LFNN based control scheme is modelled in dSPACE 1104 on hardware prototype developed on single-phase grid connected system.

4.3.4.1 Performance under non-linear load conditions

Fig. 4.67 shows the hardware results of operation of LFNN on single-phase grid connected systems. The SAPF operation is performed at 110V, 50Hz supply feeding non-linear load. Fig. 4.67 shows the steady state performance voltage and current waveform results under SAPF integrated grid connected systems. Figs. 4.67 (a-f) show the source voltage waveform ($\boldsymbol{v_s}$), load current waveform ($\boldsymbol{i_L}$), compensator current waveform ($\boldsymbol{i_f}$), source voltage THD, source current THD ($\boldsymbol{i_s}$) and load current THD. The source current is observed to be sinusoidal and in phase with the voltage. The source current THD is found to be 2.9% with LFNN controller even under higher non-linear load conditions of 30.0%. This clearly shows that the LFNN controller works well as per the design criteria.

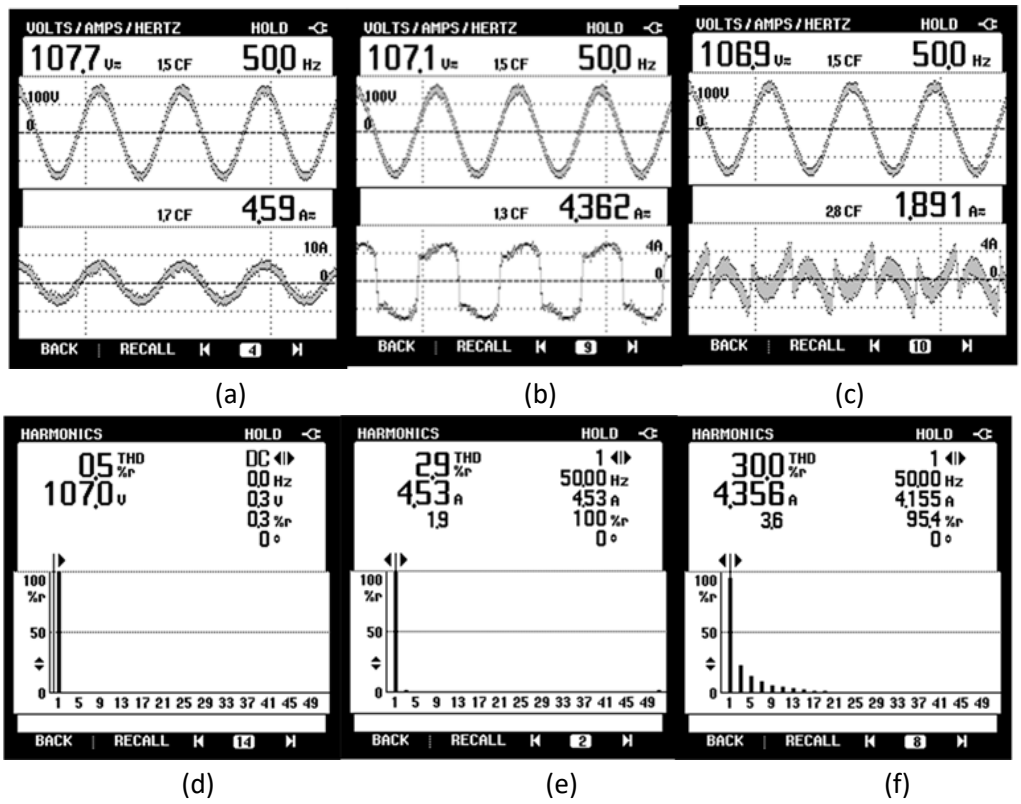

Fig. 4.67. Steady state experimental performance analysis of LFNN controller under non-linear load conditions (a) source voltage waveform (v_s) (b) load current waveform (i_L), (c) compensator current waveform (i_f) (d) source voltage THD (e) source current THD and (f) load current THD

4.3.4.3 Performance under mixed load conditions

Figs. 4.68 (a-d) show the source voltage waveform (v_s), load current waveform (i_L), compensator current waveform (i_f), source voltage THD, source current THD (i_s) and load current THD under mixed loading conditions. The source current is observed

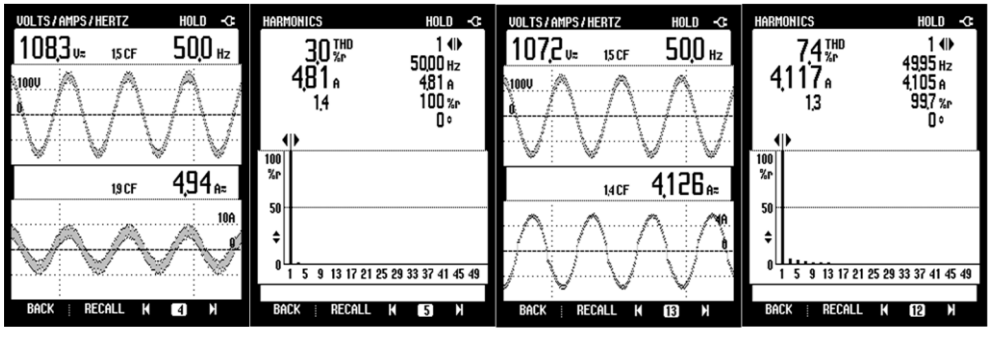

Fig. 4.68. Steady state experimental performance analysis of LFNN controller under mixed loading conditions (a) source voltage (v_s) (b) source current THD (i_s) and (c) load current (i_L) waveform (d) load current THD

to be sinusoidal and in phase with the voltage. The source current THD is found to be 3.0% under mixed load conditions of 7.4%.

4.3.4.2 Performance under linear load conditions

Figs. 4.69 (a-d) show the source voltage waveform (v_s), load current waveform (i_L), compensator current waveform (i_f), source voltage THD, source current THD (i_s)

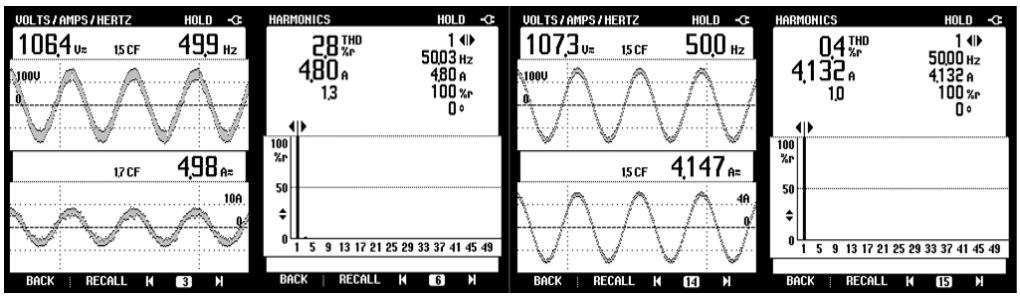

(a) (b) (c) (d)

Fig. 4.69. Steady state experimental performance analysis of LFNN controller under linear loading conditions (a) source voltage (v_s) (b) source current THD (i_s) and (c) load current (i_L) waveform (d) load current THD

and load current THD under mixed loading conditions. The source current is observed to be sinusoidal and in phase with the voltage. The source current THD is found to be 2.8% with LFNN controller under linear load which shows THD of 0.4%.

Table 4.8 shows the THD values obtained experimentally with LFNN algorithm under various loading conditions

Table 4.8. THD values obtained experimentally with LFNN algorithm under various loading conditions

TABLE	Legendre Functional Neural Network (LFNN)		
	i_L(THD)	i_S(THD)	v_s(THD)
Non-Linear Load Conditions	30.16%	2.9%	0.5%
Mixed Load Conditions	7.4%	3.0%	0.5%
Linear Load Conditions	0.4%	2.8%	0.5%

4.3.4.4 Intermediate Results with LFNN Controller

Fig. 4.70 shows the intermediate results of the LFNN algorithm showing the load current $\boldsymbol{i_L}$, load current expansion components $\boldsymbol{i_{L0}}$, $\boldsymbol{i_{L1}}$ and estimated load current, $(\boldsymbol{i_{Lest}})$ and error 'e'. It has been observed that the load expansion components sum up to $\boldsymbol{i_{LTotal}}$ which further estimates the load current. The weight vectors are regulated between 0 and 1. The sin$\boldsymbol{\theta}$ plots do not vary with the loading conditions as observed in Fig. 4.70.

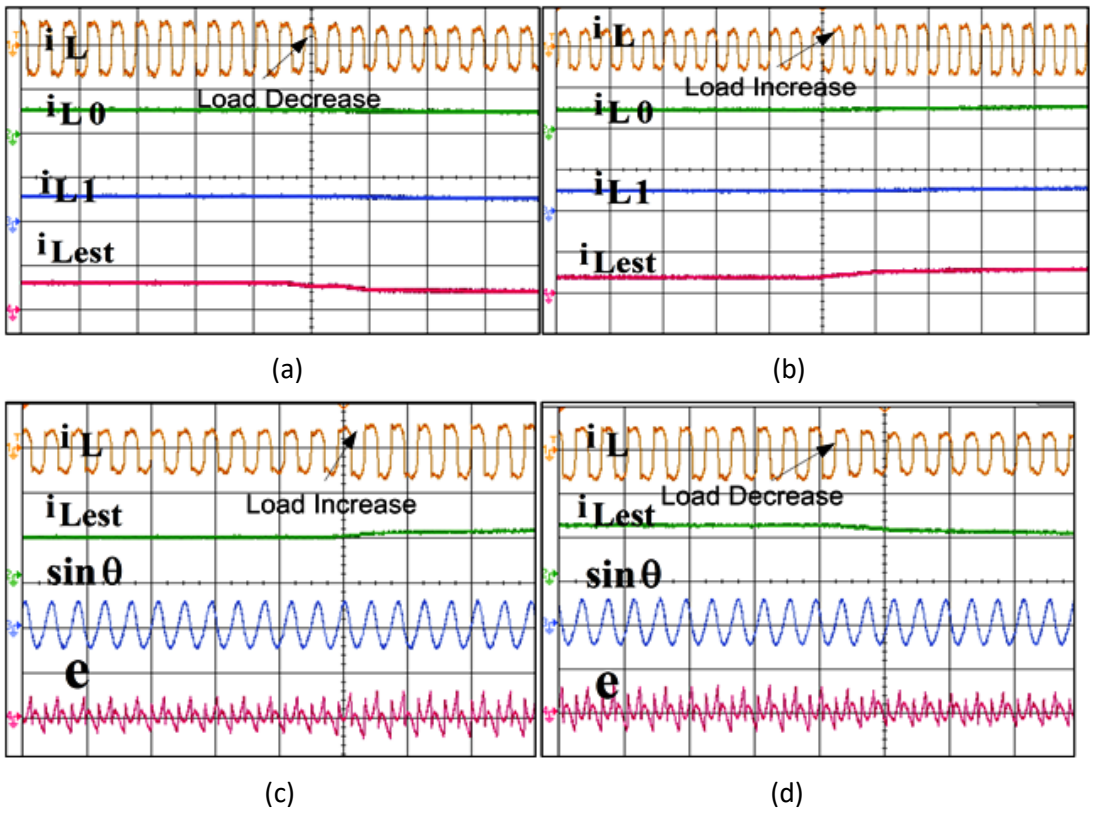

Fig. 4.70. Dynamic waveforms of LFNN observed on oscilloscope (a) i_L $(100\ A/div)$, i_{L0} $(50\ A/div)$, i_{L1} $(20A/div)$, i_{Lest} $(10\ A/div)$ under load decrease (b) i_L $(100\ A/div)$, i_{L0} $(50\ A/div)$, i_{L1} $(20\ A/div)$, i_{Lest} $(10\ A/div)$ under load increase (c) i_L $(100A/div)$, i_{Lest} $(250\ A/div)$, $sin\theta$ $(40\ A/div)$, e $(18.8\ A/div)$ under load increase (d) i_L $(100\ A/div)$, i_{Lest} $(250\ A/div)$, $sin\theta$ $(40\ A/div)$, e $(18.8\ A/div)$ under load decrease

4.3.4.5 Steady State power flow under Non-Linear load conditions

The steady state power transfer between the non-linear load, SAPF and grid is shown in Fig. 4.71. The load active power demand of 500W is met by the source active power of 540W. The reactive power of load of 140VAR is met by the compensator reactive power

of 130VAR. This proves the controller meets the objectives as per the design.

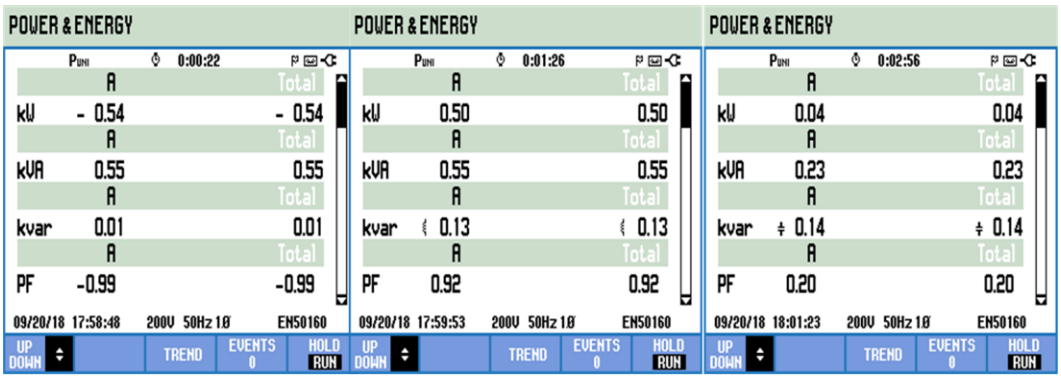

(a) (b) (c)

Fig. 4.71. Steady state experimental power analysis of LFNN controller under non-linear load conditions (a) source power (P_s) (b) load power (P_L) and (c) compensator power (P_f)

4.3.2.6 Performance Analysis with LFNN Controller for Grid Tied PV Systems

Fig. 4.72 shows the hardware operation of SAPF for single-phase grid connected systems when PV is interfaced. PV integration results are taken for a 45V, 50Hz supply feeding non-linear load. Fig. 4.72 shows the steady state performance voltage and current waveform results under SAPF integrated grid connected systems. Figs. 4.72 (a-d) shows the source voltage waveform ($\boldsymbol{v_s}$), load current waveform ($\boldsymbol{i_L}$), compensator current waveform ($\boldsymbol{i_f}$), source voltage THD, source current THD ($\boldsymbol{i_s}$) and load current THD. The source current is observed to be sinusoidal and in phase with the voltage. The source current THD is found to be 5.35% under non-linear load conditions of 32.46% with LFNN algorithm.

Since the load demand is low, PV injects power in to the grid which is seen by phase reversal in v_s and i_s plots with LFNN algorithm.

The steady state power transfer between the non-linear load is shown in Fig. 4.73. The Chroma EN50530 Sandia PV array of capacity 300W is taken. The PV array is interfaced at the DC link of inverter delivering active power of 228W. The load active

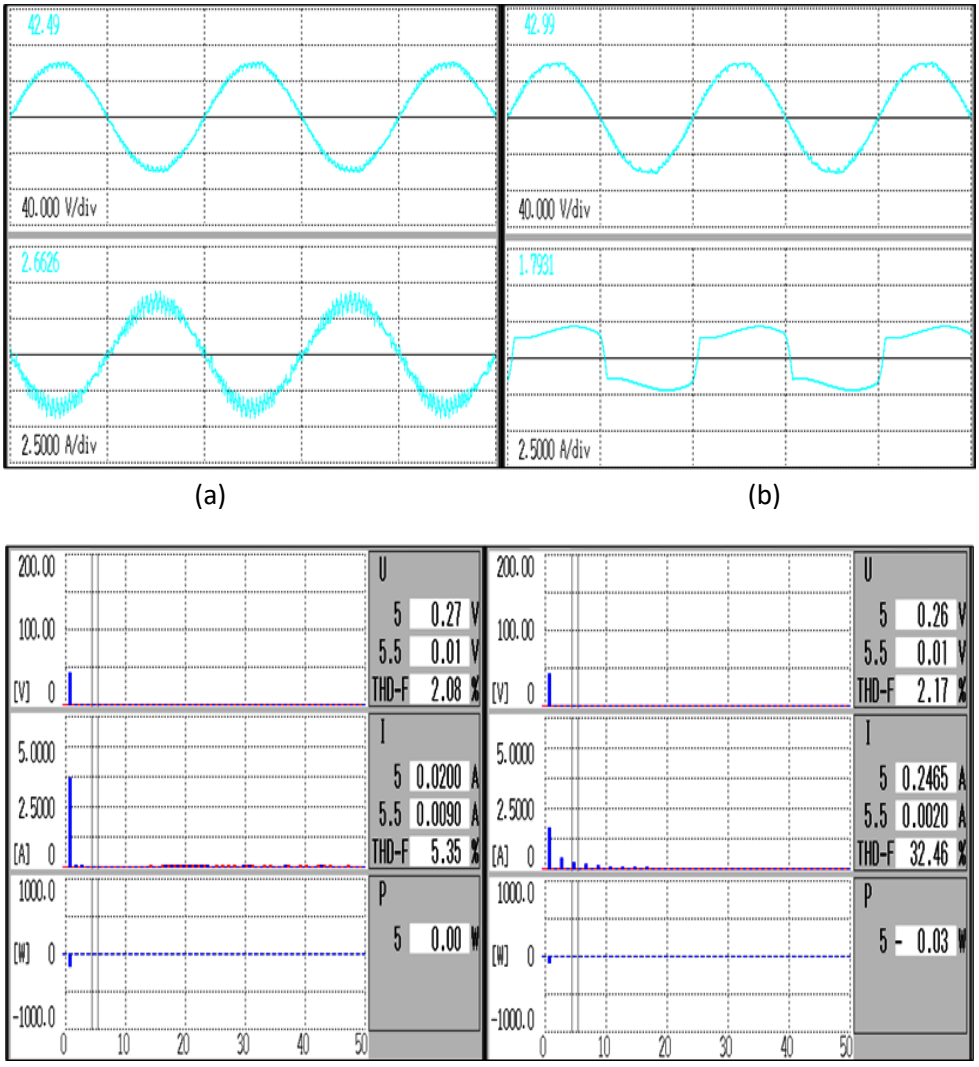

Fig. 4.72. Steady state experimental power analysis of LFNN controller under non-linear load conditions (a) source current waveform (b) load current waveform (c) source current THD and (d) load current THD

power of 71.09W is met by the compensator power of 227.87 W. The reactive power of load of 30VAR is met wholly by the compensator.

4.4 Comparative Evaluation of Developed Control Schemes

The comparison analysis of weight convergence of the proposed LFNN and TFLNN is done with the conventional algorithms SRFT and SOGI filters shown in Fig.4.74. The comparison is based on computational complexity, oscillations, settling time, response

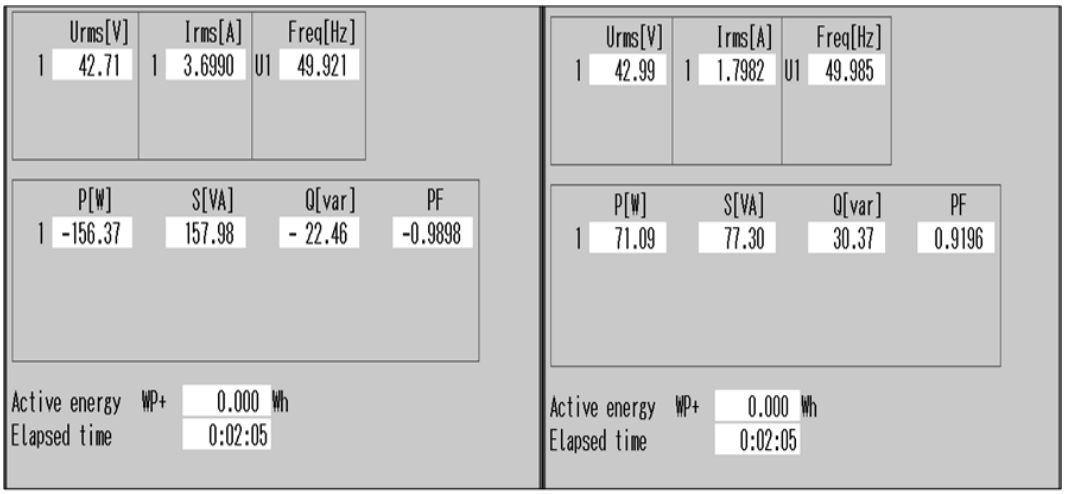

(a) (b)

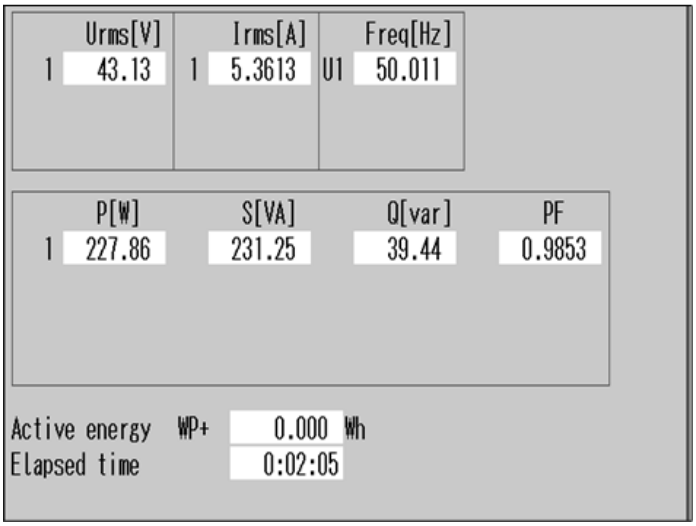

(c)

Fig. 4.73. Steady state experimental power analysis of LFNN controller under non- linear load with grid tied PV systems (a) source power (P_s) (b) load power (P_L) and (c) compensator power (P_f)

time, processing speed, MSE, sampling time, PLL requirement and nature of control filter summarized in Table. 4.9. Negligible steady state and dynamic oscillations are are observed using LFNN algorithm. The SRFT results show sustained oscillations in the tracked weight. The weights computed with SOGI filter show overshoot which settle down after 2 cycles. The settling time of SOGI is highest and the least in LFNN. The SRFT, TFLNN algorithm show almost equal settling time. The SOGI and SRFT controllers are non-adaptive in nature and require tuning of parameter for gains

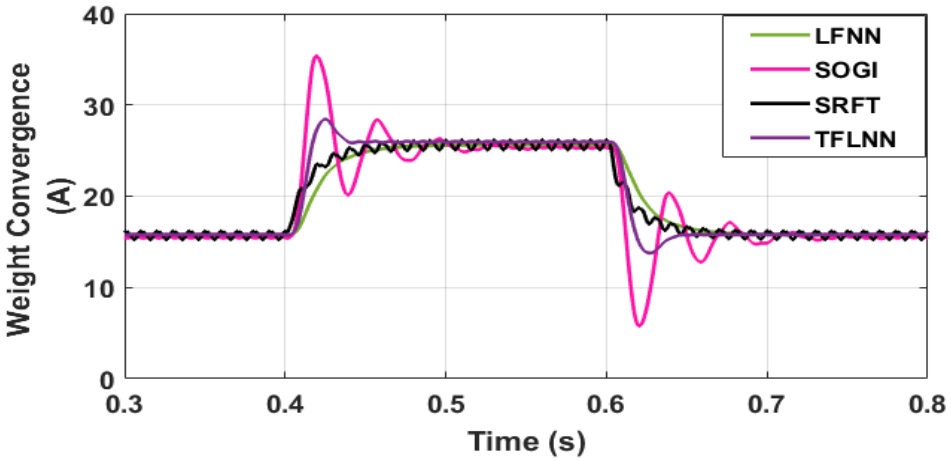

Fig. 4.74. Comparison of weight convergence analysis under load variations for shunt compensation

adjustment of steady state and dynamic state. The overshoot is highest in SOGI, less in TFLNN but least in LFNN but SRFT algorithm show continuous oscillations. No transformation blocks are required in functional NN based controllers. The THD of grid current using Legendre polynomial is 1.28% and highest THD is recorded with SRFT which is 2.47%.

TABLE 4.9. Comparison of Proposed Algorithm with Conventional Control Algorithms of weight convergence analysis under load variations for shunt compensation

Parameters	SRFT	SOGI	LFNN	TFLNN
Nature of Control Filter	Non-Adaptive	Non-Adaptive	Adaptive	Adaptive
Degree of Filter	NA	NA	Second Order	Third Order
MSE	More	Medium	Least	Least
Oscillations	High	Medium	Least	Least
Computational Complexity	More	Medium	Small	Small
Sampling Time	50µs	45µs	40µs	35µs
Settling Time	0.07s (Moderate)	0.12s (Slow)	0.03s (Fast)	0.03s (Fast)
Overshoot	Less	High	Least	Least

4.4.2 Comparison of THD Analysis

Table 4.10 shows a comparison of THD in supply current under different loading conditions with normal grid connected systems in simulink and hardware. It has been found that the SRFT shows the highest THD of 2.18% in grid current with non-linear load, 3.49% under mixed loading and 2.47% under linear loading conditions whereas the LFNN shows the lowest THD of 1.42% with non-linear load, 3.63% under mixed load, and 1.78% under linear loading conditions. These are the THD values observed under all loading conditions among all the developed controllers. In hardware it has been found that the SRFT shows the highest THD of 4.5% in grid current with non-linear load, 4.1% under mixed loading and 4.5% under linear loading conditions whereas the LFNN shows the lowest THD of 2.9% with non-linear load, 3.0% under mixed load and 2.8% under linear loading conditions.

TABLE 4.10. Comparison of THD values of the Proposed Algorithm with Conventional Control Algorithm in simulation and hardware under varying load conditions without PV integration

Loading Conditions	Non-Linear Load	Mixed Load	Linear Load	Non-Linear Load	Mixed Load	Linear Load
	Simulation Results			Hardware Results		
i_L(THD)	29.16%	18.47%	0.00%	29.9%	7.4%	0.4%
Algorithms	i_s(THD)	i_S(THD)	i_S(THD)	i_s(THD)	i_S(THD)	i_S(THD)
SRFT	2.18%	3.49%	2.47%	4.5%	4.1%	4.5%
SOGI	1.79%	2.53%	2.33%	4.1%	3.6%	4.0%
TFLNN	1.96%	3.27%	2.37%	3.1%	3.3%	3.7%
LFNN	1.42%	3.63%	1.78%	2.9%	3.0%	2.8%

The SRFT shows the worst THD in source current and the LFNN shows the best THD in source current. Hardware results are found to be in agreement with the simulation results.

4.4.2.2 Comparison of THD analysis in PV integrated grid connected systems under non-linear load conditions

Table 4.11 shows a comparison of THD in supply current in PV integrated grid connected systems under non-linear load conditions in simulink and hardware. It has been found that the SRFT shows has the highest grid current THD of 3.70% with non-linear load and the LFNN shows the lowest THD of 2.01%. In hardware it has been found that the SRFT controller shows the highest THD of 6.09% in grid current with non-linear load and the LFNN has the lowest THD of 5.35% in grid current. The THD values in grid current are slightly higher than those observed with simulation studies but

TABLE 4.11. Comparison of THD values of Different Algorithms under non-linear load conditions without/with PV integration

Algorithms	Simulation		Hardware	
	i_L=29.16%, v_S=0.01%,		i_L=32.46%,v_S=2.15%	
	Without PV	With PV	Without PV	With PV
SRFT	2.18%	3.70%	4.5%	6.09%
SOGI	1.79%	3.20%	3.8%	5.75%
TFLNN	1.96%	2.04%	3.1%	5.56%
LFNN	1.42%	2.01%	2.9%	5.35%

the trend is similar. The load current THD is ~ 32% recorded experimentally as compared to ~29% in simulation setup. Moreover, the supply is not perfectly sinusoidal as considered in simulation results.

4.5 Conclusions

This chapter focusses on the design and development of four control algorithms viz SRFT, SOGI, TFLNN and LFNN controller for shunt compensation in PV integrated single phase grid connected systems. The performance is tested using both Matlab Simulink developed models and on hardware setup in the laboratory. The performance analysis is discussed under different loading conditions i.e linear, non-linear, and mixed loading conditions under changing solar irradiation conditions. The performance of the functional NN algorithms is compared with conventional algorithms viz SRFT and SOGI. The proposed LFNN and TFLNN algorithms are designed on the basis of functional series expansion and hence they are simple to implement and need less computation. A few terms of these expansion series have been found to be suitable and sufficient. These functional NNs have further been made adaptive. The real time training of the algorithms is done by LMS algorithm. It overcomes the need of PLL synchronization, Park–Clark transformation techniques as in conventional algorithms such as SRFT. The SRFT and SOGI algorithms require transformation blocks and require tuning of gain constants to obtain the best response. Finally, a fair comparison of all the algorithms is performed by analyzing the tracking performance of all the algorithms under dynamic load variations. The proposed new algorithms LFNN and TFLNN show improved performance for SAPF operation. Further, the performance of these algorithms is quite satisfactory under PV integration.

Chapter 5

DESIGN AND ANALYSIS OF CONTROL ALGORITHMS FOR MITIGATION OF POWER QUALITY PROBLEMS IN THREE PHASE GRID CONNECTED PV SYSTEM

5.0 General

This chapter discusses the development of control algorithms for SAPF in three-phase two stage PV integrated grid connected systems for mitigating power quality problems under varying solar insolation and under different loading conditions i.e

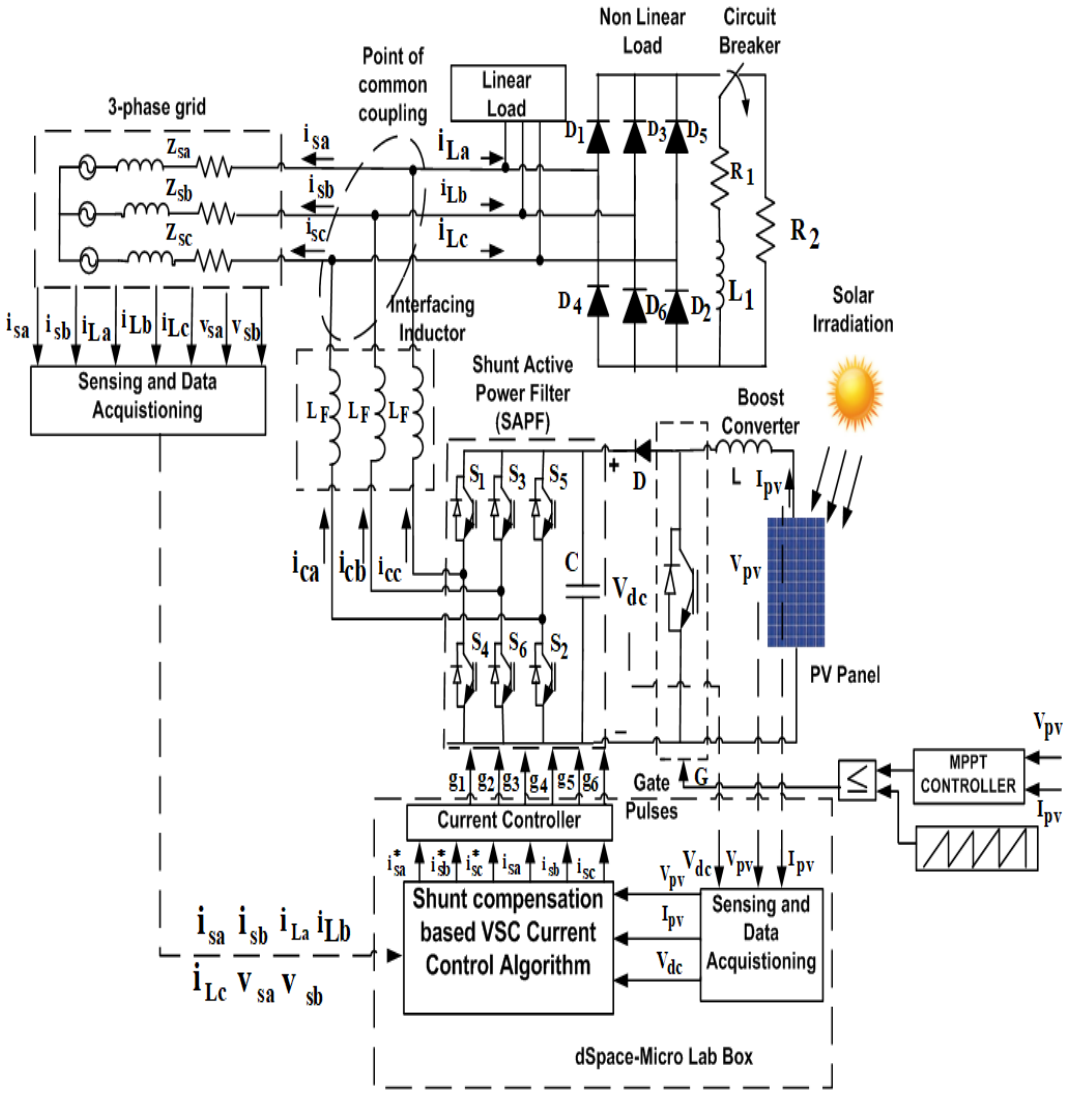

Fig. 5.1. Schematic Block Diagram of three-phase grid connected PV system

linear, non-linear, mixed loading and unbalancing load. The schematic diagram of the PV integrated three-phase grid connected systems is shown in Fig. 5.1. The SAPF is used in mitigating power quality problems such as harmonic elimination, load balancing, reactive power compensation with the help of different algorithms. The effectiveness of the control algorithms is checked using the proposed distribution system in Matlab Simulink as well as on the prototype hardware models developed in the laboratory.

5.1 Mathematical Analysis of Control Algorithms for Control of Three-phase SAPF

The mathematical analysis of control algorithms for control of SAPF in removing current based power quality problems through reference current generation in three-phase PV integrated grid connected systems is discussed below.

5.1.1 Three Phase Synchronous Reference Frame Theory (SRFT)

SRFT algorithm is used to extract the fundamental component of the load current for all the three phases. The load currents (i_{LA}, i_{LB} and i_{LC}), the grid voltages (v_{sa}, v_{sb} and v_{sc}) and the DC link voltage (V_{dc}) shown in Fig. 5.2. The load currents (i_{LA}, i_{LB} and i_{LC}) are transformed in to dq0 frame using Park transformation

$$\begin{bmatrix} i_{Ld} \\ i_{Lq} \\ i_{L0} \end{bmatrix} = \frac{2}{3} \begin{bmatrix} cos\theta & -sin\theta & \frac{1}{2} \\ \cos(\theta - \frac{2\pi}{3}) & -\sin(\theta - \frac{2\pi}{3}) & \frac{1}{2} \\ \cos(\theta + \frac{2\pi}{3}) & \sin(\theta + \frac{2\pi}{3}) & \frac{1}{2} \end{bmatrix} \begin{bmatrix} i_{LA} \\ i_{LB} \\ i_{LC} \end{bmatrix} \quad (5.1)$$

The i_{Ld} and i_{Lq} terms consist of fundamental and harmonic active and reactive current respectively.

$$i_{Ld} = i_{LdDC} + i_{LdAC} \quad (5.2)$$

$$i_{Lq} = i_{LqDC} + i_{LqAC} \quad (5.3)$$

The i_{Ld} and i_{Lq} are filtered through LPF to extract the DC component and the reactive power component is provided by shunt active power filter. The controller is designed so that the supply current should provide the DC component of load current (i_{DC}). Also, to maintain the constant DC link voltage and to compensate for losses in the DSTATCOM the loss component (i_{Loss}) from the PI controller is added. The term i_{PVff} is subtracted to account for the PV contribution.

$$i_{Ld}^{*} = i_{Lest} = i_{Ld} + i_{Loss} - i_{pvff} \tag{5.4}$$

Since the reactive power component is supported by Shunt Active Power Filter therefore the reference supply current must be in phase with the grid voltage therefore i_{Lq}^{*} and i_{Lo}^{*} must be equated to zero in equation (5.5) below. SRFT PLL shown in Fig. 5.3 is used to generate the unit-in phase ($\sin \omega t$) and unit-in quadrature ($\cos \omega t$) templates The i_{Ld}^{*} and i_{Lq}^{*} are converted to reference supply current by reverse Park transformation as

$$\begin{bmatrix} i_{sa}^{*} \\ i_{sb}^{*} \\ i_{sc}^{*} \end{bmatrix} = \begin{bmatrix} cos\theta & -sin\theta & 1 \\ \cos\left(\theta - \frac{2\pi}{3}\right) & -\sin\left(\theta - \frac{2\pi}{3}\right) & 1 \\ \cos\left(\theta + \frac{2\pi}{3}\right) & \sin\left(\theta + \frac{2\pi}{3}\right) & 1 \end{bmatrix} \begin{bmatrix} i_{Ld}^{*} \\ i_{Lq}^{*} \\ i_{Lo}^{*} \end{bmatrix} \tag{5.5}$$

The estimated fundamental component (i_{Lest}) is used to generate reference source currents ($i_{sa}^{*}, i_{sb}^{*}, i_{sc}^{*}$) for SAPF in three-phase grid connected systems discussed in Section 3.3. The reference source currents are compared with the actual source currents (i_{sa}, i_{sb} and i_{sc}) and fed to the hysteresis controller for generation of six pulses to the PWM controller.

5.1.2 Dual Second-Order Generalized Integrator (DSOGI)

DSOGI consists of two SOGI blocks with unity feedback as shown in Fig. 5.4. The three phase load currents (i_{LA}, i_{LB} and i_{LC}) are converted to ($i_{L\alpha}$) and ($i_{L\beta}$) using Clark's transformation.

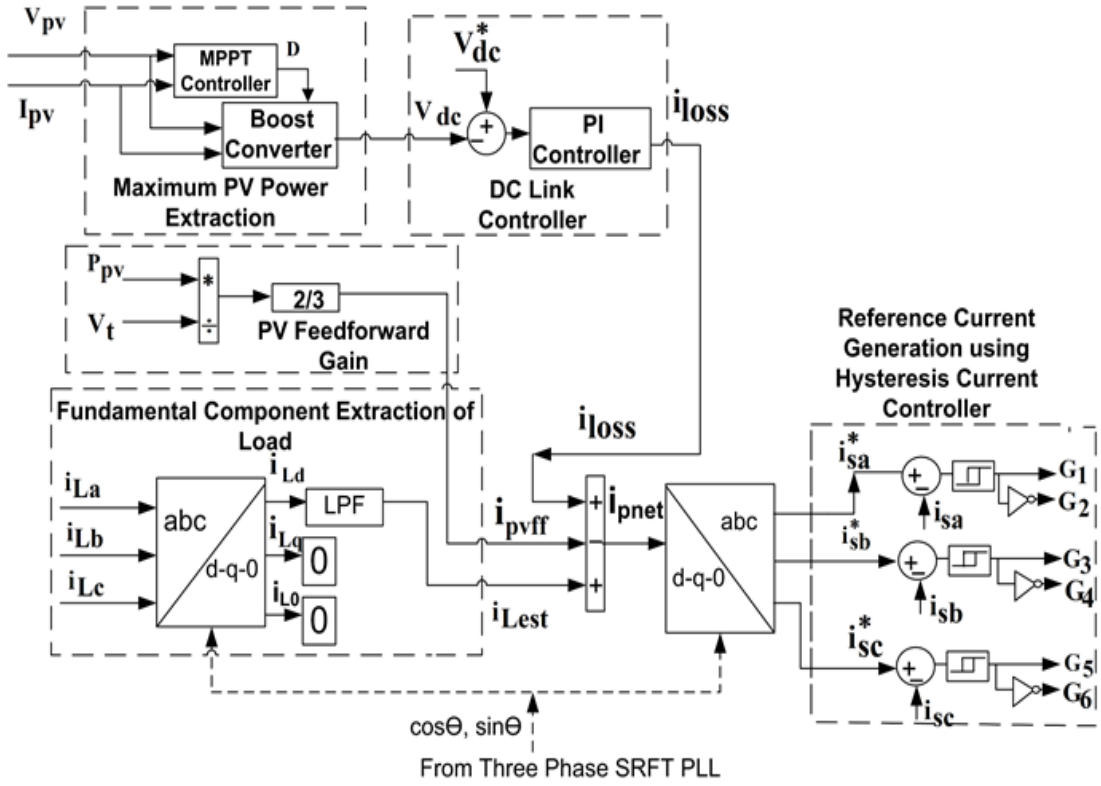

Fig. 5.2. Schematic control diagram of three phase SRFT controller

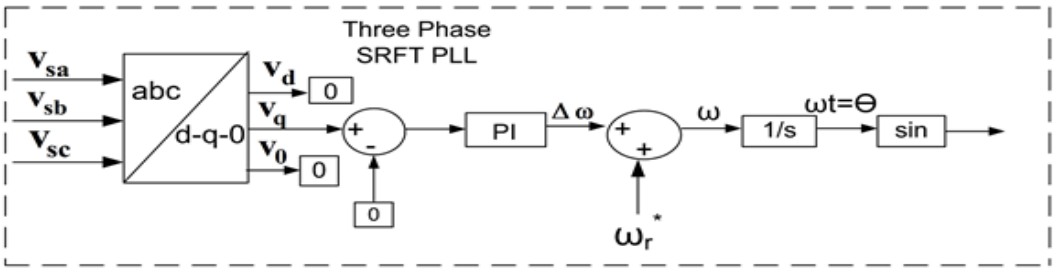

Fig. 5.3. Schematic control diagram of SRFT PLL used for the generation of unit templates

$$\begin{bmatrix} i_{L\alpha} \\ i_{L\beta} \end{bmatrix} = \sqrt{\frac{2}{3}} \begin{bmatrix} 1 & -\frac{1}{2} & -\frac{1}{2} \\ 0 & \frac{\sqrt{3}}{2} & -\frac{\sqrt{3}}{2} \end{bmatrix} \begin{bmatrix} i_{La} \\ i_{Lb} \\ i_{Lc} \end{bmatrix} \tag{5.6}$$

$$i'_{L\alpha}s)=\frac{i'_L}{i_L}=\frac{K\omega s}{s^2+K\omega s+\omega^2} \quad (5.7)$$

$$i'_{L\beta}(s)=\frac{qi'_L}{i_L}=\frac{K\omega^2}{s^2+K\omega s+\omega^2} \quad (5.8)$$

The output of $i_{L\alpha}$ and $i_{L\beta}$ is used to calculate the peak amplitude and is used to generate the reference source current.

$$i_{Lest}=\sqrt{i'^2_{L\alpha}+i'^2_{L\beta}} \quad (5.9)$$

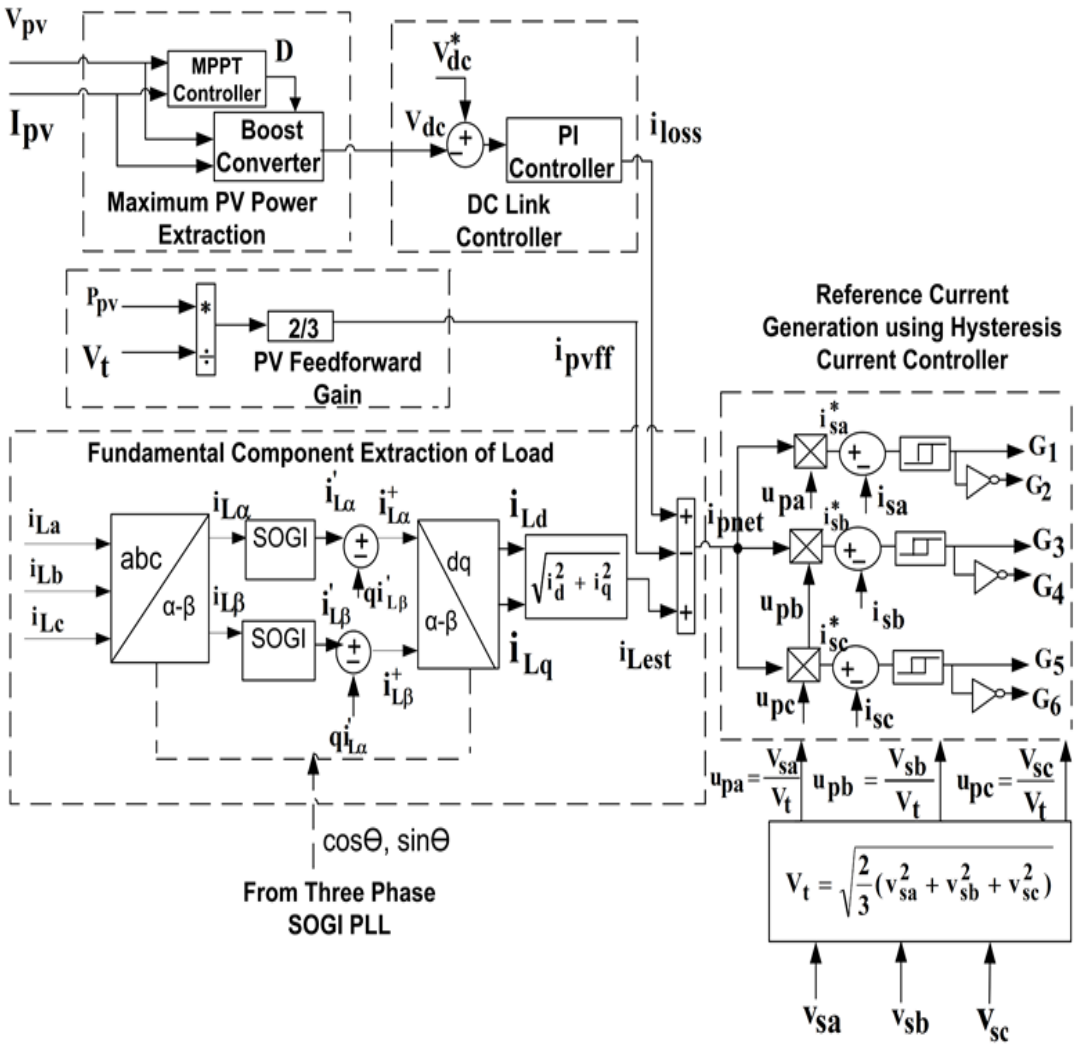

Fig. 5.4. Schematic Control Diagram of DSOGI controller

The estimated fundamental component (i_{Lest}) is used to generate reference source currents for SAPF in three-phase grid connected systems discussed in Section 3.3.

The central frequency of SOGI should correspond to the input supply frequency. Hence ω is selected to be 314 rad/s corresponding to 50 Hz.

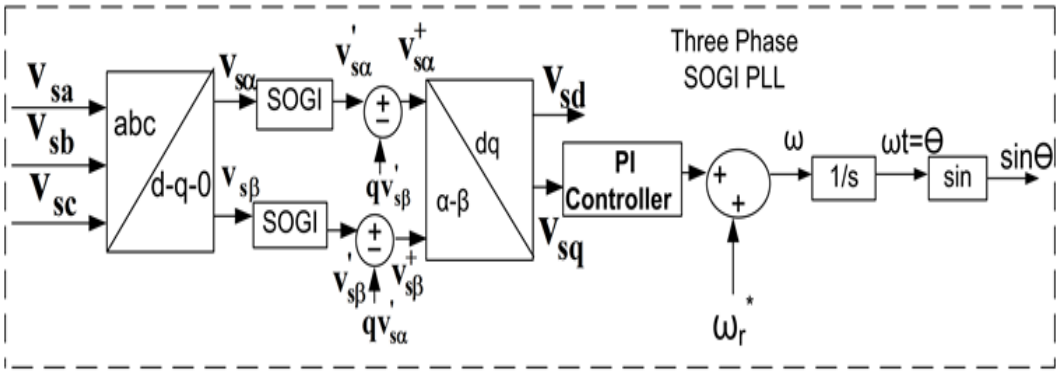

(a)

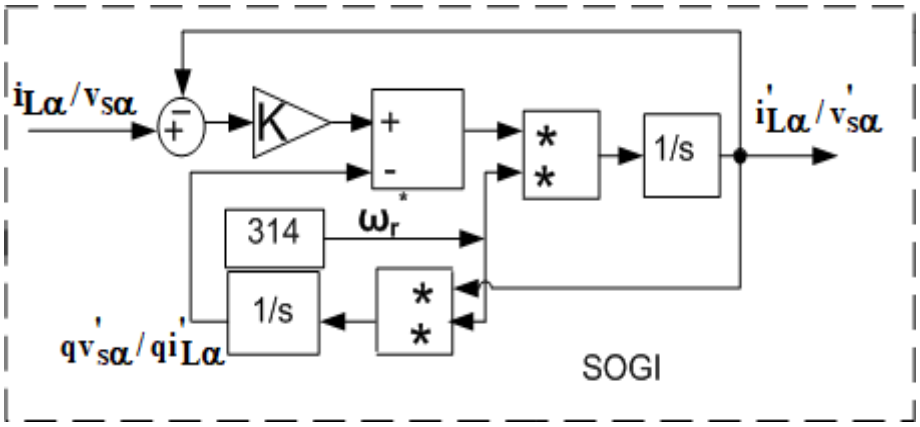

(b)

Fig. 5.5.(a) Schematic Diagram of DSOGI PLL for the generation of unit templates (b) SOGI controller to extract the in phase and quadrature controllers of load current or voltage signal

The bandwidth of both the filters (Band-pass and Low pass Filter) is controlled by gain 'K', which is related to the settling time t_s and can be determined by

$$K = \frac{9.2}{t_s * \omega} \tag{5.10}$$

The gain 'K' is chosen as 1.414 to have the trade-off between the steady state and dynamic state speed. The DSOGI PLL is shown in Fig. 5.5. is used to synchronize the signals and generate the unit-in phase ($\sin \omega t$) and unit-in quadrature ($\cos \omega t$)

templates. The reference source currents are generated by multiplying it with the unit-in phase ($\sin \omega t$) templates.

5.1.3 Adaptive Volterra Second Order Filter (AVSF)

Volterra Filter is one of the most popular non-linear adaptive filters. It was proposed by Weiner [205]. The Weiner model expands the Volterra series using orthogonal polynomial. The functional block diagram is shown in Fig. 5.6. The LMS adaptive filtering is used to extract the fundamental load current with the help of Volterra expansion terms by weight updation method of error minimization. The output i_{Lest} of the causal, time invariant filter is described by input-output relationship as

$$i_{Lest} = i_{Lk} + \sum w_1(k_1) i_L(n-k_1) + \sum\sum w_2(k_1 k_2) i_L(n-k_1) i_L(n-k_2) + \sum \dots \sum \quad (5.11)$$

where h_0 is the coefficient and the $\{h_j(k_1,\dots\dots k_j), 1.$

The second order Volterra filter is given by

$$i_{LF} = [i_L, i_L(n-1), \dots\dots\dots i_L(n-M+1), i_L^2(n), i_L^2(n-1), \dots i_L^2(n-M+1)]^{\mathrm{T}} \quad (5.12)$$

The weight vector is given by

w= $[w_1, w_2, w_3, w_4, \dots . w_M]^T$

The estimated load current (i_{Lest}) is given by

$$i_{Lest} = \sum_{i=1}^{m} w_i \, i_L \quad (5.13)$$

In similar manner using equation (5.14) to equation (5.19), all the three fundamental current components are extracted. The fundamental component of load current of phase 'a' is given by

$$i_{Lest} = i_{Lk} + \sum w_1(k_1) i_L(n-k_1) + \sum\sum w_1(k_1 k_2) i_L(n-k_1)\, i_L(n-k_2) \quad (5.14)$$

$$i_{Lesta} = i_{La} + w_a i_{La}(n-1) + w_a i_{La}(n-1) i_{La}(n-2) \quad (5.15)$$

The fundamental component of load current of phase ‘b’ is given by

$$i_{Lestb} = i_{Lk} + \sum w_1(k_1) i_L(n-k_1) + \sum\sum w_2(k_1 k_2) i_L(n-k_1)\, i_L(n-k_2) \quad (5.16)$$

$$i_{Lestb} = i_{Lb} + w_b i_{Lb}(n-1) + w_b i_{Lb}(n-1) i_{La}(n-2) \quad (5.17)$$

The fundamental component of load current of phase ‘c’ is given by

$$i_{Lestc} = i_{Lk} + \sum w_1(k_1) i_L(n-k_1) + \sum\sum w_2(k_1 k_2) i_L(n-k_1)\, i_L(n-k_2) \quad (5.18)$$

$$i_{Lestc} = i_{Lc} + w_c i_{Lc}(n-1) + w_c i_{Lc}(n-1) i_{La}(n-2) \quad (5.19)$$

The average estimated current of all the three phases is represented as

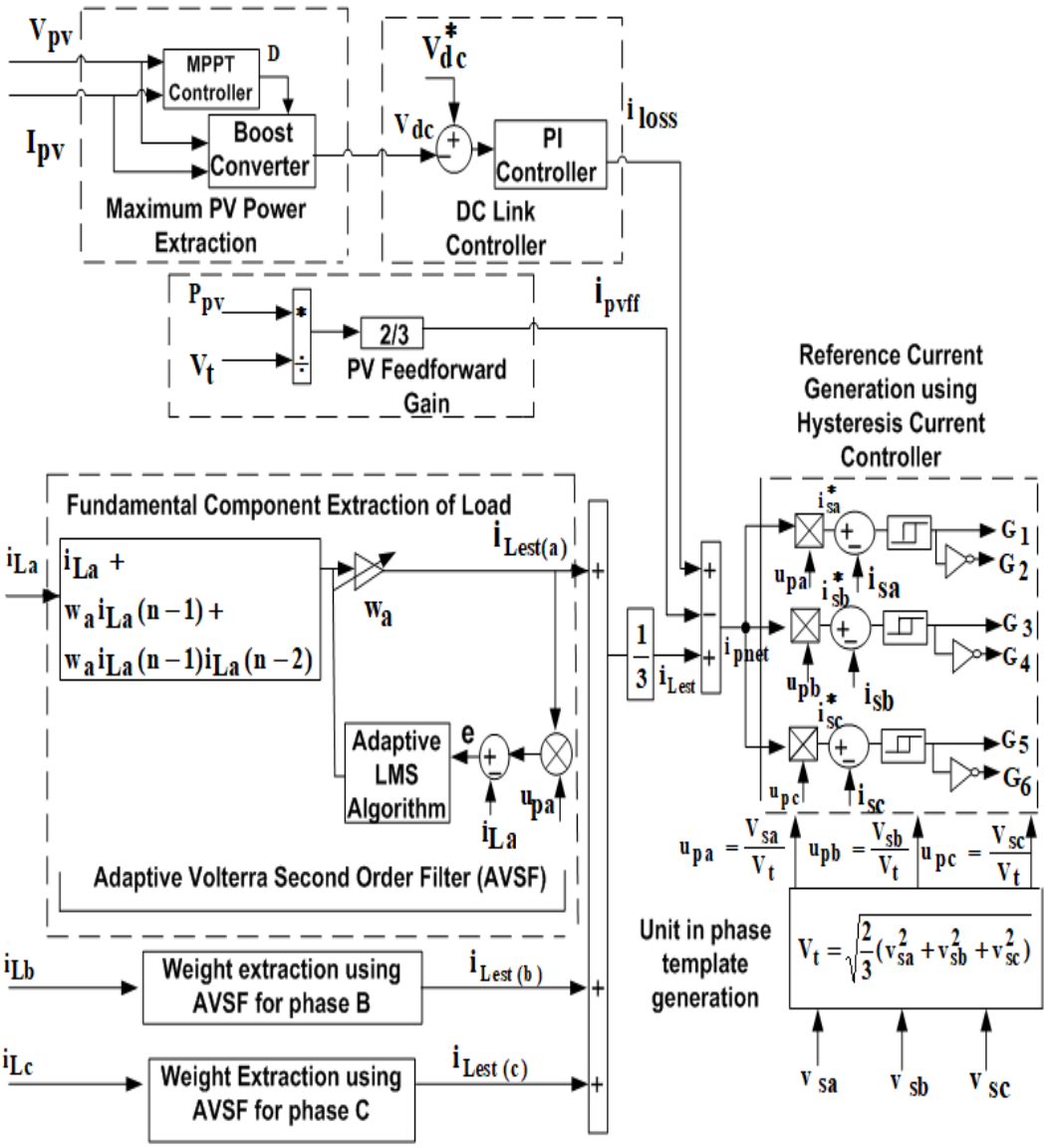

Fig. 5.6. Schematic Block Diagram of AVSF controller

$$i_{Lest} = \frac{i_{Lesta}+i_{Lestb}+i_{Lestc}}{3} \quad (5.20)$$

The estimated fundamental component is used to generate reference source currents for three-phase SAPF and gating pulses and the complete procedure discussed in Section 3.3

The Volterra filter is further made adaptive. The LMS adaptive algorithm is used for updating the weight coefficients using equation (5.21) for each phase a, b and c.

$$w(j+1) = w(j) + \eta e(j) sin\theta \quad (5.21)$$

5.1.4 Cubic Beizer Functional Expansion Based Adaptive Filter (CB-FEBAF)

CB-FEBAF follows the B-spline methods for curves and surfaces [206-210]. B-spline curve is defined as the blending differential interpolation curve used to estimate the fundamental component of load current. The fundamental component of load current is enclosed inside the convex hull of the defined control points. The four control points $i_{L(j-1)}, i_{L(j)}, i_{L(j+1)}\ and\ i_{L(j+2)}$ constitute the cubic beizer curve. The control points are updated by weight coefficients of LMS algorithm. The weights are updated in such a way that the mean square error is minimized. This error is taken as difference between the actual load current and the estimated load current. The schematic control diagram is shown in Fig. 5.7.

The B-spline curve is defined as

$$i_{Lf}(q) = \sum_{j=0}^{n} i_{Lj} B_{n,j}(q) \quad (5.22)$$

The Cubic Spline Beizer Curve follows the path through control points $i_{L(j-1)}, i_{L(j)}, i_{L(j+1)}\ and\ i_{L(j+2)}$ traced by the function i_{Lf} as

$$i_{Lf}(q) = i_{L0}B_{3,0}(q) + i_{L1}B_{3,1}(q) + i_{L2}B_{3,2}(q) + i_{L3}B_{3,3}(q) \quad (5.23)$$

The Beizer polynomials are given by

$$B_{n,j}(q) = \binom{n}{j}(1-q)^{n-j}q^{j} \quad (5.24)$$

where $\binom{n}{j}$ is given by binomial coefficients $=\frac{n!}{(n-j)!j!}$ which is defined as

$$i_{Lf}(q) = (1-q)\left(\sum_{j=0}^{n-1} i_{Lj}\, B_{j,n-1}(q)\right) + p\left(\sum_{j=1}^{n} i_{Lj}\, B_{j-1,n-1}(q)\right) \quad (5.25)$$

$$i_{Lf}(q) = (1-q)^3 i_{L0} + 3q(1-q)^2 i_{L1} + 3q^2(1-q)i_{L2} + q^3 i_{L3} \quad (5.26)$$

$$i_{Lf}(q) = (1-q^3-3q(1-q))i_{L0} + 3q(1+q^2-2q)i_{L1} + (3q^2-3q^3)i_{L2} + q^3 i_{L3} \quad (5.27)$$

$$i_{Lf}(q) = (1-q^3-3q+3q^2)i_{L0} + 3q(1+q^2-2q)i_{L1} + (3q^2-3q^3)i_{L2} + q^3 i_{L3} \quad (5.28)$$

$$i_{Lf}(q) = (1-3q+3q^2-q^3)i_{L0} + (3q-6q^2+3q^3)i_{L1} + (3q^2-3q^3)i_{L2} + q^3 i_{L3} \quad (5.29)$$

Generalizing the coefficients of the matrix we get

$$i_{LCS}(p) = [1\ q\ q^2 q^3]\begin{bmatrix} 1 & 0 & 0 & 0 \\ -3 & 3 & 0 & 0 \\ 3 & -6 & 3 & 0 \\ -1 & 3 & -3 & 1 \end{bmatrix}\begin{bmatrix} i_{L0} \\ i_{L1} \\ i_{L2} \\ i_{L3} \end{bmatrix} \quad (5.30)$$

where M=$\begin{bmatrix} 1 & 0 & 0 & 0 \\ -3 & 3 & 0 & 0 \\ 3 & -6 & 3 & 0 \\ -1 & 3 & -3 & 1 \end{bmatrix}$ is the Cubic Bezier matrix

Generalizing the knot points and restricting to few terms gives

$$i_{LF}(p) = (1-3\mathrm{q}+3\mathrm{q}^2-\mathrm{q}^3)\mathrm{i}_{\mathrm{L(j)}} + (3\mathrm{q}-6\mathrm{q}^2+3\mathrm{q}^3)\mathrm{i}_{\mathrm{L(j-1)}} + (3\mathrm{q}^2 - 3\mathrm{q}^3)\mathrm{i}_{\mathrm{L(j-2)}} + q^3\mathrm{i}_{\mathrm{L(j-3)}} \quad (5.31)$$

The coefficients of the matrix are regularly updated by weight coefficients of the LMS algorithm and summed together to get the estimated load current.

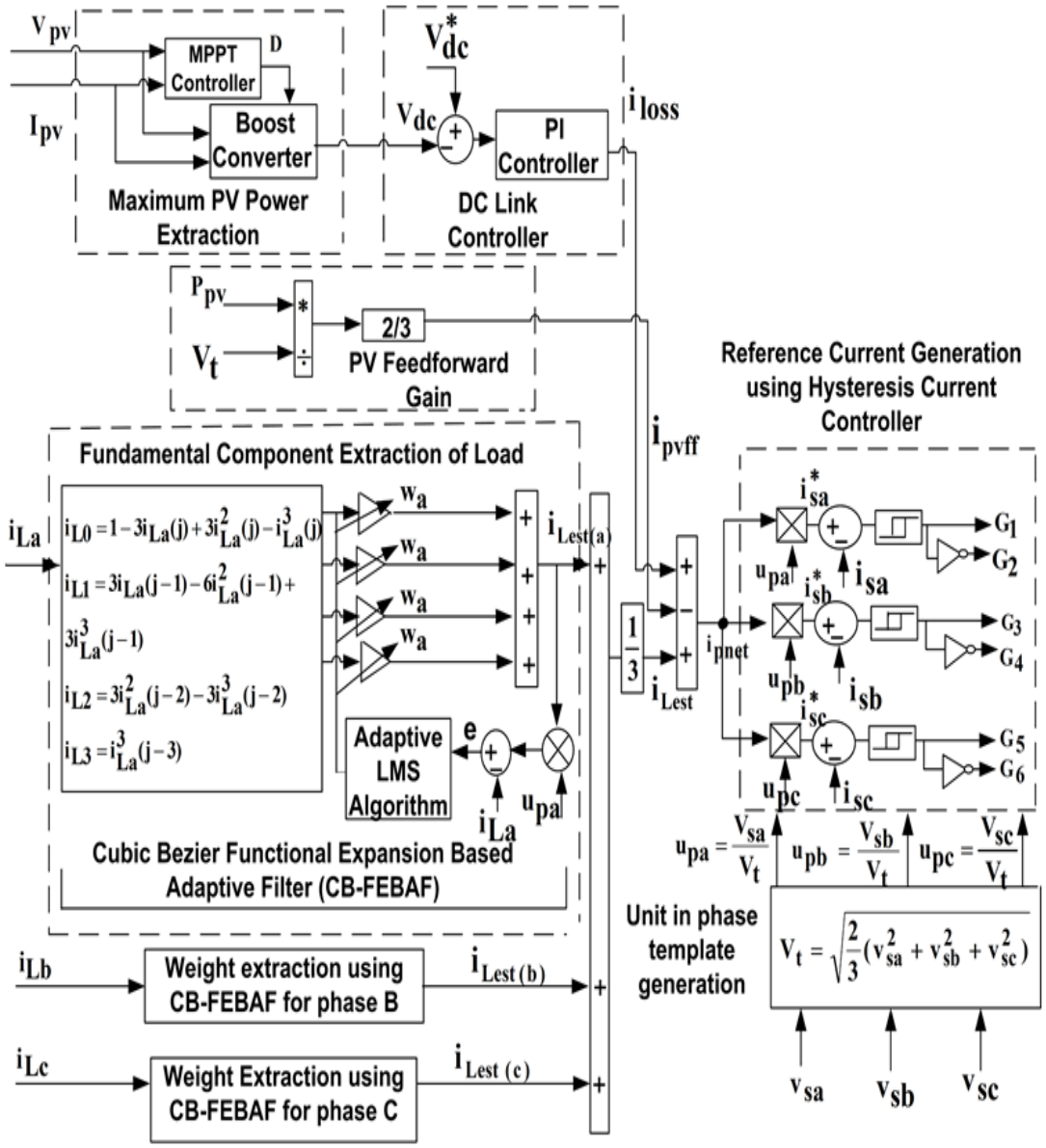

Fig. 5.7. Schematic Block Diagram of CB-FEBAF controller

$$i_{(Lest)j} = \sum w_j^T i_{LCS} = \sum w_j^T \emptyset\left(p_j^T\right) = \sum w_j^T \left[M^T p_j^T\right] \tag{5.32}$$

$$i_{(Lest)j} = \sum [w_j\left(1 - 3i_{Lj} + 3i_{Lj}^2 - i_{Lj}^3\right), w_j\left(3i_{L(j-1)} - 6i_{L(j-1)}^2 + 3i_{L(j-1)}^3\right), w_j(3\, i_{L(j-2)}^2 - 3i_{L(j-3)}^3), w_j i_{L(j-3)}^3] \tag{5.33}$$

The above matrix is formulated for each phase (a, b and c) and the average of all the three phases are taken

$$i_{Lest} = \frac{i_{Lesta}+i_{Lestb}+i_{Lestc}}{3} \quad (5.34)$$

The estimated fundamental component is further used to generate reference source currents for SAPF as discussed in Section 3.3.

The error between the actual load current and the estimated load current is given by

$$e(j) = i_{Lj} - i_{Lest(j)}sin\theta \quad (5.35)$$

The cost function 'J' is constituted and the adaptive learning mechanism is employed to minimize the above error by LMS algorithm under changing load conditions.

$$J(w, i_{Lest}) = E(e^2(j)] \quad (5.36)$$

$$J(w, i_{Lest}) = E[(i_{Lj} - i_{Lest(j)}\ sin\theta)^2] \quad (5.37)$$

The adaptive learning LMS learning algorithm is given by

$$w(j+1) = w(j) - \frac{\eta}{2}\frac{\partial J}{\partial i_{Lest(j)}} \quad (5.38)$$

Differentiating equation (5.37) we got equation (5.39)

$$\frac{\partial J}{\partial i_{Lest(j)}} = 2e(j)\frac{\partial e}{\partial i_{Lest(j)}} \quad (5.39)$$

Differentiating equation (5.35) we got equation (5.40)

$$\frac{\partial e}{\partial i_{Lest(j)}} = -sin\theta \quad (5.40)$$

Putting equation (5.40) in equation (5.39) we got

$$\frac{\partial J}{\partial i_{Lest(j)}} = -2e(j)sin\theta \quad (5.41)$$

Putting equation (5.41) in equation (5.38) we got

$$w(j+1) = w(j) + \eta e(j) sin\theta \tag{5.42}$$

The weights coefficients for each phase a, b, c are updated by the above learning LMS mechanism and then the average weight is computed. The simulation results with four control algorithms are now discussed in detail followed by hardware results on three phase system.

5.2 Simulation Results

This section discusses the modelling and simulation of SRFT, SOGI, Adaptive Volterra Second Order Filter (AVSF), Cubic Beizer Functional Expansion Based Adaptive Filter (CB-FEBAF) for SAPF in three-phase grid connected system without/ with PV interfaced systems. The PV array of capacity 750W is simulated using three Kyocera solar 320GX-LPB panels of capacity 250W connected at the DC Link of SAPF. The performance analysis under different linear, non-linear, mixed loading conditions as well as ambient conditions such as irradiation conditions for checking the effectiveness of the developed control algorithms is discussed in detail.

5.2.1. Performance analysis with Three Phase SRFT Controller

The Synchronous Reference Frame theory-based control scheme is modelled and simulated in MATLAB environment under different loading conditions as well as changing solar irradiation conditions.

5.2.1.1 Performance under changing load conditions

The steady state waveforms of source voltages (v_{sabc}), source currents (i_{sabc}), load currents (i_{Labc}) compensator currents (i_{fabc}) and DC link voltage (V_{dc}) under all different loading conditions are shown in Fig. 5.8. Non-linear load conditions are

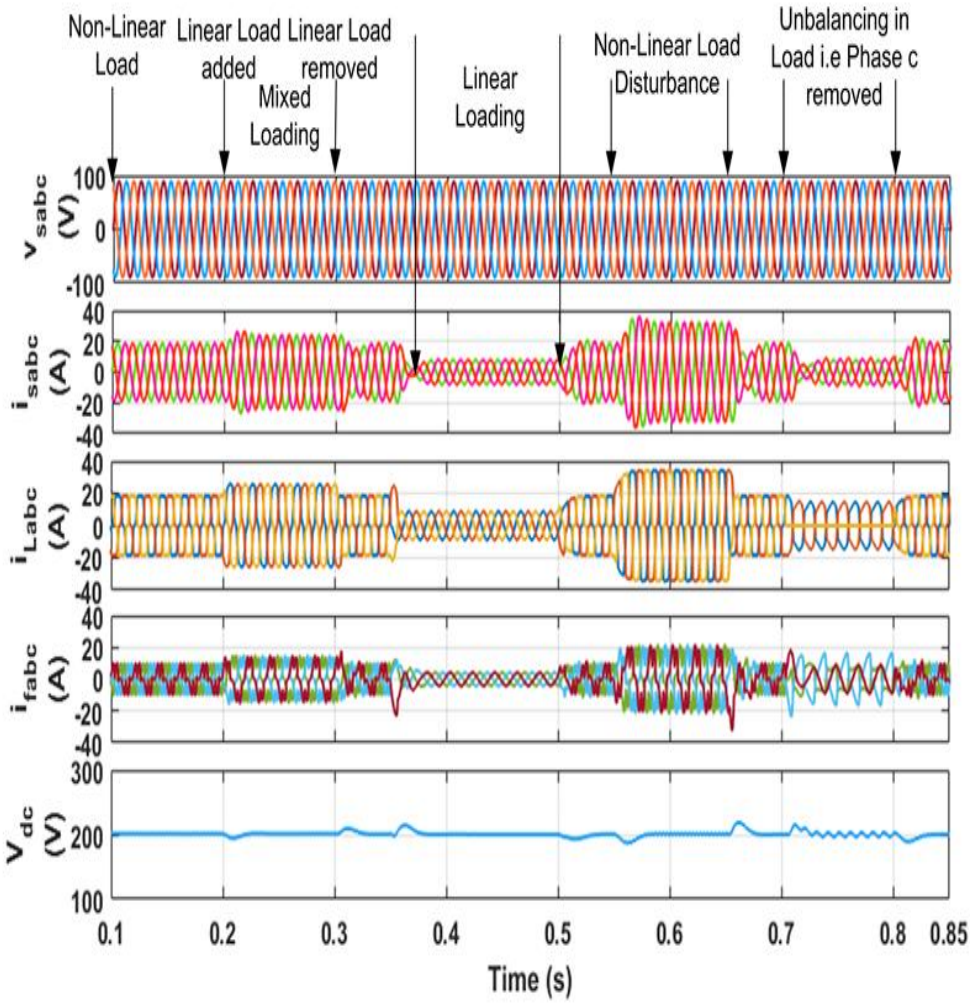

Fig. 5.8. Steady state waveforms under changing load conditions with three phase SRFT controller in simulink

simulated from 0.1s to 0.2s. The source currents are found to be sinusoidal and balanced in Fig. 5.9 when the load current has a THD of 20.26%.

At 0.2s, linear load is added and mixed loading conditions are created. The source current increases to 25A to meet the additional load demand. The THD of source current under mixed loading conditions is found to be 0.73 % when load current has a THD of 12.77% shown in Fig. 5.10.

At 0.3s, the additional linear load is removed and brought back to non-linear load conditions and current magnitude comes back to 19A. The DC link voltage is observed to be well settled at 200V.

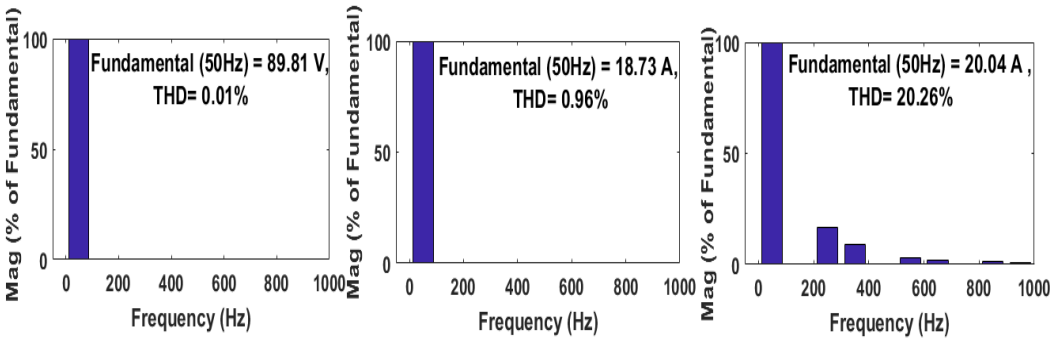

(a) (b) (c)

Fig. 5.9. THD of three phase SRFT controller for (a) source voltage (v_{sabc}) (b) source current (i_{sabc}) and (c) load current (i_{Labc}) under non-linear load conditions in simulink

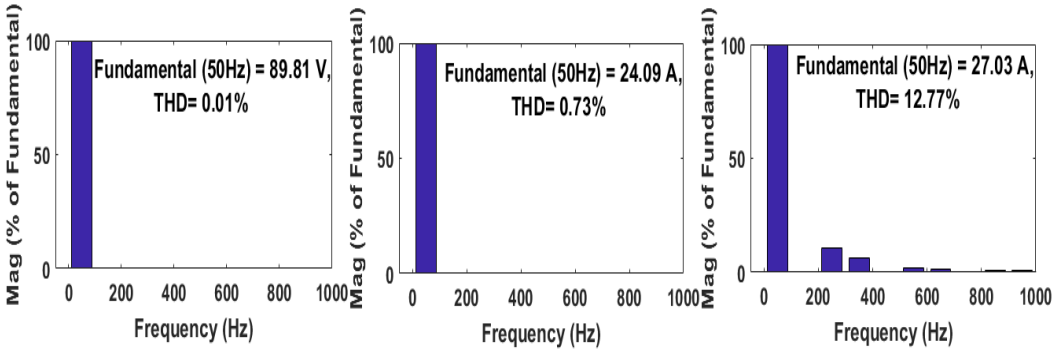

(a) (b) (c)

Fig. 5.10. THD of three phase SRFT controller for (a) source voltage (v_{sabc}) (b) source current (i_{sabc}) and (c) load current (i_{Labc}) under mixed loading conditions in simulink

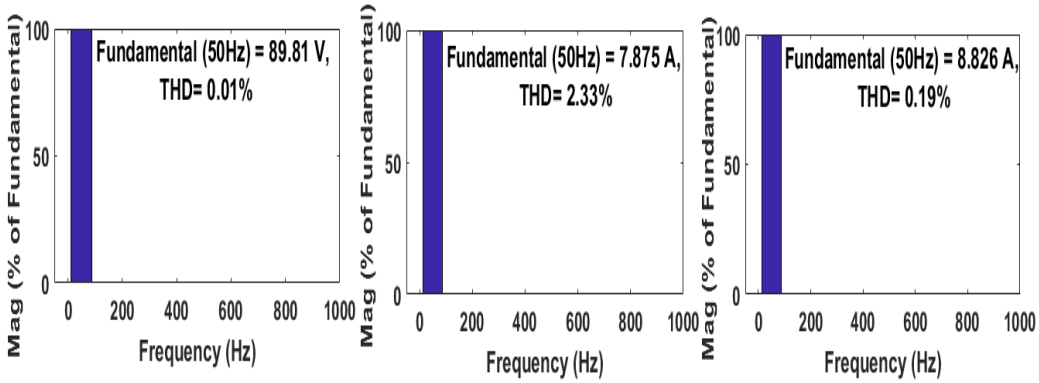

(a) (b) (c)

Fig. 5.11. THD of three phase SRFT controller for (a) source voltage (v_{sabc}) (b) source current (i_{sabc}) and (c) load current (i_{Labc}) under linear loading conditions in simulink

Under linear loading conditions from 0.35s to 0.5s, the performance of system with SRFT control is tested. The source currents and the load currents both are sinusoidal. A source current of 9A is used to meet the load demand of 9A. The THD in grid current

under linear load conditions is found to be 2.33% when the THD in load current is 0.19% as shown in Fig. 5.11.

From 0.55s to 0.65s, the non-linear load disturbance is added, the source current increases to 32A to meet the load demand of 32A. The source currents are balanced and sinusoidal.

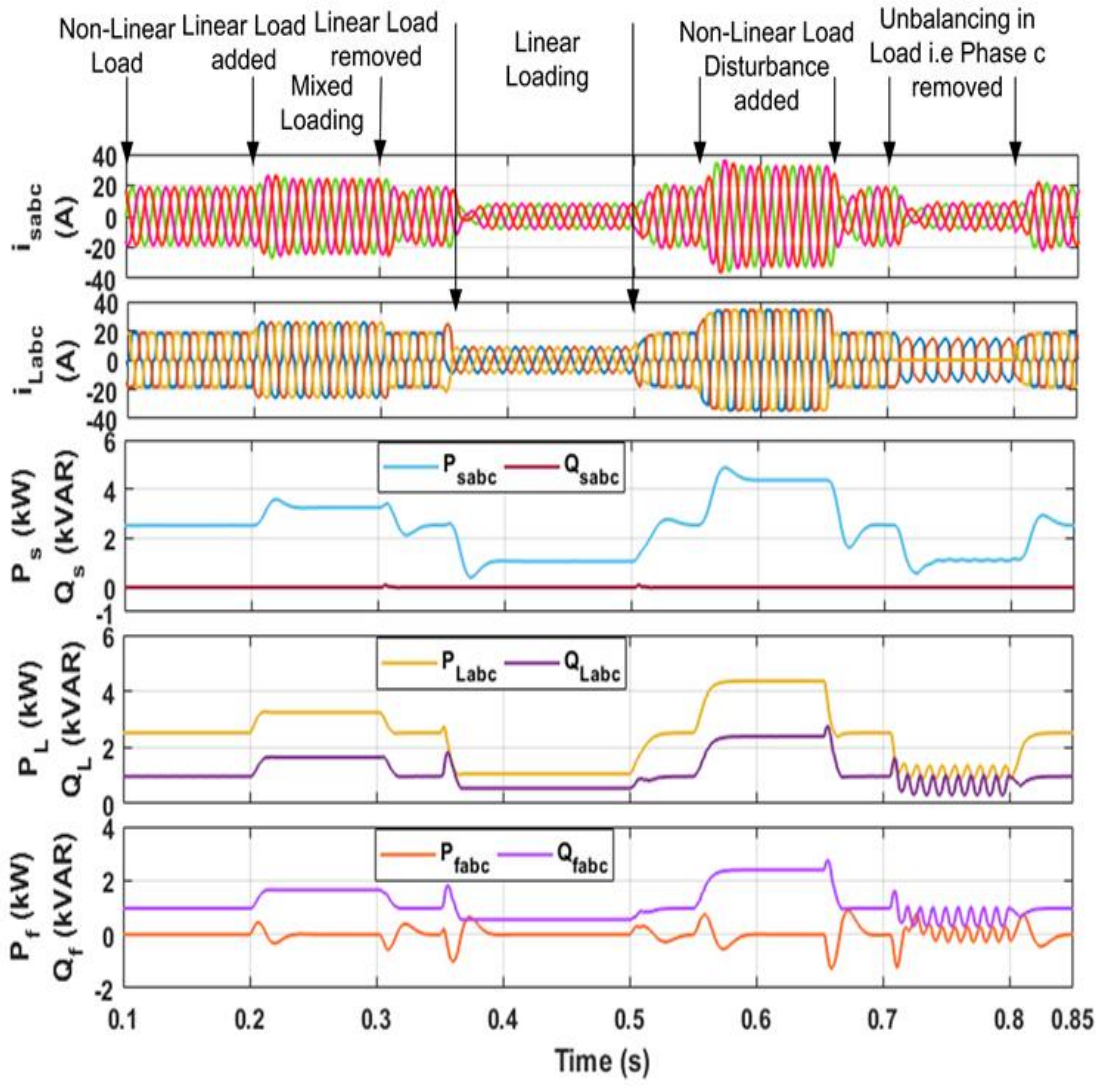

Fig. 5.12. Steady state power waveforms under changing load conditions with three phase SRFT controller in simulink

The SAPF Filter injects the necessary compensating currents to cancel the harmonics injected into the source current by the non-linear load. This makes the source currents sinusoidal under all loading conditions.

The DC link voltage shows a little dip and rise under all sudden variations in loading conditions. However, it recovers to its 200V value with in half cycle due to a properly tuned PI controller. The unbalanced load conditions are now tested from 0.7s to 0.8s and it is observed that there are sudden oscillations in DC link voltage however it is well regulated. Moreover, the supply currents are sinusoidal though reduced in magnitude.

Fig. 5.12 shows steady state power results under changing load conditions. It has been found that under non-linear load conditions from 0.1s to 0.2s, 2.5kW of load power is met by the source power of 2.5kW. Also, 970VAR of reactive power demand of load is met by the compensator which injects 970VAR. Under mixed loading conditions from 0.2s to 0.3s, 3.240 kW of load is met by the source power and 1.650 kVAR of reactive power needed by the load is met by the compensator.

Under linear loading conditions 1.060 kW of active power is met by the source active power. The reactive power of 0.545 kVAR is met by the compensator.

Under non-linear load disturbance from 0.55s to 0.65s, the load power is increased to 4.365 kW which is met by the source power. The reactive power load demand of 2.390 kVAR is met by the compensator. Under un-balancing load conditions 1 kW load is met by the source and 0.5 kVAR load demand is met by the compensator.

Fig. 5.13 shows the intermediate results of i_{Labc}, i_d ,i_q ,i_{Lest} and i_{pnet} using SRFT algorithm under changing load conditions. It has been found that the i_d increases proportionately with respect to load current variation and i_q corresponds to reactive power component of load current. u_{pa}, u_{pb} and u_{pc} correspond to the unit in phase templates obtained. The i_{pnet} is obtained by the addition of fundamental load component and the DC link voltage controller current i_{loss}. Table 5.1 shows the THD values

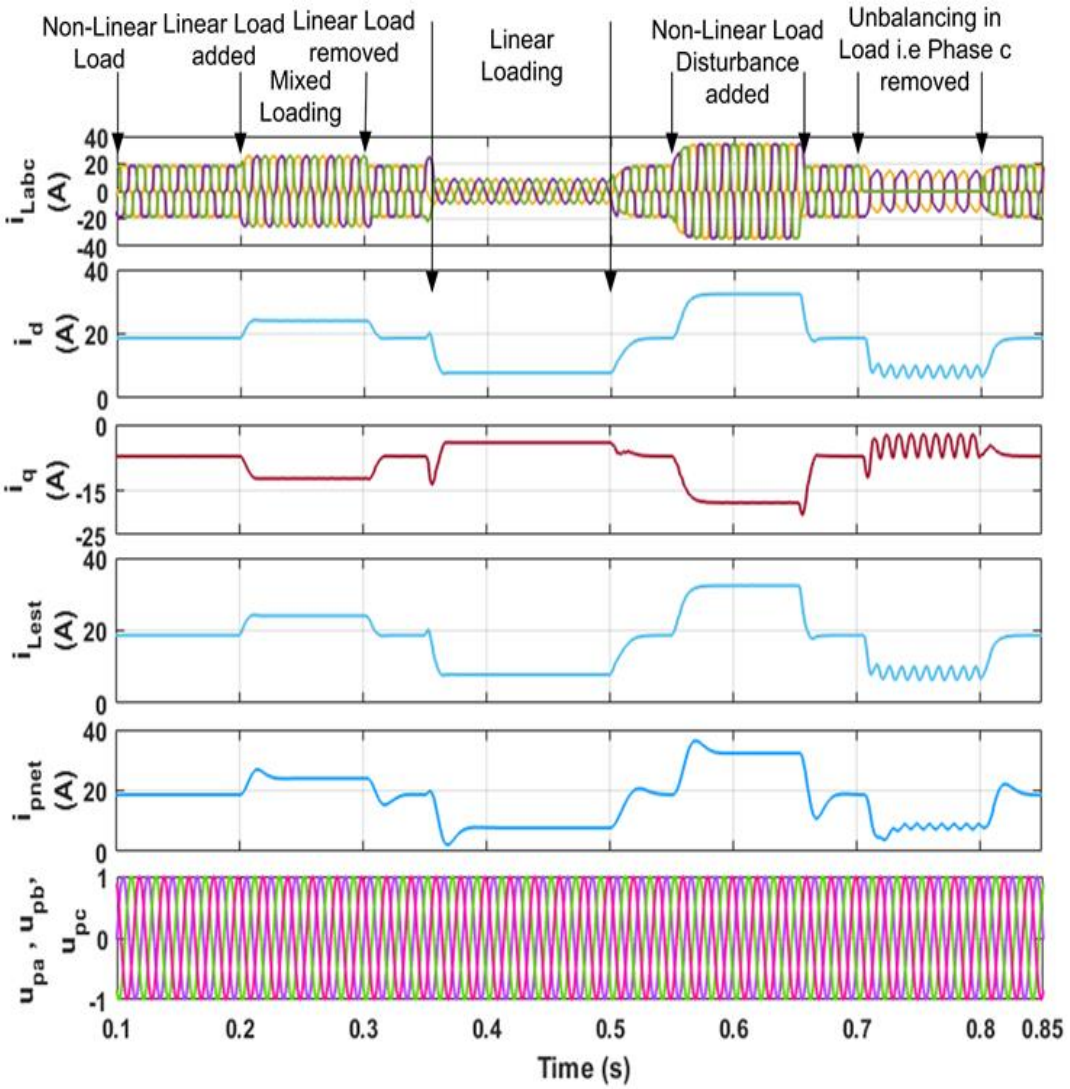

Fig. 5.13. Steady state intermediate waveforms under changing load conditions with three phase SRFT controller in simulink

obtained in simulink with SRFT algorithm for three phase system under various loading conditions.

Table 5.1. THD values obtained in simulink with three phase SRFT algorithm under various loading conditions

Loading Conditions	Three Phase Synchronous Reference Frame Theory (SRFT)		
	i_L(THD)	i_S(THD)	v_s(THD)
Non-Linear Load	20.26%	0.96%	0.01%
Mixed Load	12.77%	0.73%	0.01%
Linear Load	0.19%	2.33%	0.01%

5.2.1.2 Performance under changing solar irradiation conditions and constant load conditions

The steady state waveforms of solar irradiation $\boldsymbol{G}(\boldsymbol{I_{irr}})$, PV power $\boldsymbol{P_{pv}}$, source voltages (v_{sabc}), source currents (i_{sabc}), load currents (i_{Labc}),compensator currents (i_{fabc}) under changing irradiation conditions under non-linear load are shown in Fig. 5.14. Under normal grid conditions and non-linear load from 0.1s to 0.13s, the source current of 19A is used to meet the load current of 19A. The three Kyocera 250W PV array panels are connected in series having a maximum power capacity of 750W at

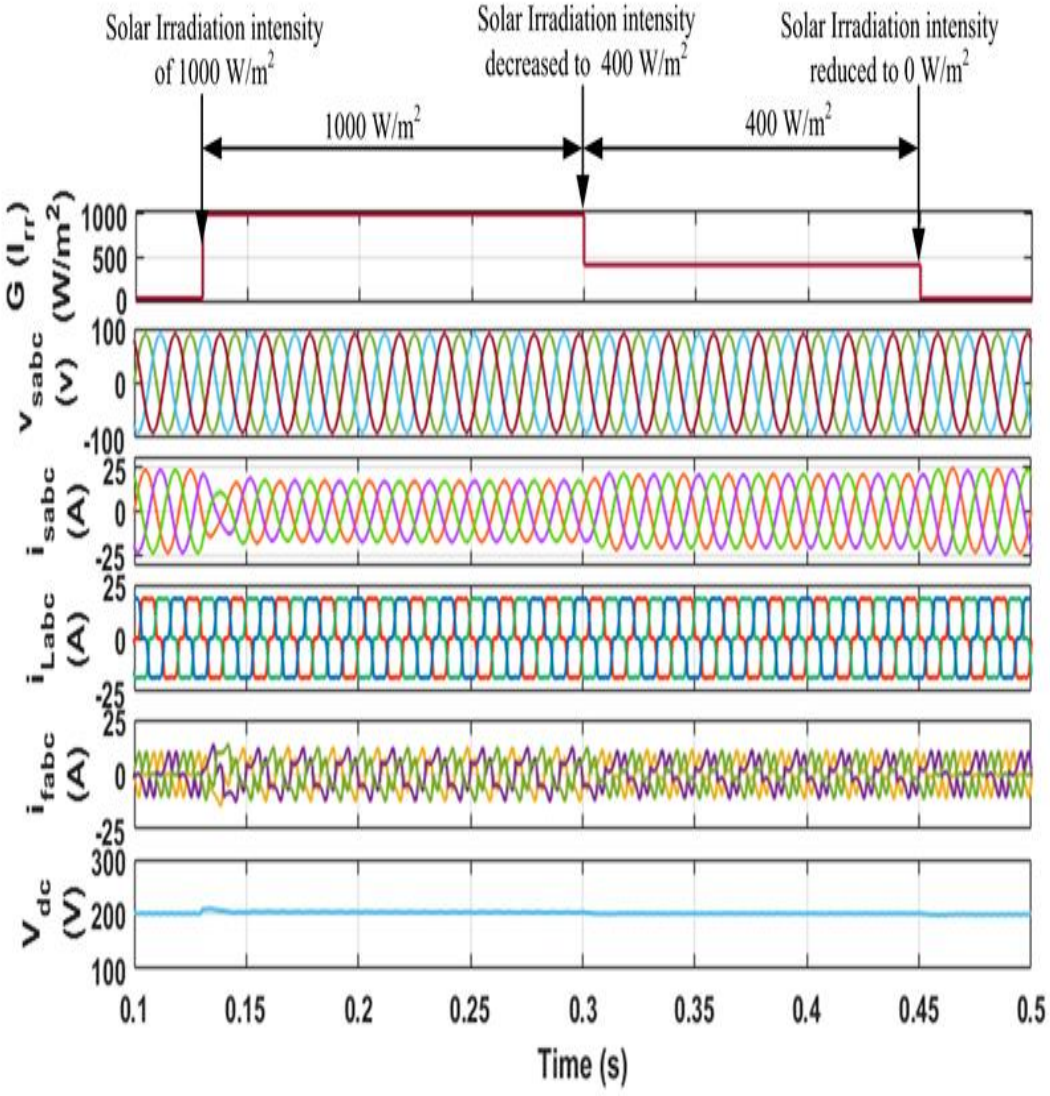

Fig. 5.14. Steady state waveforms under changing solar irradiation and constant non-linear load conditions with three phase SRFT controller in simulink

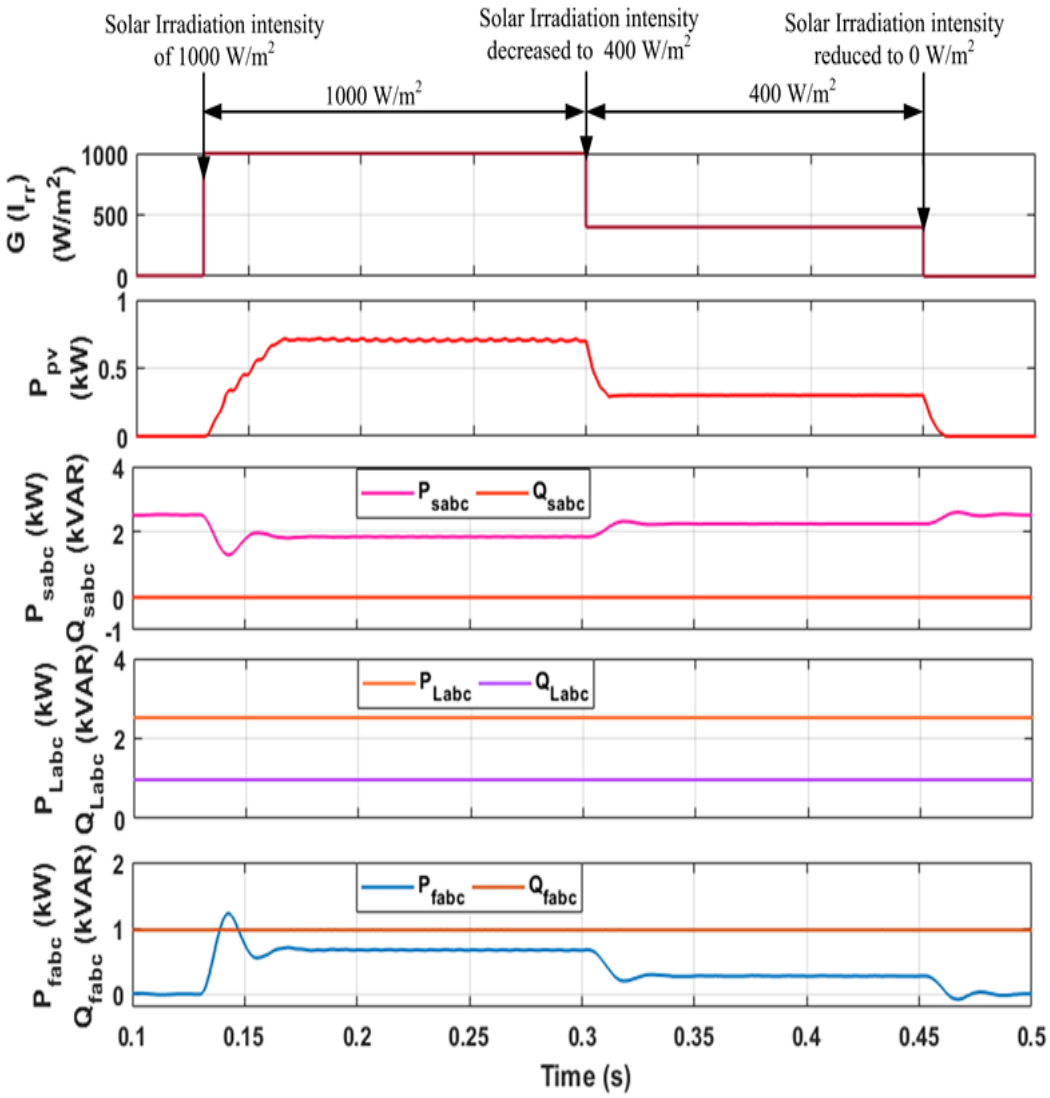

Fig. 5.15. Steady state waveforms power waveforms under changing solar irradiation with three phase SRFT controller in simulink

1000W/m^2. The array delivers active power of 660W at the DC link of inverter. From 0.13s to 0.3s, the solar irradiation of 1000W/m^2 is tested and it is found that the source current reduces to 14A to meet the load current as the load current is shared by both PV current and source current. The solar irradiation is now reduced to 400W/m^2 at t= 0.3s and the source current increases to 17A to meet the load demand, the PV current reduces and the grid current increases proportionately to meet the load demand, the PV current reduces and the grid current increases proportionately to meet the load demand of 19

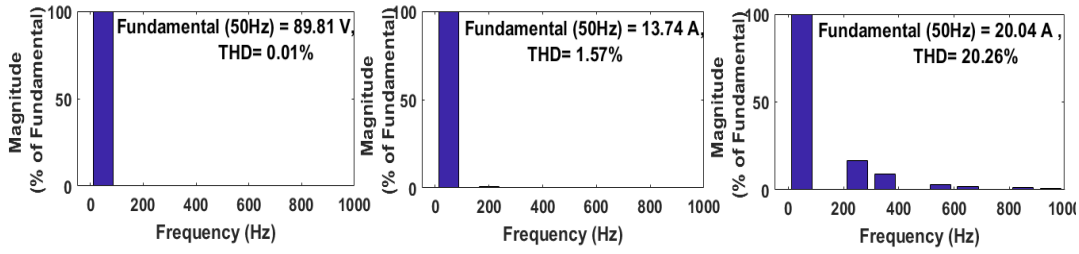

Fig. 5.16. THD of three phase SRFT controller for (a) source voltage (v_{sabc}) (b) source current (i_{sabc}) and (c) load current (i_{Labc}) under changing PV irradiation conditions for constant non- linear load conditions in simulink

A. The DC link voltage maintains a set reference value of 200V by the PI controller action.

The steady state results show power waveforms of PV power, source power, load power compensator power and are depicted in Fig. 5.15. The PV array has a capacity of 750 W under 1000W/m^2 but it is injecting 670W at the DC link of inverter. From 0.1s to 0.13s, the total load power of 2.520kW is met by the source alone as PV source is not connected. From 0.13s to 0.3s, under solar irradiation of 1000W/m^2, the load power of 2.520 kW is met partially by the source power of 1.850 kW and PV power of 0.670 kW. The solar irradiation is now reduced to 400W/m^2 from 0.3s to 0.45s, here PV power is reduced to 0.3kW and the source power increases to 2.250kW to meet the total load power of 2.5kW. From 0.45s onwards, the solar irradiation is made to zero and the load power is completely met by the source now. The THD of source current under 1000W/m^2 solar irradiation conditions is found to be 1.57% shown in Fig. 5.16 when the load current THD is 20.26%.

5.2.2. Performance analysis with DSOGI Controller

The DSOGI based control scheme is now modelled and simulated in MATLAB environment under different loading and changing solar irradiation conditions. The performance of this controller is now discussed in detail.

5.2.2.1 Performance under changing load conditions in grid connected systems

The steady state waveforms of v_{sabc},i_{sabc} ,i_{Labc} ,i_{fabc} under varying load conditions i.e., non-linear, linear and mixed loading conditions are shown in Figure 5.17. Under non-linear load conditions till 0.2s, the source current of 19A is used to meet the load demand of 20A.The THD of source current is improved to 0.90 % under non-linear load conditions having THD 30% as shown in Fig. 5.18. The compensating currents from SAPF has removed the harmonics from the source currents which were injected by the non-linear load thus the supply currents are sinusoidal and balanced as desired.

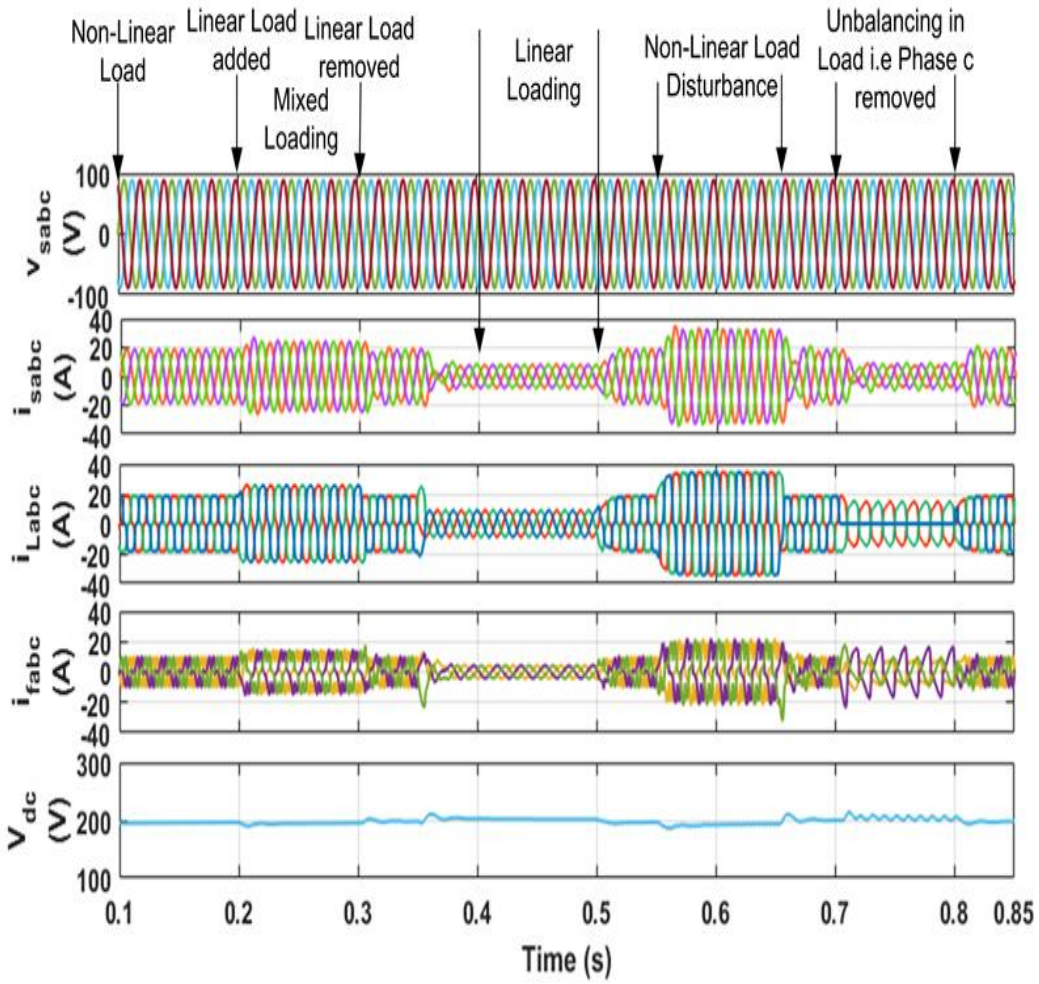

Fig. 5.17. Steady state waveforms under changing load conditions with three phase SRFT controller in simulink

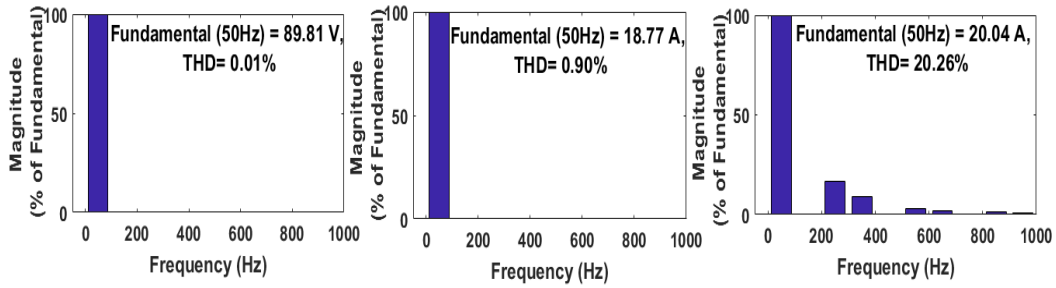

(a) (b) (c)

Fig. 5.18. THD of DSOGI controller for (a) source voltage (v_{sabc}) (b) source current (i_{sabc}) and (c) load current (i_{Labc}) under non-linear load conditions in simulink

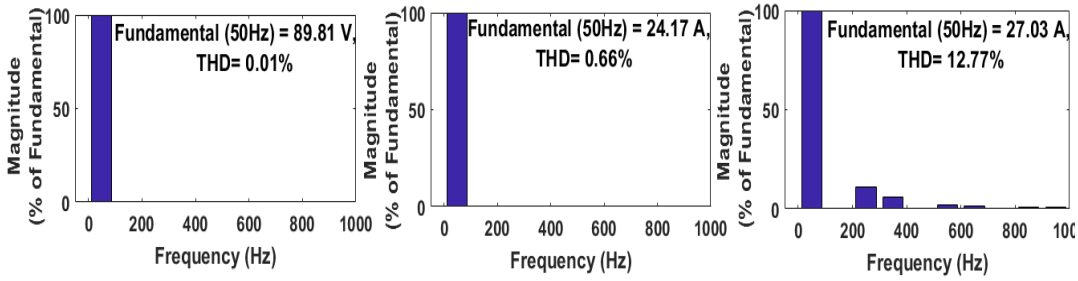

(a) (b) (c)

Fig. 5.19. THD of DSOGI controller for (a) source voltage (v_{sabc}) (b) source current (i_{sabc}) and (c) load current (i_{Labc}) under mixed loading conditions in simulink

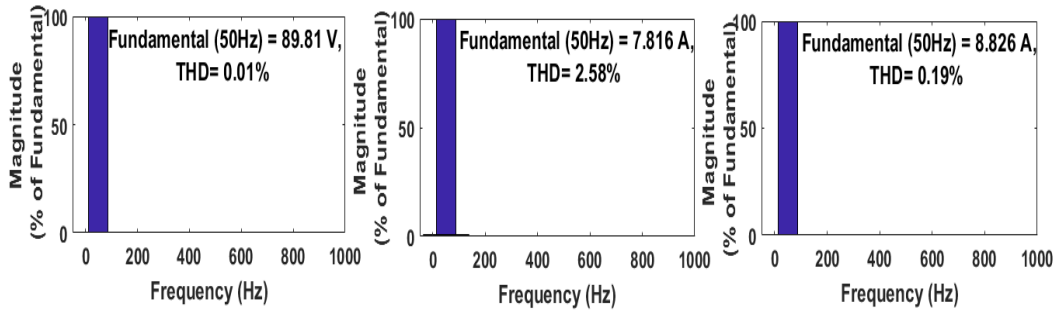

(a) (b) (c)

Fig. 5.20. THD of DSOGI controller for (a) source voltage (v_{sabc}) (b) source current (i_{sabc}) and (c) load current (i_{Labc}) under linear loading conditions in simulink

From 0.2s to 0.3s, additional linear load is added and mixed loading conditions are created and it is found that the source currents are sinusoidal and balanced and the THD has been improved to 0.67% under mixed load having THD of 12.77% as shown in Fig. 5.19.

From 0.35s to 0.5s, linear loading conditions are created and under these conditions

both source current and the load current are sinusoidal. The THD of source current is 2.58% with load THD of 0.19% shown in Fig. 5.20.

From 0.55s to 0.65s, the non-linear load is added and non-linear load disturbance is created, the source current increases to 32.5A to meet the load demand. The source currents are observed to be sinusoidal and balanced.

After 0.65s, non-linear load conditions are again resumed and source current of 20 A is used to meet the load demand of 19A.

From 0.7s to 0.8s, the unbalancing in load conditions is created by opening of one of the phases. Here the source current decreases to 14A to meet the corresponding load

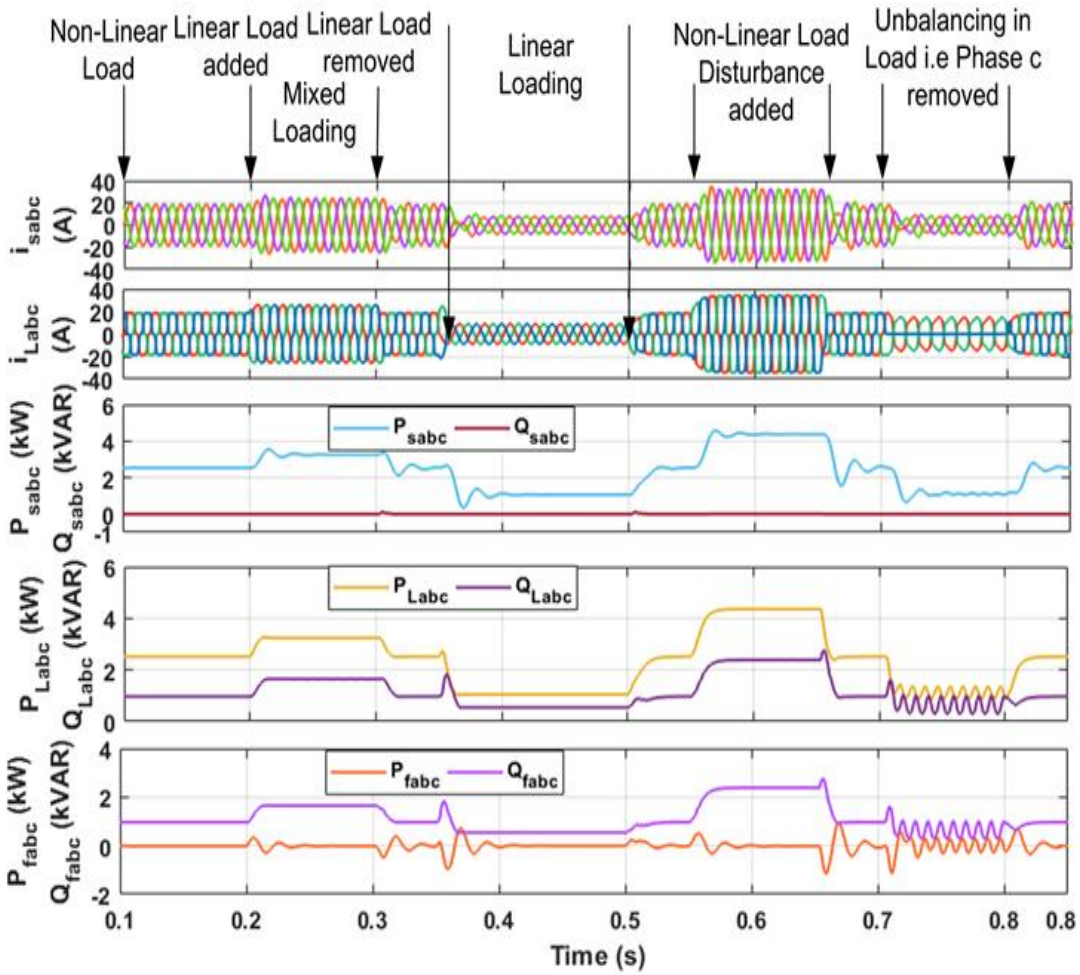

Fig. 5.21. Steady state power waveforms under changing load conditions with DSOGI controller in simulink

demand. It remains sinusoidal and balanced. After 0.8s again the non-linear load conditions of 19A are again resumed

Fig. 5.21 shows the steady state power waveforms under changing load conditions. Under non-linear load conditions till 0.3s, the source power of 2.520kW is used to meet the source power. From 0.2s to 0.3s the mixed loading conditions are there and the source power increases to 3.240kW to meet the load demand. The load power again reduces to 2.520kW under non-linear load conditions.

From 0.35s to 0.5s, the linear loading is simulated. The load power of 1.060kW is met by the source. Again from 0.5s to 0.55s the non-linear load conditions are again

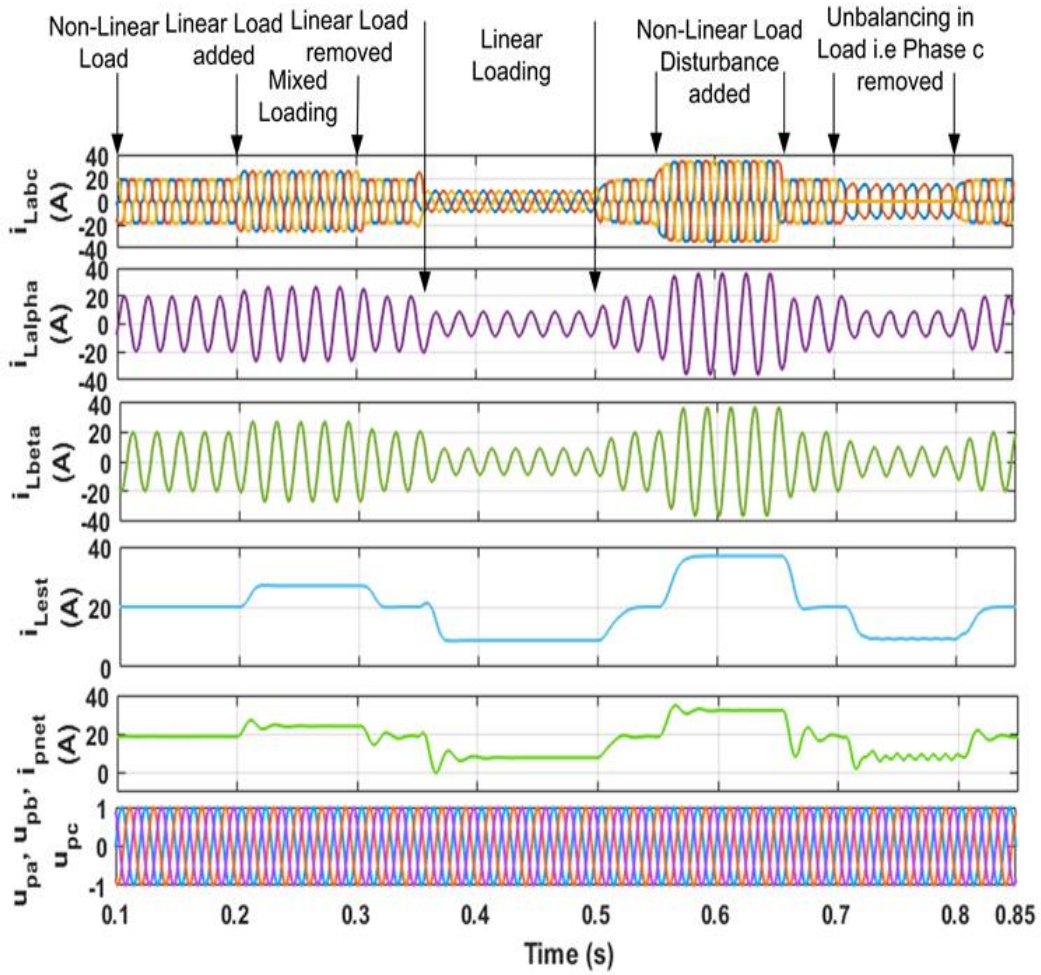

Fig. 5.22. Steady state intermediate waveforms under changing load conditions with DSOGI controller in simulink

attained.

From 0.55s to 0.65s the load demand is increased to 4.365kW which is met by the source power as the non-linear load disturbance is added. Under un-balancing load conditions where one phase is removed the load power reduces to 1kW which is met by the source power of 1kW.

Figure 5.22 shows the i_{Labc} i_{Lalpha},i_{Lbeta} ,i_{Lest} ,i_{pnet} and unit in phase templates u_{pa} , u_{pb} and u_{pc} intermediate waveforms of DSOGI under varying load conditions. The i_{Lalpha} obtained is in phase with the supply voltage and i_{Lbeta} is obtained by 90° phase shift. The i_{Lest} is the fundamental rms component estimated by the algorithm. The i_{pnet} obtained by adding the i_{Lest} with the i_{Loss} component given by DC link voltage controller.

Table 5.2 shows the THD values obtained in simulink with DSOGI algorithm for the three phase systems under various loading conditions

Table 5.2. THD values obtained in simulink with DSOGI algorithm under various loading conditions

Loading Conditions	Dual Second Order Generalised Integrator (DSOGI)		
	i_L(THD)	i_S(THD)	v_s(THD)
Non-Linear Load	20.26%	0.90%	0.01%
Mixed Load	12.77%	0.66%	0.01%
Linear Load	0.01%	2.58%	0.01%

5.2.2.2 Performance under changing solar irradiation conditions

Fig. 5.23 shows the waveforms of solar irradiation $G(I_{irr})$, PV power P_{pv}, source voltage(v_{sabc}), source current (i_{sabc}), load current (i_{Labc}),compensator current (i_{fabc})

and changing PV irradiation of 1000W/m^2 and 400W/m^2 under non-linear load conditions. From 0.1s to 0.13s the non-linear load conditions are there and 19A source current is used to meet the load demand of 19A. The three Kyocera 250W PV array panels connected in series having a maximum power capacity of 750W at 1000W/m^2 is interfaced at the DC link of SAPF. At 0.13s the solar irradiation of 1000W/m^2 is connected, it is found that the source current reduces to 14A to meet the load demand. As the load current now is partially shared by the PV current of 7.5A. The compensator has removed the source current harmonics injected by the load current. The source currents are sinusoidal and balanced. The THD of source current is 1.53% under non-linear load THD of 20.07% as shown in Fig. 5.24. From 0.3s to 0.45s the solar

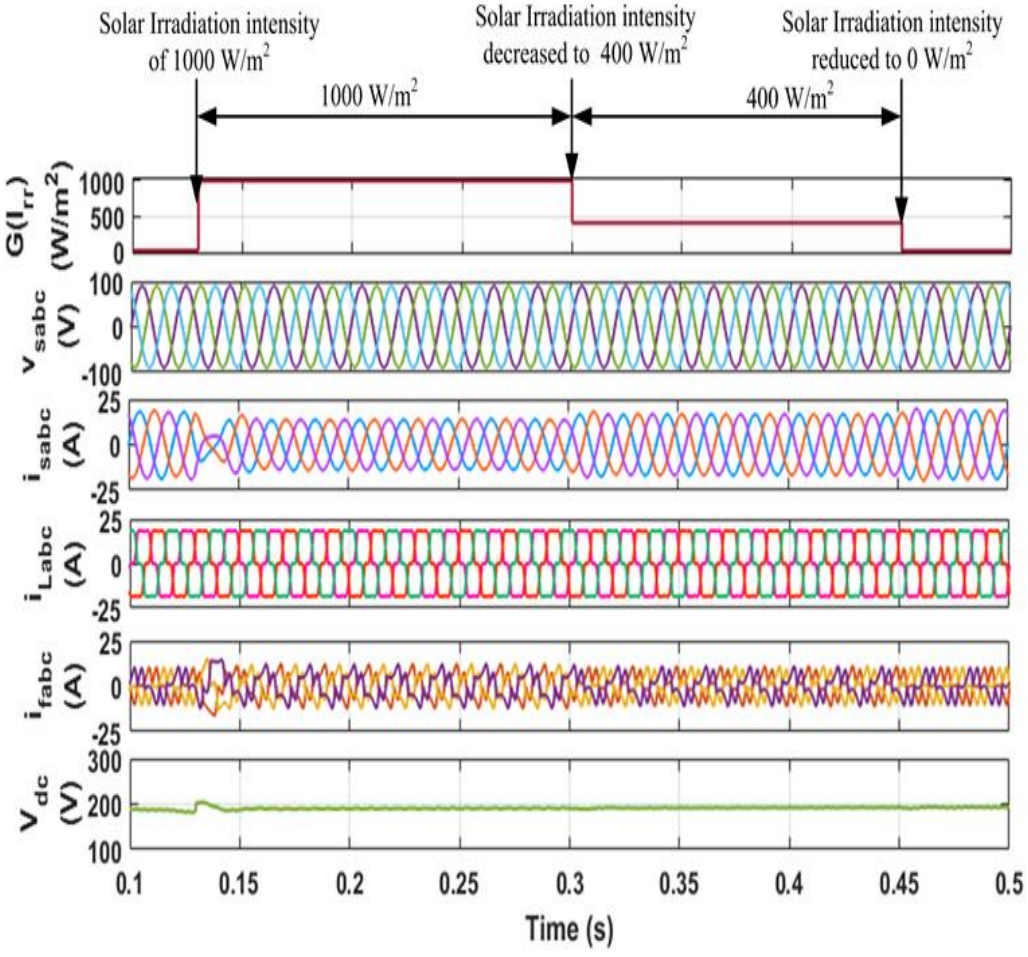

Fig. 5.23. Steady state waveforms of DSOGI controller under changing PV irradiation conditions with constant non-linear load conditions in simulink

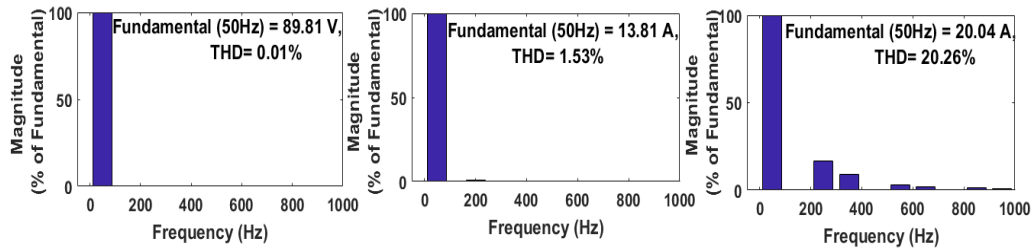

Fig. 5.24. THD of DSOGI controller for (a) source voltage (v_{sabc}) (b) source current (i_{sabc}) and (c) load current (i_{Labc}) under changing solar irradiation and constant non-linear load conditions in simulink

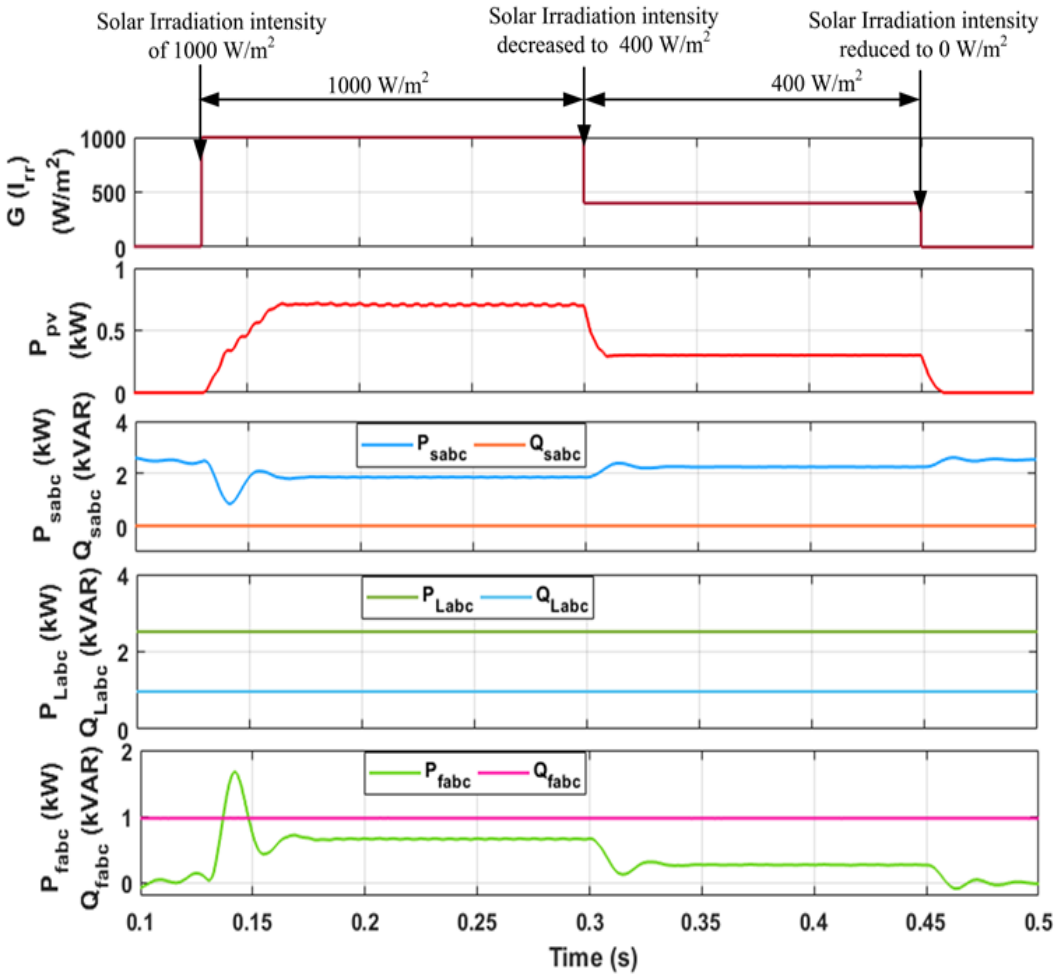

Fig. 5.25. Steady state power waveforms with DSOGI under changing PV irradiation conditions with constant non-linear load conditions in simulink

irradiation intensity is reduced to 400W/m^2, the source current increases to 17A and PV current decreases to 3.5A to meet the 19A load current. The source currents are observed to be sinusoidal and balanced.

The DC link voltage is regulated to set reference value of 200V by PI controller under solar irradiation of 1000W/m^2 and 400W/m^2.

Figure 5.25 shows the steady state power waveforms under changing solar irradiation conditions. The PV array of capacity 750W is used and it is injecting 660W power at the DC link of inverter. The source power of 2.52kW is used to meet the load demand of 2.52 kW under normal non-linear load conditions. Under solar irradiation intensity of 1000 W/m^2, the load power of 2.52kW is shared by source power of 1.85kW and PV power of 0.66kW. Under solar irradiation intensity of 400W/m^2, the source power increases to 2.260kW and PV power reduces to 0.26kW to meet the load demand of 2.52kW. The reactive VAR demand of the load is completely met by the compensator.

From 0.35s to 0.5s, the linear loading is simulated. The load power of 1.060kW is met by the source. Again from 0.5s to 0.55s, the non-linear load conditions are again attained. From 0.55s to 0.65s, the load demand is increased to 4.36kW which is met by the source power as the non-linear load disturbance is added.

Under un-balancing load conditions where one phase is removed the load power of 1kW is used to meet the source power of 1kW. Supply currents are balanced and sinusoidal even in this case with DSOGI algorithm.

5.2.3 Performance analysis with AVSF Controller

The performance of the Adaptive Volterra Second Order Filter (AVSF) based control scheme is designed and modelled under changing load conditions and changing solar irradiation conditions.

5.2.3.1 Performance under changing load conditions

The performance analysis under changing load conditions i.e, linear, non-linear

and mixed loading conditions are analyzed with steady state voltage and current waveforms of v_{sabc},i_{sabc} ,i_{Labc} ,i_{fabc} in Fig. 5.26. From 0.1s to 0.2s, the non-linear load conditions are there and the source current of 19A is used to meet the load demand of 19A. The source currents are observed to be sinusoidal and balanced. The compensator currents from the SAPF cancels the harmonics injected in to the source by the load. The source current THD under non-linear load conditions is 0.84% with load THD of 20.26% as shown in Fig. 5.27.

From 0.2s to 0.3s, the linear load is added and mixed loading conditions are created and it is found that the source current increases to 24A to meet the corresponding load demand. The source currents are observed to be sinusoidal and balanced. The source current THD has been improved to 0.61% shown in Fig. 5.28. The DC link voltage

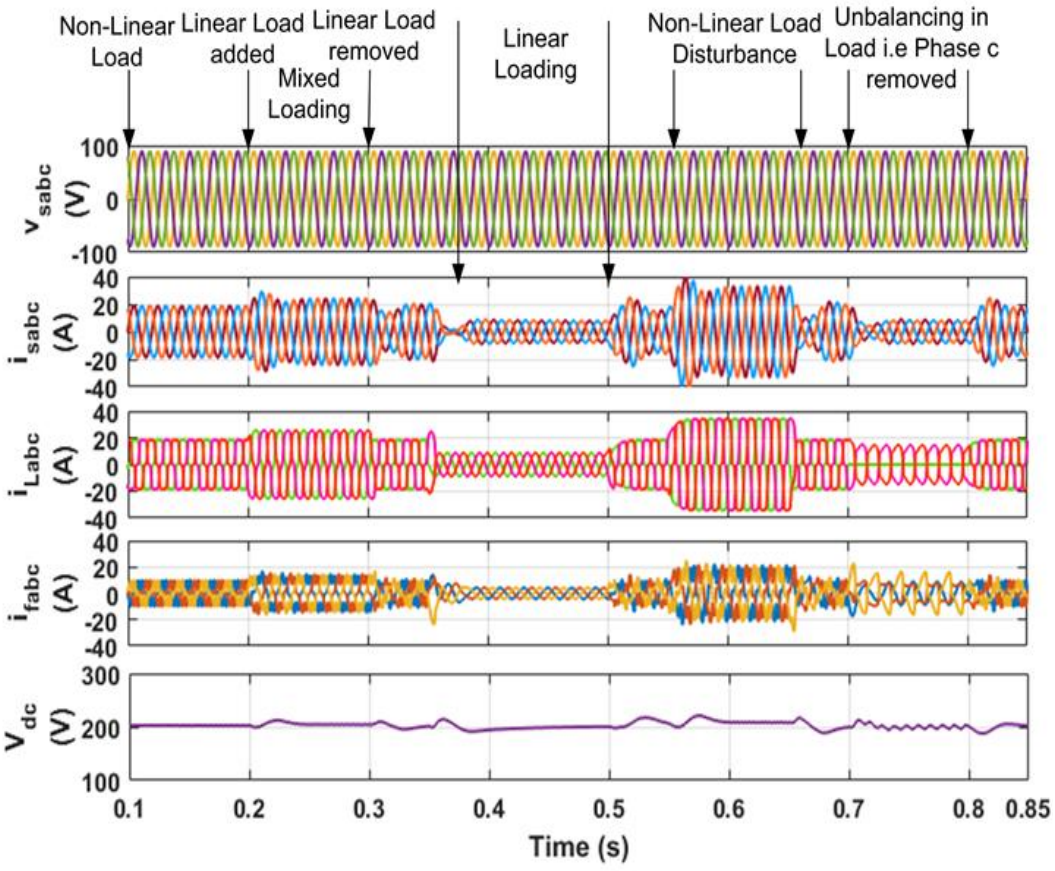

Fig. 5.26. Steady state waveforms of AVSF controller under changing load conditions in simulink

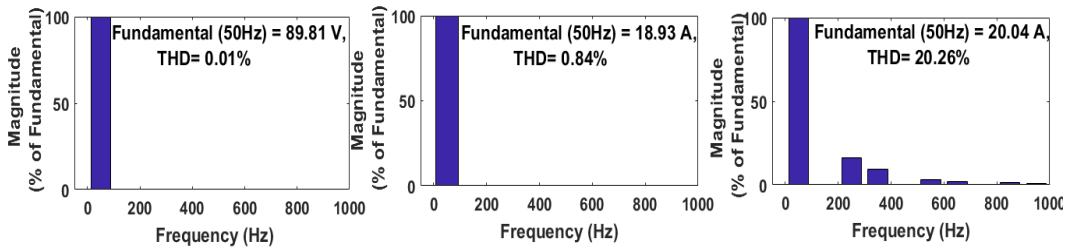

(a) (b) (c)

Fig. 5.27. THD of AVSF controller for (a) source voltage (v_{sabc}) (b) source current (i_{sabc}) and (c) load current (i_{Labc}) under non-linear load conditions in simulink

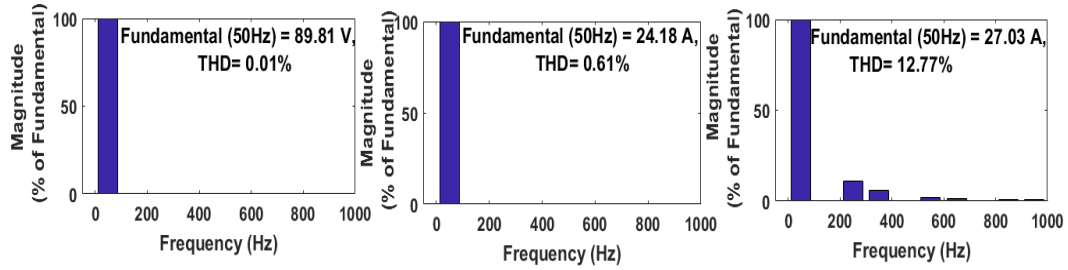

(a) (b) (c)

Fig. 5.28. THD of AVSF controller for (a) source voltage (v_{sabc}) (b) source current (i_{sabc}) and (c) load current (i_{Labc}) under mixed loading conditions in simulink

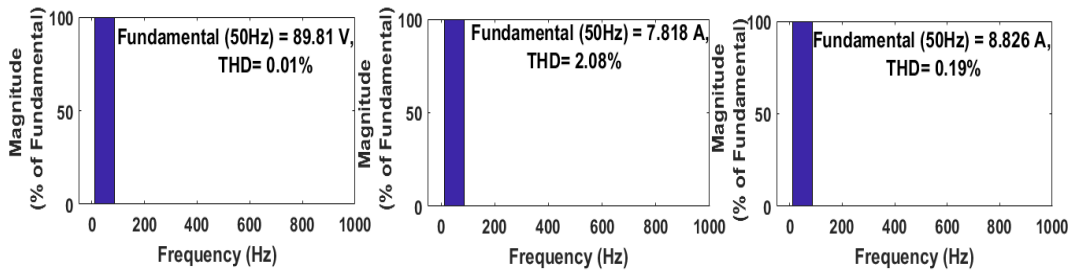

(a) (b) (c)

Fig. 5.29. THD of AVSF controller for (a) source voltage (v_{sabc}) (b) source current (i_{sabc}) and (c) load current (i_{Labc}) under linear loading conditions in simulink

shows slight dip and rise of 1V under instant of load addition and removal and attains its steady state value of 200V with in half cycle. After 0.3s, the normal non-linear load conditions are attained and the load current attains the value of 19A.

From 0.35s to 0.5s, the linear loading is there it is found that the source current and load current both are sinusoidal and balanced. The source current of 8A is used to meet the corresponding load demand. The source current THD under linear load conditions are

2.08%. shown in Fig. 5.29. The DC link voltage is maintained at reference value of 200 V.

From 0.55s to 0.65s, the non-linear load disturbance is added and the source current increases to 33A to meet the corresponding load demand. Again for 0.5s, the original non-linear load conditions are attained. The DC link voltage shows dip and rise when non-linear load disturbance is added and removed. It maintains the DC link voltage to approximately 200V reference value as desired.

From 0.7s to 0.8s, the unbalancing in load is created and it is observed that the source current magnitude decreases to 14A to meet the load demand. The source currents

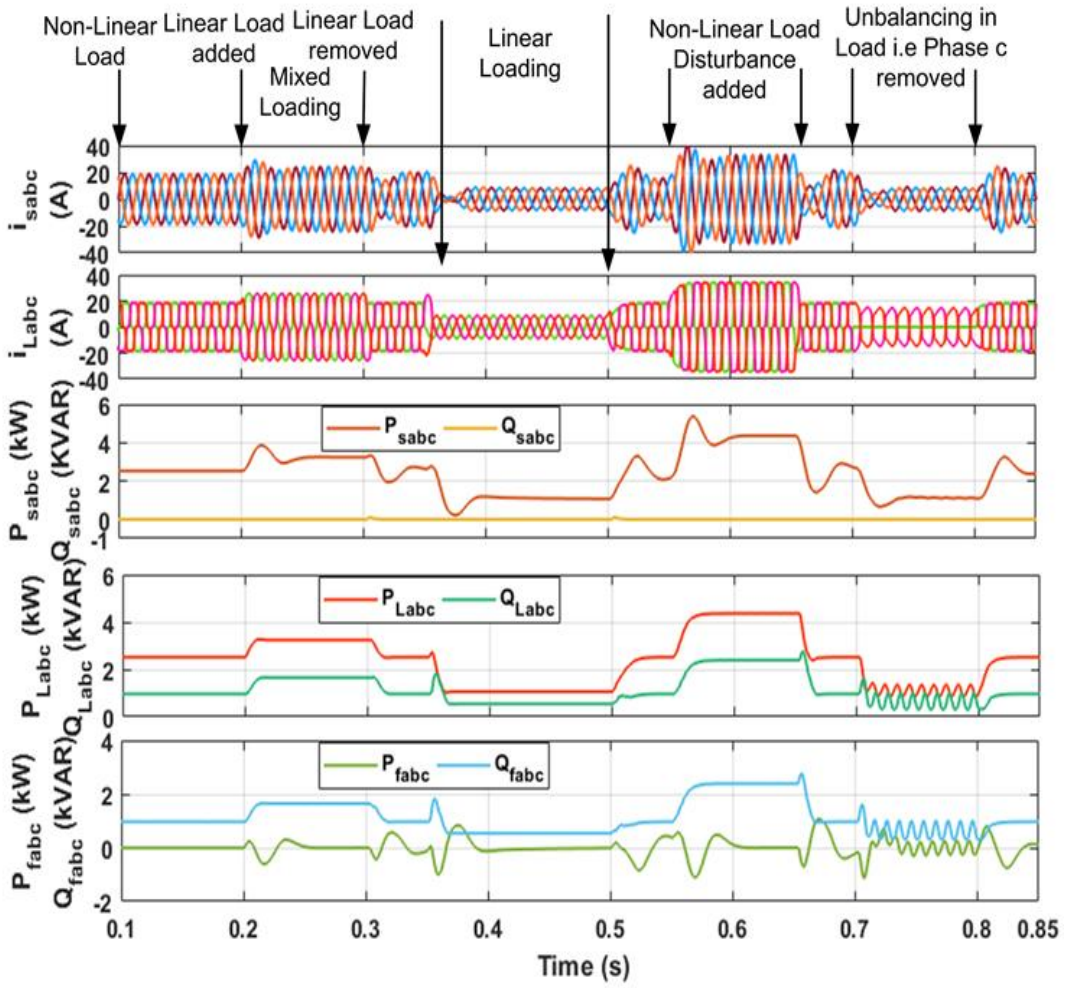

Fig. 5.30. Steady state power waveforms of AVSF controller under changing load conditions in simulink

are observed to be sinusoidal and balanced. The DC link voltage shows continuous oscillations of small magnitude under unbalancing conditions.

The steady state analysis of power waveforms under changing load conditions are shown in Fig. 5.30. The results show the sharing of power between source, load and compensator. Under non-linear load conditions till 0.2s, the load active power of 2.520 kW is met by the source active power. The reactive power demand of load is met by the compensator.

Under mixed loading conditions from 0.2s to 0.3s, the load active and reactive demand is increased which is met by the source power of 3.240 kW and the compensator provides reactive power of 1.650kVAR.

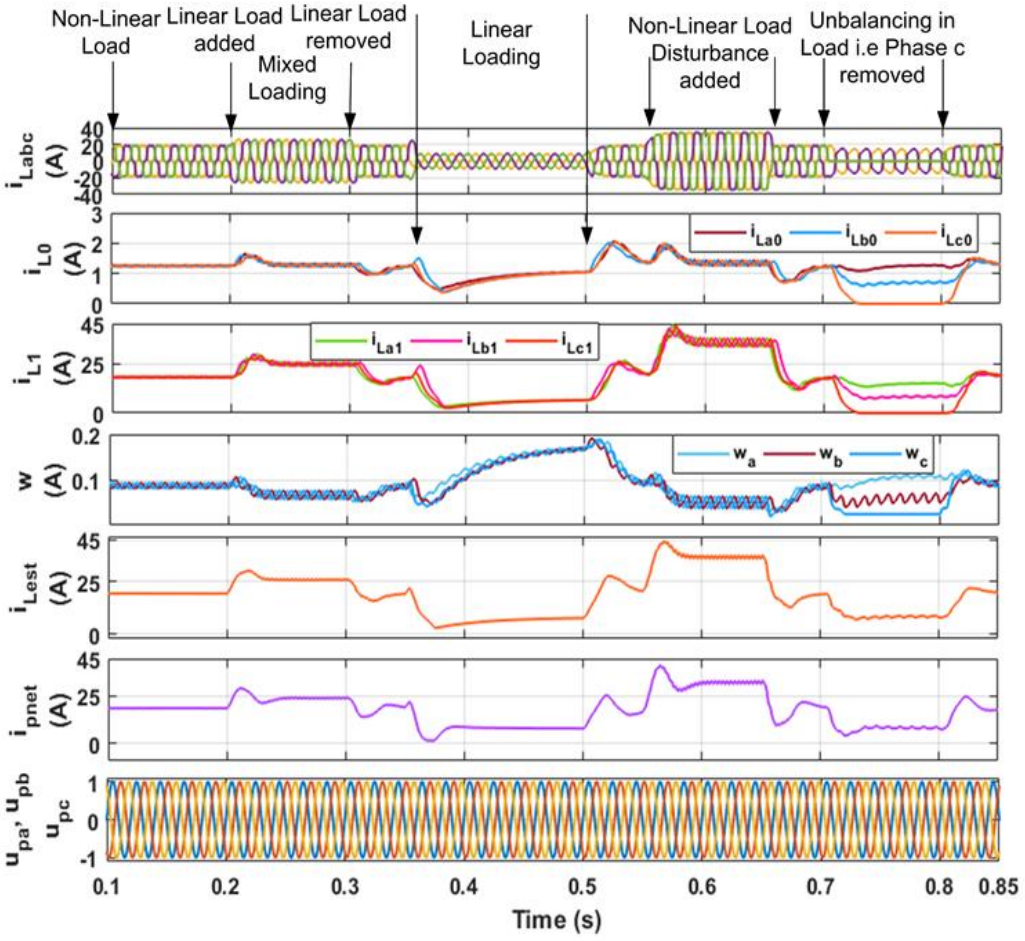

Fig. 5.31. Steady state intermediate waveforms of AVSF controller under changing load conditions in simulink

Under non-linear load disturbance added from 0.55s to 0.65s, the load active power and reactive power demand again increases which is met correspondingly by the source active power of 4.365kW and compensator reactive power of 2.390kVAR.

Under unbalanced load conditions simulated from 0.7s to 0.8s, the load active power of 1kW is met by the source, The reactive power load demand of 0.8kVAR is met by the compensator.

Figure 5.31 shows the intermediate waveform of i_{Labc} i_{L0},i_{L1} ,i_{Lest} ,i_{pnet} , w and unit in phase templates u_{pa} , u_{pb} and u_{pc} of AVSF controller under changing load conditions. The i_{L0} and i_{L1} are the expansion components of the algorithm for estimating the fundamental load current. The expansion components are regularly updated by the weights of the LMS algorithms to get the accurate estimate of the load current. The i_{pnet} is the total load current used to estimate the reference sinusoidal current by multiplying it with the unit-in phase templates in each phase. The unit-in phase templates are the sinusoidal waveforms obtained from PCC voltages itself.

Table 5.3 shows the THD values obtained in simulink with AVSF algorithm under various loading conditions i.e., non-linear load, linear load and mixed loading conditions.

Table 5.3. THD values obtained in simulink with AVSF algorithm under various loading conditions

Loading Conditions	Adaptive Volterra Second Order Filter (AVSF)		
	i_L(THD)	i_S(THD)	v_s(THD)
Non-Linear Load	20.26%	0.84%	0.01%
Mixed Load	12.77%	0.61%	0.01%
Linear Load	0.19%	2.08%	0.01%

5.2.3.2. Performance under changing PV irradiation conditions

The steady state waveforms of $G(I_{irr})$, P_{pv}, v_{sabc},i_{sabc} ,i_{Labc} ,i_{fabc} for changing PV irradiation conditions of 1000W/m^2 and 400W/m^2 under non-linear load conditions is shown in Fig. 5.32. The source current of 19A is used to meet the load current of 19 A under normal non-linear load conditions. The source currents are sinusoidal and balanced. The three Kyocera 250W PV array panels connected in series having a maximum power capacity of 750W at 1000W/m^2.Under solar irradiation conditions of 1000W/m^2, the source current has been reduced to 14A as the load current is shared by both the source current and the PV current. The source currents are observed to be sinusoidal and balanced. The THD of source current is improved to 1.44 % under non-linear load condition of 20 % shown in Fig. 5.33. Then under solar irradiation conditions of 400W/m^2, the source current increases to 17A and the PV current reduces to 3.5A to meet the load demand.

The steady state power sharing demand waveforms under changing PV irradiation conditions of 1000W/m^2 and 400W/m^2 is shown in Fig. 5.34. The Kyocera Solar PV panel has a capacity of 750W and is delivering 660W of active power at the DC link of

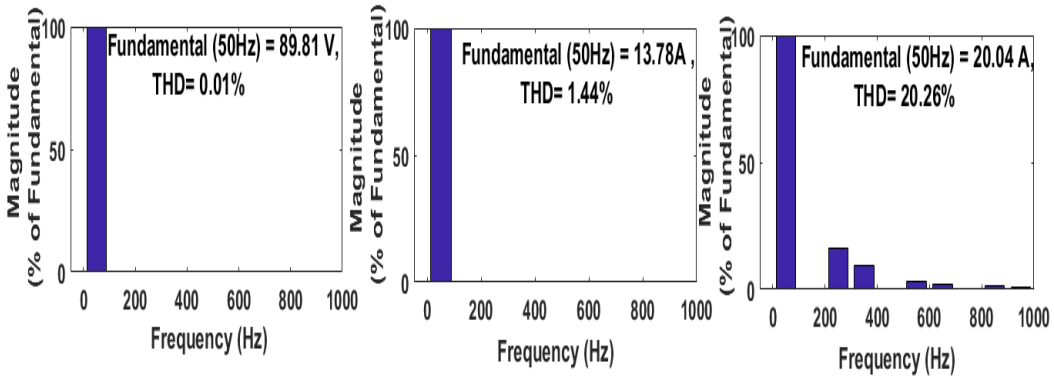

(a) (b) (c)

Fig. 5.33. THD of AVSF controller for (a) source voltage (v_{sabc}) (b) source current (i_{sabc}) and (c) load current (i_{Labc}) under changing solar irradiation with constant non-linear load conditions in simulink

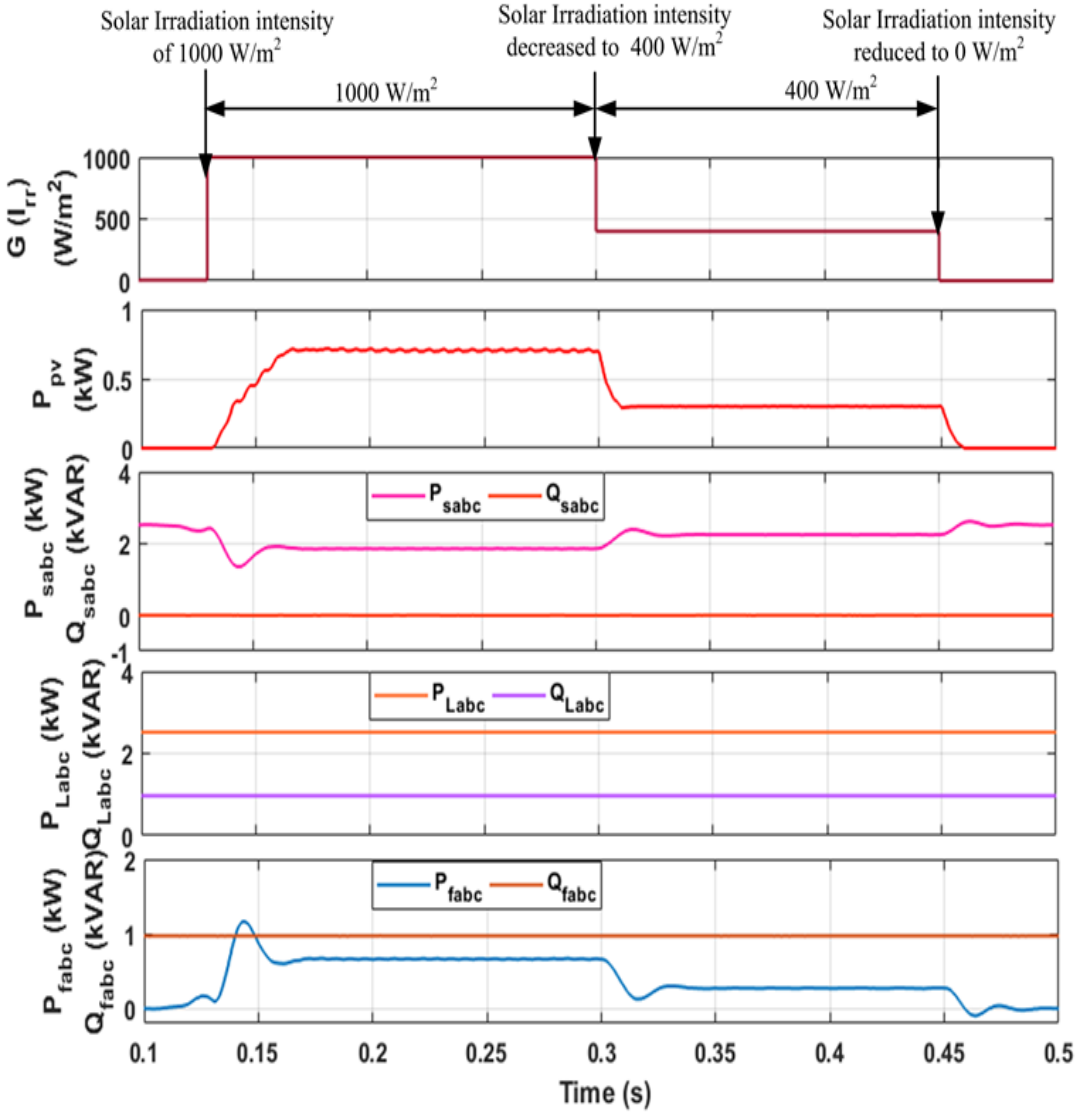

Fig. 5.34. Steady state power waveforms of AVSF controller under changing solar irradiation condition with constant non-linear load conditions in simulink

inverter. The source power of 2.520kW is used to meet the load demand. Under solar irradiation of 1000W/m^2, PV power of 0.66kW and the source power of 1.850kW is used to share the load power of 2.520kW. Under solar irradiation of 400W/m^2, the PV power has been decreased to 0.260kW and the source power has been increased to 2.260kW to meet the load power of 2.520kW. The reactive VAR of load is completely met by the compensator.

5.2.4 Performance analysis with CB-FEBAF Controller

The Cubic Bezier Functional Expansion Based Adaptive Filter based control scheme is designed and modelled for SAPF operation and its performance is tested under changing load conditions and changing solar irradiation conditions.

5.2.4.1 Performance under changing non-linear load conditions

The steady state waveforms for v_{sabc},i_{sabc} ,i_{Labc} ,i_{fabc} for performance analysis of control algorithm under varying load conditions are shown in Fig. 5.35. From 0.1s to 0.2 s under non-linear load conditions, 19A of grid current is used to meet the load demand. The source currents are observed to be sinusoidal and balanced. The THD of source currents are improved to 0.81% with non-linear load THD of 20.26 % as shown in in Fig. 5.36. The compensator has been designed to cancel the harmonics in source current injected by the non-linear load making it sinusoidal and balanced.

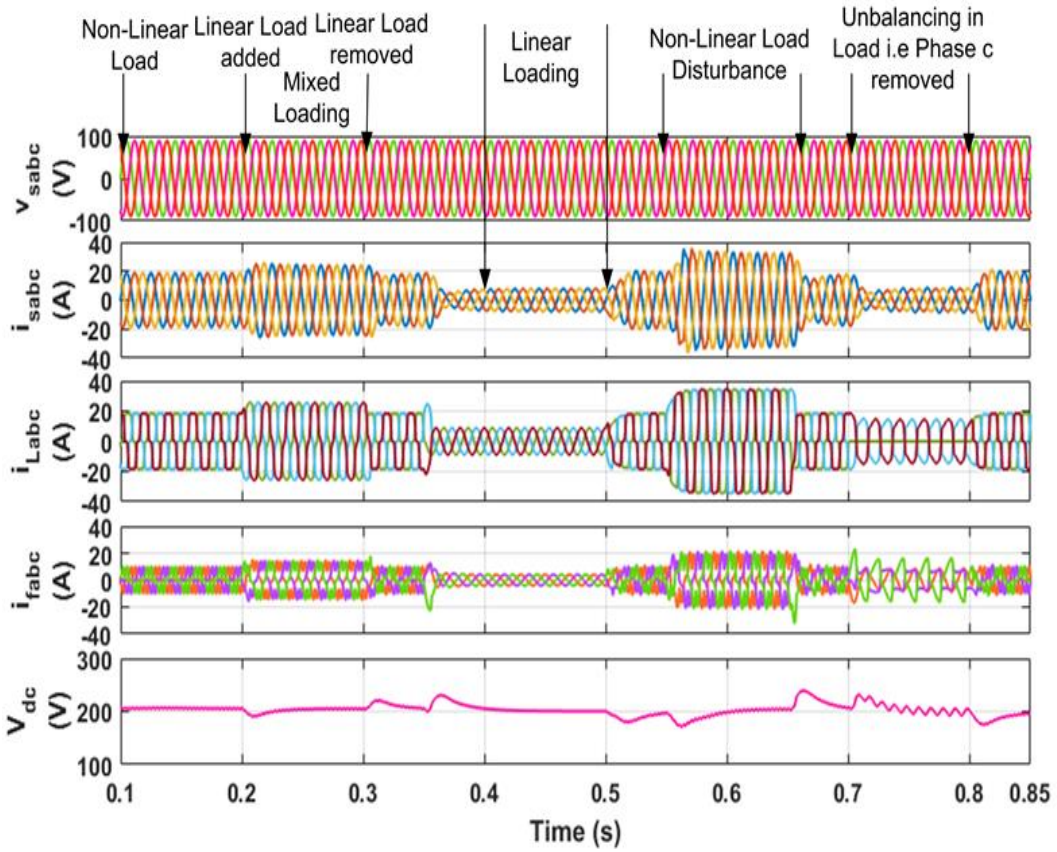

Fig. 5.35. Steady state waveforms of CB-FEBAF based controller under changing load conditions in simulink

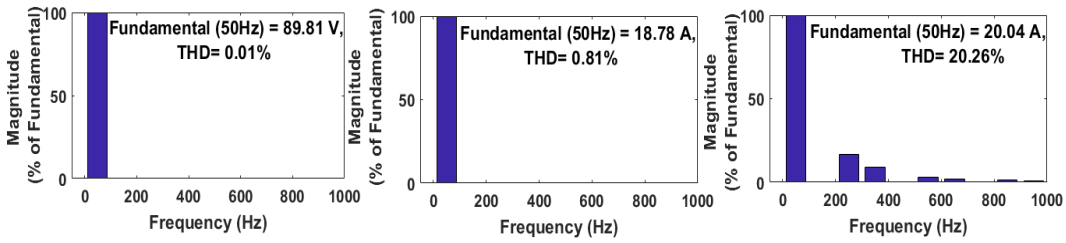

(a) (b) (c)

Fig. 5.36. THD of CB-FEBAF controller for (a) source voltage (v_{sabc}) (b) source current (i_{sabc}) and (c) load current (i_{Labc}) under non-linear load conditions in simulink

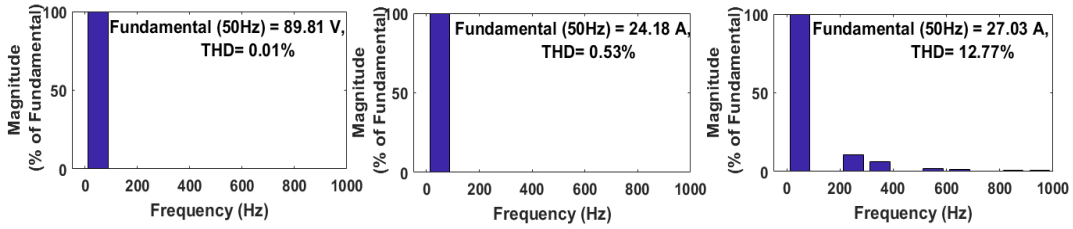

(a) (b) (c)

Fig. 5.37. THD of CB-FEBAF controller for (a) source voltage (v_{sabc}) (b) source current (i_{sabc}) and (c) load current (i_{Labc}) under mixed loading conditions in simulink

From 0.2s to 0.3s, the linear load is added and mixed loading conditions are created. The source current increases to meet the load demand. The source currents are sinusoidal and balanced and the THD of source current is found to be 0.53% under mixed loading THD of 12.77% shown in Fig. 5.37.

Linear loading is created from 0.35s to 0.5s, here both the source current and the load current are sinusoidal and THD of source current is 2.04% under linear load THD of 0.19% shown in Fig. 5.38.

Under non-linear load disturbance added from 0.55s to 0.65s, the source current increases to meet the load demand of 34A. The source currents remain sinusoidal and balanced.

Under unbalancing load conditions, the source current decreases to 14A to meet the load demand. The source currents remain sinusoidal and balanced.

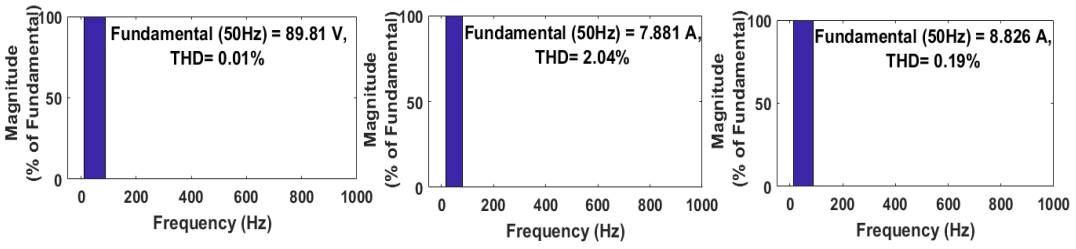

Fig. 5.38. THD of CB-FEBAF controller for (a) source voltage (v_{sabc}) (b) source current (i_{sabc}) and (c) load current (i_{Labc}) under linear load conditions in simulink

Figure 5.39 shows the steady state active power and reactive power balance between source, load and compensator. Under non-linear load conditions, the 2.520kW load power is met by the grid power. Under mixed loading conditions the source power increases to 3.240kW to meet the load power. The reactive power of load corresponding to 1.650kVAR is met by the compensator.

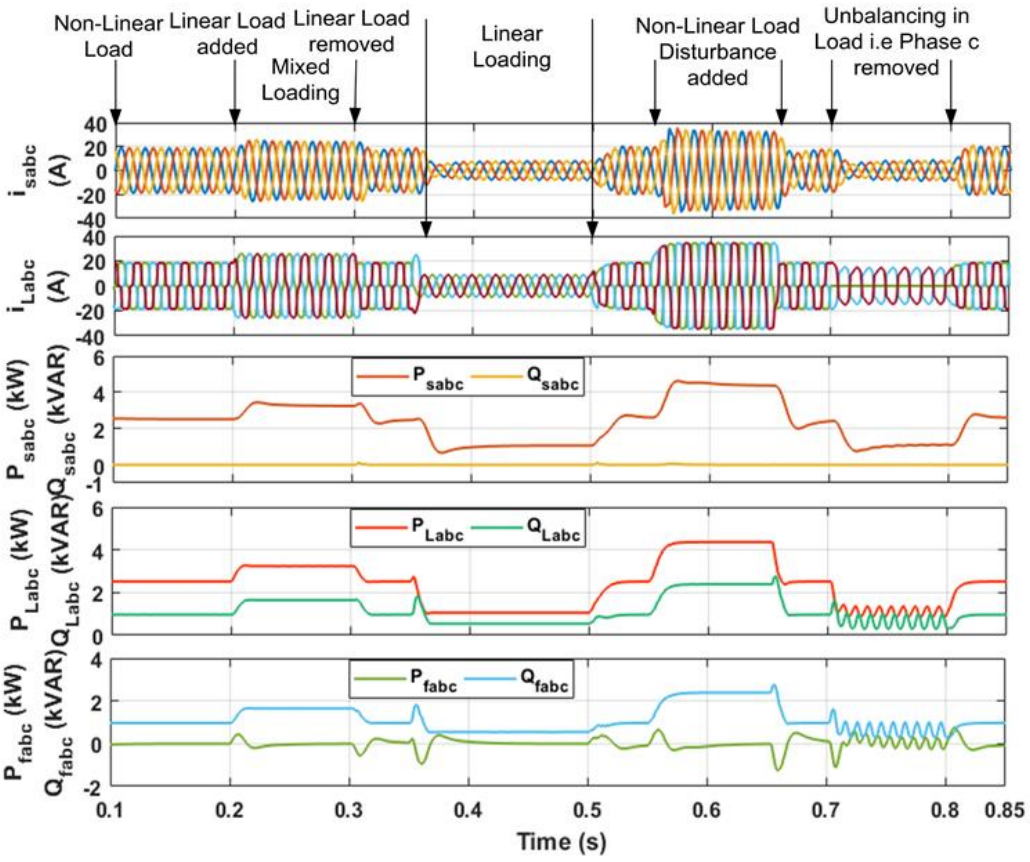

Fig. 5.39. Steady state power waveforms of CB-FEBAF controller under varying load conditions in simulink

Under linear load conditions the load power of 1.055kW is met by the source and the reactive power of 545VAR is met by the compensator.

Under non-linear load disturbance the source power increases to 4.365kW to meet the load demand. The load reactive VARs are met by the compensator.

Figure 5.40 shows the intermediate waveforms of the CB-FEBAF algorithm i_{Labc} i_{L0},i_{L1}, i_{L2}, i_{L3}, i_{Lest} ,i_{pnet} , w for its performance analysis under changing load conditions. The expansion components $i_{L0}, i_{L1}, i_{L2}, i_{L3}$ are used for estimating the fundamental component of the load current. The contribution of expansion components

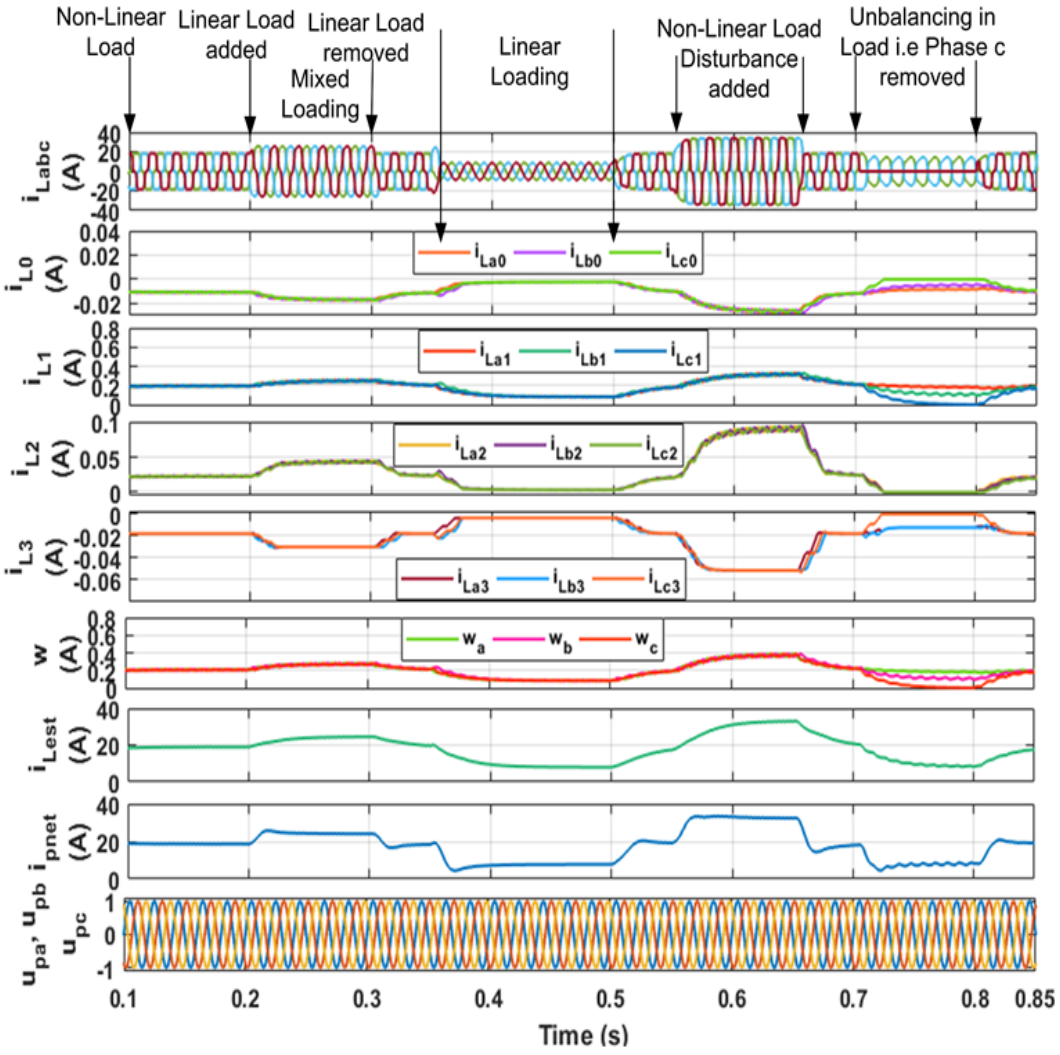

Fig. 5.40. Steady state intermediates waveforms of CB-FEBAF controller under changing load conditions in simulink

i_{L0}, i_{L3} is quite less so they can be neglected and i_{L1}, i_{L2} are sufficient in estimating the fundamental component of the load current. The expansion components are updated by weight components of the least mean square (LMS) algorithm in real time under changing load conditions. This real time and online training help to estimate the fundamental component of the load current accurately. The i_{pnet} is the total load current considering the estimated load current and the switching losses current estimated from the DC link PI controller. u_{pa} , u_{pb} and u_{pc} are the unit -in-phase sinusoidal templates obtained from the PCC voltages algorithm for generating reference currents.

Table 5.4 shows the THD values obtained in Simulink with CB-FEBAF under various loading conditions i.e., non-linear load, linear load and mixed loading conditions

Table 5.4. THD values obtained in simulink with CB-FEBAF under various loading conditions

Loading Conditions	Cubic Beizer Functional Expansion Based Adaptive Filter (CB-FEBAF)		
	i_L(THD)	i_S(THD)	v_s(THD)
Non-Linear Load	20.26%	0.81%	0.01%
Mixed Load	12.77%	0.53%	0.01%
Linear Load	0.19%	2.04%	0.01%

5.2.4.2 Performance under varying solar irradiation conditions

The steady state waveforms for non-linear under changing PV irradiation conditions of 0W/m^2, 400W/m^2 and 1000W/m^2 is shown in Fig. 5.41. Under non-linear load conditions source current of 19A is used to meet the load demand of 19A. The three Kyocera 250 W PV array panels connected in series having a maximum power capacity of 750W at 1000W/m^2.Under PV irradiation intensity of 1000W/m^2, the source current decreases from 19A to 14A as the remaining current will be provided by PV to share the

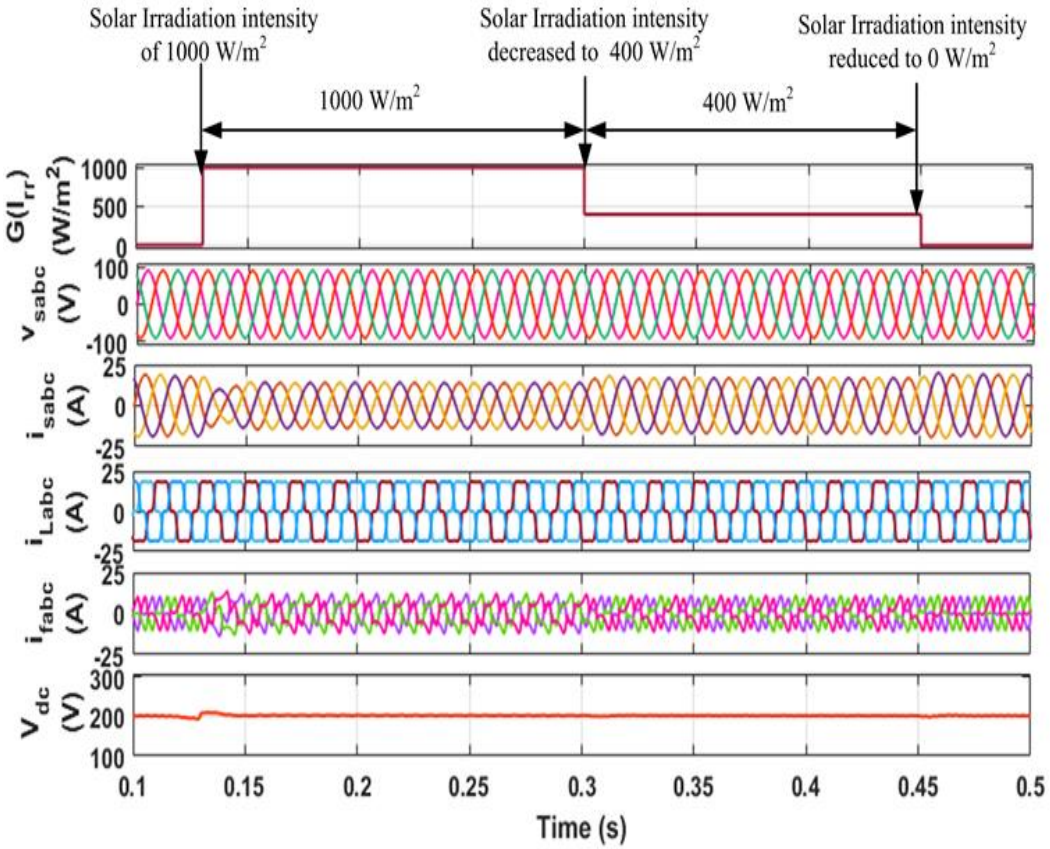

Fig. 5.41. Steady state waveforms of CB-FEBAF controller under changing solar irradiation with constant non-linear load conditions in simulink

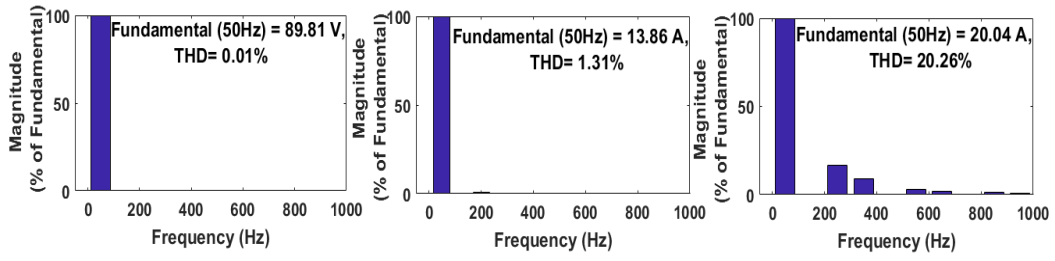

(a) (b) (c)

Fig. 5.42. THD of CB-FEBAF controller for (a) source voltage (v_{sabc}) (b) source current (i_{sabc}) and (c) load current (i_{Labc}) under changing solar irradiation with constant non-linear load conditions in simulink

load demand. The source currents are observed to be sinusoidal and balanced. The DC link voltage is maintained at 200V. The THD of source current is improved to 1.31 % under non-linear load condition of 20.26 % shown in Fig. 5.42. Under PV irradiation intensity of 400W/m^2, the grid current increases to 17A and PV current decreases to

meet the load demand of 24A still it is observed that the source currents are sinusoidal and balanced. The DC link voltage is maintained to reference set value of 200 V.

The steady state sharing of load under changing PV irradiation conditions is shown in Fig. 5.43. Under non-linear load conditions, 2.520kW is used to meet the load demand of 2.520kW. The Kyocera Solar PV array has a capacity of 750W and it delivers 660W of active power at the DC link of inverter. Under PV irradiation intensity of 1000 W/m^2, the load power of 1.850kW is shared by the grid power and PV power of 0.6kW. Under PV irradiation intensity of 400W/m^2, grid power increases to 2.260kW and the PV power decreases to 0.260kW to meet the load demand.

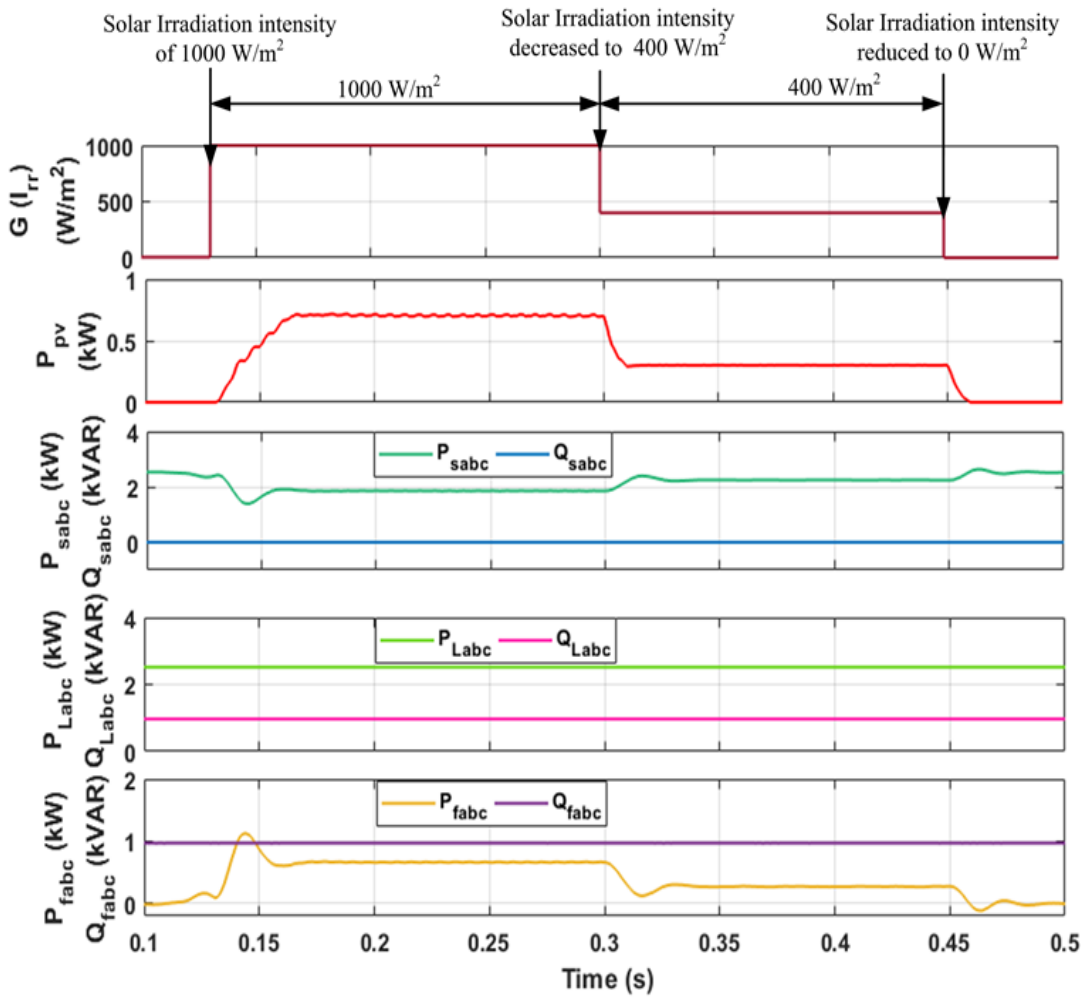

Fig. 5.43. Steady state power waveforms of CB-FEBAF controller under changing solar irradiation condition with constant non-linear load conditions in simulink

5.3 Hardware Results

This section discusses the hardware implementation results of SRFT, DSOGI, Adaptive Volterra Second Order Filter (AVSF) and Cubic Beizer Functional Expansion Based Adaptive Filter (CB-FEBAF) based controller for SAPF control. A hardware prototype of three-phase grid connected non-linear load system is developed in the laboratory using Microlab Box 1202 with and with-out PV interfaced systems. The hardware results are taken on power analyzer and DSO. The Chroma EN50530 Sandia PV array of maximum capacity 300W is interfaced at the DC link of inverter for testing PV interface results. The performance analysis under non-linear loading conditions for SAPF operation and SAPF with PV integration are studied for checking the effectiveness of these control algorithms.

5.3.1 Performance analysis with Three Phase SRFT Controller

The SRFT based control scheme is modelled in Microlab Box 1202 on hardware prototype developed on three-phase grid connected systems.

5.3.1.1 Performance under non-linear load conditions

Fig. 5.44 shows the hardware operation of SAPF on three-phase grid connected systems. The SAPF operation is performed at 40V, 50Hz supply feeding non-linear load. Fig. 5.44 shows the steady state performance results of voltage and current waveform under SAPF integrated grid connected systems. Figs. 5.44 (a-d) show the source voltage waveforms (v_{sabc}), load current waveforms (i_{Labc}), source current waveforms (i_{sabc}), source voltage THD, source current THD and load current THD. The source currents are observed to be sinusoidal and balanced. The source current THD is found to be 4.08% with SRFT algorithm under non-linear load conditions of 21.15% as shown in Fig. 5.44.

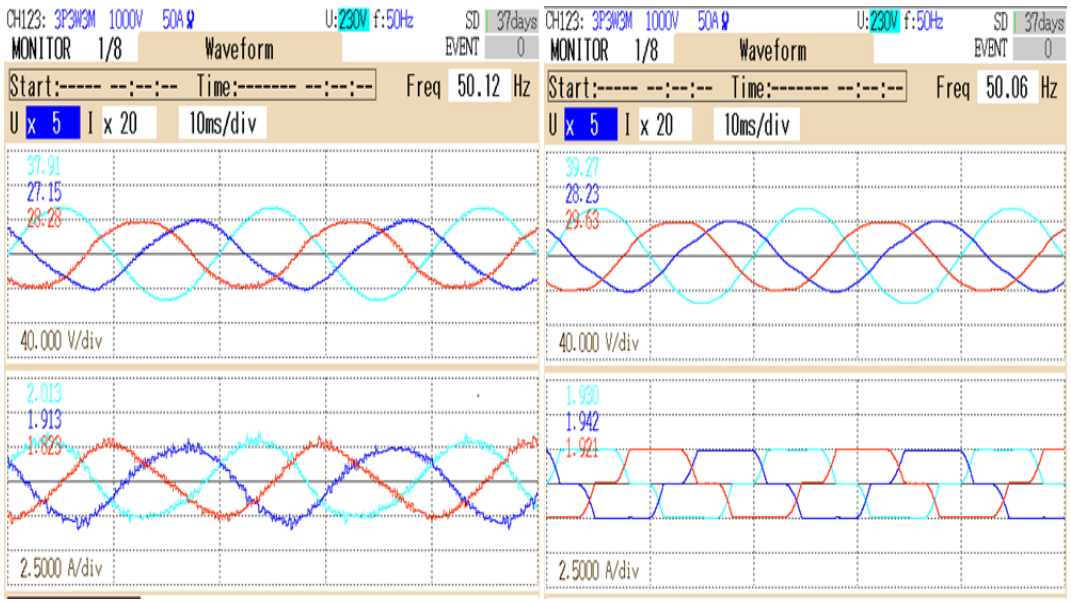

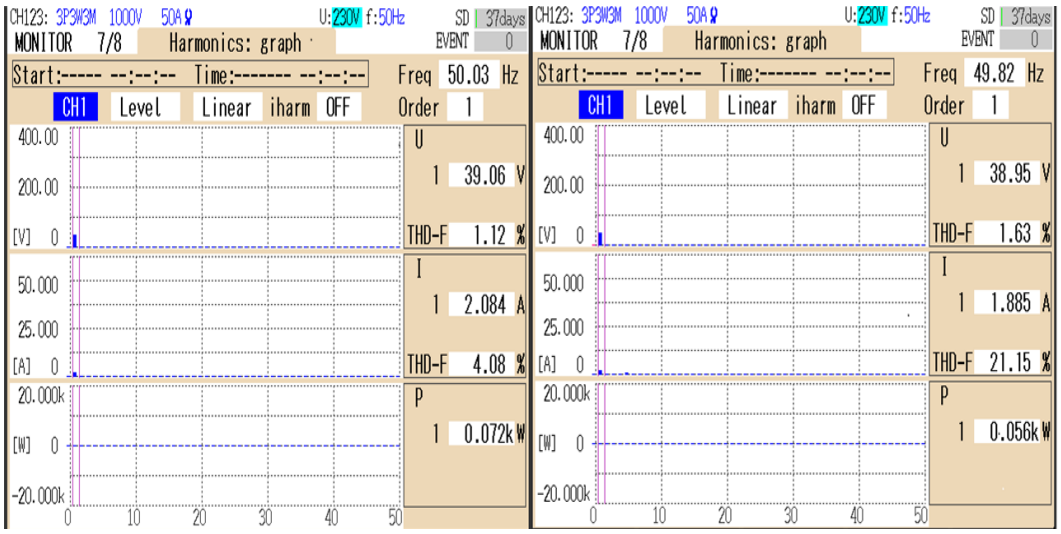

Fig. 5.44. Steady state experimental performance analysis of three phase SRFT controller under non-linear load conditions (a) source current waveforms (b) load current waveforms (c) source current THD (d) load current THD

5.3.1.2 Steady state power transfer under non-linear loading conditions

The steady state power transfer under non-linear load between source power (P_{sabc}), load power (P_{Labc}) and compensator power (P_{fabc}) is shown in Fig. 5.45. It is observed that the load active power of 98W is met by the source active power of 108W.

The reactive power of load of 31VAR is met by the compensator reactive power of 36 VAR.

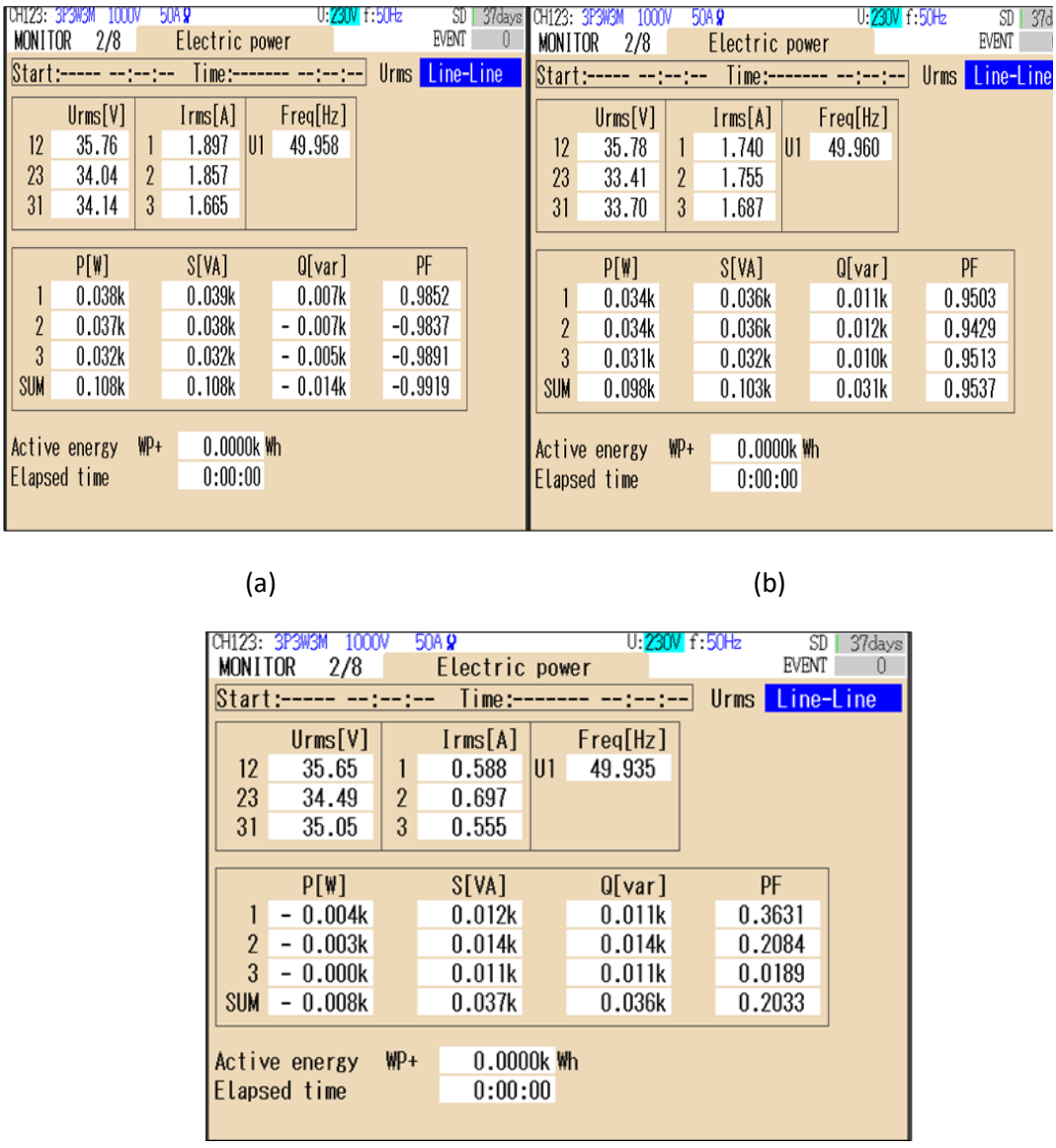

Fig. 5.45. Steady state experimental power analysis of three phase SRFT controller under non-linear load conditions (a) source power (P_{sabc}) (b) load power (P_{Labc}) and (c) compensator power (P_{fabc})

5.3.1.3 Dynamic Results with SRFT controller

Fig. 5.46 shows the dynamic results of SRFT algorithm under changing load conditions. Figs. 5.46 (a-b) show the waveform of source phase voltage (v_{sa}), load current (i_{La}), fundamental load current component (i_{Lest}), template ($\sin\theta$) under load decrease

and increase. The fundamental component is estimated accurately and decreases and increases with the corresponding load changes. The unit template obtained is perfectly sinusoidal. Figs. 5.46 (c-d) show the waveform of source phase voltage (v_{sa}), load

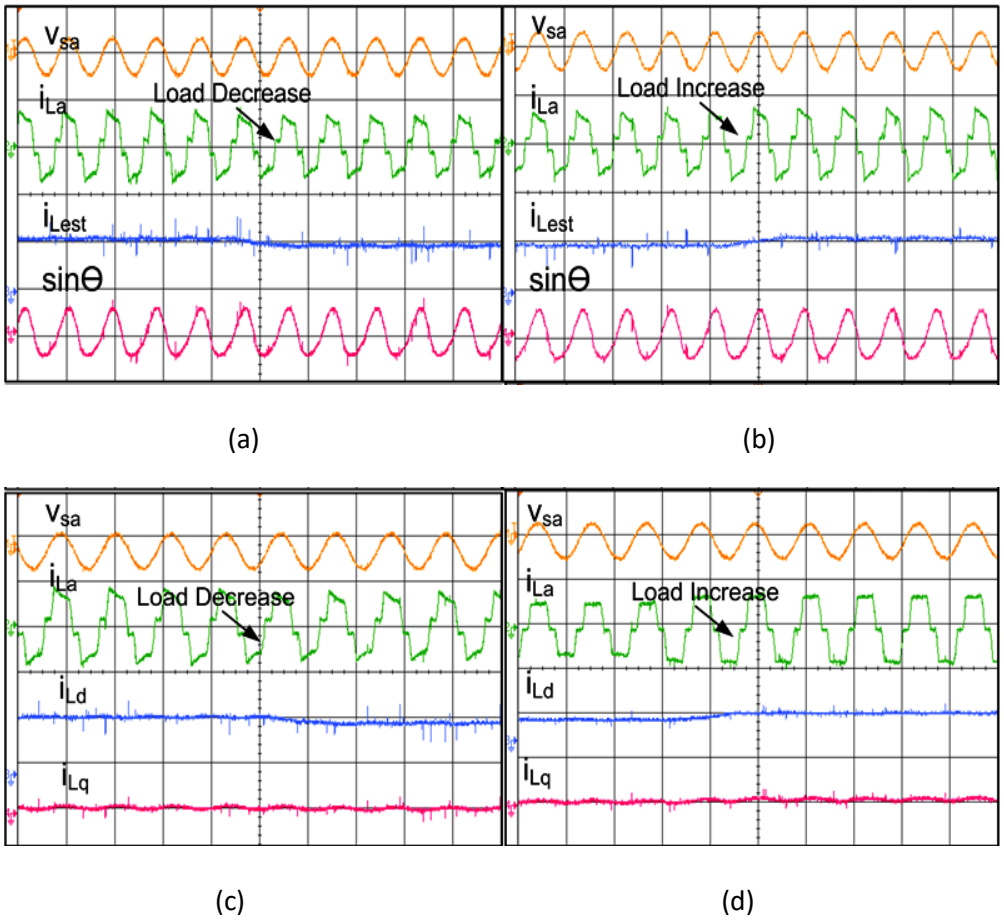

Fig. 5.46. Dynamic waveforms of three phase SRFT observed on oscilloscope (a-b) $v_{sa}(50\,V/div)$, $i_{La}\,(2\,A/div)\,i_{Lest}\,(1\,A/div)$, $sin\theta(2A/div)$ under load decrease and increase (c-d) $v_{sa}(50\,V/div)$, $i_{La}\,(\,2\,A/div)$, $i_{Ld}\,(1\,A/div)$, $i_{Lq}(2\,A/div)$ under load increase and decrease

current (i_{La}), fundamental load component (i_{Ld}), quadrature component (i_{Lq}) under load decrease and increase.

5.3.1.4 Steady state waveforms under PV integrated systems

Fig. 5.47 shows the hardware operation of SAPF on three-phase PV integrated grid connected systems. The SAPF operation is performed at 40V, 50Hz supply feeding non-linear load. Fig. 5.47 shows the steady state performance results of voltage and

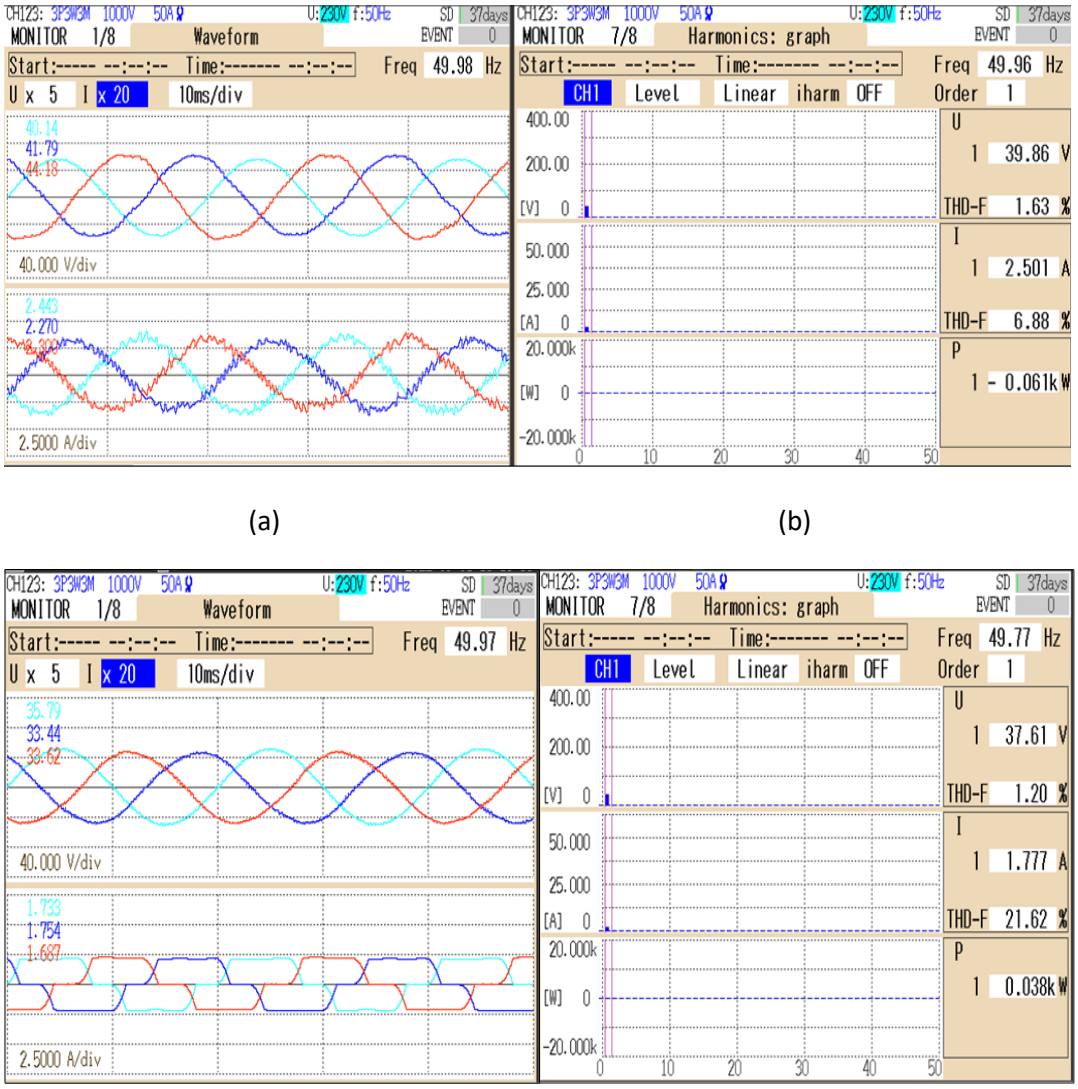

Fig. 5.47. Steady state experimental performance analysis of three phase SRFT controller under PV integrated non-linear load conditions (a) source current waveform (b) source current THD (c) load current waveform (d) load current THD

current waveform under SAPF PV integrated grid connected systems. Figs. 5.47 (a-d) shows the source voltages (v_{sabc}) waveforms, source current waveforms (i_{sabc}), source current THD, load current waveforms (i_{Labc}) and load current THD. It has been found that the source currents become 180° out of phase with the source voltage showing that the grid is absorbing active power. The source currents are observed to be sinusoidal and THD have been improved to 6.88% under non-linear load conditions of 21.62% with SRFT algorithm.

5.3.1.5 Steady state power transfer under PV integrated systems

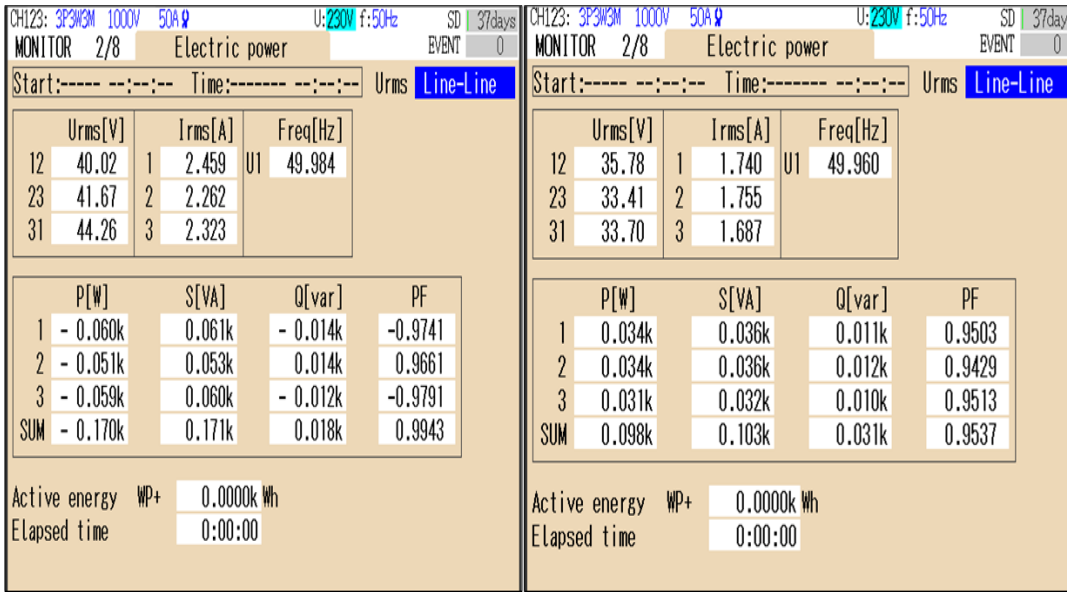

(a) (b)

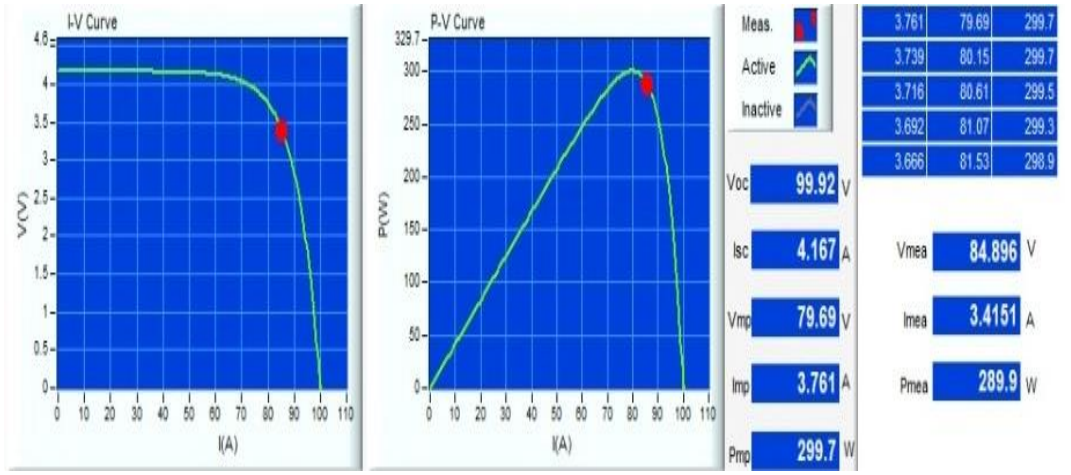

(c)

Fig. 5.48. Steady state experimental power analysis of three phase SRFT controller under PV integrated grid connected systems (a) source power (P_{sabc}) (b) load power (P_{Labc}) and (c) PV power (P_{fabc})

The PV model used for hardware testing is EN50530 with power capacity of 300W, which supplies 289.9W of active power. It has been observed that now the load demand is shared by the PV. Out of 289.9W of power given by the PV, 98W is used for meeting active power demand of load and remaining 170W is absorbed by the grid. These results are shown in Fig. 5.48.

5.3.2 Performance Analysis with DSOGI Controller

The Dual SOGI based control scheme is modelled in Microlab Box 1202 on hardware prototype developed in three-phase grid connected systems.

5.3.2.1 Performance under changing non-linear load conditions

Fig. 5.49 shows the hardware operation of SAPF on three-phase grid connected systems. The SAPF operation is performed at 40V, 50Hz supply feeding non-linear

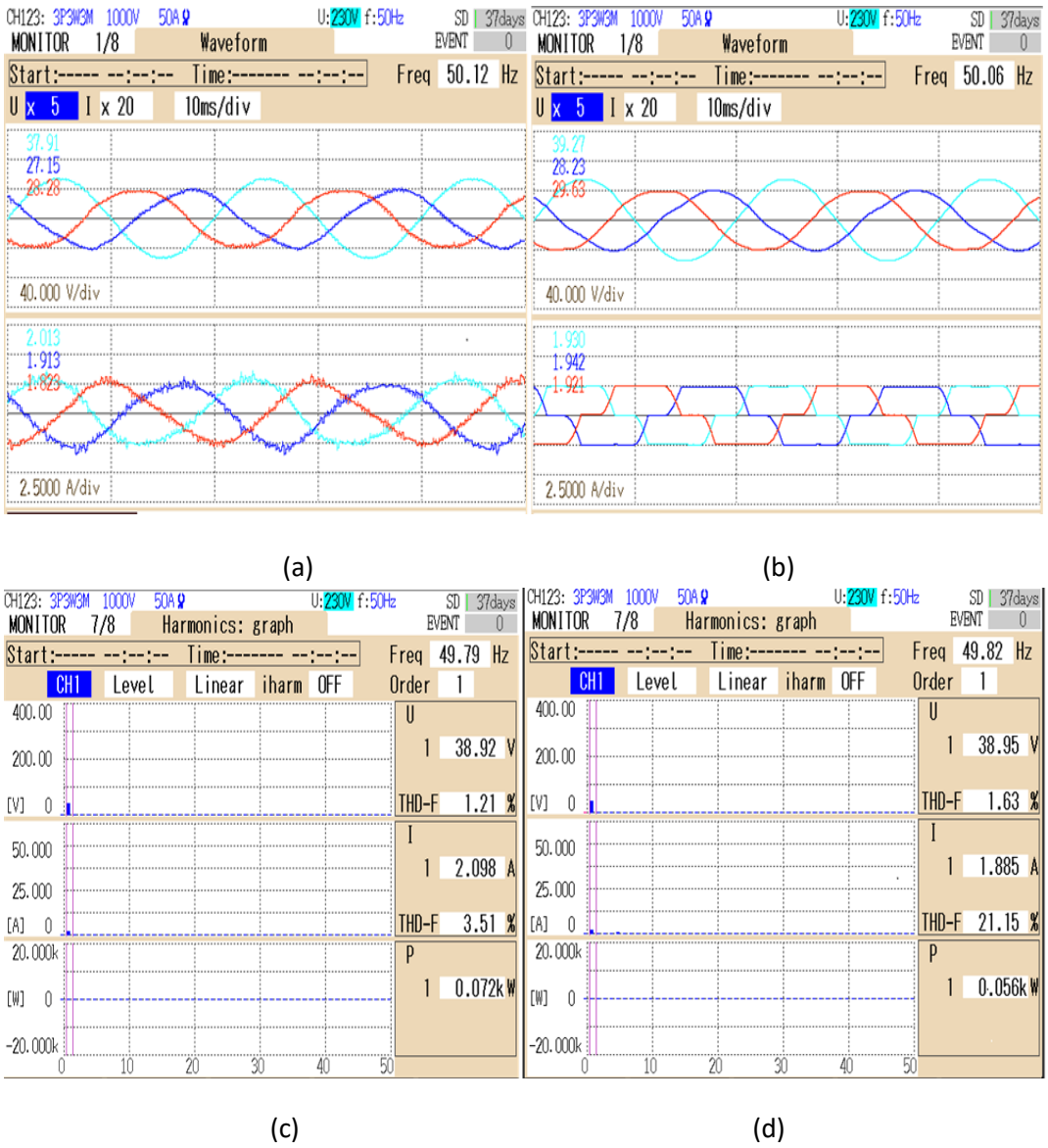

Fig. 5.49. Steady state experimental performance analysis of DSOGI controller under non-linear load conditions (a) source current waveform(b) load current waveform (c) source current THD (d) load current THD

load. Fig. 5.49 shows the steady state performance results of voltage and current waveform under SAPF integrated grid connected systems. Figs. 5.49 (a-d) show the source voltages waveforms (v_{sabc}), load current waveforms (i_{Labc}), source currents waveforms (i_{sabc}), source voltage THD, source current THD and load current THD. The source currents are observed to be sinusoidal and balanced. The source current THD is found to be 3.51% under non-linear load conditions of 21.15%.

5.3.2.2 Steady state power transfer under non-linear loading conditions

Fig. 5.50. Steady state experimental power analysis of DSOGI controller under non-linear loading conditions (a) source power (P_{sabc}) (b) load power (P_{Labc}) and (c) compensator power (P_{fabc})

The steady state power transfer under non-linear load between source power (P_{sabc}), load power (P_{Labc}) and compensator power (P_{fabc}) is shown in Fig. 5.50. The load active power of 98W is met by the source active power of 106W. The reactive power of load of 31VAR is met by the compensator reactive power of 36VAR.

5.3.2.3 Dynamic Results with DSOGI Controller

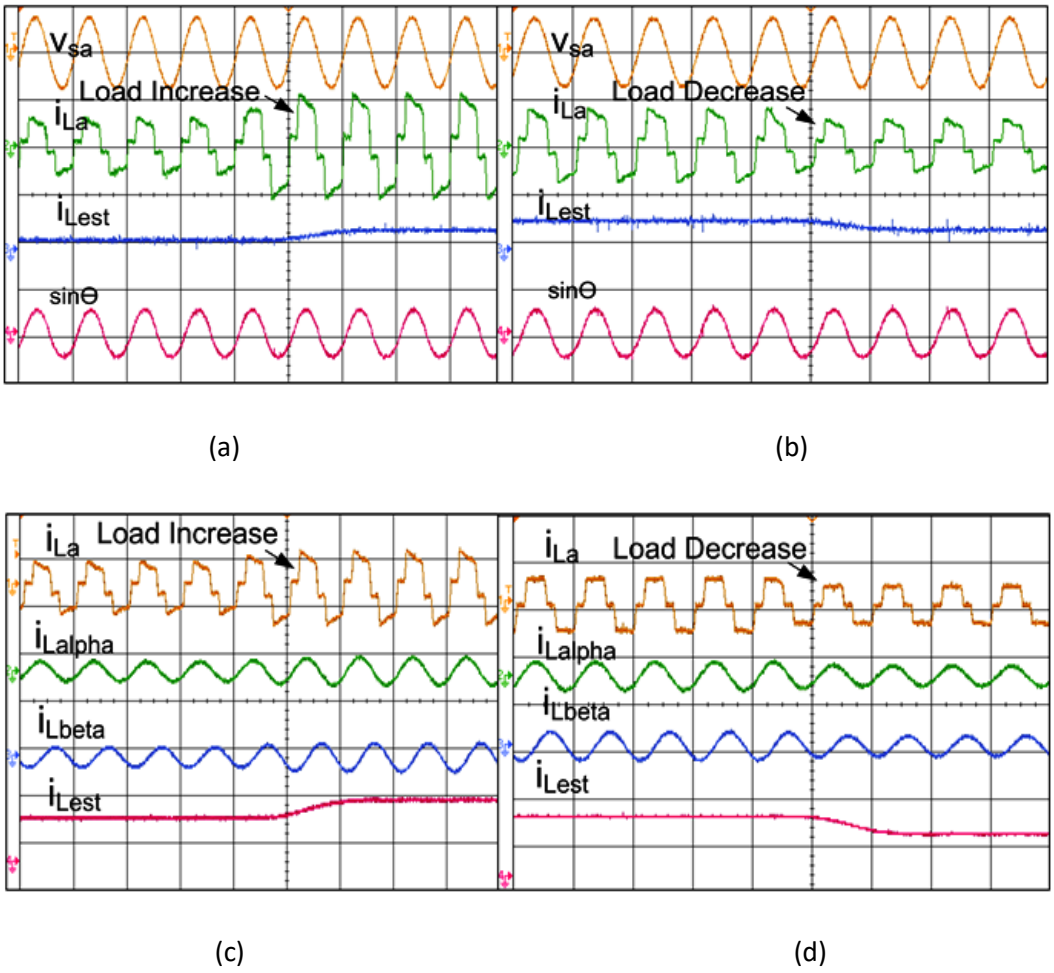

Fig. 5.51. Dynamic waveforms of DSOGI observed on oscilloscope (a-b) $v_{sa}(50\,V/div)$, $i_{La}\,(1A/div)$, $i_{Lest,}$(1A/div), $sin\theta\,(2A/div)$ under load decrease and increase (c-d) $i_{La}\,(1\text{A/div}), i_{Lalpha}\,(5\text{A/div})\; i_{Lbeta}\,(5A/div), i_{Lest}\,(2\,A/div)$under load increase and decrease

Fig. 5.51 shows the dynamic results of SOGI algorithm under changing load conditions. Figs. 5.51 (a-b) show the waveform of source voltage (v_{sa}), load current (i_{La}), fundamental load current component (i_{Lest}), unit-template (sinθ) under load

decrease and increase. The fundamental component is estimated and decreases and increases with corresponding load change. The unit template obtained is perfectly sinusoidal. Figs. 5.51 (c-d) show that the i_{Lalpha} is in phase with the source voltage and i_{Lbeta} is 90° out of phase with the voltage. The i_{Lest} is the active component of load current is obtained by taking the square of the magnitude of the i_{Lalpha} and i_{Lbeta}.

5.3.2.4 Steady state waveforms under PV integrated conditions

Fig. 5.52 shows the hardware operation of SAPF on three phase PV integrated grid

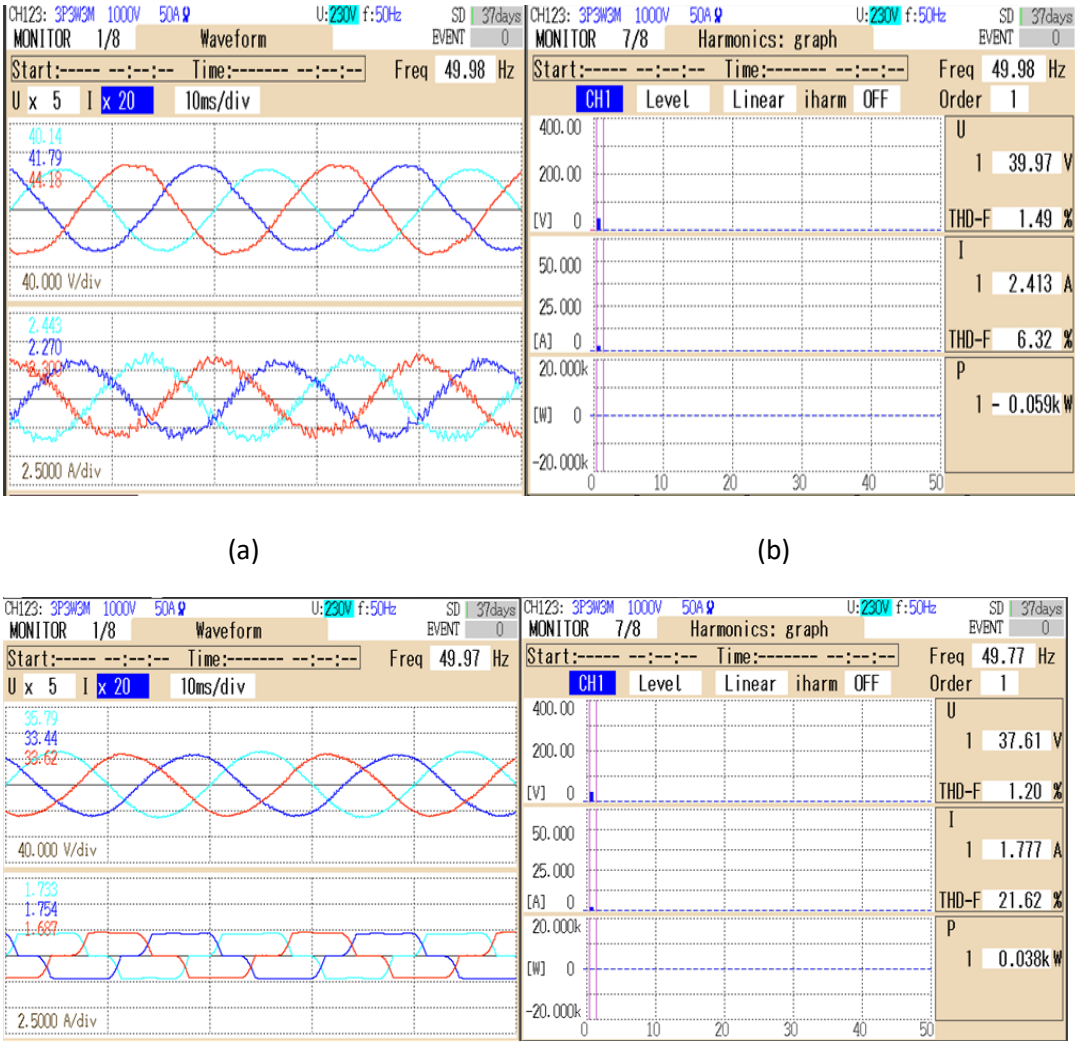

(a) (b)

(c) (d)

Fig. 5.52. Steady state experimental performance analysis of DSOGI controller under PV integrated non-linear load conditions (a) source current waveform (b) source current THD (c) load current waveform (d) load current THD

connected systems. The SAPF operation is performed at 40V, 50Hz supply feeding non-linear load. Fig. 5.52 shows the steady state performance voltage and current waveform results under SAPF PV integrated grid connected systems. Figs. 5.52 (a-d) show the source voltages (v_{sabc}) waveforms, source currents waveforms (i_{sabc}), source current THD and load current THD. It has been found that the source currents are 180° out of

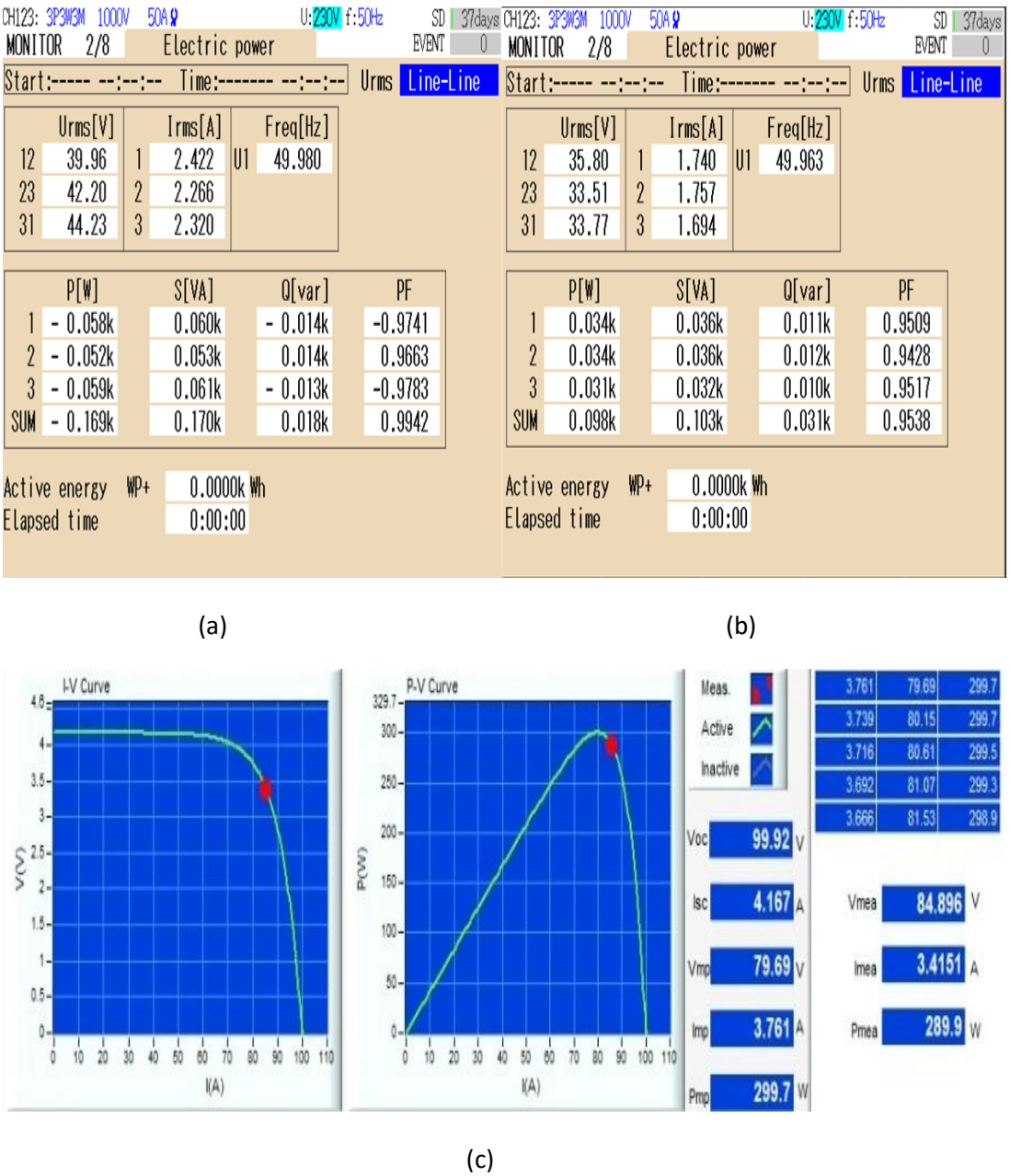

Fig. 5.53. Steady state experimental power analysis of DSOGI controller under PV integrated grid connected systems (a) source power (P_{sabc}) (b) load power (P_{Labc}) and (c) PV power (P_{fabc})

phase with the source voltage showing that the grid is absorbing active power. The source currents are observed to be sinusoidal and THD has been improved to 6.32% under non-linear load conditions of 21.62%.

5.3.2.5 Steady state power transfer under PV integrated conditions

The PV model used for testing is EN50530 with power capacity of 300W which supplies 289.9W of power. It has been observed in Fig. 5.53 that now the load demand is completely shared by the PV simulator. Out of 289.9W of power given by the PV simulator, 98W is used for meeting active power demand of load and remaining 169W is absorbed by the grid.

5.3.3 Performance analysis with AVSF Controller

The AVSF based control scheme is modelled in Microlab Box 1202 on hardware prototype developed in three-phase grid connected systems. The performance results are shown in Fig. 5.54.

5.3.3.1 Performance under changing non-linear load conditions

Fig. 5.54 shows the hardware operation of SAPF on three-phase grid connected systems. The SAPF operation is performed at 110V, 50Hz supply feeding non-linear load. Figs. 5.54 (a-d) shows the source voltages waveforms (v_{sabc}), load current waveform (i_{Labc}), source current waveforms (i_{sabc}), source voltage THD, source current THD and load current THD. The source currents are observed to be sinusoidal and balanced. The source current THD is found to be 3.07% under non-linear load conditions when load current has THD of 21.5%.

5.3.3.2 Steady state power transfer under non-linear loading conditions

The steady state power transfer under non-linear load between source power (P_{sabc}), load power (P_{Labc}) and compensator power (P_{fabc}) is shown in Fig. 5.55. The load active power of 98W is met by the source active power of 107W. The reactive power of load of 31VAR is met by the compensator reactive power of 38VAR.

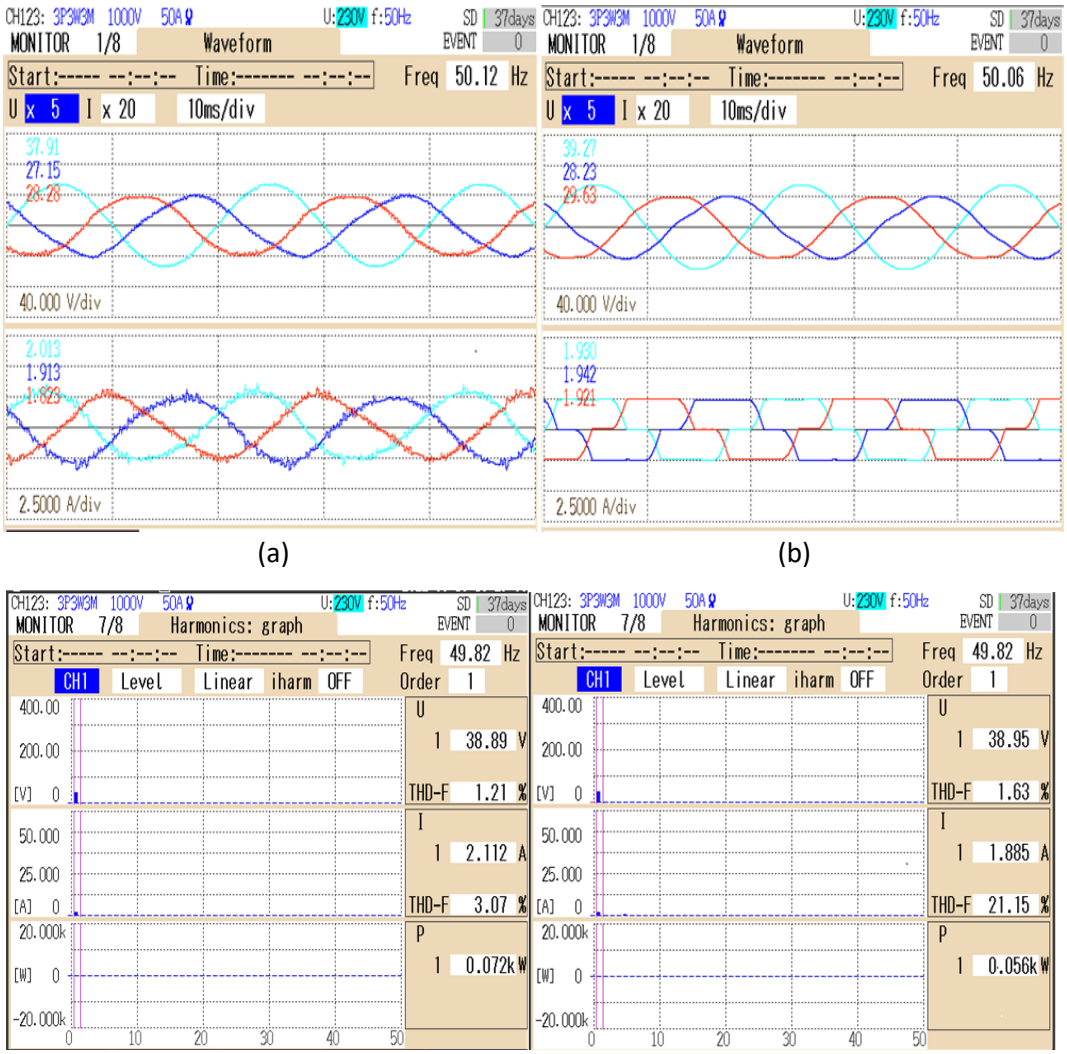

Fig. 5.54. Steady state experimental performance analysis of AVSF controller under non-linear load conditions (a) source current waveform (b) load current waveform (c) source current THD (d) load current THD

5.3.3.3 Dynamic Results with AVSF Controller

Fig. 5.56 shows the dynamic results of AVSF algorithm under changing load conditions. Figs. 5.56 (a-b) show the waveform of source voltage (v_{sa}), load current

(i_{La}), fundamental load current component (i_{Lest}), unit-template (sinθ) under load decrease and increase. The estimated load current also increases and decreases with the load change as shown below. The i_{La0} and i_{La1} are the expansion components of the algorithm used for estimating the fundamental load current. The expansion components are regularly updated by the weight of the LMS algorithm to get the accurate estimate of the load current. The i_{Laest} is the total estimated load current of phase 'a' used to estimate the reference sinusoidal current by multiplying it with the unit-in phase templates of phase 'a'. The error plot is also shown which shows the difference between the estimated and actual current.

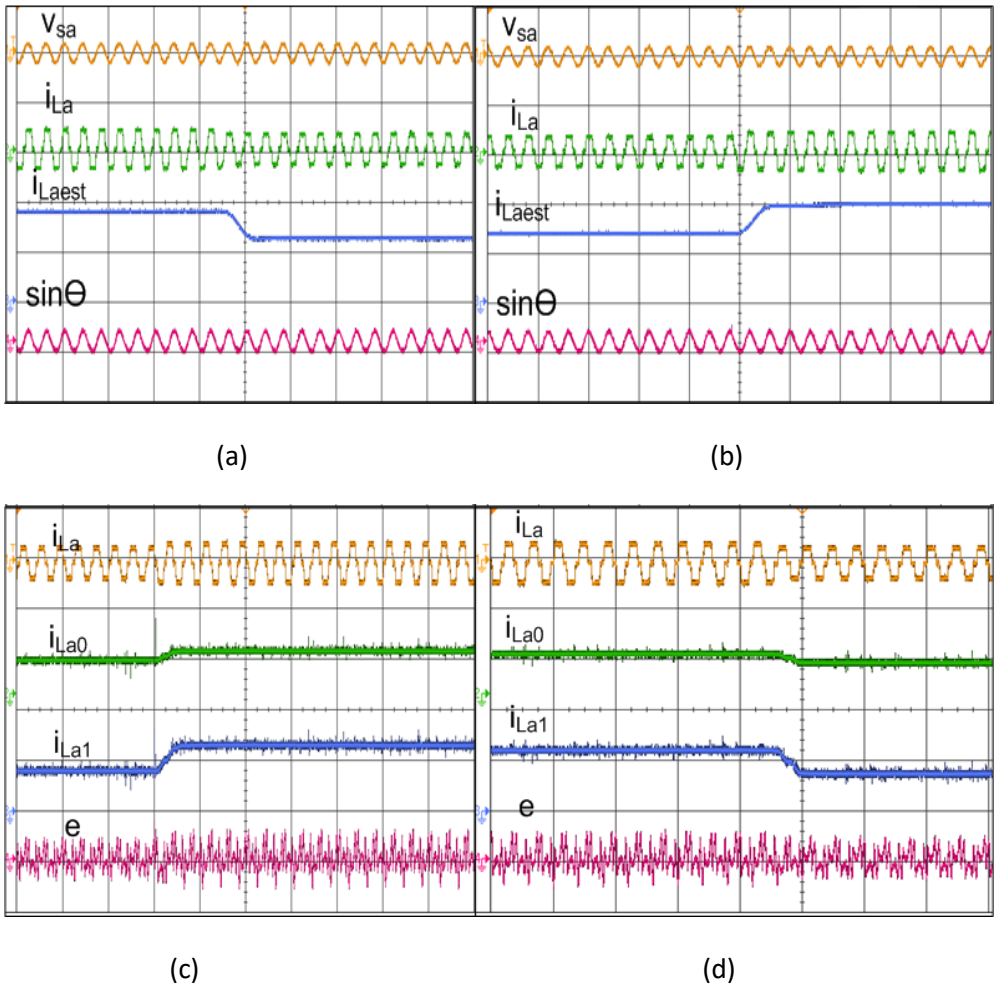

Fig. 5.56. Dynamic waveforms of AVSF controller observed on oscilloscope (a-b) $v_{sa}(50\,V/div)$, $i_{La}\,(2A/div)$, $i_{Lest}\,(1A/div), sin\theta$(2A/div) under load decrease and increase (c-d) $i_{La}\,(2A/div)$, $i_{L0a}\,(1\,A/div)$, $i_{L1a}\,(1A/div), e(1\,A/div)$ under load increase and decrease

5.3.3.4 Steady state waveforms under PV integrated conditions

Fig. 5.57 shows the hardware operation of SAPF on three-phase PV integrated grid connected systems. The SAPF operation is performed at 40V, 50Hz supply feeding non-linear load. Fig. 5.57 shows the steady state performance voltage and current waveform results under SAPF PV integrated grid connected systems. Figs. 5.57 (a-d) show the source voltage waveforms (v_{sabc}), source currents waveforms (i_{sabc}), source current

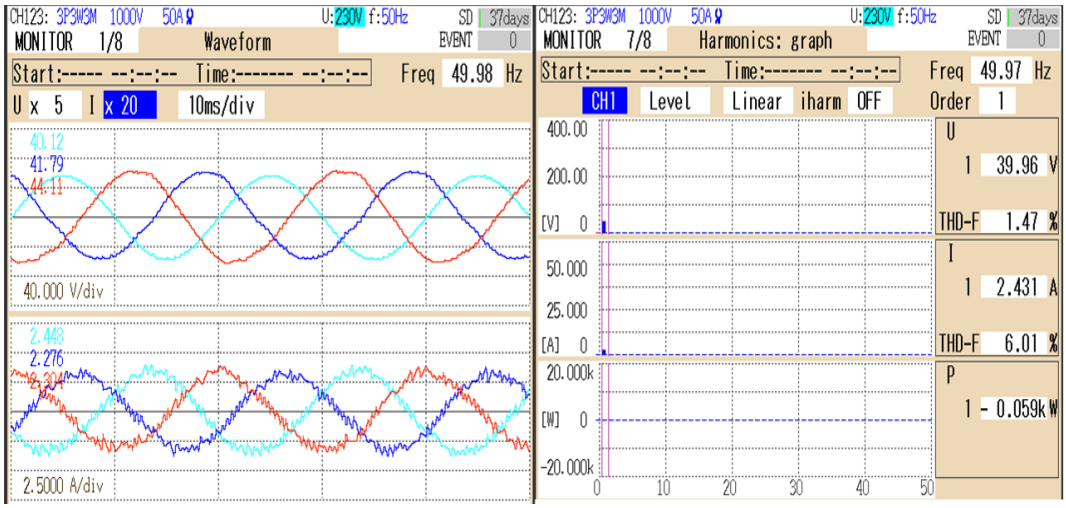

(a) (b)

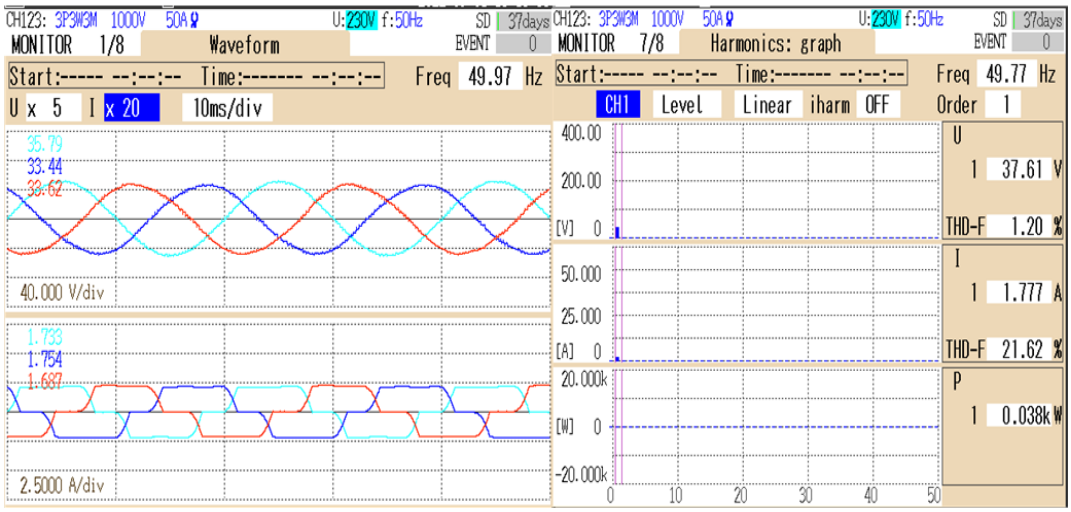

(c) (d)

Fig. 5.57. Steady state experimental performance analysis of AVSF controller under PV integrated non-linear load conditions (a) source current waveform (b) load current waveform (c) source current THD (d) load current THD

source current THD and load current THD. It has been found that the source currents are 180° out of phase with the source voltages showing that the grid is absorbing active power. The source currents are observed to be sinusoidal and THD has been improved to 6.01% under non-linear load conditions of 21.62%.

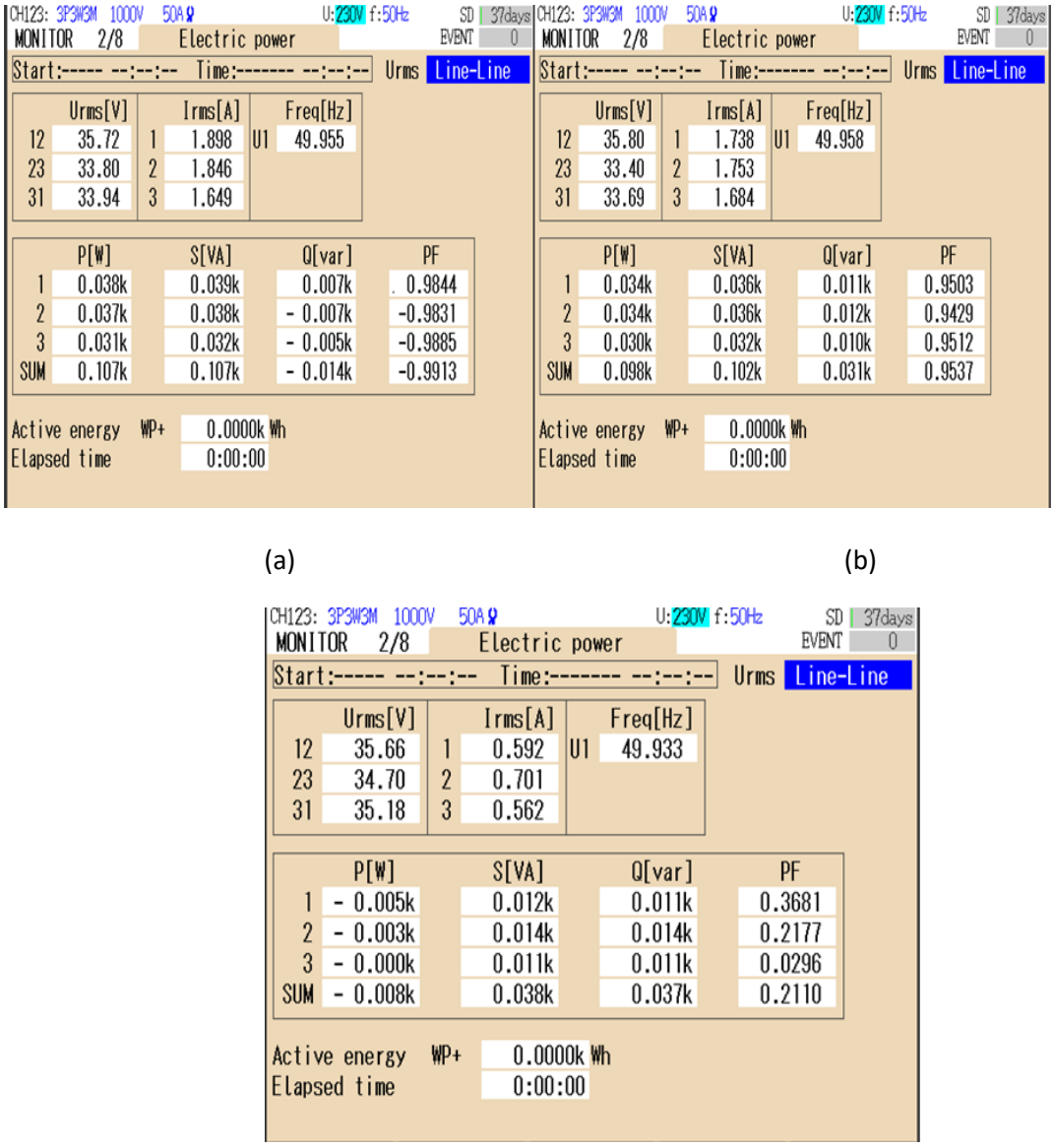

Fig. 5.55. Steady state experimental power analysis of AVSF controller under non-linear loading conditions (a) source power (P_{sabc}) (b) load power (P_{Labc}) and (c) compensator power (P_{fabc})

5.3.3.5 Steady state power transfer under PV integrated conditions

The PV model used is EN50530 with power capacity of 300W, and supplying 289.9W of power. It has been observed in Fig.5.58 that now the load demand is shared by the PV simulator. Out of 289.9W of power given by the PV simulator, 98W is used for meeting active power demand of load and remaining 169W is absorbed by the grid and rest 22W are losses.

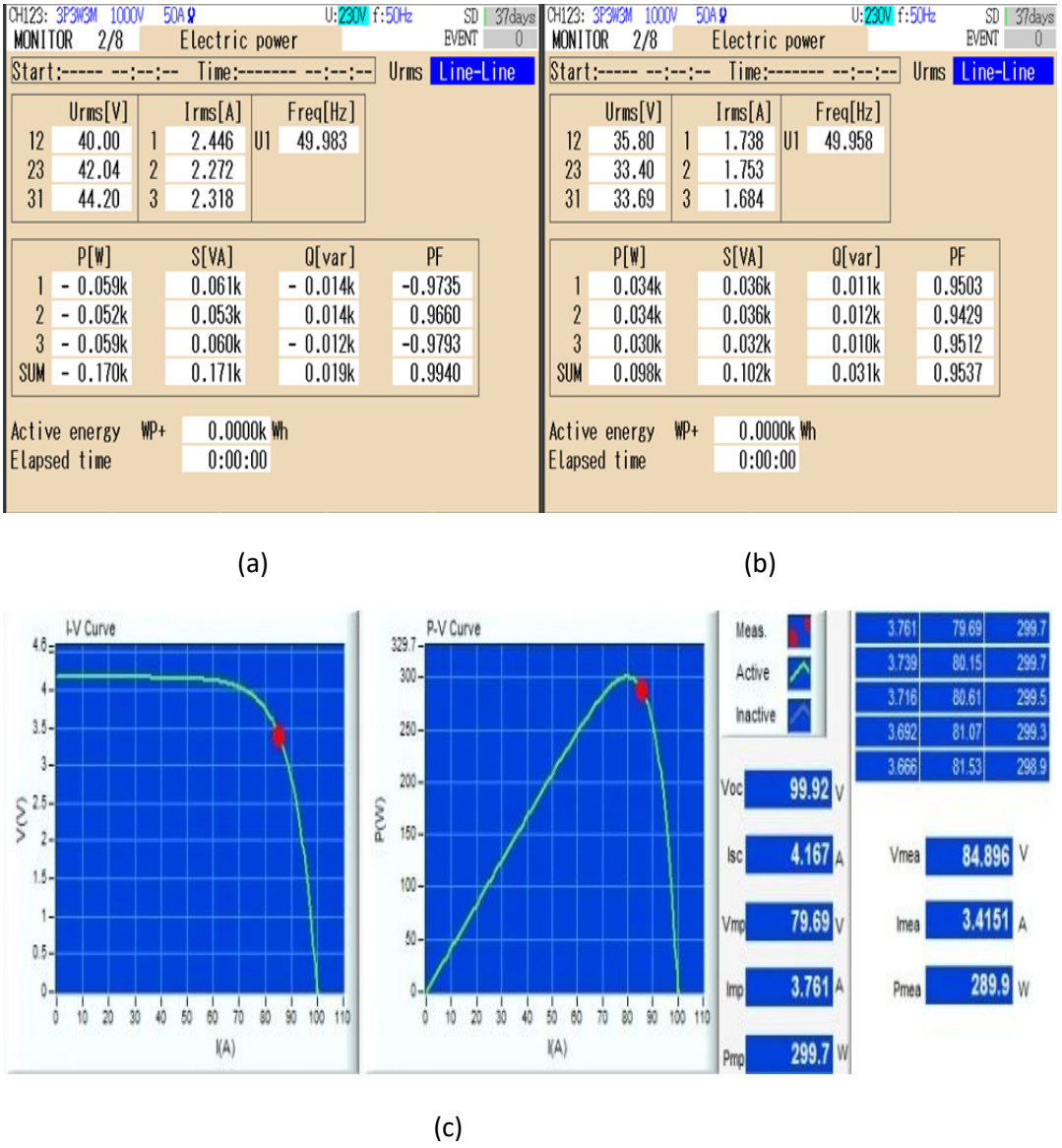

Fig. 5.58. Steady state experimental power analysis of AVSF controller under PV integrated grid connected systems (a) source power (P_{sabc}) (b) load power (P_{Labc}) and (c) PV power (P_{fabc})

5.3.4. Performance analysis with CB-FEBAF Controller

The CB-FEBAF based control scheme is modelled in Microlab Box 1202 on hardware prototype developed in three-phase grid connected system

5.3.4.1 Performance under changing non-linear load conditions

Fig. 5.59 shows the hardware operation of SAPF on three-phase grid connected systems. The SAPF operation is performed at 40V, 50Hz supply feeding non-linear load. Fig. 5.59 shows the steady state performance voltage and current waveform results

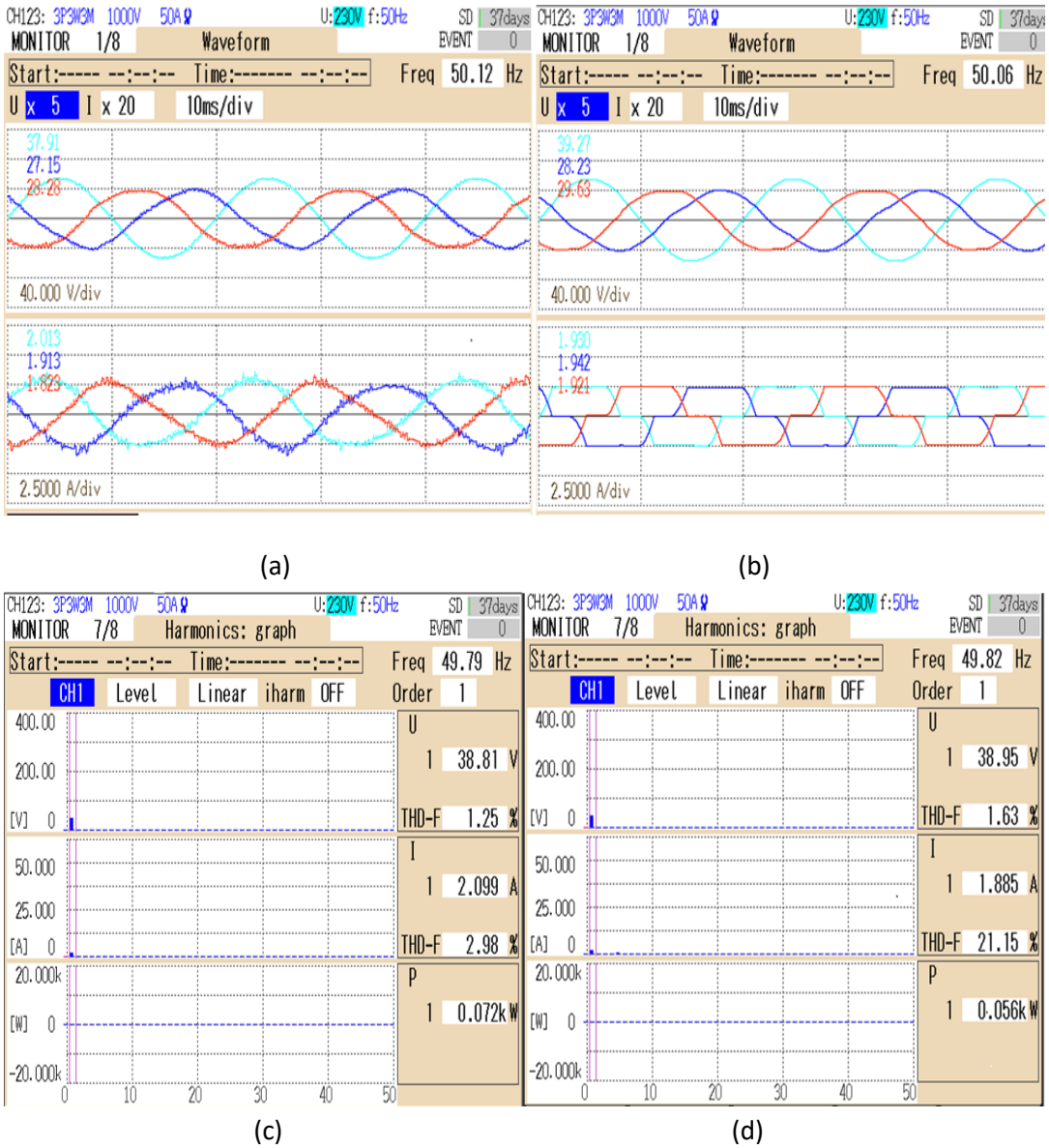

Fig. 5.59. Steady state experimental performance analysis of CB-FEBAF controller under non-linear load conditions (a) source current waveform (b) load current waveform (c) source current THD (d) load current THD

under SAPF integrated grid connected system. Figs. 5.59 (a-d) show the source voltages waveforms (v_{sabc}), source currents waveforms (i_{sabc}), load currents waveforms (i_{Labc}), source voltage THD, source current THD and load current THD. The source currents are observed to be sinusoidal and balanced. The source current THD is found to be 2.98% under non-linear load conditions of 21.5%.

5.3.4.2 Steady state power transfer under non-linear loading condition

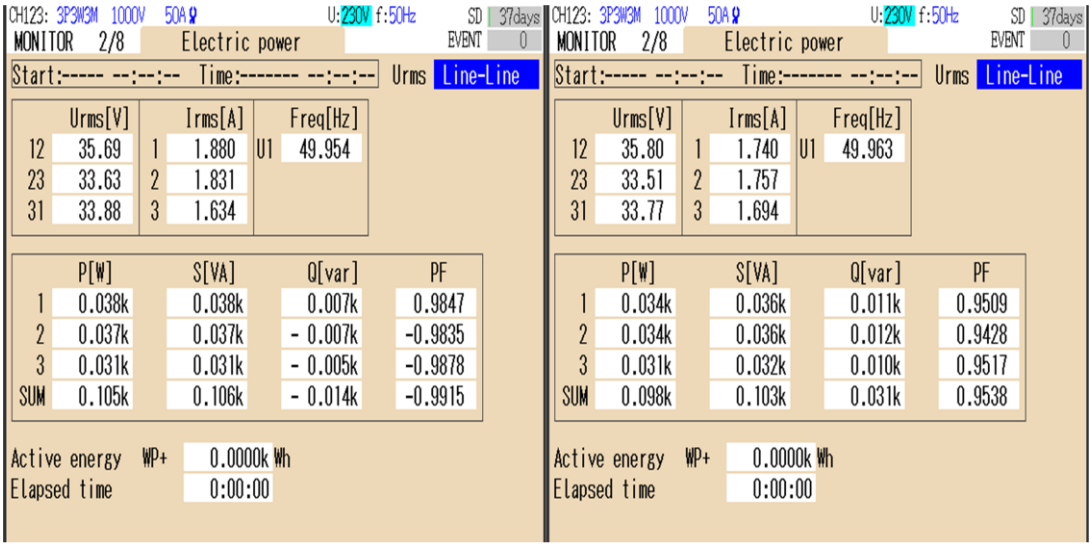

(a) (b)

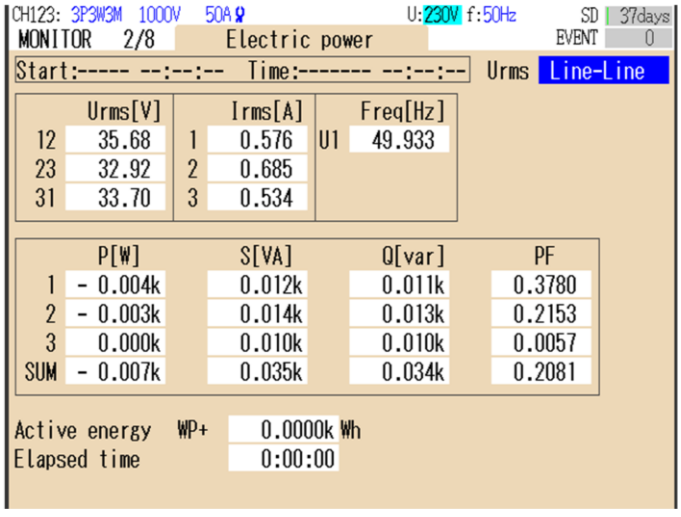

(c)

Fig. 5.60. Steady state experimental power analysis of CB-FEBAF controller under non-linear load conditions (a) source power (P_{sabc}) (b) load power (P_{Labc}) and (c) compensator power (P_{fabc})

The steady state power transfer under non-linear load between source power, load power and compensator power are shown in Fig. 5.60. The load active power demand of 98W is met by the source active power of 107W. The reactive power of load of 31VAR is met by the compensator reactive power of 38VAR.

5.3.4.3 Dynamic Results with CB-FEBAF Controller

Fig. 5.61 (a) shows the waveforms of source voltage (v_{sa}), source current (i_{sa}), load current (i_{La}) and error (e) during the open loop conditions as well as under closed loop

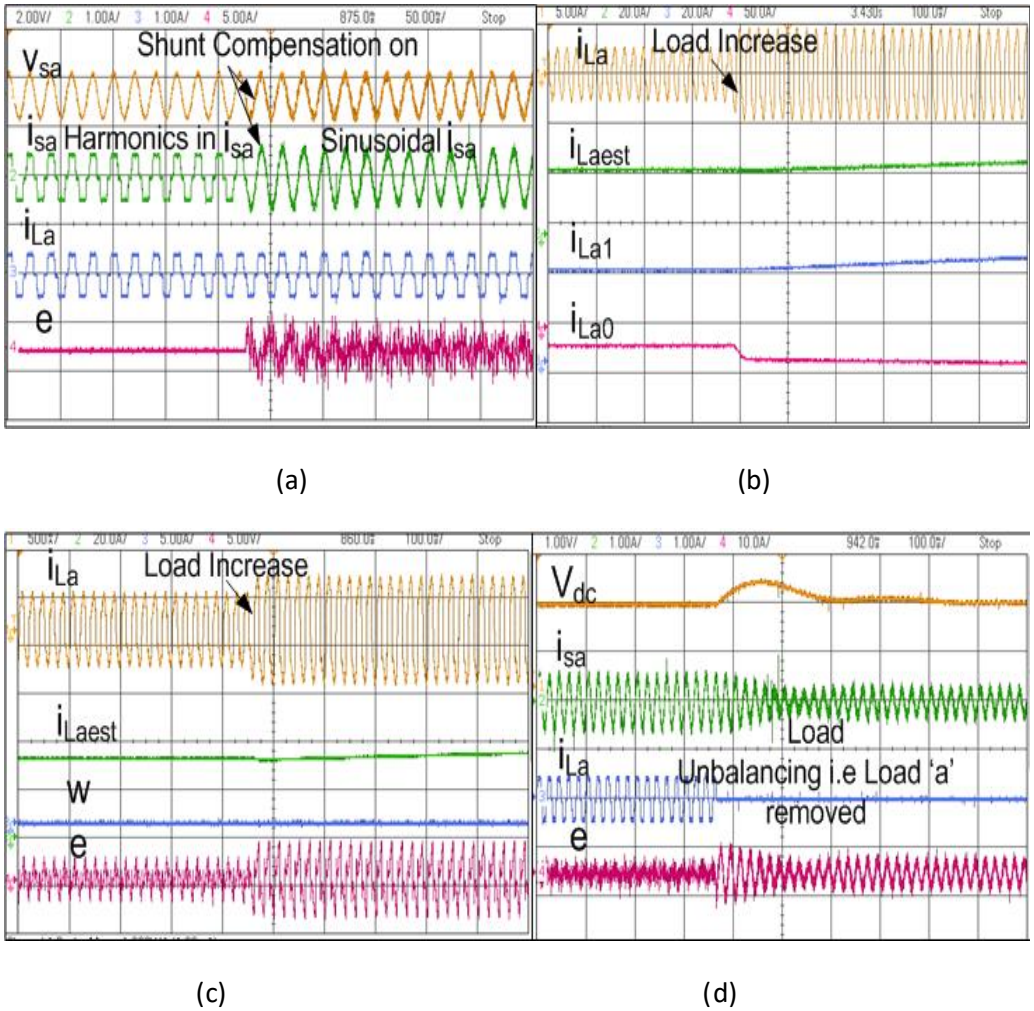

Fig. 5.61. Dynamic waveforms of CB-FEBAF observed on oscilloscope (a) $v_{sa}(2\,V/div), i_{sa}\,(1\,A/div),\ i_{La}\,(1\,A/div), e$ (5A/div) when shunt compensation is on (b) $i_{La}\,(5\,A/div),\ i_{Laest}\,(20\,A/div), i_{La1}\,(20\,A/div),\ i_{La0}\,(50\,A/div)$ under load increase (c) $i_{La}\,(500\,mA/div), i_{Laest}\,(20\,A/div),\ w(5\,A/div),\ e(5V/div)$ under load increase (d) $V_{dc}(1\,V/div), i_{sa}(1\,A/div)\ i_{La}\,(1\,A/div), e$ (10 A/div) during load unbalancing

conditions. The open loop conditions represent the situation when no gate pulse is given to SAPF. The closed loop conditions represent the situation when the gate pulses are given to the SAPF. The source current contains the harmonics and is distorted during the open loop condition i.e., when the shunt compensation is off. The source current becomes sinusoidal when gate signal is provided to the SAPF. Fig. 5.61 (b) shows the intermediate waveforms of the CB-FEBAF algorithm i_{La}, i_{Laest}, i_{La0},i_{La1} for its performance analysis under changing load conditions. The expansion components i_{La0},i_{La1} are used to estimate the fundamental component of the load current. Fig. 5.61 (c) shows the intermediate waveforms of the CB-FEBAF algorithm and plots of i_{La}, i_{Laest}, w and 'e' under load increase are shown. The expansion components are updated by weight components of the least mean square (LMS) algorithm in real time under changing load conditions. This real time and online training help to estimate the fundamental component of the load current accurately. The i_{Laest} is the estimated load current of phase 'a'. Fig. 5.61 (d) shows the waveforms of the source voltage (v_{sa}), source current (i_{sa}), load current (i_{La}) and error (e) during unbalancing load conditions.

5.3.4.4. Steady state waveforms under PV integrated conditions

Fig. 5.62 shows the hardware operation of SAPF on three-phase PV integrated grid connected systems. The SAPF operation is performed at 40V, 50Hz supply feeding non-linear load. Fig. 5.62 shows the steady state performance voltage and current waveform results under SAPF PV integrated grid connected systems. Figs. 5.62 (a-d) show the source voltages waveforms (v_{sabc}), source currents waveform (i_{sabc}), load currents waveforms (i_{Labc}), source current THD and load current THD. It has been found that the source current are 180° out of phase with the source voltages showing that the grid is absorbing active power. The source currents are observed to be sinusoidal and THD has been improved to 5.86% under non-linear load having THD of 21.62%.

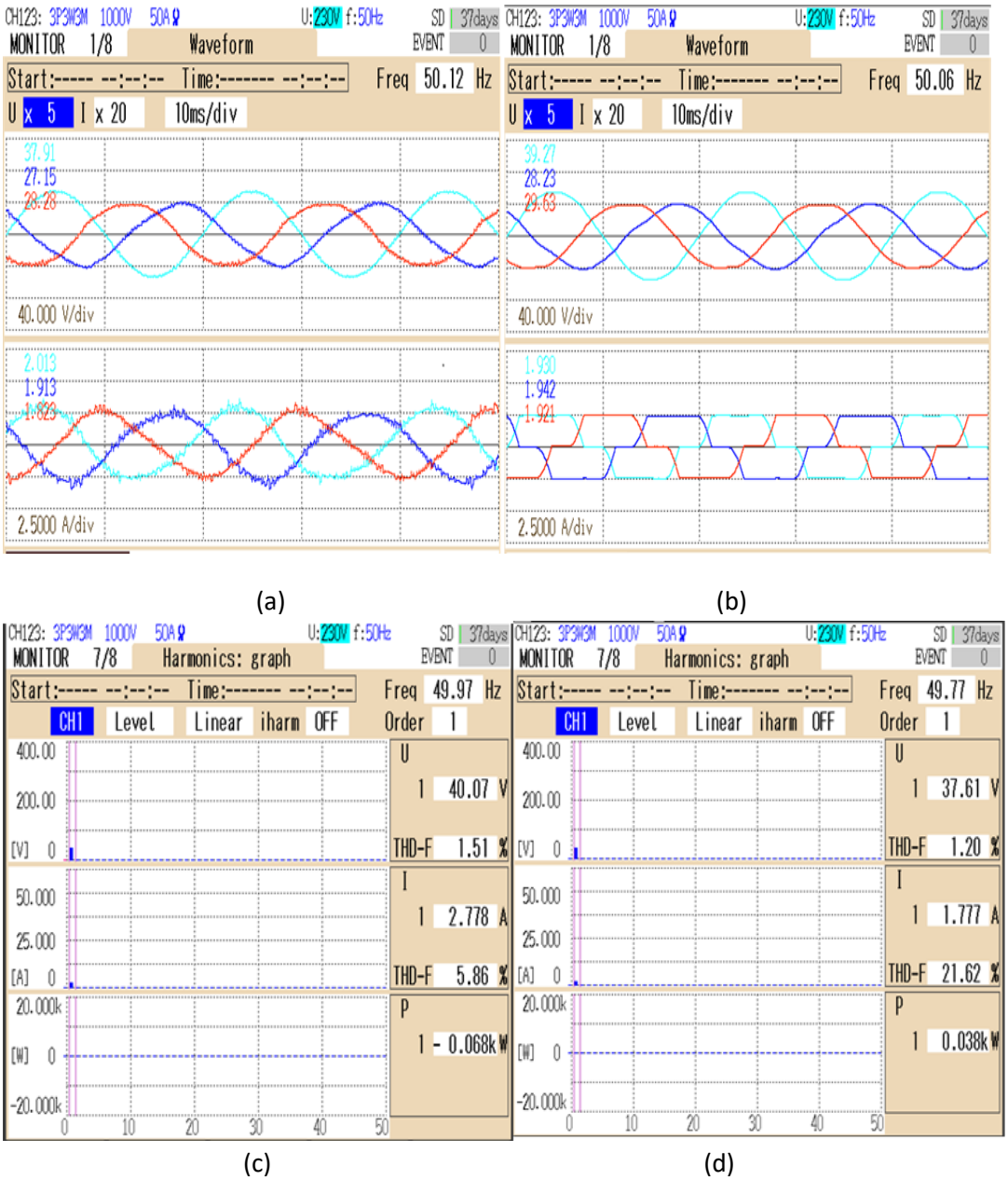

Fig. 5.62. Steady state experimental performance analysis of CB-FEBAF controller under non-linear load conditions (a) source currents waveforms (b) load currents waveforms (c) source current THD (d) load current THD

5.3.4.5 Steady state power transfer under PV integrated conditions

The PV model used is EN50530 with power capacity of 300W, and supplying 289.9W of power. It has been observed in Fig. 5.63 that now the load demand is shared by the PV simulator. Out of 289.9W of power given by the PV simulator, 98W is used for meeting active power demand of load and remaining 170W is absorbed by the grid.

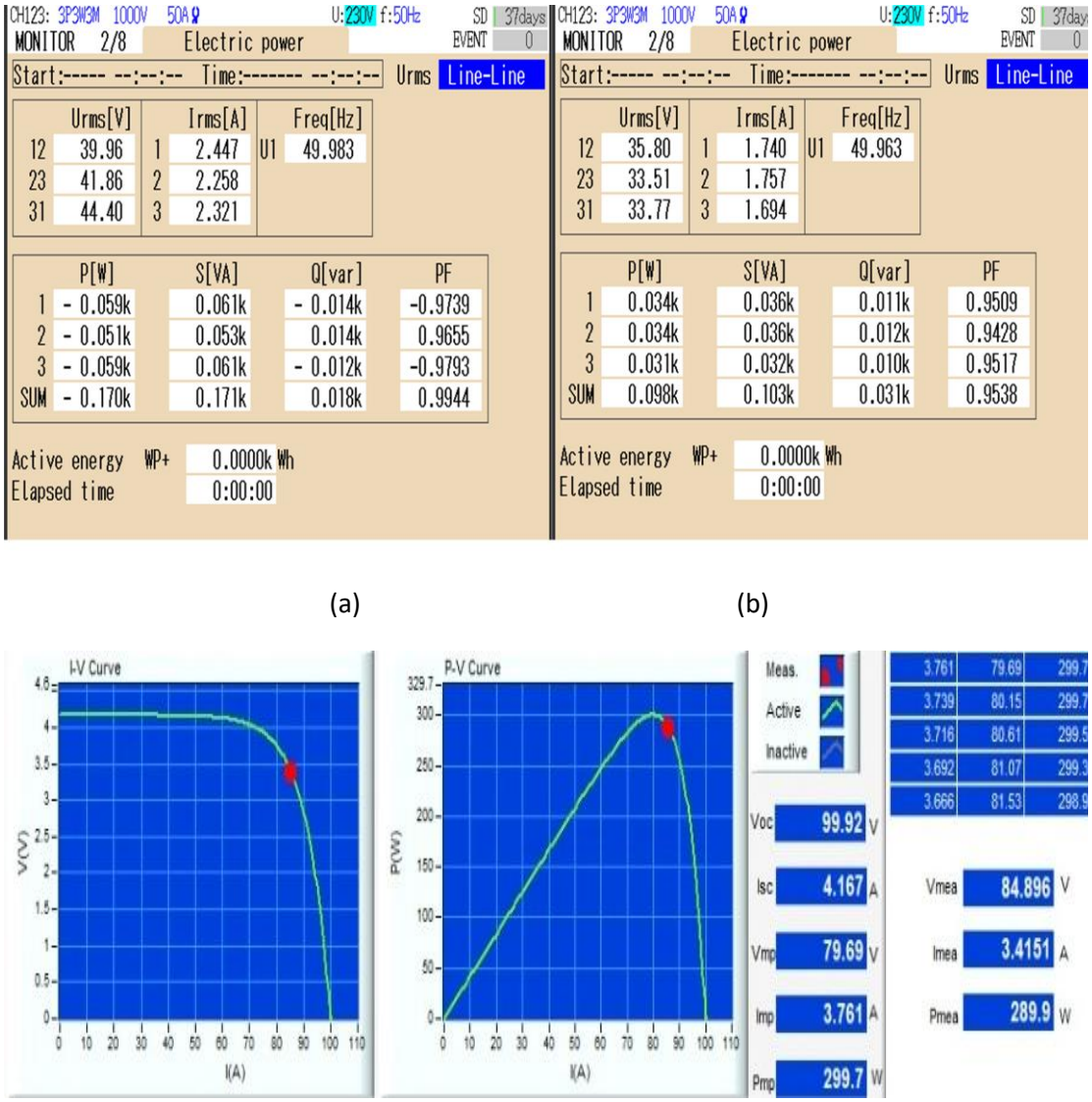

(a) (b)

(c)

Fig. 5.63. Steady state experimental power analysis of CB-FEBAF controller under PV integrated grid connected systems (a) source power (P_{sabc}) (b) load power (P_{Labc}) and (c) PV power (P_{fabc})

5.4 Comparative Evaluation of Proposed Control Schemes

5.4.1 Comparison under load variations

The comparison analysis of the four developed algorithms viz three phase SRFT, DSOGI, AVSF and CB-FEBAF is shown in Fig. 5.64. The comparison is based on various important parameters such as nature of filter, computational complexity, PLL

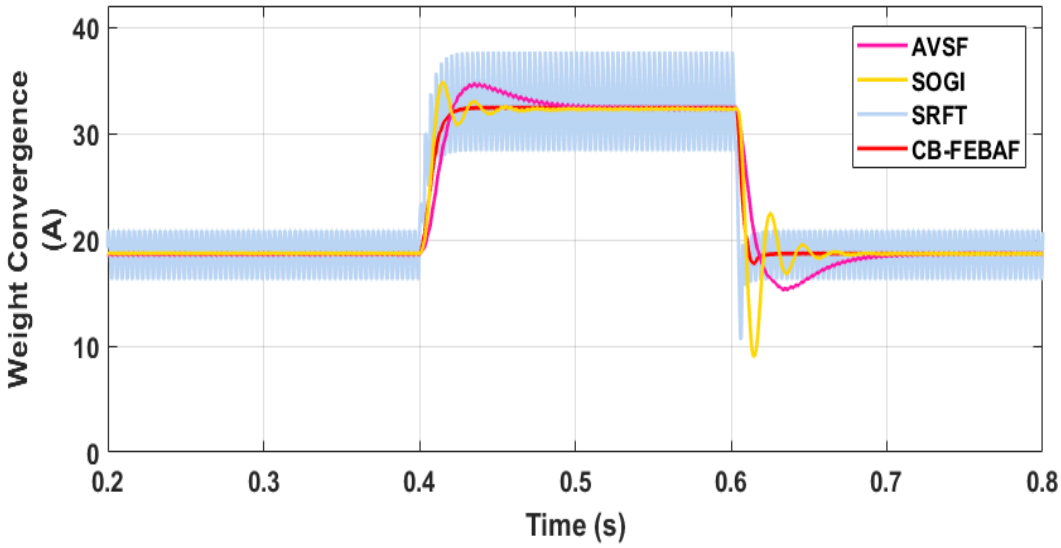

Fig. 5.64. Comparison analysis of weight convergence under load variations of different control algorithms for shunt compensation

required**,** convergence rate, THD of supply current, settling time, oscillations, response time, DSP speed which are summarized in Table 5.5. The CB-FEBAF shows fast transient response and shows almost no oscillations in tracking steady state and dynamic state behavior. SRFT shows highly sustained continuous oscillations. DSOGI shows 3-4 dynamic oscillations peaks before settling down. AVSF shows one dynamic peak and then settles down. The settling time of CB-FEBAF is 0.003s and that of AVSF is the highest. The AVSF and CB-FEBAF is made adaptive by training it online by LMS algorithm. Three Phase SRFT and DSOGI are algorithms that are parameter dependent and require optimized parameter tuning and hence not well suitable under all dynamic conditions. They require PLL and hence computation is complex. The computational complexity of CB-FEBAF algorithm is less and the sampling time taken for running the algorithm experimentally is 35µs which is the least of all the three. The THD of grid current using CB-FEBAF filter is 1.34% which is the lowest and satisfies IEEE-1547 standard for shunt compensation in grid connected PV system. Hence the performance of this proposed algorithm is far superior.

TABLE 5.5. Comparison analysis of weight convergence under load variations of different control algorithms for shunt compensation

Parameters	SRFT	SOGI	AVSF	CB-FEBAF
Nature of Control Filter	Non-Adaptive	Non-Adaptive	Adaptive	Adaptive
Degree of Filter	NA	NA	Second Order	Third Order
MSE	More	Medium	Least	Least
Oscillations	High	Medium	Least	No
Computational Complexity	More	Medium	Medium	Small
Sampling Time	50µs	45 µs	40µs	35µs
Settling Time	0.03 s Moderate	0.08 s Slow	0.08 s Slow	0.03 s Fast
Overshoot	Less	3V	3V	Least
THD in Grid Current (Simulink)	0.96%	0.90%	0.84%	0.81%

5.4.2 Comparison under analysis in normal grid conditions under varying load conditions

Table 5.6 shows the comparison of THD in supply current under different loading conditions with normal grid connected systems in simulink. It has been found that the three Phase SRFT shows the highest grid current THD of 0.96% with non-linear load, 0.73% under mixed loading and 2.33% under linear loading conditions whereas the CB-FEBAF has the lowest THD of 0.81 % in grid current with non-linear load, 0.53% with

mixed load and 2.04% with linear loading conditions. the lowest THD under all loading conditions.

TABLE 5.6. Comparison of THD values of different algorithms in simulink under varying loading conditions without PV integration

S.NO.	Algorithms	Non-Linear Load	Mixed Load	Linear Load
		i_s(THD)	i_S(THD)	i_S(THD)
	Without Compensation	20.26%	12.77%	0.19%
1.	Three Phase SRFT	0.96%	0.73%	2.33%
2.	Dual SOGI	0.90%	0.66%	2.58%
3.	AVSF	0.84%	0.61%	2.08%
4.	CB-FEBAF	0.81%	0.53%	2.04%

Table 5.7 shows a comparison of THD in supply current under different loading conditions with normal grid connected systems in hardware. It has been found that the three phase SRFT shows the highest THD of 4.08% in grid current under non-linear load whereas the CB-FEBAF has the lowest THD of 2.98 % under non-linear loading conditions

Table 5.7. Comparison of THD values of different algorithms under Hardware Testing with Non-Linear load conditions

S.No	Algorithms	Non-Linear Load
		$i_s(THD)$
	Without Compensation	21.15%
1.	Three Phase SRFT	4.08%
2.	DSOGI	3.51%
3.	AVSF	3.07%
5.	CB-FEBAF	2.98%

5.4.3 Comparison under analysis in normal grid conditions with PV integrated grid connected systems

Table 5.8 shows a comparison of THD in supply current in PV integrated grid connected systems under non-linear load conditions in simulink and hardware. It has been found that the SRFT shows the highest THD of 1.57% with non-linear load and the CB-FEBAF shows the lowest THD of 1.31%. In hardware it is found that the SRFT has the highest THD of 6.88% with non-linear load and the CB-FEBAF has the lowest THD of 5.86%. The THD obtained in hardware testing are marginally above the simulation testing results. The difference could be due to the fact the supply voltage itself is distorted in the laboratory and the testing has been done on the reduced voltage levels. However, the performance aspects of different algorithms are in line with simulation results.

TABLE 5.8. Comparison of proposed algorithm with conventional control algorithm in Simulink and Hardware with PV and without PV integration under non-linear load

Algorithms	Shunt Compensation in Matlab Simulink under non-linear load		Shunt Compensation in Hardware under non-linear load	
	i_L=20.26%, V_S=0.01%,		i_L=21.15%,V_S=1.12%	
	Without PV	With PV	Without PV	With PV
Three SRFT	0.96%	1.57%	4.08%	6.88%
Dual SOGI	0.90%	1.53%	3.51%	6.32%
AVSF	0.84%	1.44%	3.07%	6.01%
CB-FEBAF	0.81%	1.31%	2.98%	5.86%

5.5 Conclusions

This chapter discusses the design, mathematical modelling and analysis of algorithms viz three phase SRFT, DSOGI, AVSF and CB-FEBAF for control of SAPF and PV integration in three phase grid connected systems. . The results have been taken

on Matlab Simulink software and validated through hardware studies. The results without/with PV integration on three phase systems have been tested under linear load, non-linear load and mixed loading conditions. Detailed control analysis for the developed systems is shown in this chapter. The performance of the system with CB-FEBAF gives the best results followed by AVSF, DSOGI and Three Phase SRFT. The results with SRFT technique show continuous sustained oscillations in steady state and dynamic state conditions. AVSF and CB-FEBAF algorithms are based on the functional expansion of the input load current and are made robust and adaptive by updating the coefficients using LMS technique. Real time training of algorithms helps to track the changes faster and give quick response under different loading conditions and irradiation conditions. The CB-FEBAF shows very fast transient response and shows almost no oscillations in steady state and dynamic state behavior. The AVSF and CB-FEBAF are also real time adaptive techniques and overcome the drawbacks of conventional time domain algorithms. However, three Phase SRFT and DSOGI algorithms require tuning of the gain parameters. Hardware results are also in agreement with the simulation results.

CHAPTER-6

SYNCHRONIZATION TECHNIQUES FOR GRID TIED SYSTEM

6.0 General

This chapter discusses the development of the Phase Locked Loop techniques developed for synchronization of single-phase non-ideal and weak grids. The performance is tested under various grid disturbances such as distorted grid conditions, voltage sag, voltage swell, frequency change, phase change and DC offset. The effectiveness of the proposed PLLs in steady state and dynamic conditions is studied in Matlab Simulink and through hardware prototype developed in the laboratory under several grid conditions. The unit template-based scheme can be realized as the simplest PLL but does not work well under distorted grid conditions. Hence, there is a need to design, develop and test new synchronization techniques for their effectiveness.

6.1 Mathematical Analysis of PLL Schemes

The mathematical analysis of different conventional and adaptive PLL techniques is discussed in this section. These are developed for detecting the phase angle accurately and generating sinusoidal unit template and filtered voltage under weak grid conditions.

6.1.1 Synchronous Reference Frame Theory (SRFT) PLL

Single-phase voltage (v_s) generates two orthogonal signals ($v_{s\alpha}, v_{s\beta}$) from the single-phase voltage. The single-phase input from the grid voltage is depicted as

$$v_{s\alpha} = V_m \sin \omega t \tag{6.1}$$

where V_m is the peak amplitude grid voltage

The 90° delayed signal is given by

$$v_{s\beta} = V_m \sin(\omega t + \frac{\pi}{2}) \quad (6.2)$$

The orthogonal voltages are converted in to dq reference frame using Park transformation

$$\begin{bmatrix} v_{sd} \\ v_{sq} \end{bmatrix} = \begin{bmatrix} \sin \omega t & -cos\omega t \\ cost & sin\omega t \end{bmatrix} \begin{bmatrix} v_{s\alpha} \\ v_{s\beta} \end{bmatrix} \quad (6.3)$$

v_{sd} contains the information about the amplitude of the grid voltage and v_{sq} gives the information about the phase angle error. During ideal grid conditions when there are no harmonics and distortions, the PLL estimates phase angle (θ) till it equals the grid angle (ωt).

$$v_{sd} = cos(\omega t - \theta) \quad (6.4)$$

$$v_{sq} = sin(\omega t - \theta) \quad (6.5)$$

The PLL is synchronized to the grid when the phase angle error is zero i.e phase angle tracked by PLL (θ) is close to actual grid voltage angle (ωt) and then it can be said that PLL is locked, then $sin(\omega t - \theta) \approx (\omega t - \theta)$. Hence for small value of ($\omega t - \theta$)

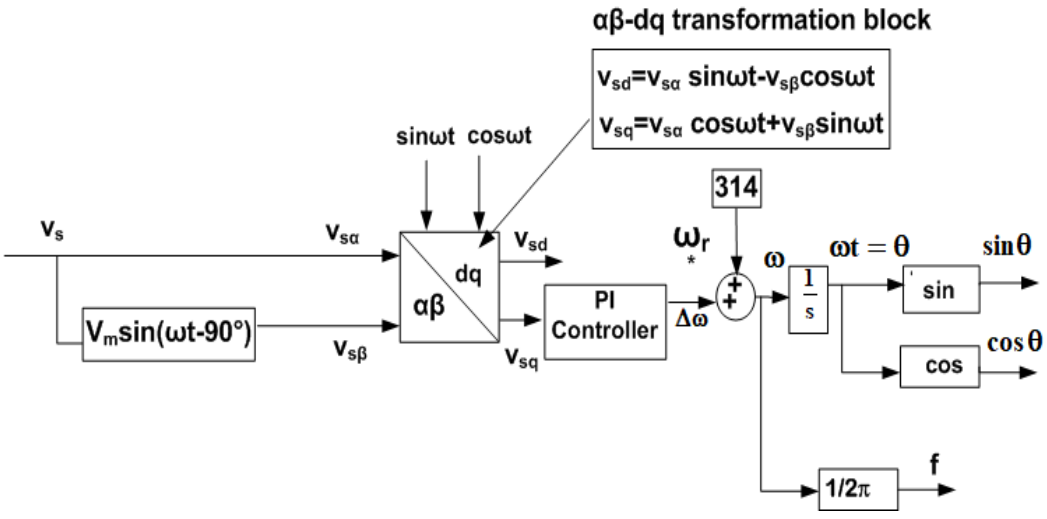

Fig. 6.1. Basic Block Diagram of SRFT PLL

$$v_{sq} \approx (\omega t - \theta) \tag{6.6}$$

The PI controller is used to regulate $V_{sq} \approx 0$ and eliminate the steady state error and the output is fed back to generate the angle and sine values.

It has been observed that any error in phase angle is reflected in the q term. The control diagram of SRFT PLL is shown in Fig. 6.1.

6.1.2 Second Order Generalized Integrator (SOGI) PLL

SOGI PLL has been designed to improve the performance of basic SRFT PLL. SOGI-PLL is used as an adaptive pre-filter to generate in-quadrature (qv_s') and in-phase signal (v_s') through quadrature signal generator. The control diagram of SOGI PLL is shown in Fig. 6.2. The two outputs (v_s') and (qv_s') are interconnected by the transfer function having the characteristics of low pass and band-pass filter given by

$$v_{s\alpha}(s)=\frac{v_s'}{v_s} = \frac{K\omega s}{s^2+K\omega s+\omega^2} \tag{6.7}$$

$$v_{s\beta}(s)=\frac{qv_s'}{v_s} = \frac{K\omega^2}{s^2+K\omega s+\omega^2} \tag{6.8}$$

where 'K' decides the filtering capability and affects the bandwidth of the closed loop system. A small value of 'K' leads to reduced bandwidth and makes the dynamic response slower.

The SOGI filtered signals $v_{s\alpha}$, $v_{s\beta}$ are now fed to the SRF-PLL as shown in Fig. 6.1 for enhanced performance. The entire scheme is shown in Fig. 6.2.

The SOGI PLL consists of two feedback loops in cascade i.e the QSG (Quadratic Signal generator) provides the phase angle and frequency to the Park transformation block.

$$\begin{bmatrix} v_{sd} \\ v_{sq} \end{bmatrix} = \begin{bmatrix} \sin \omega t & -cos\omega t \\ cos\omega t & sin\omega t \end{bmatrix} \begin{bmatrix} v_{s\alpha} \\ v_{s\beta} \end{bmatrix} \tag{6.9}$$

The frequency is fed back to the SOGI-QSG to tune the detected frequency and to make it adaptive and the PLL is locked to the input phase angle. The center frequency corresponds to the input frequency to get the equal component of in-phase and quadrature components.

The bandwidth of both the filters (Band-pass and Low pass Filter) is controlled by gain 'K' which is related to the settling time t_s and can be determined by [175].

$$K = \frac{9.2}{t_s * \omega} \tag{6.10}$$

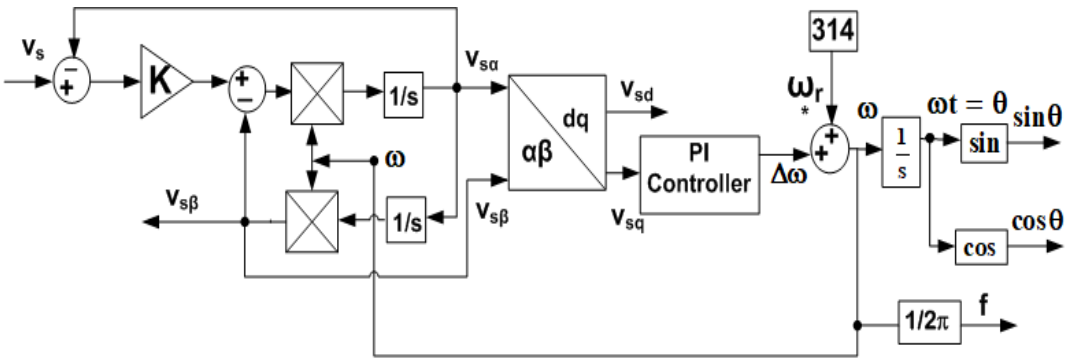

Fig. 6.2. Basic Block Diagram of SOGI PLL

6.1.3 Quadratic Bernstein Functional Blending Neural Network (QB-FBNN) PLL

The Quadratic Bernstein Polynomial Expansion belongs to the family of Spline curves [206-210]. These are powerful models for estimating non-linear systems. They exhibit Spline interpolating properties having values between 0 to 1 and for any degree, and all the Bernstein coefficients sum up to one. Therefore, the challenge to select the differentiable activation function is altogether eliminated. The expansion exhibits the maximum differentiable and convex hull property of the polynomial ensuring the smoothness of the estimated interpolated curve. The schematic control diagram of QB-FBNN PLL is shown in Fig. 6.3.

The single-phase grid voltages (v_s) is converted in to $\alpha\beta$ frame by 90° delay. The input voltage signal is considered as $v_{s\alpha}$ while 90° shifted signal component is the $v_{s\beta}$

$$v_{s\alpha} = V_m \sin \omega t \tag{6.11}$$

$$v_{s\beta} = V_m \sin(\omega t + \frac{\pi}{2}) \tag{6.12}$$

$v_{s\alpha}$ and $v_{s\beta}$ are converted to dq frame using Park Transformation. v_{sd} gives the amplitude of the voltage estimated and v_{sq} gives the information about the phase angle error

$$\begin{bmatrix} v_{sd} \\ v_{sq} \end{bmatrix} = \begin{bmatrix} \sin \omega t & -cos\omega t \\ cos\omega t & sin\omega t \end{bmatrix} \begin{bmatrix} v_{s\alpha} \\ v_{s\beta} \end{bmatrix} \tag{6.13}$$

v_{sq} is given as input to the QB-FBNN PLL and it maintains its value to zero through closed loop system regardless of the changes in frequency, phase, voltage dip, rise and harmonic distortion in weak grids. The QB-FBNN PLL controller computes the $v_{sq(est)}$ as follows

$$v_{sqF}(t) = \sum_{k=0}^{m} v_{sq}\, B_{m,k}(t) \tag{6.14}$$

where Bernstein Coefficient $B_{m,k}(t)$ is defined as

$$B_{m,k}(t) = \binom{m}{k} (1-q)^{m-k} q^k \tag{6.15}$$

such that $\sum_{k=0}^{m} B_{m,k}(t) = 1$ unlike other higher order polynomials

$$v_{sqF}(t) = \sum_{k=0}^{m} v_{sq} \binom{m}{k} (1-q)^{m-k} q^k \tag{6.16}$$

where $\binom{m}{k} = \frac{m!}{(m-k)!k!}$ which can be expressed recursively as

$$v_{sqF}(t) = (1-q)\left(\sum_{k=0}^{m-1} v_{sqk}\, B_{m-1,k}(q)\right) + t\left(\sum_{k=1}^{m} v_{sqk}\, B_{k-1,m-1}(q)\right) \tag{6.17}$$

The above expression is a linear interpolation between two-degree $m-1$ Bernstein

curves. For quadratic Bernstein Curve we have m=2,

$$v_{sqF}(k) = \sum_{k=0}^{2} v_{sqk} B_{2,k}(k) \quad k = 0,1 \ldots . m \tag{6.18}$$

$$v_{sqF}(t) = v_{sq0} B_{2,0}(q) + v_{sq1} B_{2,1}(q) + v_{sq2} B_{2,2}(q) \tag{6.19}$$

$$v_{sqF}(t) = (1-q)^2 v_{sq0} + 2q(1-q) v_{sq1} + q^2 v_{sq2} \tag{6.20}$$

$$v_{sqF}(t) = (1 + q^2 - 2q) v_{sq0} + 2(q - q^2) v_{sq1} + q^2 v_{sq2} \tag{6.21}$$

$$v_{sqF}(t) = v_{sq0} + q(-2v_{sq0} + 2v_{sq1}) + q^2(v_{sq0} - 2v_{sq1} + v_{sq2}) \tag{6.22}$$

$$v_{sqF}(\mathrm{t}) = [1 \; q \; q^2] \begin{bmatrix} 1 & 0 & 0 \\ -2 & 2 & 0 \\ 1 & -2 & 1 \end{bmatrix} \begin{bmatrix} v_{sq0} \\ v_{sq1} \\ v_{sq2} \end{bmatrix} \tag{6.23}$$

Generalizing the above matrix, we get

$$v_{sqF}(\mathrm{t}) = [(q^2 - 2q + 1) v_{sq(k-2)}, (-2q^2 + 2q + 1) v_{sq(k-1)}, \; q^2 v_{sq(k)}] \tag{6.24}$$

$$v_{sqF} = [v_{sq0}(\mathrm{k}), v_{sq1}(\mathrm{k}), v_{sq2}(\mathrm{k})] \tag{6.25}$$

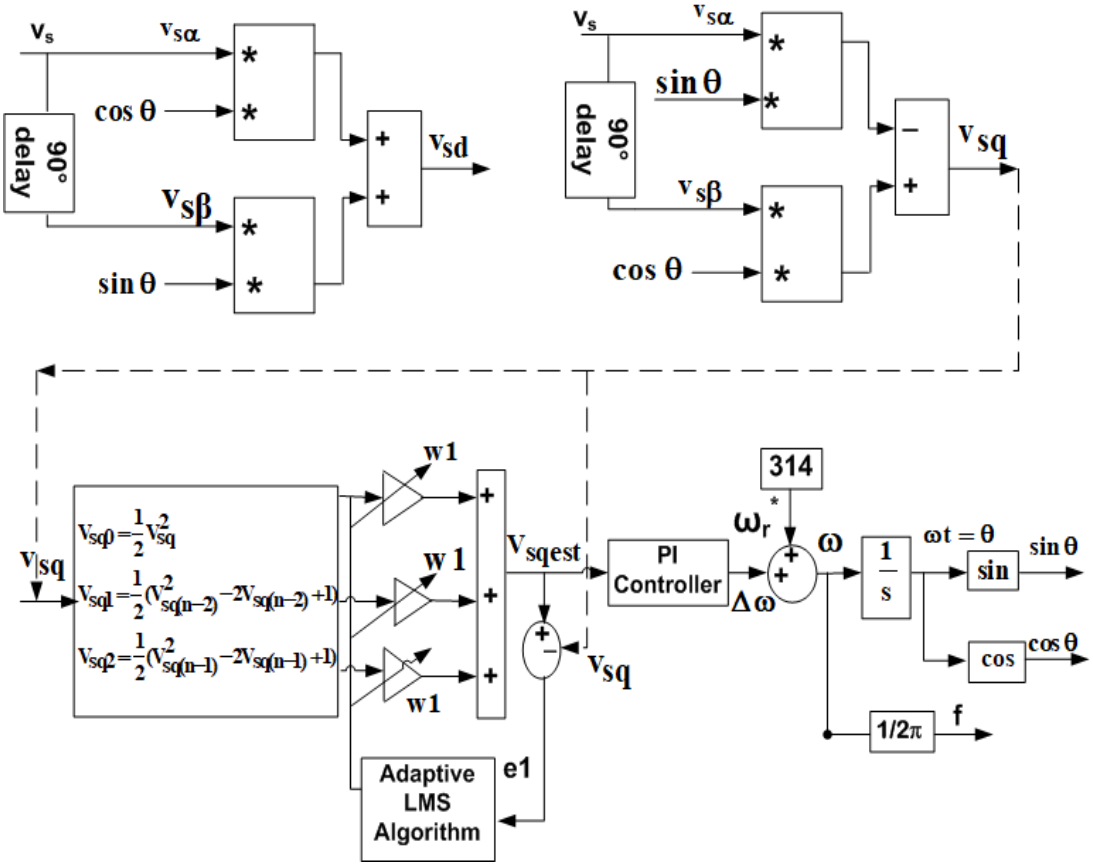

Fig. 6.3. Basic Block Diagram of QB-FBNN PLL

$$v_{sqest} = [\mathrm{w}v_{sq0}(\mathrm{k})+\mathrm{w}\, v_{sq1}(\mathrm{k})+\mathrm{w}v_{sq2}(\mathrm{k})] \quad (6.26)$$

The estimated quadrature voltage computed by QB-FBNN based controller is given by

$$v_{sqest}(\mathrm{t}) = w[v_{sq}^2(k-2) - 2v_{sq}(k-2) + v_{sq}(k-2) - 2v_{sq}^2(k-1) + 2v_{sq}(k-1) + v_{sq}(k-1) + v_{sq}^2(k)] \quad (6.27)$$

The adaptive PLL closed loop control is implemented, which is used to minimize the error between the reference quadrature voltage V_{sq} and the estimated quadrature voltage V_{sqest} . This is done by training the algorithm in real time by using Least Mean Square (LMS) algorithm.

Least mean square algorithm updates the algorithm coefficients by updating corresponding weight parameter $'\mathrm{w}'$calculated through error 'e'. This adaptive control of reactive voltage component (V_{sqest}) to zero help in tracking the grid parameters such as voltage, frequency, dc offset and phase angle oscillations fast and give quick response without delay

$$e = v_{sq}(\mathrm{t}) - v_{sqest}(\mathrm{t}) \quad (6.28)$$

where $\sin\theta$ is the synchronization template obtained from the QB-FBNN PLL. This error computed in equation (6.28) is minimized by updating the weights in real time by LMS Algorithm

$$w(k+1) = w(k) - \frac{\mu}{2}\frac{\partial E(e^2)}{\partial i_{Lest}} \quad (6.29)$$

$$w(k+1) = w(k) + \mu e sin\theta \quad (6.30)$$

where μ indicates the learning parameter, e indicates the error and E indicates the expected mean error. The V_{sqest} calculated is given as input to the PI controller. The PI controller computes the error in angular frequency ($\Delta\omega$). The error in angular frequency is summed with the natural frequency (ω_r^*) to get the estimated angular frequency

$$\omega_{est} = \omega_r^* + \Delta\omega \quad (6.31)$$

The estimated frequency (ω_{est}) is integrated to get the grid voltage angle (θ_{est}) .

$$\int \omega_{est}\, dt = \theta_{est} \quad (6.32)$$

The estimated voltage angle (θ_{est}) is used to get the unit in-phase template and the quadrature template for generation of reference signal.

6.1.4 Fractional Delay Newton Langrangian Interpolation (FD-NSLI) PLL

The Fractional Delay Interpolation concept is proposed by Newton Langrangian [211-213] to allow arbitrary fractional sampling. This concept is developed in the form of PLL which minimizes synchronization error in tracking the various grid parameters such as voltage, frequency, dc offset and phase angle oscillations fast and give quick response without delay. The structure of the algorithm is flexible and its interpolation order can be altered in real time. The output of the filter is always less than one and thus leads to faster convergence and thus making the system stable. Its schematic control diagram is shown in Fig. 6.4.

The single-phase grid voltage is split in to corresponding orthogonal voltage signals as

$$v_{s\alpha} = V_m \sin \omega t \quad (6.33)$$

$$v_{s\beta} = V_m \sin(\omega t + \frac{\pi}{2}) \quad (6.34)$$

where $v_{s\alpha}$, $v_{s\beta}$ are given as input to Park Transformation block

The quadrature voltage (v_{sqest}) estimated by Fractional Delay approximation functions which can be expressed as:

$$v_{sqest}(z) = \sum_{k=0}^{N} L_k(k)\, \Delta^k v_{sq}(z) \quad (6.35)$$

where $\sum_{k=0}^{N} L_k(k)\, \Delta^k = z^{-\Delta}$ for (6.36)

and Δ denotes delay factor expressed as Δ= {0, 1, ,.N}

The z-transform of N^{th} order Lagrangian Interpolation controller and its transfer function can be expressed as

$$v_{sqest}(z) = z^{-\Delta} v_{sq}(z) \tag{6.37}$$

$$v_{sqTF}(z) = z^{-\Delta} = \frac{v_{sqest}(z)}{v_{sq}(z)} \tag{6.38}$$

The Newton Langrangian Expansion of $v_{sqTF(\Delta)}(z)$ in terms of z^{-1} is given as

$$v_{sqTF(\Delta)}(z) = v_{sqTF(\Delta)}(0) + v_{sqTF(\Delta)}(1)z^{-1} + \dots\dots\dots v_{sqTF(\Delta)}(N)z^{-N} \tag{6.39}$$

The Taylor series expansion of above equation is obtained by replacing $z^{-1} = q$ in $v_{sqTF(\Delta)}(q^{-1}) = q^{\Delta}$ about q=1 we get

$$v_{sqTF(\Delta)}(q^{-1}) = v_{sqTF(\Delta)}(1) + v'_{sqTF(\Delta)}(1)(q-1) + \frac{1}{2}v''_{sqTF(\Delta)}(1)(q-1)^2 + \frac{1}{3!}v'''_{LsqTF(\Delta)}(1)(q-1)^3 + \cdots \tag{6.40}$$

$$= 1 + \Delta q^{\Delta-1}|_{p=1}(q-1) + \frac{1}{2}\Delta(\Delta-1)q^{\Delta-2}|_{p=1}(q-1)^2 + \cdots \dots \tag{6.41}$$

$$= 1 + \Delta(q-1) + \frac{1}{2}\Delta(\Delta-1)(q-1)^2 + \frac{1}{3!}\Delta(\Delta-1)(\Delta-2)(q-1)^3 \tag{6.42}$$

The above derivatives are taken with respect to q = z^{-1} e.g. $v'_{sqTF(\Delta)}(q) \triangleq \frac{d}{dq}q^{\Delta} = \Delta q^{\Delta-1}$.

Now Generalizing the Taylor series expansion at order N we get

$$\hat{v}_{sqTF(\Delta)}(q^{-1}) \triangleq 1 + \Delta(q-1) + \frac{1}{2}\Delta(\Delta-1)(q-1)^2 + \frac{1}{3!}\Delta(\Delta-1)(\Delta-2)(q-1)^3 + \cdots \dots \dots \frac{1}{N!}[\prod_{k=0}^{N-1}(\Delta-k)](q-1)^N] \tag{6.43}$$

$$\triangleq \mathscr{v}_{sqTF(\Delta)}(0) + \mathscr{v}_{sqTF(\Delta)}(1)(q-1) + \mathscr{v}_{sqTF(\Delta)}(2)(q-1)^2 + \mathscr{v}_{sqTF(\Delta)}(3)(q-1)^3 + \cdots \dots \mathscr{v}_{sqTF(\Delta)}(N)(q-1)^N \tag{6.44}$$

where

$$\vartheta_{sqTF(\Delta)}(N) \triangleq \frac{1}{N!}\prod_{k=0}^{N-1}(\Delta - k) = \frac{\Delta(\Delta-1)(\Delta-2)(\Delta-n+1)}{n!} \quad (6.45)$$

Replacing q by z^{-1} in Eq. (6.43) and manipulating signs we get equation (6.46). The Hold and Sample Block (H &S) block is used in which each output sample obtains the value of the previously arrived input sample.

$$\hat{v}_{sqTF(\Delta)}(q^{-1}) \triangleq 1 - \Delta(1 - z^{-1}) + \frac{1}{2}\Delta(1-\Delta)(1-z^{-1})^2 - \frac{1}{3!}\Delta(1-\Delta)(\Delta - 2)(1-z^{-1})^3 + \cdots \ldots \ldots \frac{1}{N!}[\prod_{k=0}^{N-1}(\Delta - k)](z^{-1}-1)^N \quad (6.46)$$

The error between the reference quadrature voltage $v_{sq}(\mathrm{t})$ and the estimated quadrature voltage $v_{sqest}(\mathrm{t})$ is minimized by adaptive PLL closed loop control. The error computed is minimized be updating the angle 'Δ' by gradient descent algorithm. Now substituting the $\nabla_{i_{Lest}}\epsilon(n)$ in equation of gradient Descent algorithm in equation (6.48) results in adaptive LMS algorithm.

$$e = v_{sq}(\mathrm{t}) - v_{sqest}(\mathrm{t}) \quad (6.47)$$

The reactive voltage component estimated (v_{sqest}) is regulated to zero by adaptive closed loop PLL control. This helps in tracking the grid parameters such as voltage, frequency, DC offset and phase angle oscillations quickly.

The delay Δ is updated by LMS algorithm.

$$\Delta(n+1) = \Delta(n) - \frac{\mu}{2}\nabla_\theta\epsilon(n) \quad (6.48)$$

where $\nabla_\theta\epsilon(n) = \frac{\partial\epsilon(\mathrm{n})}{\partial i_{Lest}}$denotes the MSE

$$\text{MSE} = \epsilon(\text{n}) = \text{E}[e^2] = (v_{sq}(\text{t}) - v_{sqest}(\text{t}))^2 \quad (6.49)$$

where $\nabla_\theta \epsilon(n) = \frac{\partial \epsilon(\text{n})}{\partial i_{Lest}}$denotes the MSE

$$\text{MSE} = \epsilon(\text{n}) = \text{E}[e^2] = (v_{sq}(\text{t}) - v_{sqest}(\text{t}))^2 \quad (6.49)$$

Differentiating equation (6.49) gives,

$$\frac{\partial \epsilon(\text{n})}{\partial v_{qest}} = -2\, sin\theta\left(v_{sq}(\text{t}) - v_{sqest}(\text{t})\right) = -2esin\Theta \quad (6.50)$$

$$\Delta(n+1) = \Delta(n) - \frac{\mu}{2}(-2e\, sin\Theta)$$

where μ indicates the learning parameter, e indicates the error and sinθ is the synchronization template obtained from the FD-NSLI PLL.

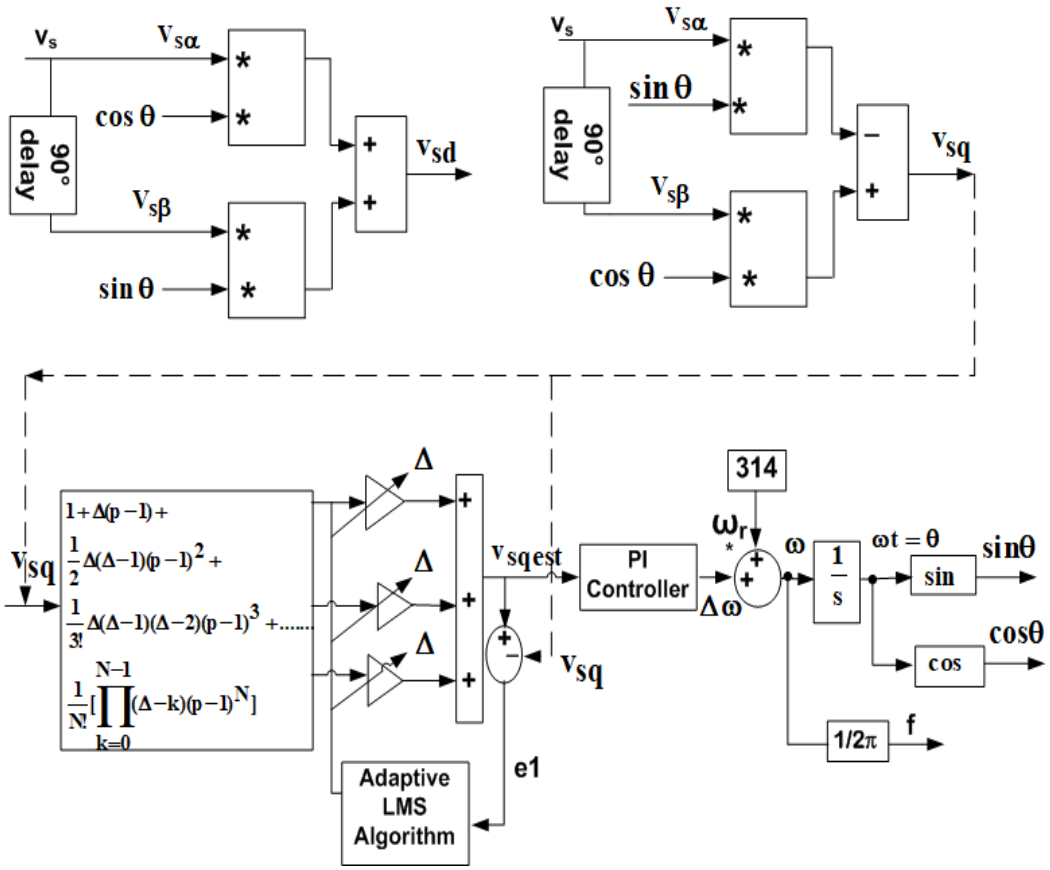

Fig. 6.4. Basic Block Diagram of FD-NSLI PLL

The v_{sqest} calculated is given as input to the PI controller. The PI controller computes the error in angular frequency (Δω). The error in angular frequency summed with the natural frequency (ω_r^*) to get the estimated angular frequency

$$\omega_{est} = \omega_r^* + \Delta\omega \tag{6.51}$$

The estimated frequency (ω_{est}) is integrated to get the grid voltage angle (θ_{est}) .

$$\int \omega_{est}\, dt = \theta_{est} \tag{6.52}$$

The estimated voltage angle (θ_{est}) is used to get the unit in-phase template and the quadrature template for generation of reference signal. The templates sinθ and cosθ can now be computed easily and used for synchronization process.

6.2 Simulation Results

Proper synchronization of inverter to the grid requires the use of PLL. The unit template-based scheme can be realized as PLL but it doesn't work well under distorted grid conditions. This section discusses the simulation results of conventional and adaptive PLL such as SRFT PLL, SOGI PLL, QB-FBNN PLL and FD-NSLI PLL under different grid disturbances.

6.2.1 Performance Analysis with SRFT PLL

The performance of the PLL is observed under various grid voltage disturbances such as voltage sag, swell, distorted grid, phase change and frequency change conditions.

The waveforms of source voltage (v_s), voltage magnitude $v_{sd}(pu)$, frequency (f), unit template ($sin\theta$), grid phase angle (θ) are shown in Fig. 6.5 under voltage sag, swell and distorted grid, phase change and frequency change conditions. It has been

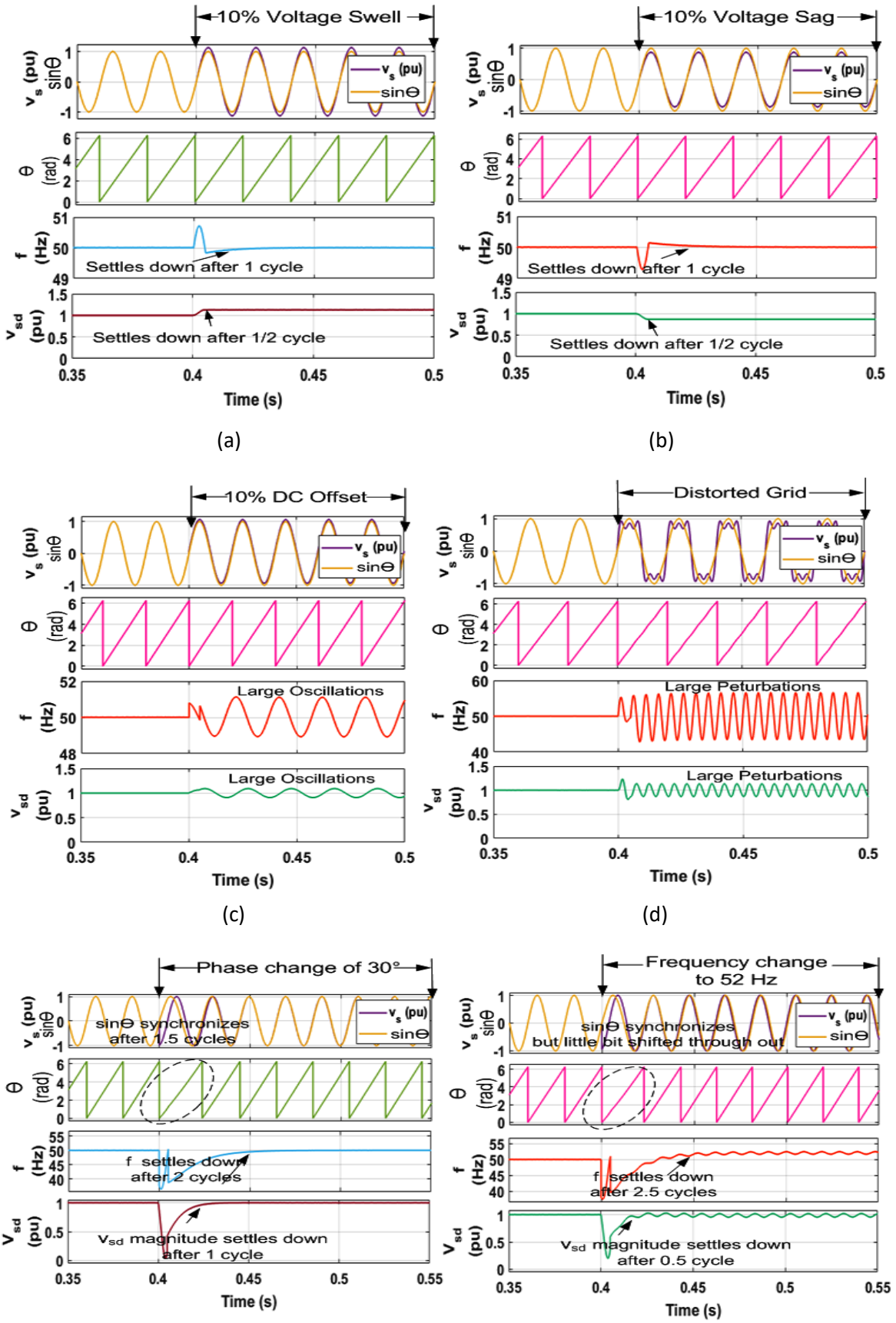

Fig. 6.5. Performance of SRFT algorithm as PLL under various grid conditions (a) voltage swell of 10% (b) voltage sag of 10% (c) 10% DC offset (d) Distorted Grid (e) phase change of 30º (f) frequency change to 52 Hz in simulink

found that the template obtained are perfectly sinusoidal and in phase with the grid voltage under all disturbances of voltage sag, swell and distorted grid.

Under voltage swell of 10% in grid voltage as shown in Fig. 6.5 (a), it has been observed that the SRFT PLL estimates voltage magnitude correctly and it is calculated correctly within half cycle. The templates obtained are sinusoidal i.e. θ and $sin\ (\theta)$ is estimated correctly. The frequency shows a little rise but settles down quickly to 50 Hz.

Under voltage sag of 10% in Fig. 6.5 (b), the voltage magnitude estimated by SRF-PLL is calculated correctly with fast response. The templates obtained are sinusoidal. The frequency shows a little dip and recovers quickly to 50 Hz.

Under distorted grid conditions when 20% harmonics are injected in to the grid shown in Fig. 6.5(c), it is found that the SRFT PLL produces sinusoidal templates. The estimated quantities v_{sd} and frequency however show continuous oscillations.

The 10% DC offset is introduced in the grid voltage as shown in Fig. 6.5 (d). The quantities v_{sd}, f, θ and $sin\theta$ are estimated correctly by the PLL. The tracked frequency and v_{sd} show large perturbations during DC offset.

The phase change of 30° is introduced in the grid supply voltage shown in Fig. 6.5 (e). It has been observed that the phase change has been tracked in 2 cycles for both synchronizing template and frequency. However, a large dip and rise in frequency and v_{sd} are observed during this period.

The frequency change from 50Hz to 52Hz is simulated in the grid supply voltage as shown in Fig. 6.5 (f). It has been observed that the large spikes are observed in estimated frequency. The voltage and sinusoidal template are little bit out of phase throughout. The frequency settles down after 2.5 cycles.

The problem with SRFT PLL observed in simulation results is that the tracked frequency shows continuous oscillations.

6.2.2 Performance Analysis with SOGI-PLL

The mitigation of voltage-based power quality problems existing in weak grid conditions such as voltage sag, swell, DC offset, phase change and frequency change conditions such as voltage sag, swell, DC offset, phase change and frequency change are discussed in the below section with the help of designed SOGI-PLL.

Under 10% voltage sag and swell of 10% shown in Figs. 6.6 (a) and (b), it is observed that voltage v_{sd} is estimated accurately within 2 cycles and the synchronising template θ and $sin\theta$ are accurately tracked. The frequency shows very little perturbations but soon settles down to 50 Hz.

Under harmonics (20%) in grid voltage from 0.4s to 0.5s shown in Fig. 6.6 (c), the little oscillations in v_{sd} and frequency are observed. The phase angle θ is perfectly tracked. The unit-in phase template $sin\theta$ obtained is perfectly sinusoidal.

With 10% DC offset in Fig. 6.6 (d) in the supply voltage, tracking of v_{sd} and frequency is observed. There are very negligible oscillations in v_{sd} and tracked frequency compared to SRFT PLL. The θ and $sin\theta$ are accurately tracked.

During phase change of 30° introduced in the grid voltage shown in Fig. 6.6(e), a quite large deviation in voltage v_{sd} is observed and frequency and settles down to 50 Hz after 5 cycles. The synchronizing template i.e θ and $sin\theta$ are accurately tracked after 2.5 cycles and $sin\theta$ is in phase with the grid voltage.

During frequency change of 2Hz (50Hz to 52Hz) introduced in the grid voltage in Fig. 6.6 (f) it has been observed that there is large dip in magnitude of voltage and

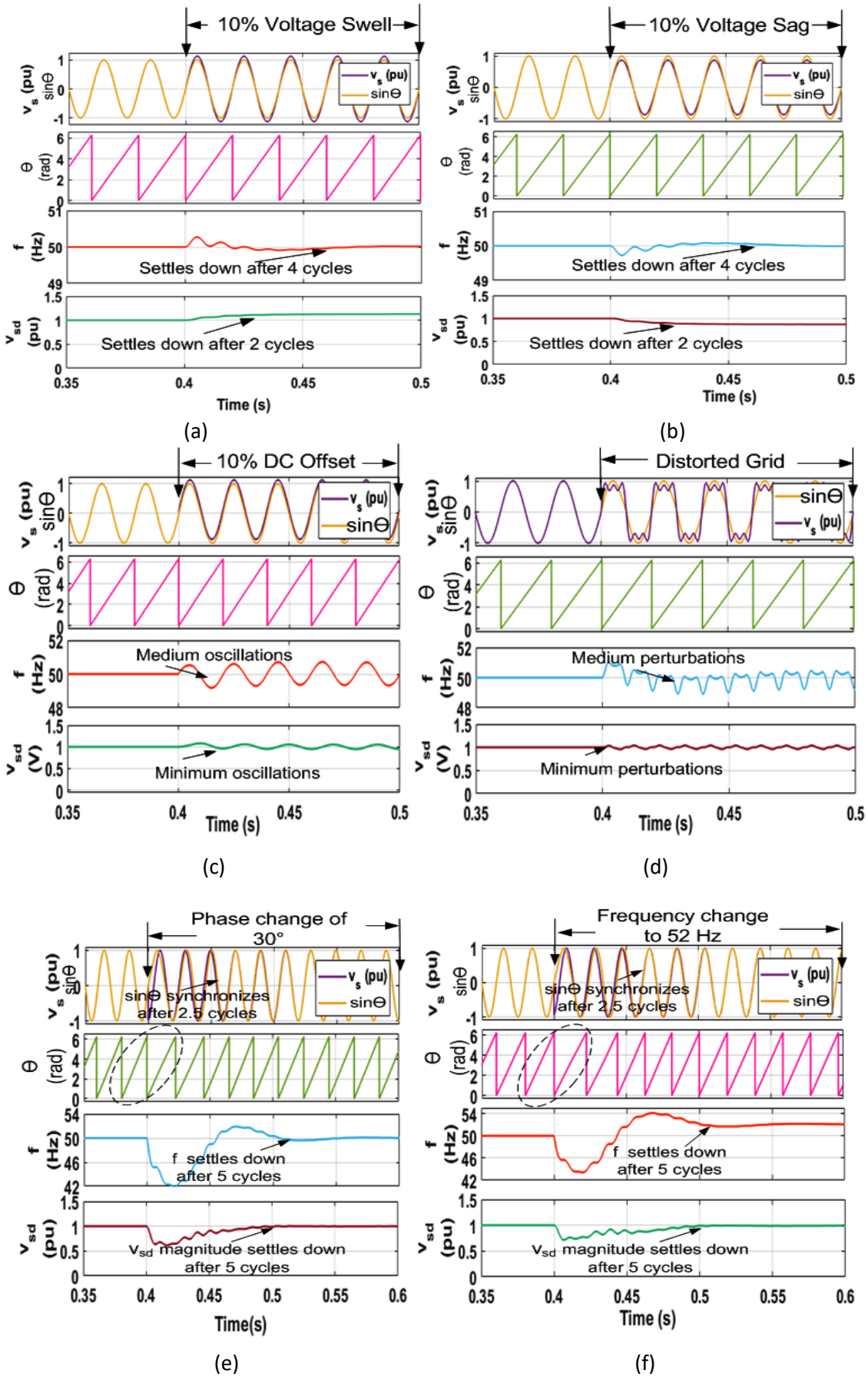

Fig. 6.6. Performance of SOGI PLL under various grid conditions (a) voltage swell of 10% (b) voltage sag of 10% (c) 10% DC offset (d) Distorted Grid (e) phase change of 30º (f) frequency change to 52Hz in simulink

frequency estimated. The oscillations are also observed in voltage and frequency and v_{sd} and settles down after 5 cycles. Proper synchronising templates are generated after 2.5 cycles.

6.2.3 Performance Analysis with QB-FBNN PLL

The performance of QB-FBNN PLL is observed under various weak grid conditions suffering from voltage quality problems such as voltage sag, swell, frequency, and phase change and the results are shown in Fig. 6.7.

Under voltage swell of 10% from 0.25s to 0.35s, shown in Fig. 6.7 (a) the voltage magnitude increases and is correctly estimated with fast response. The frequency shows a little deviation from its 50Hz value and settles down to reference with in less than half cycle. The synchronization template θ and $sin\theta$ are correctly tracked

Under voltage sag of 10% from 0.1s to 0.2s, shown in Fig. 6.7 (b) the voltage magnitude estimated decreases and is correctly measured and frequency show very little deviation of 0.5Hz and soon settles down to 50Hz with in less than half cycle. The θ and $sin\theta$ are perfectly sinusoidal and in phase with the voltage.

The phase change of 30º is introduced in grid voltage in Fig. 6.7 (c). The estimated frequency shows a dip of 7Hz and voltage estimated shows a dip of 0.18pu. The synchronizing template sinϴ deviates initially and then correctly estimates and come in phase with the voltage within 3.5 cycles. This shows the effectiveness of the designed PLL which works effectively.

The frequency change of 2Hz is observed in grid voltage in Fig. 6.7(d). The dip of frequency and voltage magnitude is observed. The synchronizing template tracks within

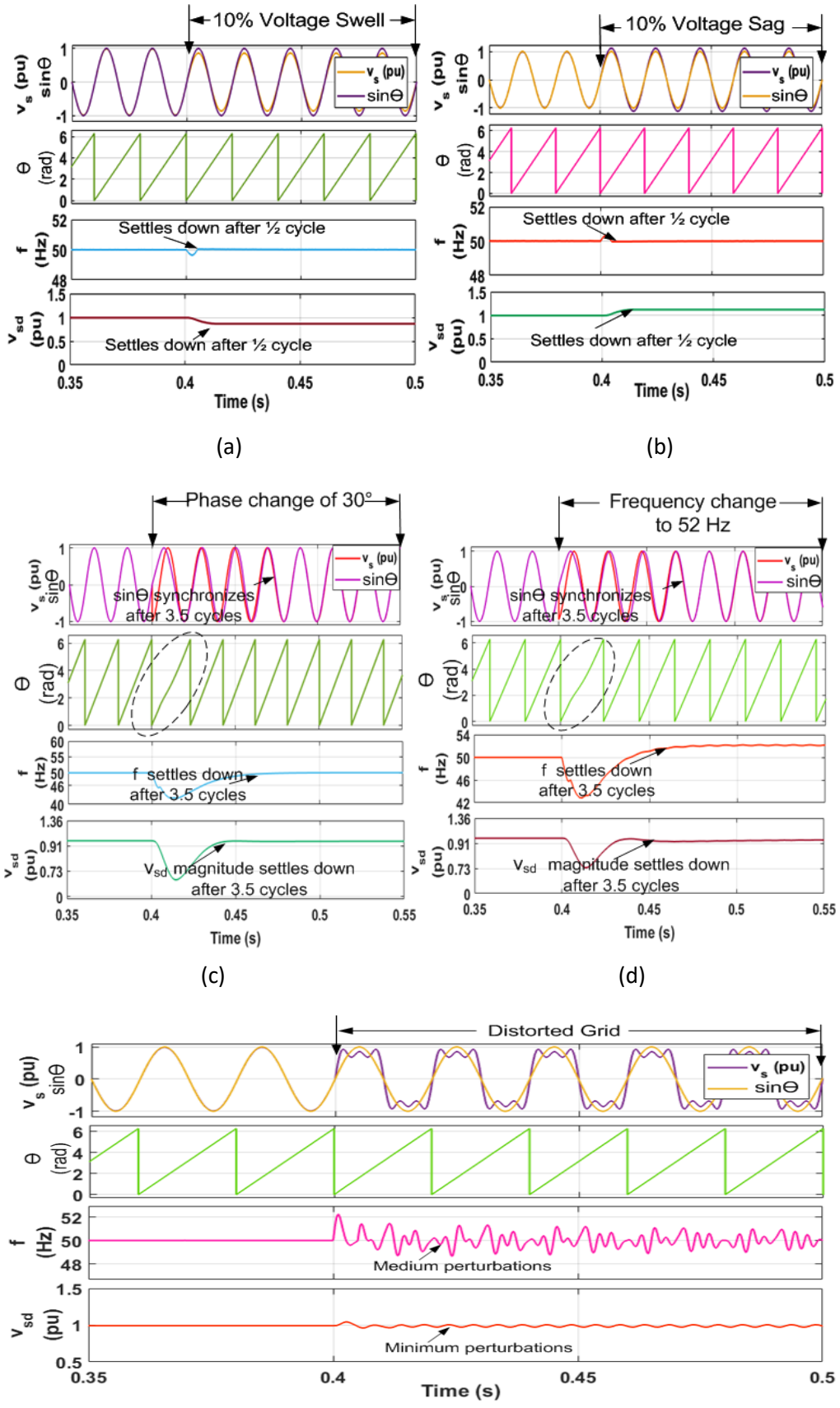

Fig. 6.7. Performance of QB-FBNN PLL under various grid conditions (a) voltage swell of 10% (b) voltage sag of 10% (c) phase change of 30º (d) frequency change (e) Distorted Grid to 52Hz in simulink

3.5 cycles.

Under 20% harmonics injected in to the grid supply voltage in Fig. 6.7 (e), it has been observed that the estimated voltage magnitude and the frequency shows minimal oscillations compared to the above techniques. The θ and $sin\ \theta$ are perfectly sinusoidal and in phase with the supply voltage

6.2.4 Performance Analysis with FD-NSLI PLL

The performance analysis of FD-NSLI PLL under weak grid conditions suffering from voltage sag, swell, DC offset, harmonics, phase change and frequency change is discussed. The performance evaluation is done on the basis of parameters v_s , i_s, i_L, θ, V_{DC}, $sin\theta$ and frequency f shown in Fig. 6.8.

Under the voltage swell of 10% in grid voltage, it has been observed that the voltage amplitude estimated increases. The frequency shows a little rise of 0.2Hz and settles down to 50Hz again within 0.75 cycle. The synchronizing signal sinϴ is sinusoidal and in phase with the supply voltage.

Under the voltage sag of 10% in grid voltage in Fig. 6.8 (b), it has been observed that the voltage amplitude estimated decreases showing voltage sag properly. The frequency shows a little dip of 0.2Hz and settles down to 50Hz again within 0.75 cycle. The synchronizing signal sinϴ is sinusoidal and in phase with the supply voltage

Under distorted grid voltage having THD of 20% in Fig. 6.8(c), the estimated synchronizing signal sinϴ is sinusoidal and in phase with the voltage. The estimated voltage magnitude and frequency show minimal perturbations under distorted grid.

The voltage shows 10% dc offset in grid voltage shown in Fig. 6.8 (d). The

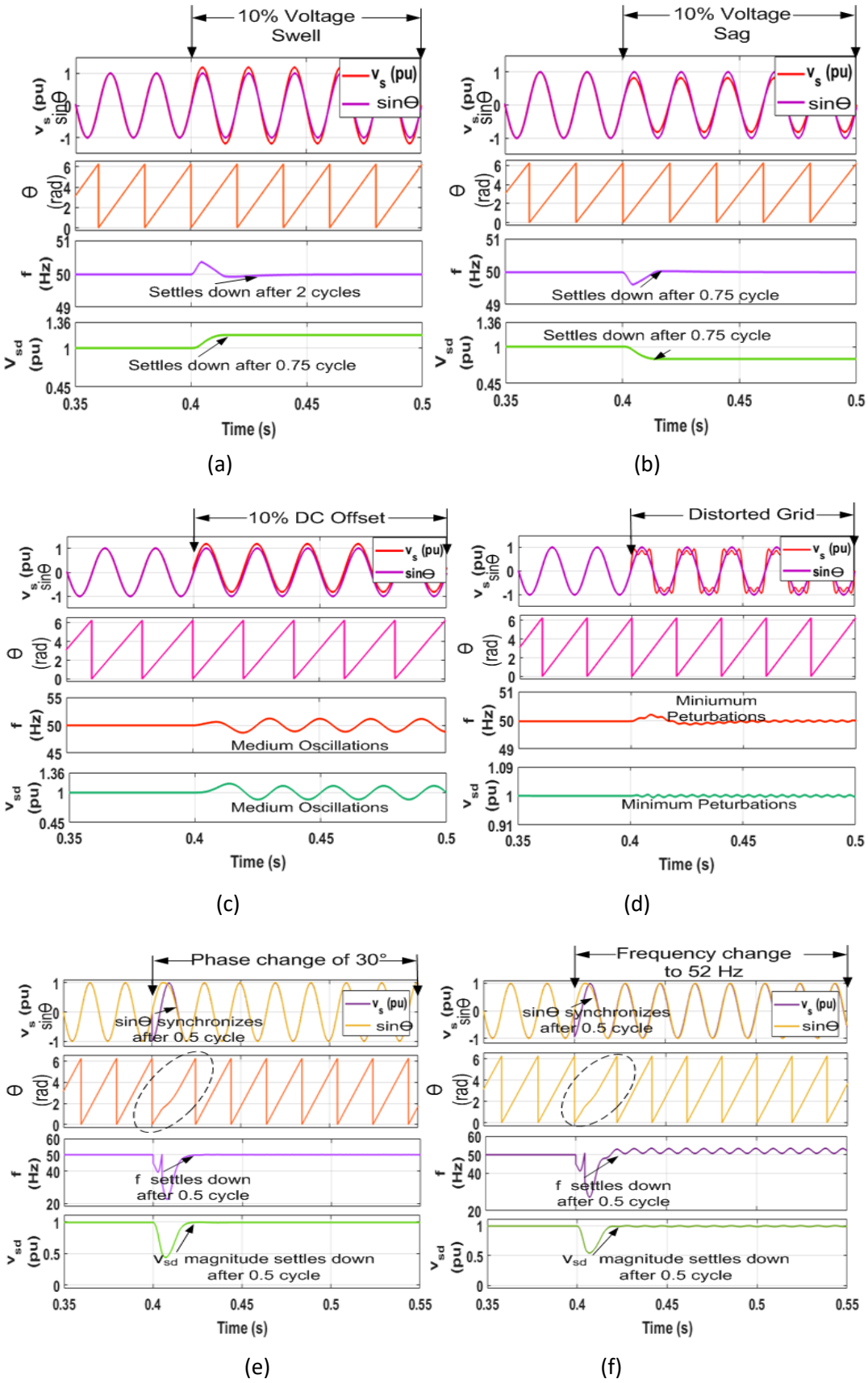

Fig. 6.8. Performance of FD-NSLI PLL under various grid conditions (a) voltage swell of 10% (b) voltage sag of 10% (c) 10% DC offset (d) Distorted Grid (e) phase change of 30º (f) frequency change to 52Hz in simulink

voltage magnitude and frequency tracked shows minimum oscillations during the transient.

In Fig. 6.8 (e), under phase change of 30° introduced in supply the v_{sd} and f exhibits a small deviation of 3V and settles down with in 1 cycle with zero steady state error. The synchronization template is correctly tracked with in <1/2 cycle and is in phase with the voltage.

In Fig. 6.8 (f), under frequency change of 2Hz is simulated from 1.43s to 2s, tracked v_{sd} and f show little deviation and minimal oscillations during change in frequency and settles down with zero steady state error within 1 cycle. The synchronization template θ and $sin\theta$ are correctly tracked within 1 cycle and in phase with the voltage.

However, the new frequency is tracked effectively showing that the proposed FD-NSLI controller works effectively as a PLL also.

6.3 Hardware Results

The section discusses the hardware results of conventional and adaptive PLLs such as SRFT PLL, SOGI PLL, QB-FBNN PLL and FD-NSLI PLL under grid disturbances such as voltage sag, voltage swell, DC offset, phase change and frequency change conditions.

6.3.1 Performance Analysis with SRFT PLL

The performance of the PLL is observed under various grid voltage disturbances such as voltage sag, swell, distorted grid, phase change and frequency change conditions.

The waveforms of v_s , v_{sd}, f, $sin\theta$, θ are shown in Fig. 6.9 under voltage sag, swell and distorted grid, phase change and frequency change conditions. It has been

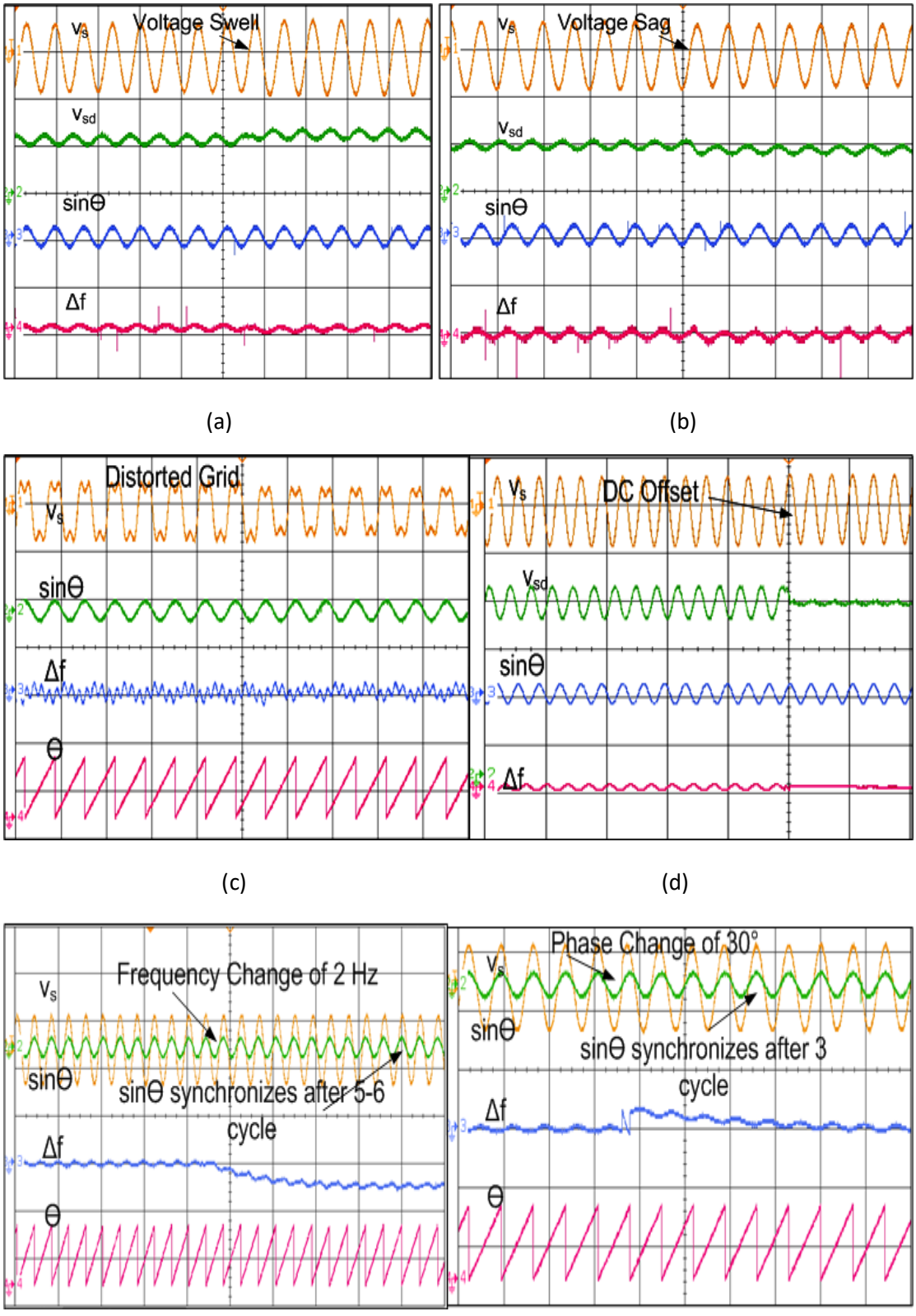

Fig. 6.9. Dynamic performance results of SRFT algorithm as PLL under various grid conditions (a) voltage swell of 10% (b) voltage sag of 10% (c) Distorted Grid (d) 10% DC offset (e) phase change of 30º (f) frequency change to 52Hz

found that the template obtained are perfectly sinusoidal and in phase with the grid voltage under all disturbances of voltage sag, swell and distorted grid.

Under voltage swell and sag of 10% in grid voltage, a little dip in Δf is observed under sag and swell after that it returns to its normal condition instantly in 0.005 cycles. The templates obtained are sinusoidal shown in Figs. 6.9 (a-b).

A frequency change of 2Hz is introduced in the grid supply voltage shown in Fig. 6.9 (c). It has been observed that the template tracks the frequency change in 5-6 cycles.

The phase change of 30° is introduced in the grid supply voltage as shown in Fig. 6.9 (d). It has been observed that the template tracks the phase change after 3 cycles.

Under 20% harmonics in grid voltage, continuous oscillations in Δf are observed. The sinϴ obtained is perfectly sinusoidal shown in Fig. 6.9 (e).

In 10% DC offset oscillations in v_{sd} and frequency are observed. The $sin\theta$ appears to be accurately tracked shown in Fig. 6.9(f)

6.3.2 Performance Analysis with SOGI-PLL

The performance of the SOGI PLL is observed under various grid voltage disturbances such as voltage sag, swell, distorted grid, phase change and frequency change conditions shown in Fig. 6.10.

Under voltage swell and sag of 10% in grid connected systems a little variation in Δf is observed under sag and swell after that the tracked frequency returns to its normal condition with in 0.005 cycles. The templates obtained are sinusoidal shown in Fig. 6.10 (a) and Fig. 6.10 (b).

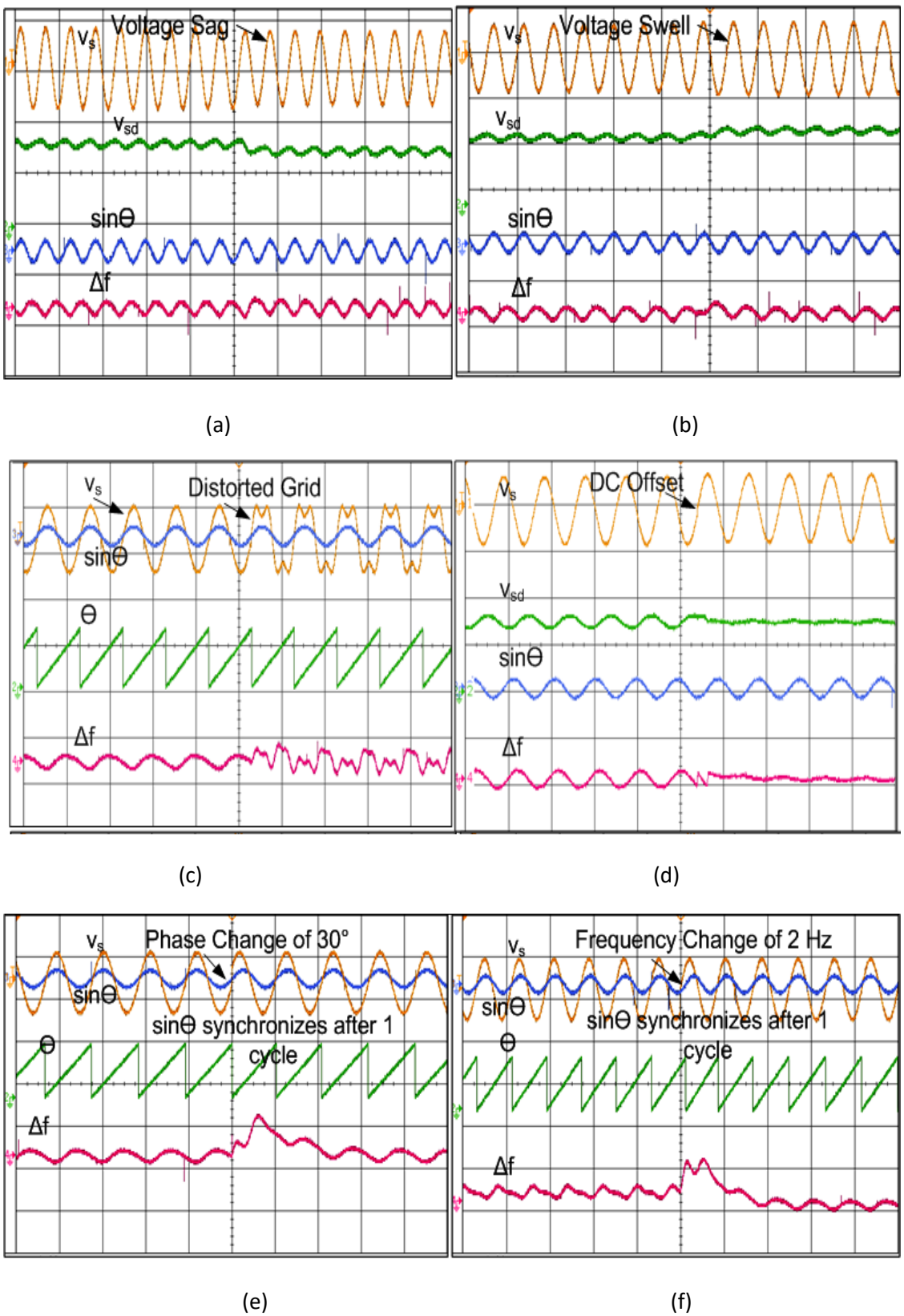

Fig. 6.10. Dynamic performance results of SOGI PLL under various grid conditions (a) voltage swell of 10% (b) voltage sag of 10% (c) Distorted Grid (d) 10% DC offset (e) phase change of 30º (f) frequency change to 52Hz on oscilloscope

The phase change of 30° is introduced in the grid supply voltage as shown in Fig. 6.10 (c). It has been observed that the template tracks the phase change after 1 cycle.

The frequency change of 2Hz is introduced in the grid supply voltage shown in Fig. 6.10 (d). It has been observed that the template tracks the frequency change in 1 cycle.

Under 20% harmonics in grid voltage, continuous oscillations in Δf are observed but the magnitude of oscillations is less than SRFT PLL shown in Fig. 6.10 (e). The sinϴ obtained is perfectly sinusoidal.

In 10% DC offset there is very minute oscillations in v_{sd} and frequency compared to SRFT PLL. The θ and $sin\theta$ are accurately tracked shown in Fig. 6.10 (f).

6.2.3 Performance Analysis with QB-FBNN PLL

The performance of QB-FBNN PLL is observed under various weak grid conditions suffering from voltage quality problems such as voltage sag, swell, frequency, and phase change.

Under voltage swell and sag of 10% under normal grid conditions, the voltage magnitude also increases and decreases and is correctly estimated with fast response. The synchronization template sinϴ is correctly tracked and is sinusoidal in shape shown in Fig. 6.11 (a-b).

A phase angle change of 30° is introduced in the grid supply voltage shown in Fig. 6.11 (c). It has been observed that the correct template is obtained after 2 cycles.

The frequency change of 2Hz is introduced in the grid supply voltage shown in Fig. 6.11 (d). It has been observed that the template tracks the frequency change in 3-4

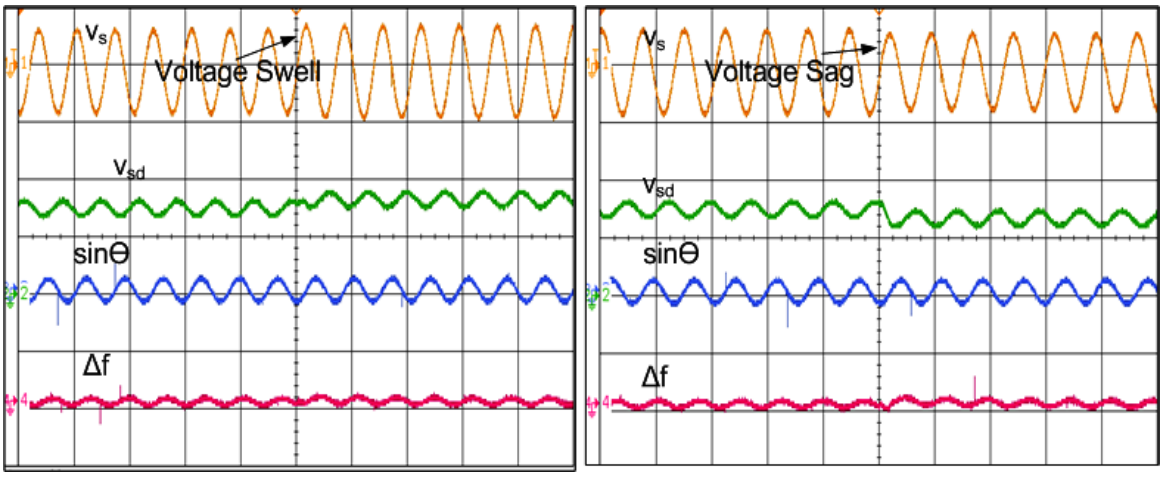

(a)

(b)

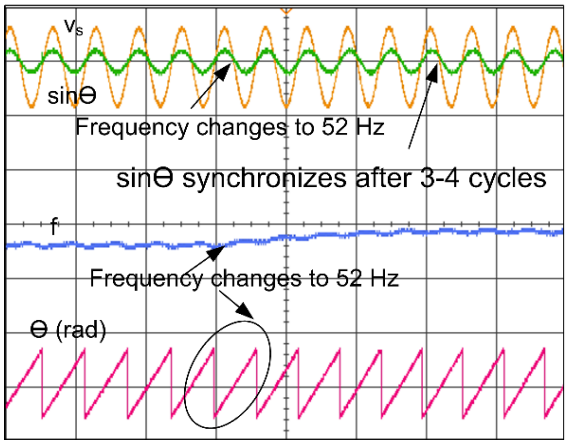

(c)

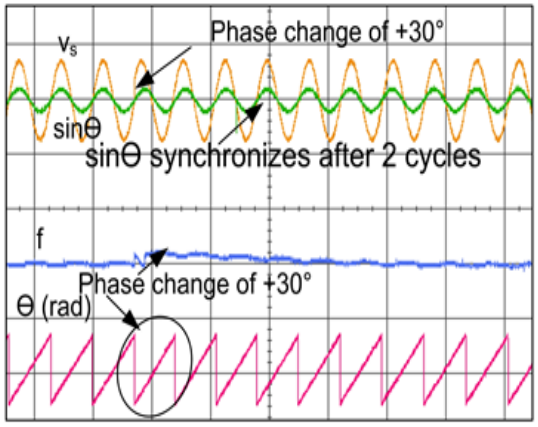

(d)

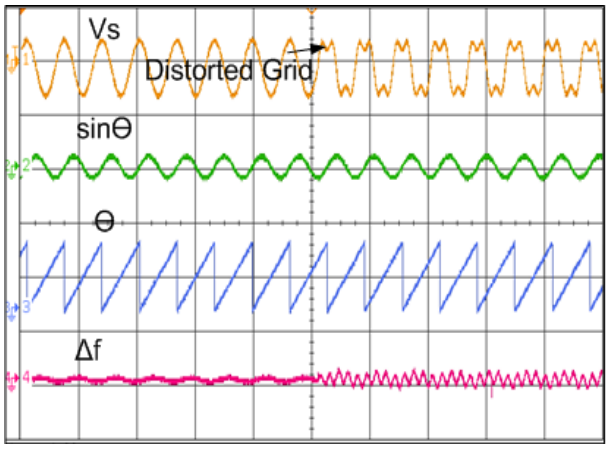

(e)

Fig. 6.11. Dynamic performance results of QB-FBNN PLL under various grid conditions (a) voltage swell of 10% (b) voltage sag of 10% (c) phase change of 30º (d) frequency change to 52Hz (e) Distorted Grid on oscilloscope

in 3-4 cycles.

Under 20% harmonics injected in to the grid supply voltage under sag and swell in Fig. 6.11(e), the voltage magnitude also increases and decreases and is correctly estimated with fast response. The synchronization template sin(Θ) is correctly tracked and is sinusoidal in shape.

6.2.4 Performance Analysis with FD-NSLI PLL

Under the voltage swell of 10% in grid voltage shown in Fig. 6.12 (a), it has been observed that the voltage amplitude estimated increases. The frequency Δf shows oscillations. The synchronizing signal sinΘ is sinusoidal and in phase with the supply voltage.

Under the voltage sag of 10% in grid voltage shown in Fig. 6.12 (b), it has been observed that the voltage amplitude estimated decreases showing voltage sag properly. The frequency Δf shows oscillations. The synchronizing signal sinΘ is sinusoidal and in phase with the supply voltage

Under distorted grid voltage having THD of 20% in Fig. 6.12 (c). The estimated synchronizing signal sinΘ is sinusoidal and in phase with the voltage. The voltage magnitude and frequency estimated shows minimal oscillations under distorted grid.

The voltage shows 10% DC offset in grid voltage shown in Fig. 6.12 (d). The estimated synchronizing signal sinΘ is sinusoidal and in phase with the voltage. The voltage magnitude and frequency tracked shows perturbations during the transient.

The frequency change of 2Hz is observed in grid voltage in Fig. 6.12 (e). The dip of frequency and voltage magnitude is observed. The synchronizing template tracks the

the voltage correctly within 1 cycle.

The phase change of 30º is introduced in grid voltage in Fig. 6.12 (f). The synchronizing template sinΘ deviates initially and then correctly estimates and come in

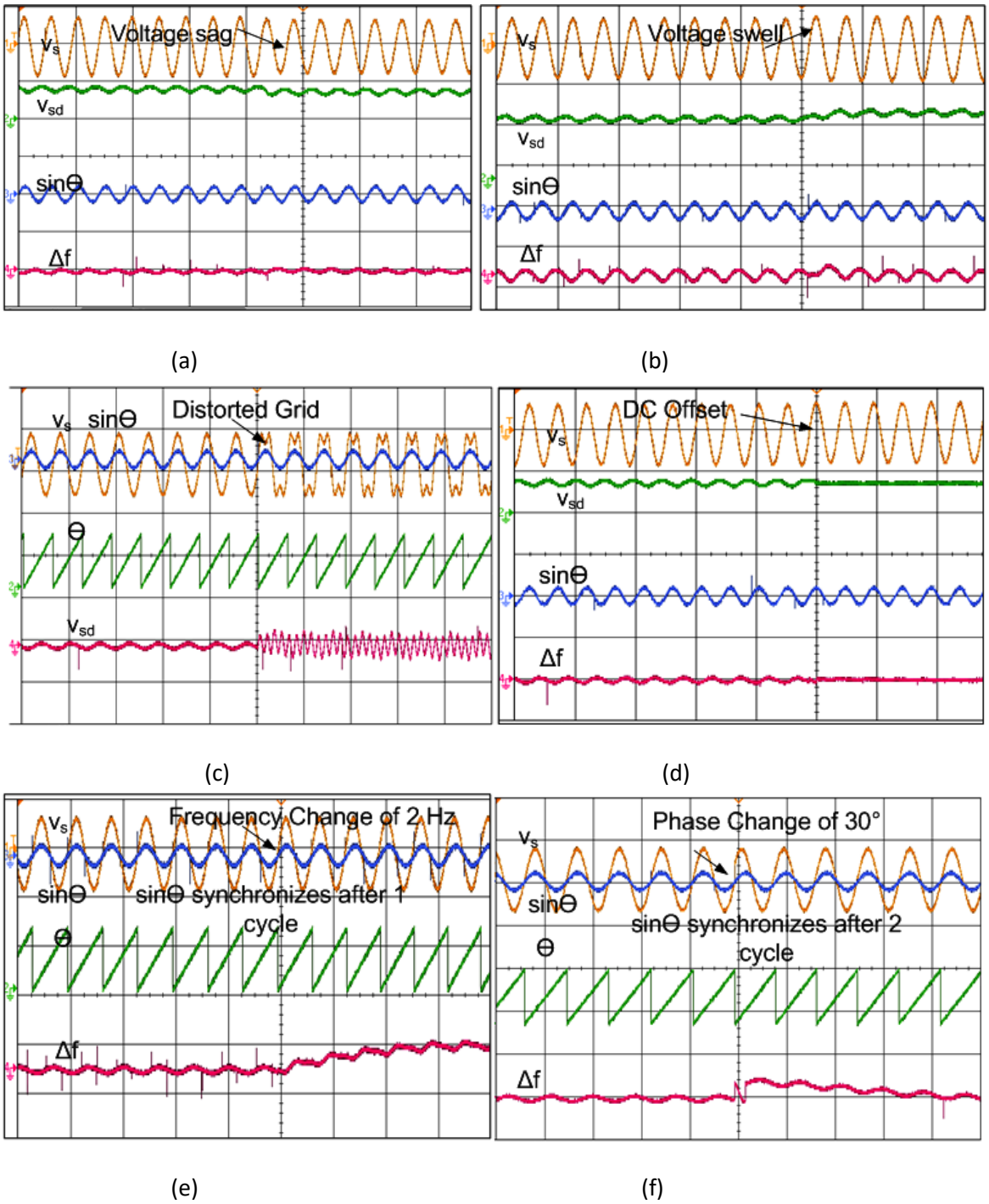

Fig. 6.12. Dynamic performance results of FD-NSLI algorithm as PLL under various grid conditions (a) voltage swell of 10% (b) voltage sag of 10% (c) Distorted Grid (d) 10% DC offset (e) phase change of 30º (f) frequency change to 52Hz on oscilloscope

phase with the voltage within 2-3 cycles. This shows the effectiveness of the designed PLL which works effectively.

However, the new frequency is tracked effectively showing that the proposed FD-NSLI controller works effectively as a PLL also.

6.3 Comparison Analysis of Different PLLs

Fig. 6.13 shows the comparison results for four PLLs viz. SOGI-PLL, SRFT-PLL, proposed QB-FBNN and FD-NSLI based PLL. In Fig. 6.13 (a) shows the harmonics in grid voltage having THD of 20%. It has been observed that the FD-NSLI PLL shows very minute oscillations in frequency. SOGI-PLL and QB-FBNN PLL show minimal oscillations and SRFT PLL shows very high amplitude oscillations hence poor performance. Fig. 6.13 (b) shows the grid voltage with 10% offset. Frequency estimation is observed in all the three cases. It has been found that SOGI PLL shows minimal oscillations and the high spikes are observed in frequency estimation with SRFT PLL; whereas QB-FBNN PLL does not work under DC offset. Fig. 6.13 (c) shows the variations in frequency during Phase change of 30º. It has been found SRFT shows the highest overshoot. FD-NSLI PLL shows medium overshoot whereas SOGI PLL and QB-FBNN PLL shows the minimum overshoot. However, frequency in FD-NSLI settles down very fast with in half cycle. Very minute oscillations are observed in SOGI PLL. Fig. 6.13 (d) shows the frequency change of 50Hz to 52Hz, it has been observed that SRFT PLL shows the highest overshoot in the beginning and then continuous sustained oscillations during this duration. FD-NSLI shows medium overshoot and SOGI PLL and QB FBNN PLL shows minimal overshoot. SOGI PLL

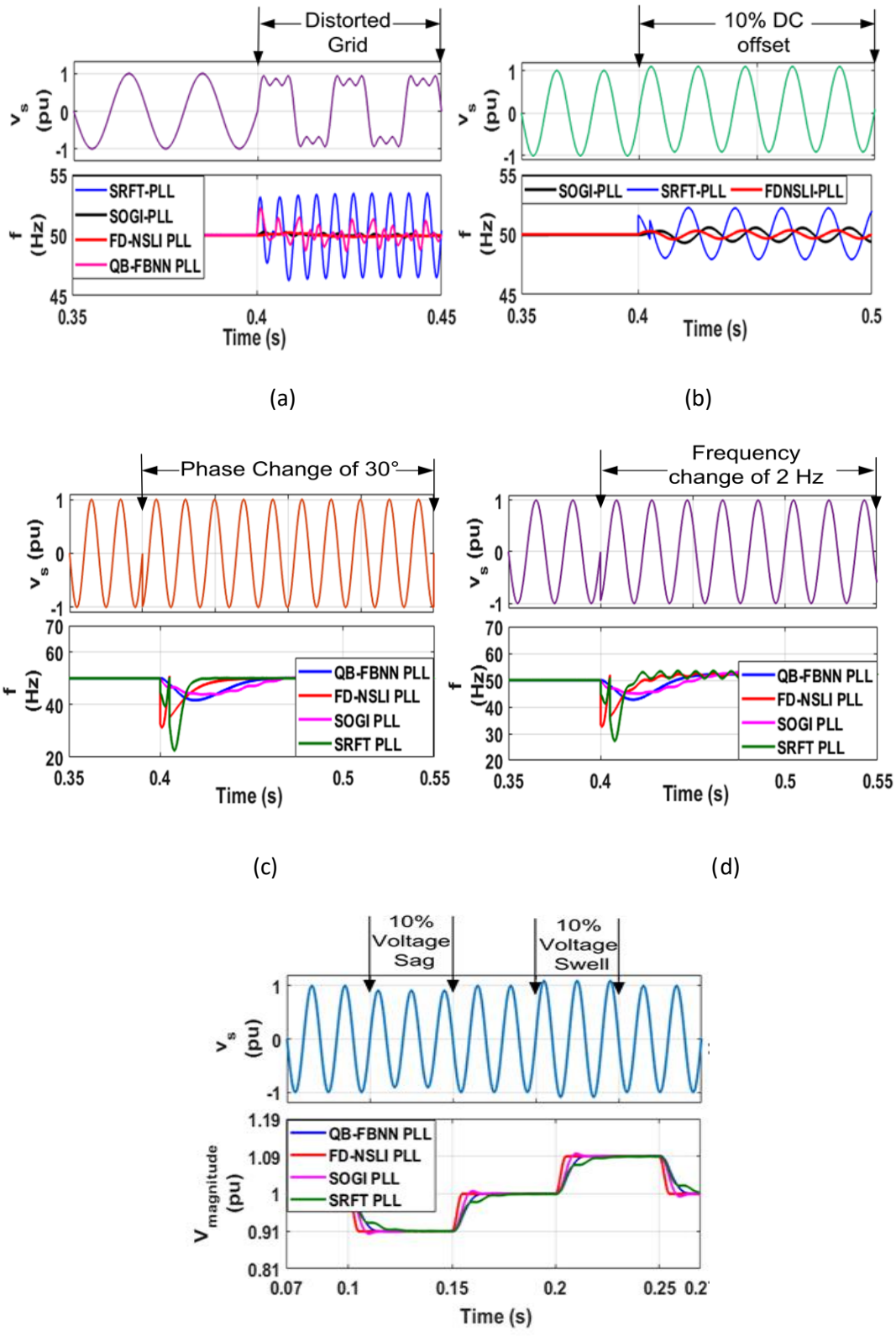

Fig. 6.13. Comparison analysis of various PLLs (a) Distorted Grid (b) 10% DC offset (c) Frequency characteristics during phase change of 30° (d) Frequency tracking during frequency change of 2Hz (e) for amplitude estimation under 10% voltage sag and swell

also shows minimal oscillations during steady state and FD-NSLI shows almost no oscillations.

Fig. 6.13 (e) shows the amplitude tracking ($v_{sd} = v_{magnitude}$) and the time taken by PLLs to settle down to steady state value has been recorded. FD-NSLI PLL takes vey less time to down settle down whereas SRFT PLL takes the highest time to settle down. Table 6.1 shows the comparison analysis in simulink of different PLL techniques under various weak grid condition parameters.

Table 6.1. Comparison analysis in simulink of different PLL techniques under various weak grid conditions

S.No	**Parameter**	**FD-NSLI PLL**	**QB-FBNN PLL**	**SOGI PLL**	**SRFT PLL**
1.	Complexity	Medium	Low	Medium	Medium
2.	Type	Adaptive	Adaptive	Non-Adaptive	Non-Adaptive
3.	Time taken for amplitude estimation under voltage sag and swell	0.75 cycle	0.5 cycle	2 cycles	0.5 cycle
4.	Oscillations in frequency in distorted grid	Negligible Amplitude Oscillations	Minimum Amplitude Oscillations	Medium Amplitude Oscillations	Very High Amplitude Sustained Oscillations
5.	Oscillations in frequency during dc offset	Negligible Amplitude Oscillations	Does Not work	Medium Amplitude Sustained Oscillations	Very High Amplitude Sustained Oscillations
6.	Oscillations in Frequency during Frequency change and Phase Change	Negligible Amplitude Oscillations	Minimum Amplitude Oscillations	Medium Amplitude Sustained Oscillations	Very High Amplitude Sustained Oscillations
7.	Overshoot/Undershoot in frequency characteristics during Phase change	Medium	Low	Low	Very High

9.	Time Taken by frequency to track Phase angle change	0.5 cycle	~3.5 cycle	5 cycles	2.5 cycles
10.	Time Taken by frequency to track frequency change	0.5 cycle	~3.5 cycle	5 cycles	2 cycles

6.4 Conclusions

This chapter discusses the design, mathematical modelling and analysis of different phase locked loop techniques viz SRFT PLL, SOGI PLL, FD-NSLI and QB-FBNN PLL. All the phase locked loops have been designed for grid synchronization. The PLL are designed to estimate grid phase angle, frequency change, voltage sag and swell conditions as well as distorted grid conditions under same test conditions. The results have been taken on Matlab-Simulink and validated through hardware studies. Detailed control analysis for the developed techniques has been performed. The performance of the system with FD-NSLI PLL gives the best results followed by QB-FBNN PLL, SOGI and SRFT PLL. All the PLLs have been tested extensively for achieving for grid synchronization under various test conditions such as voltage sag. swell, DC offset, harmonics, phase change and frequency change. It has been observed that the FD-NSLI PLL shows negligible oscillations in tracking frequency variations. QB-FBNN PLL and SOGI-PLL shows some minimal oscillations and SRFT PLL shows very high amplitude oscillations hence poor performance. Comparison of the new developed PLLs with the conventional PLLs such as SOGI PLL and SRFT PLL have also been discussed in detail. FD-NSLI PLL and QB-FBNN PLL show self-adaptive nature which makes the PLL fast and avoids tuning it under several disturbances. The proposed FD-NSLI PLL and QB-FNN PLLs are able to work as effective synchronization techniques

under weak grid conditions. The experimental results obtained in the chapter match the findings of the simulation results.

CHAPTER-7

PERFORMANCE ANALYSIS OF PV INTERFACED GRID CONNECTED SYSTEMS WITH BATTERY SUPPORT

7.0 General

This chapter discusses design and analysis of a PV based system with battery energy storage system connected to non-linear loads. The simulation of considered system is performed in Matlab using Simulink in both grid connected and islanded mode. The schematic diagram of PV based system with battery energy storage system is shown in Fig. 7.1. In grid connected mode, the controller is designed to operate in current control mode and performs shunt compensation and improves power factor of supply currents to unity. In islanded mode, the controller is designed to operate in voltage control mode. A Static Transfer Switch (STS) is used for bidirectional power flow and seamless transfer is possible between both the modes. The battery dynamics are controlled by bidirectional DC-DC converter. The flow of power between battery, PV and grid is controlled to maintain the power balance. Performance aspects of this integrated system are discussed with the Synchronous Reference Frame Theory (SRFT) and Grid Sequence Separator (GSS) based developed controllers.

7.1 Performance Analysis of PV Interfaced Grid system with Battery Support

The performance analysis in steady state and dynamic state characteristics of PV interfaced with battery grid connected systems is discussed below. The following controllers viz Synchronous Reference Frame Theory and Grid Sequence Separator Based Control are discussed in detail.

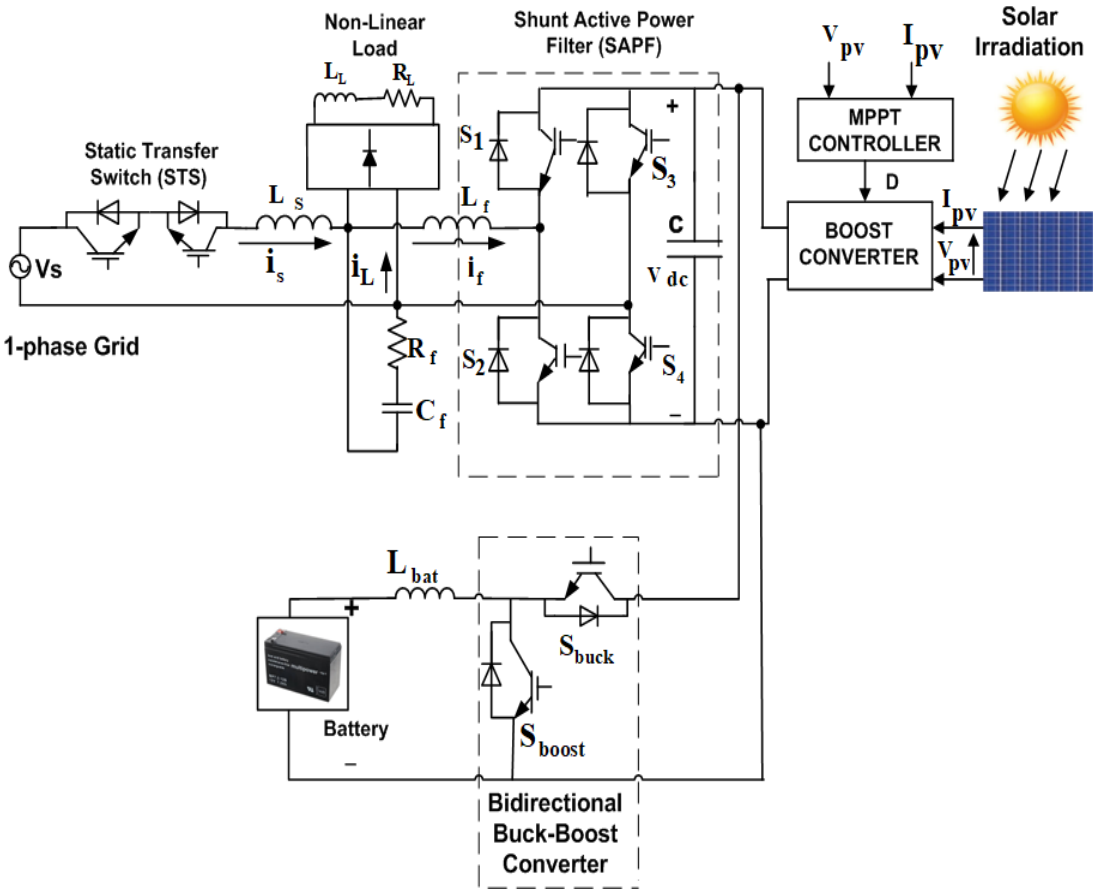

Fig. 7.1. Schematic diagram of battery interfaced PV integrated grid connected system

7.1.1 Synchronous Reference Frame Theory (SRFT)

The Synchronous Reference Frame theory-based control scheme is modelled and simulated in MATLAB environment under both grid connected and islanding mode of operation.

7.1.1.1 VSC in Current control Mode in the Grid Connected Case

A single-phase system can be represented as a two-phase orthogonal system in $\alpha\beta$ frame. The sensed grid connected current and voltages are taken in α frame. The signals in $'\beta'$ frame is generated by shifting the $'\alpha'$ frame by 90° lag. Using the above approach, the load current in $\alpha\beta$ frame is represented by

$$\begin{bmatrix} i_{L\alpha} \\ i_{L\beta} \end{bmatrix} = \begin{bmatrix} i_L(\omega t + \varphi) \\ i_L(\omega t + \varphi + \frac{\pi}{2} \end{bmatrix} \quad (7.1)$$

The stationary frame $i_{L\alpha}$ and $i_{L\beta}$ is transformed to synchronously rotating frame i_{Ld} and i_{Lq} by using Clark's transformation matrix

$$\begin{bmatrix} i_{Ld} \\ i_{Lq} \end{bmatrix} = \begin{bmatrix} \sin \omega t & -cos\omega t \\ cos\omega t & sin\omega t \end{bmatrix} \begin{bmatrix} i_{L\alpha} \\ i_{L\beta} \end{bmatrix} \quad (7.2)$$

where $\omega t = \theta$ is input phase angle information of grid voltage signal.

The load current i_{Ld} is decomposed to fundamental and harmonic active component of load current and i_{Lq} is decomposed to fundamental reactive and harmonic component of load current using appropriate low pass filters.

$$i_{Ld} = \overline{i_{Ld}} + \widetilde{i_{Ld}} \quad (7.3)$$

$$i_{Lq} = \overline{i_{Lq}} + \widetilde{i_{Lq}} \quad (7.4)$$

The fundamental component is thus extracted with the help of LPF and the load harmonics and the reactive power components are contributed by Shunt Active Power Filter. Thus, the controller is designed such that the supply current must meets the fundamental 'd' component of the load current and the 'q' component of load current is completely met by the compensator.

$$\begin{bmatrix} i_{LD}^* \\ i_{Lq}^* \end{bmatrix} = \begin{bmatrix} \overline{i_{Ld}} + 0 \\ 0 + 0 \end{bmatrix} \quad (7.5)$$

The reference source currents are produced by taking the inverse of Equation (7.2)

$$\begin{bmatrix} i_{s\alpha}^* \\ i_{s\beta}^* \end{bmatrix} = \begin{bmatrix} \sin \omega t & -cos\omega t \\ cos\omega t & sin\omega t \end{bmatrix}^{-1} \begin{bmatrix} \overline{i_{Ld}} \\ 0 \end{bmatrix} \quad (7.6)$$

$$\begin{bmatrix} i_{s\alpha}^* \\ i_{s\beta}^* \end{bmatrix} = \begin{bmatrix} \sin \omega t & cos\omega t \\ -cos\omega t & sin\omega t \end{bmatrix} \begin{bmatrix} \overline{i_{Ld}} \\ 0 \end{bmatrix} \quad (7.7)$$

However, a loss term i_{Loss} is incorporated in Equation (7.8)

$$i_{LD}^* = \overline{i_{Ld}} + i_{Loss} \quad (7.8)$$

The i_{Loss} is provided by the source current to maintain the constant DC link voltage and to meet the losses in the SAPF. The schematic diagram showing current control mode is shown in Fig. 7.2.

$$\begin{bmatrix} i_{s\alpha}^{*} \\ i_{s\beta}^{*} \end{bmatrix} = \begin{bmatrix} \sin\omega t & cos\omega t \\ -cos\omega t & sin\omega t \end{bmatrix} \begin{bmatrix} \overline{i_{Ld}} + i_{Loss} \\ 0 \end{bmatrix} \tag{7.9}$$

The PV and Battery contributions viz i_{PVff} and i_{battff} are reflected on the grid side and shown as

$$i_{pvff} = \frac{2*P_{pv}}{V_{sd}^{+}} \tag{7.10}$$

$$i_{battff} = \frac{2*P_{batt}}{V_{sd}^{+}} \tag{7.11}$$

The total current drawn from the grid is obtained by

$$i_{Lt} = i_{Lest} - i_{pvff} - i_{battff} \tag{7.12}$$

$$i_{s}^{*} = i_{Lt} * sin\theta \tag{7.13}$$

The difference between the actual source current and the reference source current is given to the hysteresis controller for the generation of pulses in current control mode

$$e_2 = i_{s}^{*} - i_{s} \tag{7.14}$$

7.1.1.2 VSC in Voltage Control Mode in Islanding Case

The aim of the islanded control is to work well when there is grid failure. A smooth transition from grid connected to islanded mode is always desired. The control diagram of the microgrid showing transition and voltage control mode in islanding case is shown in Fig. 7.2.

The controller action decides whether to operate the PV based battery integrated system either in islanding mode or grid connected mode. The magnitude (v_s) and frequency (f_s) generated by the grid must be comparable with that generated by load voltage (v_L)

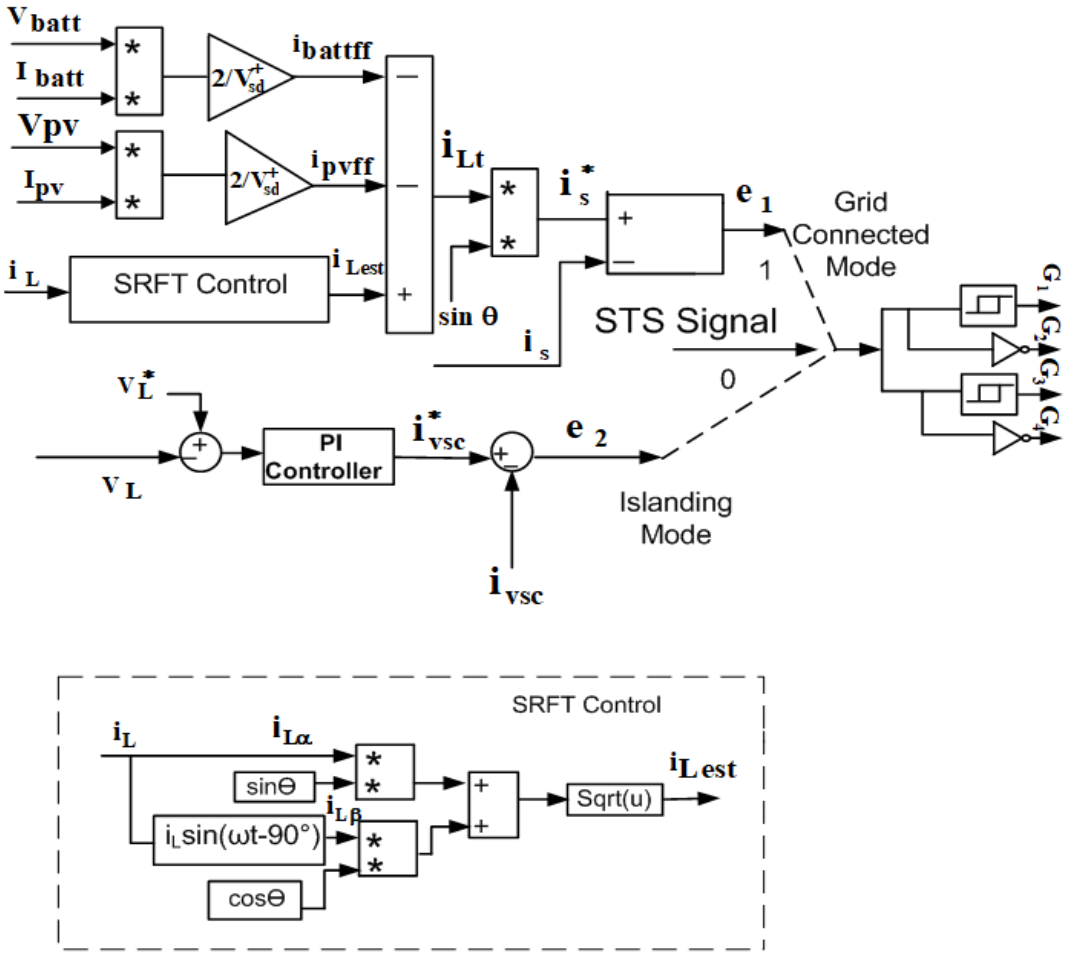

Fig. 7.2. Control Diagram of SRFT based Microgrid

and frequency (f_L) measured at PCC.

If the voltage and frequency of supply/grid are within the range (i.e. $0.9 < \mathrm{v}_s(\mathrm{pu}) < 1.05$ and $49.2Hz < f_s < 50.2Hz$) then '1' signal is given to the STS and when mismatch takes place then '0' signal is given to the STS, STS=1 denotes grid connected mode while STS=0 denotes islanded mode as shown in Fig. 7.2. A seamless transition to islanding mode is achieved as illustrated in flow chart in Fig. 7.3 (a) and graphical representation in Fig. 7.3 (b). In islanded mode, the reference PCC voltage is generated as

$$v_L^* = V_{mL} sin\omega t \tag{7.15}$$

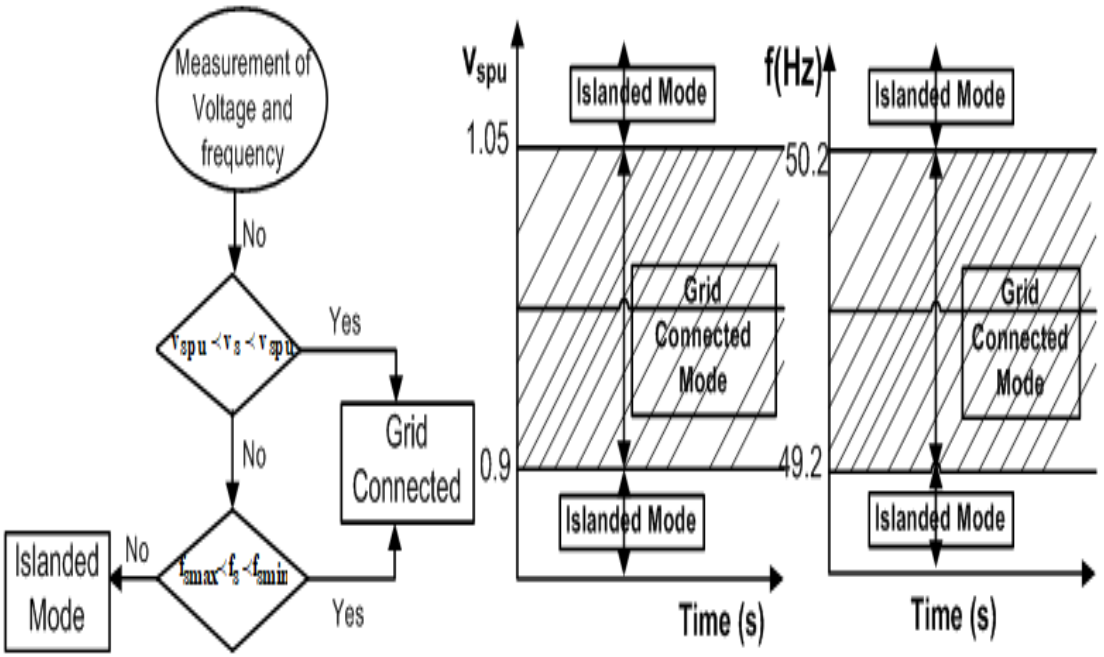

(a) (b)

Fig. 7.3. (a) Flow chart (b) Graphical representation for smooth transition between grid connected and Islanding Mode

The controller action decides whether to operate the PV based battery integrated system either in islanding mode or grid connected mode. The magnitude ($\boldsymbol{v_s}$) and frequency ($\boldsymbol{f_s}$) generated by the grid must be comparable with that generated by load voltage ($\boldsymbol{v_L}$) and frequency ($\boldsymbol{f_L}$) measured at PCC.

The PCC voltage (v_L) generated is compared with the sensed PCC Voltage and is fed to the PI controller and generates the reference VSC current.

$$e_1 = v_L^* - v_L \tag{7.16}$$

The PI controller output at 'm' instant is calculated as

$$i_{vsc}^*(m) = i_{vsc}^*(m-1) + K_{pv}\{v_L(m) - v_L(m-1)\} + K_{iv}v_L^* \tag{7.17}$$

The reference VSC current is compared with the sensed VSC current and given to the hysteresis controller for the generation of PWM pulses. This is depicted in Fig. 7.2.

7.1.3 Synchronization Controller for grid voltage and load voltage

It is used to generate θ_L and θ_s of load voltage and supply voltage simultaneously. The grid voltage and load voltage are used to compare the magnitude, phase angle and grid frequency by phase locked loop techniques. The schematic diagram of the synchronization controller is shown in Fig. 7.4.

Using the single-phase voltage (V_s) two orthogonal signals ($v_{s\alpha}, v_{s\beta}$) are generated from the single-phase voltage. The single-phase input from the grid voltage

$$v_{s\alpha} = V_m \sin \omega t \tag{7.18}$$

The delayed signal is given by

$$v_{s\beta} = V_m \sin(\omega t + \tfrac{\pi}{2}) \tag{7.19}$$

The orthogonal voltages are converted in to dq reference frame using Park transformation

$$\begin{bmatrix} v_{sd} \\ v_{sq} \end{bmatrix} = \begin{bmatrix} \sin \omega t & -cos\omega t \\ cos\omega t & sin\omega t \end{bmatrix} \begin{bmatrix} v_{s\alpha} \\ v_{s\beta} \end{bmatrix} \tag{7.20}$$

v_{sd} contains the information about the amplitude of the grid voltage and v_{sq} gives the information about the phase angle error. During ideal grid conditions when there are no harmonics and distortions, the estimated phase angle (θ) is equal to the grid angle (ωt).

$$v_{sd} = cos(\omega t - \theta) \tag{7.21}$$

$$v_{sq} = sin(\omega t - \theta) \tag{7.22}$$

The PLL is synchronized when the phase angle error is zero i.e. phase angle tracked by PLL is close to the actual voltage angle then the PLL is said to be locked, then $sin(\omega t - \theta) \approx (\omega t - \theta)$.

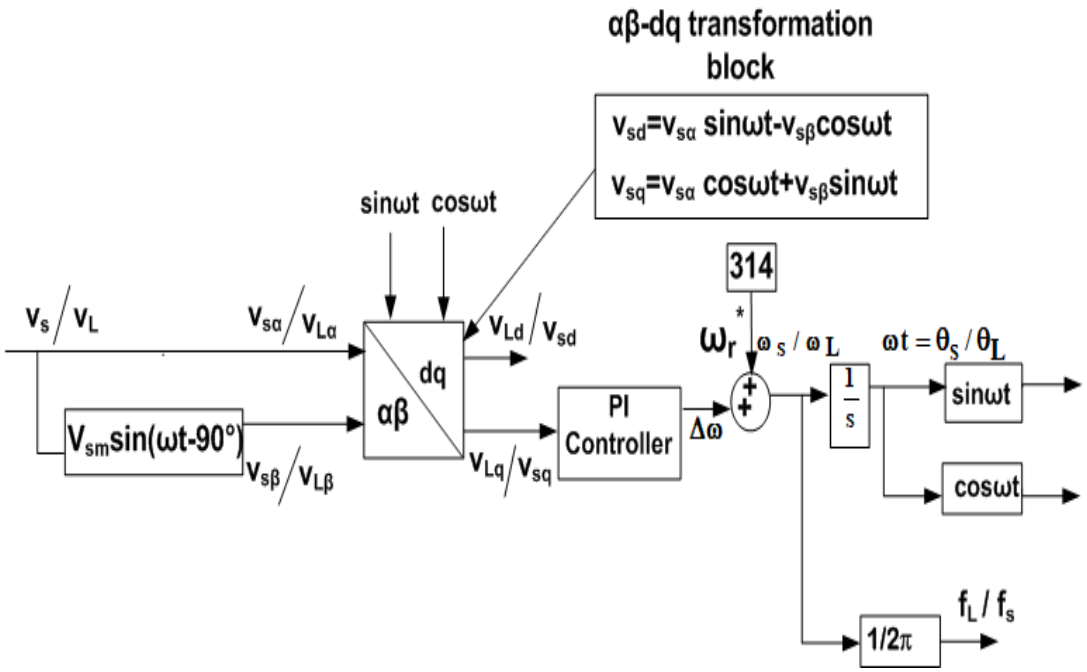

Fig. 7.4. Synchronization Controller for SRFT PLL

$$v_{sq} \approx (\omega t - \theta) \tag{7.23}$$

The PI controller is used to eliminate the steady state error and the output is fed back to generate the angle and sine values. It has been observed that any error in phase angle lock process will get reflected in q term.

v_{sq} obtained is applied as input to the PI controller whose output provides the error in angular frequency (Δω). This angular frequency error is added to the natural frequency (ω_r^*) to get the estimated angular frequency

$$\omega_{est} = \omega_r^* + \Delta\omega \tag{7.24}$$

The estimated frequency (ω_{est}) is integrated to get the grid voltage angle (θ_{est}) .

$$\int \omega_{est}\, dt = \theta_{est} \tag{7.25}$$

The estimated voltage angle (θ_{est}) is used to get the unit in-phase template and the quadrature template for generation of reference signal.

$$\omega_{est} = 2 * pi * f_s \tag{7.26}$$

The estimated source phase angle (θ_s) is compared with the load phase angle (θ_L) to detect the difference, the PLL voltage is compared with the load voltage magnitude and the f_s is compared with the f_L. If they are found to be in mentioned operating range then the grid connected mode is maintained otherwise control shifts to islanded mode.

7.2.2 Grid Sequence Separator (GSS)

The Grid Sequence Separator based control scheme is modelled and simulated in MATLAB environment under both grid connected and islanded mode of operation.

7.2.2.1 Current Control Mode in the Grid Connected Case

Grid Sequence Separator (GSS) based controller works on the principle of Delayed Signal Cancellation Technique. Here the time delayed version of the signal in dq frame is added to its actual signal to cancel the effect of individual harmonics. The control diagram is shown in Fig. 7.5.

$$i'_{Ldq} = \frac{1}{2}\left[i_{Ldq}(t) + i_{Ldq}\left(t - \frac{T_o}{n}\right)\right] \tag{7.27}$$

where T_o is the fundamental time period of the load current and n is the delay factor. The load current consisting of harmonic order h' can be defined in dq frame as

$$i_{Ld}^{h'} = I_h \cos(h'\omega t) \tag{7.28}$$

$$i_{Lq}^{h'} = I_h \sin(h'\omega t) \tag{7.29}$$

where $h' = h - 1$, h represents harmonic order in $\alpha\beta$ frame.

From (7.27), (7.28) and (7.29) and using trigonometric properties we get

$$i'_{Ldq} = I_h\left[\cos\left(h'\omega t - \frac{h'\pi}{n}\right) + j\sin\left(h'\omega t - \frac{h'\pi}{n}\right)\right]\cos\left(\frac{h'\pi}{n}\right) \tag{7.30}$$

Representing the above equation (7.30) in Euler form and polar form we get

$$i_{Ldq}^{h'} = \cos(\frac{h'\pi}{n}) \cdot e^{-j\frac{\pi h'}{n}} I_h e^{jh'\omega t} \tag{7.31}$$

$$= \cos\left(\frac{h'\pi}{n}\right) \angle -\frac{\pi h'}{n} \tag{7.32}$$

By selecting the suitable value of n and h', the required harmonics can be removed. It has been found that the harmonic order h' in dq frame is one less than h when studied in $\alpha\beta$ frame. Therefore, fifth harmonic in $\alpha\beta$ frame is removed when $h' = -6$ and n=4. Similarly, the 11th harmonic in $\alpha\beta$ frame is removed when $h' = -12$ and n=8.

GSS controller is transformed again to $\alpha\beta$ frame from dq frame

$$\begin{bmatrix} i_{L\alpha}^{'h}(t) \\ i_{L\beta}^{'h}(t) \end{bmatrix} = \frac{1}{2}\left\{ \begin{bmatrix} i_{L\alpha}^{h}(t) \\ i_{L\beta}^{h}(t) \end{bmatrix} \begin{bmatrix} \cos(\frac{2\pi}{n}) & -\sin(\frac{2\pi}{n}) \\ \sin(\frac{2\pi}{n}) & \cos(\frac{2\pi}{n}) \end{bmatrix} \begin{bmatrix} i_{L\alpha}^{h}\left(t - \frac{T_o}{n}\right) \\ i_{L\beta}^{h}\left(t - \frac{T_o}{n}\right) \end{bmatrix} \right\} \tag{7.33}$$

The estimated current from the GSS controller is calculated as

$$i_{Lest} = \sqrt{i_{L\alpha}^2 + i_{L\beta}^2} \tag{7.34}$$

The PV and Battery contribution reflected in the grid is shown by

$$i_{PVff} = \frac{2*P_{pv}}{V_{sd}^+} \tag{7.35}$$

$$i_{battff} = \frac{2*P_{batt}}{V_{sd}^+} \tag{7.36}$$

The total current drawn from the grid is obtained by

$$i_{Lt} = i_{Lest} - i_{pvff} - i_{battff} \tag{7.37}$$

$$i_s^* = i_{Lt} * sin\theta \tag{7.38}$$

The difference between the actual source current and the reference source current is given to the hysteresis controller for the generation of pulses in current control mode

$$e_2 = i_s^* - i_s \tag{7.39}$$

7.2.2.2 VSC in Voltage Control in Islanding mode

The aim of the designed controller is to have smooth transition from grid connected to islanded mode. The controller is used to operate the PV Based Battery integrated system either in islanding mode and grid connected mode. The magnitude (v_s) and frequency (f_s) generated by the grid must be comparable with that generated by load voltage (v_L) and frequency (f_L) measured at PCC.

If the voltage and frequency are within the range (i.e., $0.9 < V_s(pu) < 1.05$ and $49.2Hz < f_s < 50.2Hz$) then '1' signal is given to the STS and when mismatch takes place then '0' signal is given to the STS and seamless transition to islanding mode is achieved as illustrated in flow chart above in Fig. 7.3. In islanded mode, the reference PCC voltage is generated as

$$v_L^* = V_{mL} sin\omega t \tag{7.40}$$

The PCC voltage (v_L) generated is compared with the sensed PCC Voltage and is fed to the PI controller and generates the reference VSC current.

$$v_{eL} = v_L^* - v_L \tag{7.43}$$

The PI controller output at 'm' instant is calculated as

$$i_{vsc}^*(m) = i_{vsc}^*(m-1) + K_{pv}\{v_{eL}(m) - v_{eL}(m-1)\} + K_{iv} v_{eL}^* \tag{7.44}$$

The reference VSC current is compared with the sensed VSC current and given to the hysteresis controller for generation of PWM pulses.

7.2.2.3 Design of Synchronization Controller

It is used to generate θ_L and θ_s of load voltage and supply voltage simultaneously. The grid voltage and load voltage are used to compare the magnitude,

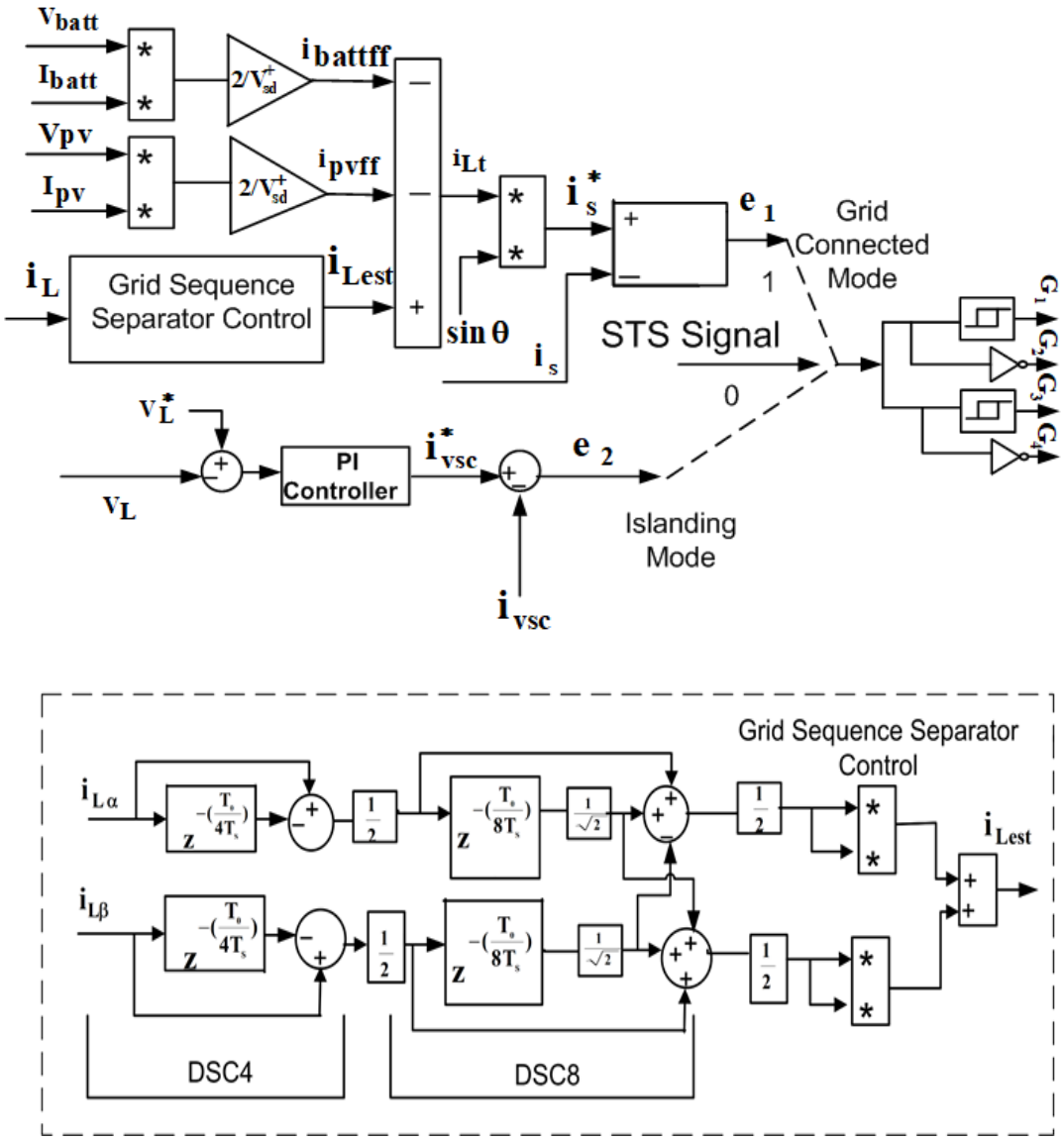

Fig. 7.5. Control Diagram of GSS controller based Microgrid

phase angle and grid frequency by Phase Locked Loop Techniques. The schematic diagram of the synchronization controller is shown in Fig. 7.6.

Grid Sequence Separator (GSS) PLL in $\alpha\beta$ frame is represented as

$$\begin{bmatrix} v'^{h}_{\alpha}(t) \\ v'^{h}_{\beta}(t) \end{bmatrix} = \frac{1}{2}\left\{ \begin{bmatrix} v^{h}_{\alpha}(t) \\ v^{h}_{\beta}(t) \end{bmatrix} \begin{bmatrix} \cos\left(\frac{2\pi}{n}\right) & -\sin\left(\frac{2\pi}{n}\right) \\ \sin\left(\frac{2\pi}{n}\right) & \cos\left(\frac{2\pi}{n}\right) \end{bmatrix} \begin{bmatrix} v^{h}_{\alpha}\left(t-\frac{T_o}{n}\right) \\ v^{h}_{\beta}\left(t-\frac{T_o}{n}\right) \end{bmatrix} \right\} \quad (7.45)$$

The orthogonal voltages are converted in to dq reference frame using Park transformation

$$\begin{bmatrix} v_d \\ v_q \end{bmatrix} = \begin{bmatrix} \sin \omega t & -cos\omega t \\ cos\omega t & sin\omega t \end{bmatrix} \begin{bmatrix} v_\alpha \\ v_\beta \end{bmatrix} \quad (7.46)$$

v_{sd} contains the information about the amplitude of the grid voltage and v_{sq} gives the information about the phase angle error. During ideal grid conditions when there are no harmonics and distortions, the estimated phase angle (θ) is equal to the grid angle (ωt).

$$v_{sd} = cos(\omega t - \theta) \quad (7.47)$$

$$v_{sq} = sin(\omega t - \theta) \quad (7.48)$$

The PLL is synchronized when the phase angle error is zero i.e phase angle tracked by PLL is closed to actual voltage angle and we say that PLL is locked, then $sin(\omega t - \theta) \approx (\omega t - \theta)$.

$$v_{sq} \approx (\omega t - \theta) \quad (7.49)$$

The PI controller is used to eliminate the steady state error and the output is fed back to generate the angle and sine/ cosine values of the tracked angle. It has been observed that any error in phase angle lock process will get reflected in V_q term

V_q is applied as input to the PI controller whose output provides the error in angular frequency (Δω). This angular frequency error is added to the natural frequency (ω_r^*) to get the estimated angular frequency

$$\omega_{est} = \omega_r^* + \Delta\omega \quad (7.50)$$

The estimated frequency (ω_{est}) is integrated to get the grid voltage angle (θ_{est}) .

$$\int \omega_{est}\, dt = \theta_{est} \quad (7.51)$$

The estimated voltage angle (θ_{est}) is used to get the unit in-phase template and the quadrature template for generation of reference signal.

$$\omega_{est} = 2 * pi * f_s \tag{7.52}$$

The estimated source phase angle (θ_s) is compared with the load phase angle (θ_L) to detect the range, the source voltage is compared with the load voltage magnitude and the f_s is compared with the f_L. If they are in given operating range then the grid connected mode is maintained otherwise islanded mode is achieved.

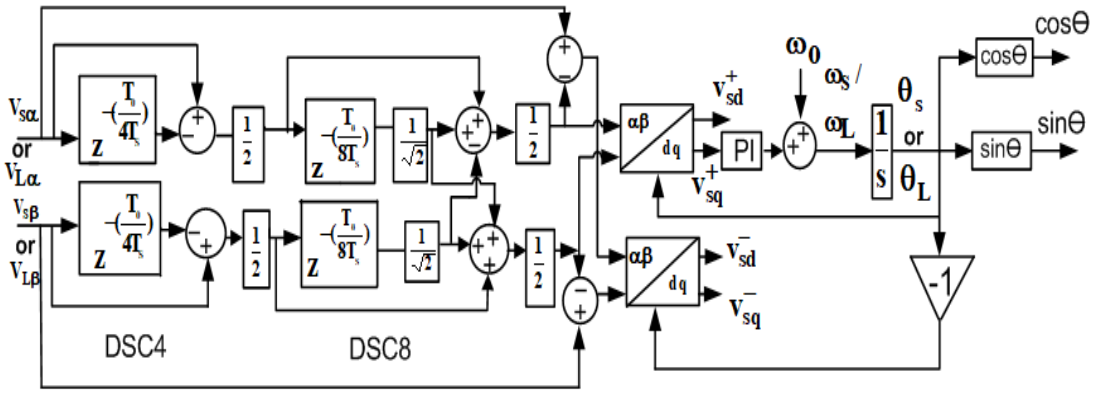

Fig. 7.6. Synchronization Controller for GSS-PLL

7.2 Simulation Results

This section discusses the performance aspects of SRFT and GSS based controller in PV interfaced battery connected system. The three PV Kyocera 320GX-LPB panels of 750W capacity is used delivering 660W at the DC link of inverter after double stage topology switching losses. The lead acid battery of 120V, 20Ah capacity is used and load of 7.5Ω and 40mH inductor is used. The active power demand of load is around 650W and after load increase the active power demand of load increases to 900W. The performance analysis under both grid connected and islanding mode is discussed.

7.2.1 Performance Analysis with SRFT Controller

7.2.1.1 Simulation response of PV-BES System in Grid connected and Islanded Mode

Fig. 7.7 shows the performance analysis of SRFT controller under grid connected and islanded mode. The response of waveforms of solar irradiation G (I_{rr}), source voltage (v_s), source current (i_s), load current (i_L), DC Link voltage (V_{dc}), compensator current (i_f) and PCC voltage (V_L) are recorded.

In grid connected mode with solar irradiation intensity of 1000 W/m^2 till 0.3s, the synchronization controller sends the '1' signal to the Static Transfer Switch (STS). The VSC is working in current control mode and the performs the function of shunt compensation. The source current is sinusoidal and in phase with the voltage. The THD in source current in SRFT controller is 2.18% when the load current THD is 29.19% shown in Fig. 7.8. The PCC voltage is sinusoidal. The DC link voltage is maintained at

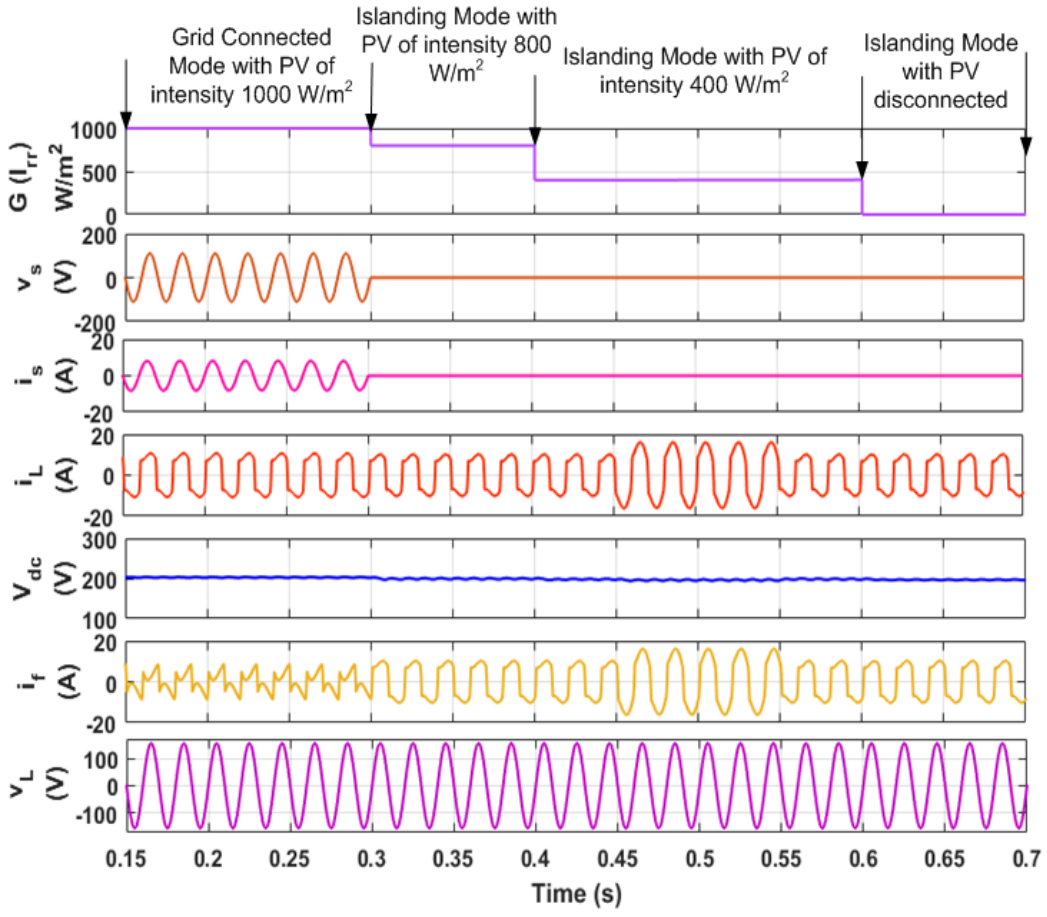

Fig. 7.7. Steady state voltage waveforms of SRFT controller under grid connected and islanded mode

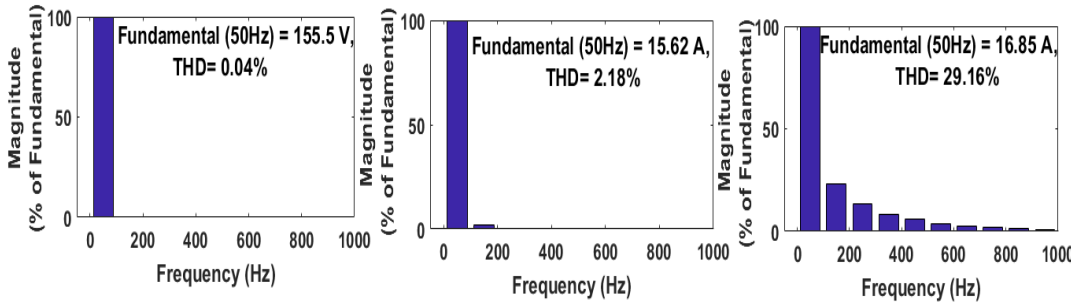

(b) (b) (c)

Fig. 7.8. THD of SRFT controller for (a) source voltage (v_s) (b) source current (i_s) and (c) load current (i_L) under non-linear load conditions in simulink

200V. The load needs 650W of power. Its 450W power is met by the source and remaining 200W is met by the PV. Remaining power of around 460W is used for charging the battery.

From 0.3s onwards, the grid is disconnected and performance of the system is discussed under islanded mode with varying PV irradiation intensity of 800W/m^2 and 400W/m^2. The synchronization controller sends the '0' signal to the Static Transfer Switch and the mode shifts from current control mode to islanding mode without any oscillations and transients.

Under islanding mode with solar irradiation intensity of 800W/m^2 from 0.3s to 0.4s shown in Fig. 7.9 and Fig. 7.10, the load demand of 550W is completely met by the PV array of 550W. It is observed that the I_{batt} is approximately zero and SOC is almost constant at 89.99998. The battery is neither charging nor discharging.

Under islanding mode with solar irradiation intensity of 400W/m^2 from 0.4s to 0.6s, the load demand of 500W is shared by both the PV source of 250W and the battery power of 250W. The increase in load is made from 0.45s to 0.55s, it has been found that the load power of 800W is met by the battery power of 500 W and PV power of 300W. The extra load is removed at 0.55s, and the load power condition of 500W is

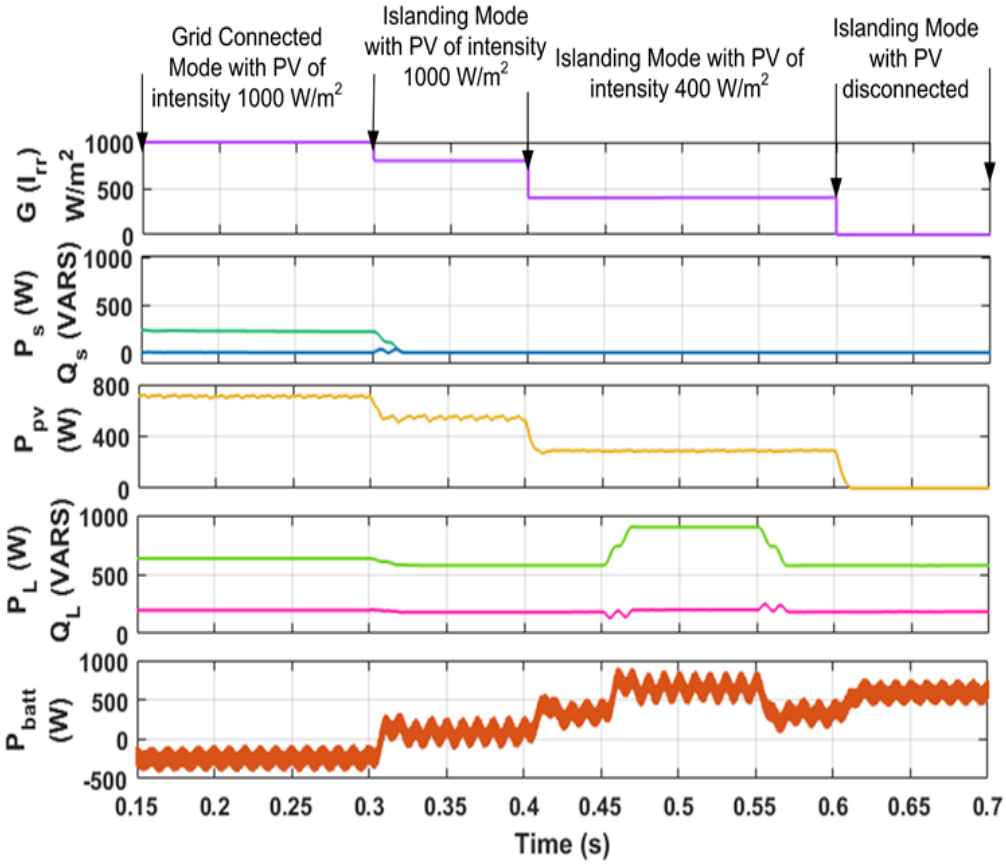

Fig. 7.10. Power waveforms of SRFT controller for developed system

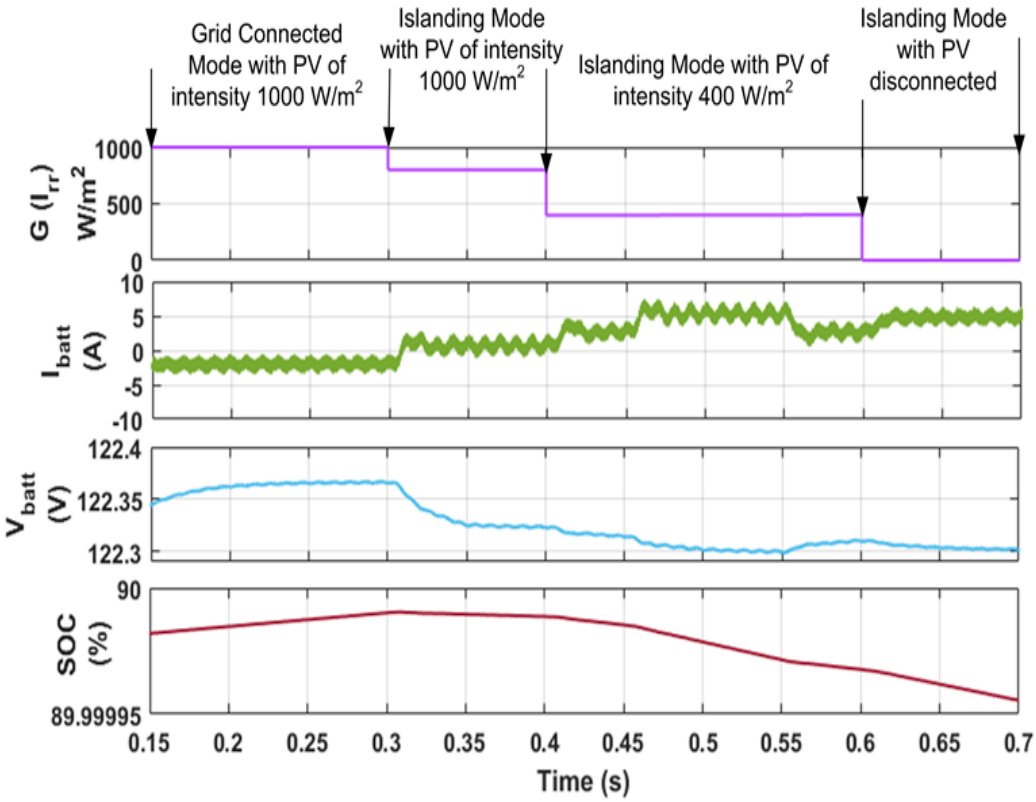

Fig. 7.9. Intermediate waveforms of SRFT Controller for developed system

again resumed.

After 0.6s, islanding mode with no PV irradiation is simulated load demand is met completely by the battery. The SOC is decreasing from 89.99999 to 89.99995. The I_{batt} is discharging with current of 8A and the battery voltage is decreasing. The total connected load is met by the battery. I_{batt} is discharging with current of 8A and the battery voltage is decreasing. The total connected load is met by the battery.

7.2.2 Performance Analysis with GSS Controller

7.2.2.1 Simulation Response of PV-BES System in Grid connected and Islanded Modes

Fig. 7.11 shows the performance of PV-BES system under grid connected and islanded mode. The results of solar irradiation G (I_{rr}), source voltage (v_s), source current (i_s), load current (i_L), DC Link voltage (V_{dc}), compensator current (i_f) and PCC voltage (v_L) are recorded.

Fig. 7.11 shows the results in grid connected mode with solar irradiation intensity of 1000W/m^2 till 0.3s. The source current is sinusoidal and in phase with the voltage. It meets the required load demand. The THD of source current in GSS controller is 1.86% when the load current THD is 29.19% The PCC voltage is also sinusoidal. The DC link voltage is maintained at 200 V value. In grid connected mode, the battery current is negative, which signifies charging mode. This is shown in Fig. 7.13. The battery voltage increases and the SOC is also linearly increasing as shown in Fig. 7.13. In grid connected mode shown in Fig. 7.14, the load power of 600 W is met by the grid power of 400W and 200W by PV power. The remaining PV power of 500 W is used for charging the battery.

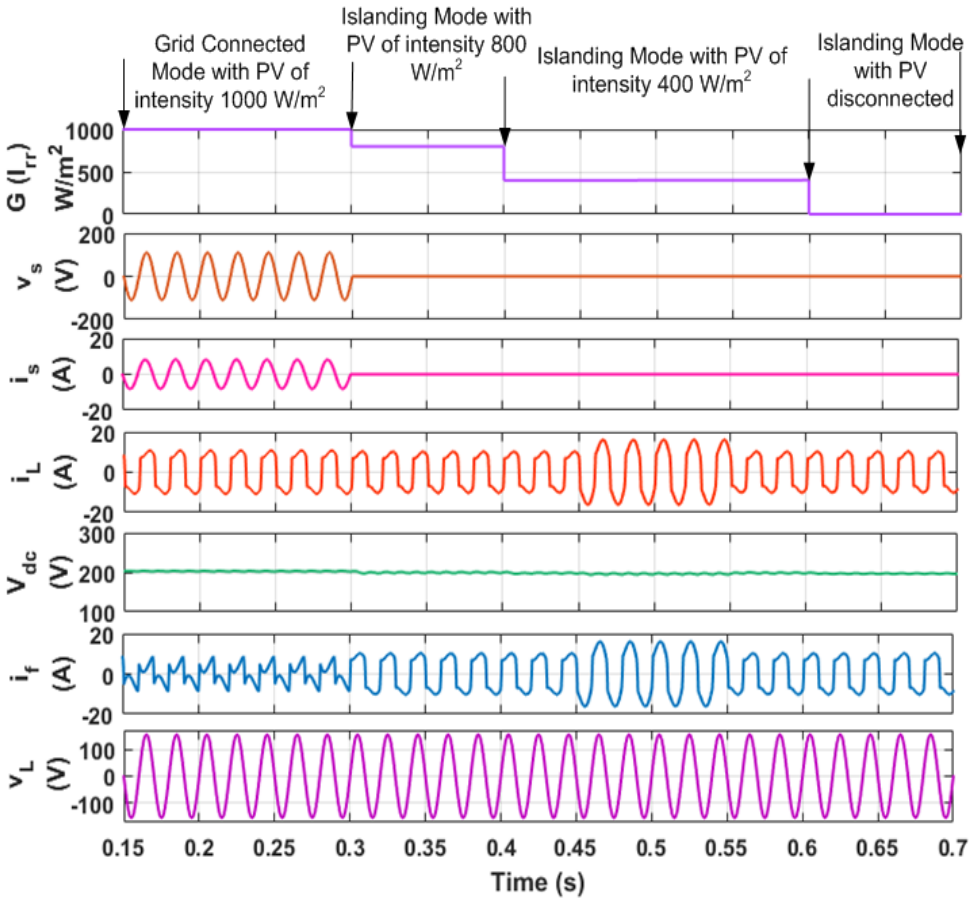

Fig. 7.11. Steady state voltage waveforms under grid connected and islanded mode of GSS controller for developed system

The synchronization controller sends the '0' signal to the Static Transfer Switch (STS) and islanding is achieved smoothly i.e., without any transients in voltage and current.

In islanding mode with 800W/m^2 from 0.3s to 0.4s, v_s and i_s are not present due to grid failure. The load power of 500W is completely met by the PV power of 500W. The battery is delivering zero power. SOC is maintained constant.

In islanding mode with 400W/m^2 from 0.4s to 0.6s, the battery is discharging with 2A current source. SOC also decreases slightly. The load power is shared by the PV power of 300W and battery power of 200W till 0.45s. The load is increased at 0.45s to 0.55s, it has been found that the load power of 800W is met by the battery power of

500W and PV power of 300W. The extra load is removed at 0.55s, and the load power condition of 500W is again resumed.

From 0.6s to 0.7s, the islanding mode is achieved with PV disconnected. The load demand of 500W is met completely by the battery power of 500W.

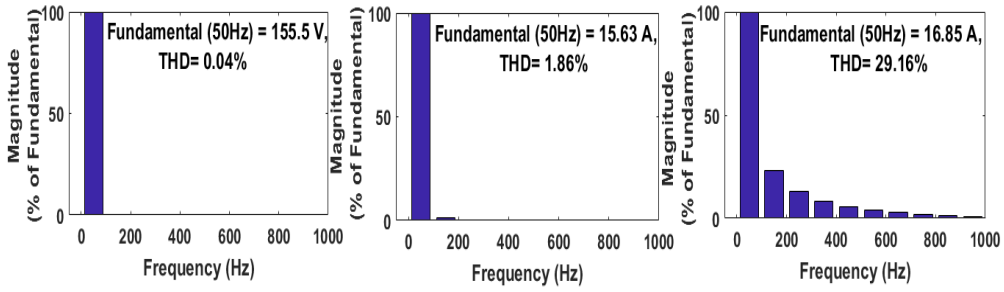

Fig. 7.12. THD of GSS controller for (a) source voltage (v_s) (b) source current (i_s) and (c) load current (i_L) under non-linear load conditions in simulink

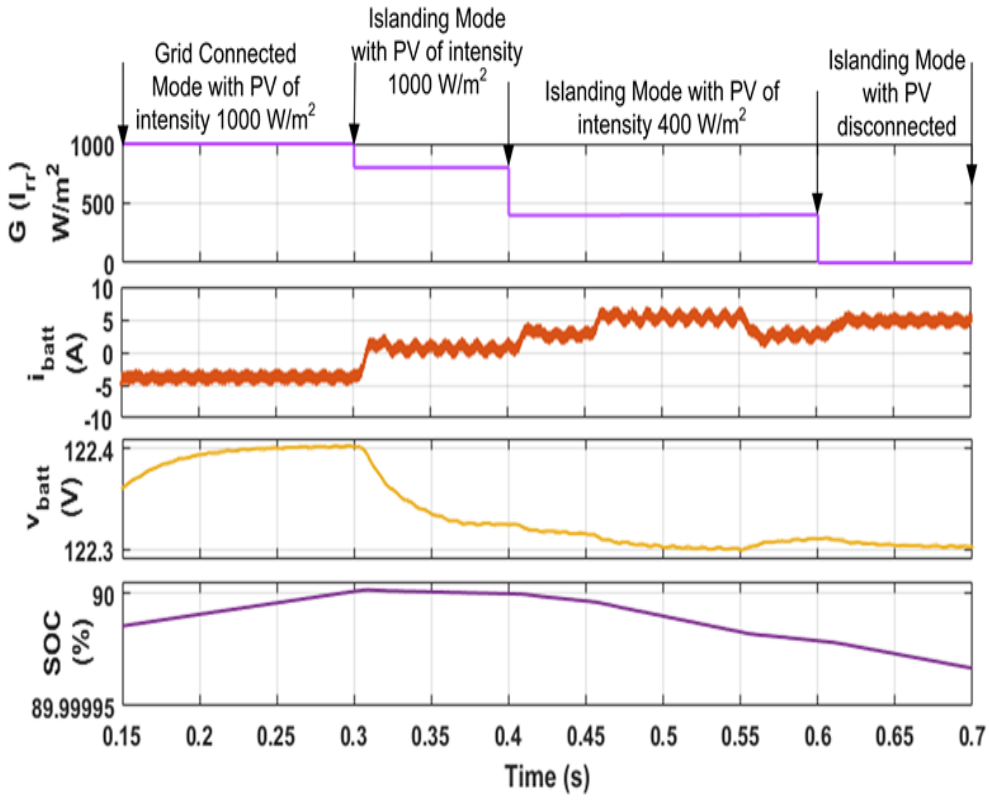

Fig. 7.13. Steady state intermediate waveforms of GSS based Controller for developed system

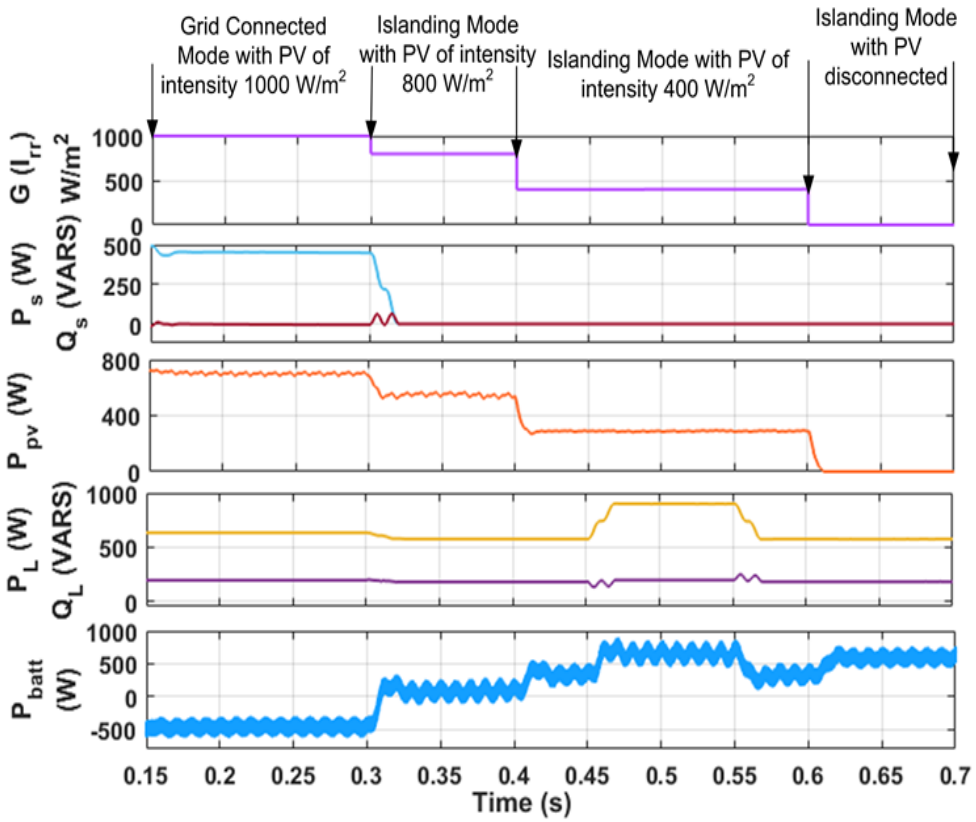

Fig. 7.14. Power waveforms of GSS controller for developed system

7.4 Comparison Evaluation of Proposed Control Schemes

The comparison analysis of the developed algorithms viz SRFT and GSS controller for shunt compensation in grid connected mode under load variation is shown

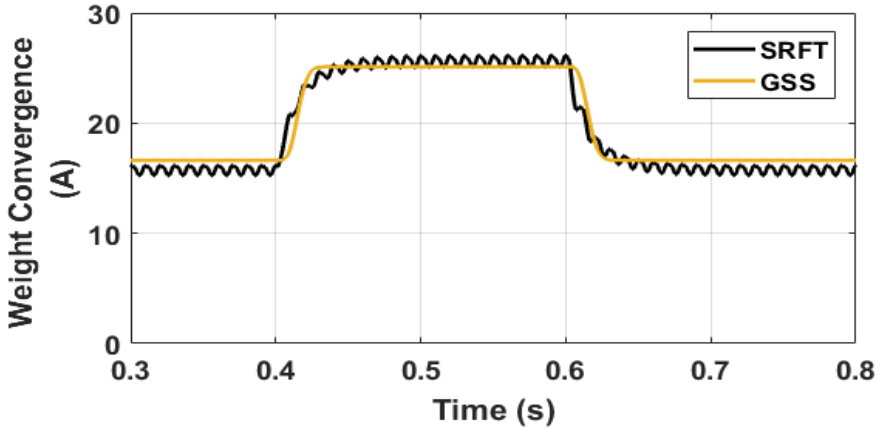

Fig. 7.15 Comparison of weight convergence analysis during load variations of different control algorithms in grid connected mode

in Fig. 7.15. The comparison is based on the various important parameters such as convergence rate, THD of supply current, settling time, oscillations and response time. The GSS controller shows fast transient response hence faster convergence rate and response time. It has negligible oscillations in steady state and dynamic state where as SRFT controller shows continuous oscillations under both steady state and dynamic state. The settling time of GSS PLL is at 0.05s whereas of SRFT PLL is 0.07s. The THD of GSS controller is 1.86% and THD of SRFT controller is 2.18%.

7.5 Conclusions

This chapter discusses the simulation, design and performance analysis of PV interfaced battery connected system in grid connected and islanding mode. The grid mode operation is discussed in current control mode and islanding operation is discussed in voltage control mode. The SRFT and Grid Sequence Separator (GSS) control are discussed in detail for both the modes. Simulation results have been shown for the improvement of PQ of PV interfaced battery system. Simulation test results have been taken for varying solar irradiation in both the modes under non-linear load conditions. The detailed analysis of GSS-control has been discussed in this chapter. Results show that the working of GSS control shows fast transient response hence faster convergence rate and response time during grid connected mode than SRFT control with THD in source current as 1.86%. Results show that the working of both the control in islanded mode are quite similar in performance aspects.

CHAPTER-8

CONCLUSIONS AND FUTURE SCOPE OF WORK

The main objective of the thesis work is to mitigate power quality problems in single-phase and three-phase grid connected distribution systems. The non-linear loads in PV integrated systems deteriorate the grid current and grid voltage. The mitigation objective is achieved by developing adaptive control algorithms for power quality improvement. Adaptive Phase locked Loop Techniques are developed under weak grid conditions of voltage sag, swell, DC-offset, frequency change and phase change. Simulation and hardware results have been performed to verify the efficiency of the control algorithms under various loading conditions i.e non-linear load, mixed loading conditions and linear loading conditions. The conclusion of the thesis work is discussed in the next section

8.1 Conclusions

Chapter 1 presents the introduction of the thesis work, which discusses the power quality issues in grid voltage and grid current due to non-linear loads in distribution systems and the state of art techniques to mitigate these power quality problems.

Chapter 2 discusses the literature review on current based power quality problems in single phase and three phase grid connected systems, phase locked loop techniques in weak grid connected systems and PV integrated battery connected systems in grid connected and islanding mode.

Chapter 3 discusses the design and analysis of PV integrated grid connected systems The configuration of SAPF, its design parameters and figures in single phase and three phase PV integrated grid connected systems. The design of PV array, inductor and

capacitor of boost converter and battery integrated grid connected systems parameters are discussed.

Chapter 4 This chapter discusses the design and development of four control algorithms viz SRFT, SOGI, TFLNN and LFNN controller for shunt compensation in PV integrated grid connected systems. The performance is tested under both Matlab Simulink developed model and on hardware setup in the laboratory. The performance analysis is discussed under different loading conditions i.e., linear, non-linear and mixed loading conditions along with changing solar irradiation conditions. The performance of the functional NN algorithms is compared with conventional algorithms viz SRFT and SOGI. The proposed LFNN and TFLNN algorithms are designed on the basis of functional series expansion and hence they are simple to implement and need less computation. A few terms of these expansion series have been found to be suitable and sufficient. These functional NNs have further been made adaptive. The real time training of the algorithms is done by LMS algorithm. It overcomes the need of PLL synchronization, Park–Clark transformation techniques as in conventional algorithms such as SRFT. The SRFT and SOGI techniques require transformation blocks and require tuning of gain constants to obtain the best response. Finally, a fair comparison of all the algorithms is performed the tracking performance of all the algorithms are performed under dynamic load variations. The proposed new algorithms LFNN and TFLNN meet the stipulated level of THD of below 5% for SAPF operation. Further, the performance of these algorithms is quite satisfactory under PV integration also.

Chapter 5 discusses the design mathematical modelling and analysis of algorithms viz Three Phase SRFT, DSOGI, AVSF and CB-FEBAF. The results have been taken on Matlab Simulink software and validated through hardware studies. The results without/with PV integration on three phase systems have been tested under linear load,

non-linear load and mixed loading conditions. Detailed control analysis for the developed systems is shown in the Chapter. The performance of the system with CB-FEBAF gives the best results followed by AVSF, DSOGI and Three Phase SRFT. Performance with the Three Phase SRFT technique shows continuous sustained oscillations in extracted current waveform in steady state and dynamic state conditions. The AVSF and CB-FEBAF algorithms are based on the functional expansion of the input and also made robust and adaptive by updating coefficients by LMS algorithm. The real time training helps to track the changes faster and give quick response under different loading conditions and irradiation conditions. The CB-FEBAF algorithm shows very fast transient response and almost no oscillations in steady state and dynamic state behavior. The AVSF and CB-FEBAF techniques are real time adaptive in nature therefore overcome the drawbacks of conventional time domain algorithms, SRFT and SOGI of tuning gain parameters 'K'. The functional techniques developed do not need PLL for generation of unit templates which make the algorithm complex. Hardware results are also in agreement with the simulation results.

Chapter 6 discusses the design mathematical modelling and analysis of algorithms viz SRFT PLL, SOGI PLL, FD-NSLI and QB-FBNN PLL and these algorithms have been designed for grid synchronization. The results have been taken on Matlab-Simulink and validated through hardware studies. Detailed control analysis for the developed systems has been done. The performance of the system with FD-NSLI PLL gives the best results followed by QB-FBNN PLL, SOGI and SRFT PLL. All the algorithms for PLL have been tested extensively for achieving grid synchronization under various test conditions. It has been observed that the FD-NSLI PLL shows almost no oscillations in tracking frequency, QB-FBNN PLL and SOGI-PLL show minimal oscillations and SRFT PLL shows very high amplitude oscillations

hence poor performance. Comparison with the conventional algorithms such as SOGI-PLL and SRFT PLL has also been discussed in detail in the chapter. The PLL are designed to estimate grid phase angle, frequency change, voltage sag and swell conditions as well as distorted grid conditions. Self-adaptive nature of the designed PLLs makes the controller fast and avoids tuning it under several disturbances thereby making the synchronization control effective. The experimental results obtained in both the cases match the findings of the simulation results.

Chapter 7 discusses the simulation, design and performance analysis of PV interfaced battery connected system in grid connected and islanding mode is discussed. The grid mode operation is discussed in current control mode and islanding operation is discussed in voltage control mode. The SRFT and Grid Sequence Separator (GSS) PLL control are developed and discussed in detail in both the modes. Simulation results have been shown for the improvement of PQ of PV interfaced battery system.

8.2 Future Scope of Work

The thesis work has discussed the design and mathematical model analysis of shunt compensation in single phase and three phase PV integrated grid connected systems. It also discusses design and analysis of different Phase locked loop techniques in weak grid connected systems. Further PV integrated battery systems are also designed and discussed in grid connected and islanding mode.

The PV integrated systems have been developed using Matlab Software. This work can be extended in hardware mode too. New control algorithms can be developed and tested for grid synchronization, large interconnected systems and work can be extended to larger size and multi machine systems. Stability aspects of different control algorithms can also be thoroughly investigated as an extension of this thesis.

LIST OF PUBLICATIONS

- **Papers (s) published in Peer Reviewed Referred International SCI Journals:**

  1. Arora A. Singh A.: 'Design and analysis of functional link artificial neural network controller for shunt compensation', IET Gener. Transm. Distrib., 2019, 13, (11), pp. 2280–2289.

  2. Arora, A., Singh, A.: Design and implementation of Legendre-based neural network controller in grid-connected PV systems. IET Renewable Power Gener 13(15), 2783– 2792 (2019) [Impact Factor: 1.435 (SCIE Indexed)]

  3. Ankita Arora, Alka Singh, Development and performance analysis of cubic Bezier functional expansion-based adaptive filter for grid-interfaced PV system, Wiley-International Transactions on Electrical Energy Systems, 10.1002/2050-7038.12840, 31, 10, (2021).

  4. Ankita Arora, Alka Singh, Design and analysis of Quadratic Bernstein Functional Blending Neural Network for shunt compensation and Phase Locked Loop, Springer-Electrical Engineering, 10.1007/s00202-022-01571-y, (2022).

  5. Ankita Arora, Alka Singh, Fractional Delay Newton structure for Lagrangian Interpolation in PV integrated Grid Connected System. (Under Review)

- **Paper(s) Published in Peer Reviewed International Conferences:**

  1. A. Arora and A. Singh, "Design and Implementation of Biquad Filter for Shunt Compensation under Normal and Distorted Grid Conditions," 2020 IEEE 9th Power India International Conference (PIICON), 2020, pp. 1-6, doi: 10.1109/PIICON49524.2020.9112949.

  2. A. Arora and A. Singh, "Design and Implementation of Grid Sequence Separator Based Control for Single-Phase Microgrid," 2020 IEEE 17th India Council International Conference (INDICON), 2020, pp. 1-7, doi: 10.1109/INDICON49873.2020.9342103.

REFERENCES

[1] B. Singh, A. Chandra, K. Al-Haddad, “Power Quality,Problems and Mitigation Techniques”, John Wiley and Sons, U.K., 2015.

[2] Antonio Moreno-Munoz, “Power Quality: Mitigation Technologies in a Distributed Environment”, Springer-Verlag London limited, London, 2007

[3] A. Ghosh and G. Ledwich, “Power Quality Enhancement Using Custom Power Devices”, Springer international Edition, New Delhi, India, 2009.

[4] Arrillaga, J., Watson, N.R., and Chen, S., “Power System Quality Assessment”, John Wiley & Sons, Inc., New York,2000.

[5] Bollen, H.J., “Understanding Power Quality Problems”, 1st edn, Standard Publishers Distributors, New Delhi, 2001.

[6] Sankaran, C., “Power Quality”, CRC Press, New York,2002.

[7] Moreno-Munoz, A., “Power Quality: Mitigation Technologies in a Distributed Environment”, Springer, London,2007.

[8] Kazibwe, W.E. and Sendaula, M.H., “Electrical Power Quality Control Techniques”, Van Nostrand Reinhold Company,1993.

[9] Bollen, M.H.J., “Understanding Power Quality Problems: Voltage Sags and Interruptions, IEEE Press Series on Power Engineering”, John Wiley & Sons, Inc., New York,2000.

[10] R. Ghandehari and A. Shoulaie, "Evaluating Voltage Notch Problems Arising from AC/DC Converter Operation," in *IEEE Transactions on Power Electronics*, vol. 24, no. 9, pp. 2111-2119, Sept. 2009, doi: 10.1109/TPEL.2009.2021058.

[11] Schlabbach, J., Blume, D., and Stephanblome, T., “Voltage Quality in Electrical Power Systems”, Power Engineering and Energy Series, IEEE Press,2001.

[12] Sung-Min Woo, Dae-Wook Kang, Woo-Chol Lee and Dong-Seok Hyun, "The distribution STATCOM for reducing the effect of voltage sag and swell," *IECON'01. 27th Annual Conference of the IEEE Industrial Electronics Society (Cat. No.37243)*, 2001, pp. 1132-1137 vol.2, doi: 10.1109/IECON.2001.975939.

[13] A. Luna et al., "Grid Voltage Synchronization for Distributed Generation Systems Under Grid Fault Conditions," in IEEE Transactions on Industry Applications, vol. 51, no. 4, pp. 3414-3425, July-Aug. 2015, doi: 10.1109/TIA.2015.2391436.

[14] R. N. Beres, X. Wang, M. Liserre, F. Blaabjerg and C. L. Bak, "A Review of Passive Power Filters for Three-Phase Grid-Connected Voltage-Source Converters," in *IEEE Journal of Emerging and Selected Topics in Power*

Electronics, vol. 4, no. 1, pp. 54-69, March 2016, doi: 10.1109/JESTPE.2015.2507203

[15] M. Liserre, F. Blaabjerg and S. Hansen, "Design and control of an LCL-filter based three-phase active rectifier," Conference Record of the 2001 IEEE Industry Applications Conference. 36th IAS Annual Meeting (Cat. No.01CH37248), 2001, pp. 299-307 vol.1, doi: 10.1109/IAS.2001.955428.

[16] J. C. Das, "Passive filters - potentialities and limitations," in IEEE Transactions on Industry Applications, vol. 40, no. 1, pp. 232-241, Jan.-Feb.2004, doi: 10.1109/TIA.2003.821666.

[17] E.F. El-Saadany, M.M.A. Salama and A.Y. Chikhani, "Passive filter design for harmonic reactive power compensation in single phase circuits supplying nonlinear loads", IEE Proc. Gen. Transm. and Distrib., vol. 147, pp. 373–380, 2000, doi: 10.1049/ip-gtd:20000654.

[18] H. Akagi, "Active Harmonic Filters," in *Proceedings of the IEEE*, vol. 93, no. 12, pp. 2128-2141, Dec. 2005, doi: 10.1109/JPROC.2005.859603.

[19] J. Nastran, R. Cajhen, M. Seliger and P. Jereb, "Active power filter for nonlinear AC loads," in *IEEE Transactions on Power Electronics*, vol. 9, no. 1, pp. 92-96, Jan. 1994, doi: 10.1109/63.285498.

[20] J. W. Dixon, J. J. Garcia and L. Moran, "Control system for three-phase active power filter which simultaneously compensates power factor and unbalanced loads," in *IEEE Transactions on Industrial Electronics*, vol. 42, no. 6, pp. 636-641, Dec. 1995, doi: 10.1109/41.475504.

[21] Y. Pal, A. Swarup and B. Singh, "A Review of Compensating Type Custom Power Devices for Power Quality Improvement," *2008 Joint International Conference on Power System Technology and IEEE Power India Conference*, 2008, pp. 1-8, doi: 10.1109/ICPST.2008.4745338.

[22] F. B. Libano, S. L. Muller, R. A. Marques Braga, J. V. Rossoni Nunes, O. S. Mano and I. A. Paranhos, "Simplified Control of the Series Active Power Filter for Voltage Conditioning," *2006 IEEE International Symposium on Industrial Electronics*, 2006, pp. 1706-1711, doi: 10.1109/ISIE.2006. 295827.

[23] Zhaoan Wang, Qun Wang, Weizheng Yao and Jinjun Liu, "A series active power filter adopting hybrid control approach," in *IEEE Transactions on Power Electronics*, vol. 16, no. 3, pp. 301-310, May 2001, doi: 10.1109/63.923761.

[24] L. Moran, P. Werlinger, J. Dixon and R. Wallace, "A series active power filter which compensates current harmonics and voltage unbalance simultaneously," *Proceedings of PESC '95 - Power Electronics Specialist Conference*, 1995, pp. 222-227, vol.1, doi: 10.1109/PESC.1995.474816.

[25] Y. R. Ikhe and M. Upadyay, "Novel control method for compensation of voltage sags and swells using dynamic voltage restorer," 2016 International Conference on Signal Processing, Communication, Power and Embedded System (SCOPES), 2016, pp. 59-62, doi: 10.1109/SCOPES.2016.7955521.

[26] J. G. Nielsen and F. Blaabjerg, "A detailed comparison of system topologies for dynamic voltage restorers," in *IEEE Transactions on Industry Applications*, vol. 41, no. 5, pp. 1272-1280, Sept.-Oct. 2005, doi: 10.1109/TIA.2005.855045.

[27] M. J. Newman, D. G. Holmes, J. G. Nielsen and F. Blaabjerg, "A dynamic voltage restorer (DVR) with selective harmonic compensation at medium voltage level," in *IEEE Transactions on Industry Applications*, vol. 41, no. 6, pp. 1744-1753, Nov.-Dec. 2005, doi: 10.1109/TIA.2005. 858212.

[28] D. D. Sabin, "Application Of Custom Power Devices For Enhanced Power Quality," IEEE Power Engineering Society. 1999 Winter Meeting (Cat. No.99CH36233), 1999, pp. 1126-1126, doi: 10.1109/PESW.1999.747362.

[29] J. S. Subjak and J. S. McQuilkin, "Harmonics-causes, effects, measurements, and analysis: an update," in *IEEE Transactions on Industry Applications*, vol. 26, no. 6, pp. 1034-1042, Nov.-Dec. 1990, doi: 10.1109/28.62384.

[30] A. Cavallini and G. C. Montanari, "Compensation strategies for shunt active-filter control," in *IEEE Transactions on Power Electronics*, vol. 9, no. 6, pp. 587-593, Nov. 1994, doi: 10.1109/63.334773.

[31] J. Hafner, M. Aredes and K. Heumann, "A shunt active power filter applied to high voltage distribution lines," in *IEEE Transactions on Power Delivery*, vol. 12, no. 1, pp. 266-272, Jan. 1997, doi: 10.1109/61.568249.

[32] T.-J. Park, G.-Y. Jeong and B.-H. Kwon, "Shunt active filter for reactive power compensation," International Journal of Electronics, vol. 88, iss. 12, pp.1257-1269, 2001, doi: https://doi.org/10.1080/00207210110092735.

[33] L. Xu, O. Anaya-Lara, V. G. Agelidis and E. Acha, "Development of prototype custom power devices for power quality enhancement," *Ninth International Conference on Harmonics and Quality of Power. Proceedings (Cat. No.00EX441)*, 2000, pp. 775-783, vol.3, doi: 10.1109/ICHQP.2000.896828.

[34] Xu, L., Agelidis, V.G., and Acha, E., "Development considerations of DSP-controlled PWM VSC-based STATCOM". IEE Proceedings – Electric Power Applications, 148(5), 449–455,2001, doi: 10.1049/ip-epa:20010527.

[35] V. Khadkikar and A. Chandra, "UPQC-S: A Novel Concept of Simultaneous Voltage Sag/Swell and Load Reactive Power Compensations Utilizing Series Inverter of UPQC," in *IEEE Transactions on Power Electronics*, vol. 26, no. 9, pp. 2414-2425, Sept. 2011, doi: 10.1109/TPEL.2011.2106222.

[36] P. E. Melin *et al*., "Analysis, Design and Control of a Unified Power-Quality Conditioner Based on a Current-Source Topology," in *IEEE Transactions on Power Delivery*, vol. 27, no. 4, pp. 1727-1736, Oct. 2012, doi: 10.1109/TPWRD.2012.2199524.

[37] Remus Teodorescu, Denmark Marco Liserre, Pedro Rodr´ıguez, "Grid Converters for Photovoltaic and Wind Power Systems", Power, Energy and Industry Applications, A John Wiley and Sons, Ltd., 2007.

[38] N. R. Tummuru, M. K. Mishra and S. Srinivas, "Dynamic Energy Management of Renewable Grid Integrated Hybrid Energy Storage System," in *IEEE Transactions on Industrial Electronics*, vol. 62, no. 12, pp. 7728-7737, Dec. 2015, doi: 10.1109/TIE.2015.2455063.

[39] M. H. Rehmani, M. Reisslein, A. Rachedi, M. Erol-Kantarci and M. Radenkovic, "Integrating Renewable Energy Resources Into the Smart Grid: Recent Developments in Information and Communication Technologies," in *IEEE* Transactions on Industrial *Informatics*, vol. 14, no. 7, pp. 2814-2825, July 2018, doi: 10.1109/TII.2018.2819169.

[40] Y. Xiong and X. Yang, "Government subsidies for the chinese photovoltaic industry," Energy Policy, vol. 99, pp. 111-119, Dec. 2016 https://doi.org/10.1016/j.enpol.2016.09.013

[41] B. Kroposki and B. Mather, "Rise of Distributed Power: Integrating Solar Energy into the Grid [Guest Editorial]," in *IEEE Power and Energy Magazine*, vol. 13, no. 2, pp. 14-18, March-April 2015, doi: 10.1109/MPE.2014.2381411.

[42] M. Karimi, H. Mokhlis, K. Naidu, S. Uddin and A.H.A. Bakar, "Photovoltaic penetration issues and impacts in distribution network—A review," Ren. Sustainable Energy Review, vol. 53, pp. 594–605, Jan. 2016. https://doi.org/10.1016/j.rser.2015.08.042.

[43] H. Liu, P. C. Loh, X. Wang, Y. Yang, W. Wang and D. Xu, "Droop Control With Improved Disturbance Adaption for a PV System With Two Power Conversion Stages," in *IEEE Transactions on Industrial Electronics*, vol. 63, no. 10, pp. 6073-6085, Oct. 2016, doi: 10.1109/TIE.2016.2580525.

[44] C. Jain and B. Singh, "An Adjustable DC Link Voltage-Based Control of Multifunctional Grid Interfaced Solar PV System," in *IEEE Journal of Emerging and Selected Topics in Power Electronics*, vol. 5, no. 2, pp. 651-660, June 2017, doi: 10.1109/JESTPE.2016.2627533.

[45] M. Mirhosseini, J. Pou and V. G. Agelidis, "Single- and Two-Stage Inverter-Based Grid-Connected Photovoltaic Power Plants With Ride-Through Capability Under Grid Faults," in *IEEE Transactions on Sustainable Energy*, vol. 6, no. 3, pp. 1150-1159, July 2015, doi: 10.1109/TSTE.2014.2347044.

[46] R. A. Mastromauro, M. Liserre and A. Dell'Aquila, "Control Issues in Single-Stage Photovoltaic Systems: MPPT, Current and Voltage Control," in *IEEE Transactions on Industrial Informatics*, vol. 8, no. 2, pp. 241-254, May 2012, doi: 10.1109/TII.2012.2186973.

[47] S. B. Kjaer, J. K. Pedersen and F. Blaabjerg, "A review of single-phase grid-connected inverters for photovoltaic modules," in *IEEE Transactions on Industry Applications*, vol. 41, no. 5, pp. 1292-1306, Sept.-Oct. 2005, doi: 10.1109/TIA.2005.853371.

[48] Y. Chen and K. Smedley, "Three-Phase Boost-Type Grid-Connected Inverter," in *IEEE Transactions on Power Electronics*, vol. 23, no. 5, pp. 2301-2309, Sept. 2008, doi: 10.1109/TPEL.2008.2003025.

[49] B. N. Alajmi, K. H. Ahmed, G. P. Adam and B. W. Williams, "Single-Phase Single-Stage Transformer less Grid-Connected PV System," in *IEEE*

Transactions on Power Electronics, vol. 28, no. 6, pp. 2664-2676, June 2013, doi: 10.1109/TPEL.2012.2228280.

[50] R. Khanaki, M. A. M. Radzi and M. H. Marhaban, "Comparison of ANN and P&O MPPT methods for PV applications under changing solar irradiation," *2013 IEEE Conference on Clean Energy and Technology (CEAT)*, 2013, pp. 287-292, doi: 10.1109/CEAT.2013.6775642.

[51] B. Subudhi and R. Pradhan, "A Comparative Study on Maximum Power Point Tracking Techniques for Photovoltaic Power Systems," in *IEEE Transactions on Sustainable Energy*, vol. 4, no. 1, pp. 89-98, Jan. 2013, doi: 10.1109/TSTE.2012.2202294.

[52] T. Esram and P. L. Chapman, "Comparison of Photovoltaic Array Maximum Power Point Tracking Techniques," in IEEE Transactions on Energy Conversion, vol. 22, no. 2, pp. 439-449, June 2007, doi: 10.1109/TEC.2006.874230.

[53] G. J. Kish, J. J. Lee and P. W. Lehn, "Modelling and control of photovoltaic panels utilising the incremental conductance method for maximum power point tracking," IET Renewable Power Generation, vol. 6, no. 4, pp. 259-266, July 2012.doi:10.1049/iet-rpg.2011.0052

[54] K. H. Hussein, I. Muta, T. Hoshino, and M. Osakada, "Maximum photovoltaic power tracking: An algorithm for rapidly changing atmospheric conditions," IEE Proc. Gener., Transmiss. Distrib., vol. 142, no. 1, pp. 59– 64, Jan. 1995, doi: 10.1049/ip-gtd:19951577.

[55] C. -S. Chiu and Y. -L. Ouyang, "Robust Maximum Power Tracking Control of Uncertain Photovoltaic Systems: A Unified T-S Fuzzy Model-Based Approach," in *IEEE Transactions on Control Systems Technology*, vol. 19, no. 6, pp. 1516-1526, Nov. 2011, doi: 10.1109/TCST.2010.2093900.

[56] E. Bianconi *et al*., "A Fast Current-Based MPPT Technique Employing Sliding Mode Control," in *IEEE Transactions on Industrial Electronics*, vol. 60, no. 3, pp. 1168-1178, March 2013, doi: 10.1109/TIE.2012.2190253.

[57] IEEE Working Group on Power System Harmonics, "Power system harmonics: an overview", IEEE Transactions on Power Apparatus and Systems, 102(8), 2455–2460,1983.

[58] Wakileh, M.G.J., "Power Systems Harmonics", Springer, New York,2001

[59] IEEE Recommended Practice and Requirements for Harmonic Control in Electric Power Systems," in IEEE Std 519-2014 (Revision of IEEE Std 519-1992) , pp.1-29, June 11 2014. doi: 10.1109/IEEESTD.2014.68264592.

[60] H. Lu, G. Wu and H. Biyawerwala, "Application of IEEE 1547-2018 on Large-scale DER Interconnections with Proposed Operation Mode and Control Method," 2020 IEEE/PES Transmission and Distribution Conference and Exposition (T&D), 2020, pp. 1-5, doi: 10.1109/TD39804.2020.9300006.

[61] IEEE, 1547-2018, "IEEE Standard for Interconnection and Interoperability of Distributed Energy Resources With Associated Electric Power Systems Interfaces", 2018

[62] IEEE Recommended Practice for Powering and Grounding Electronic Equipment, IEEE Std. 1100, 1999.

[63] IEEE Recommended Practice for Monitoring Electric Power Quality," in IEEE Std 1159- 2009 (Revision of IEEE Std 1159-1995) , vol., no., pp.c1-81, June 26 2009

[64] IEEE standard definitions for the measurement of electric power quantities under sinusoidal, non-sinusoidal, balanced, or unbalanced conditions," IEEE std. 1459, Mar, 19, 2010.

[65] Electromagnetic compatibility (EMC) - Part 4-15: Testing and measurement techniques - Flickermeter - Functional and design specifications, IEC Std. 61000, 4-15, 2010.

[66] IEC 61000-3-2 (1995) Electromagnetic Compatibility (EMC) – Part 3: Limits – Section 2: Limits for Harmonic Current Emissions (Equipment Input Current

[67] A. K. Barnes, J. C. Balda and C. M. Stewart, "Selection of converter topologies for distributed energy resources," *2012 Twenty-Seventh Annual IEEE Applied Power Electronics Conference and Exposition (APEC)*, 2012, pp. 1418-1423, doi: 10.1109/APEC.2012.6166006..

[68] B. Singh, P. Jayaprakash, D. P. Kothari, A. Chandra and K. A. Haddad, "Comprehensive Study of DSTATCOM Configurations," in *IEEE Transactions on Industrial Informatics*, vol. 10, no. 2, pp. 854-870, May 2014, doi: 10.1109/TII.2014.2308437.

[69] B. Singh, P. Jayaprakash and D. P. Kothari, "A T-Connected Transformer and Three-leg VSC Based DSTATCOM for Power Quality Improvement," in *IEEE Transactions on Power Electronics*, vol. 23, no. 6, pp. 2710-2718, Nov. 2008, doi: 10.1109/TPEL.2008.2004273.

[70] M. Forouzesh, Y. -F. Liu and P. C. Sen, "A Novel Soft-Switched Three-Phase Three-Wire Isolated AC-DC Converter With Power Factor Correction," *2022 IEEE Applied Power Electronics Conference and Exposition (APEC)*, 2022, pp. 887-894, doi: 10.1109/APEC43599.2022.9773554.

[71] Y. Hoon, M. A. M. Radzi, M. K. Hassan, and N. F. Mailah, "Enhanced instantaneous power theory with average algorithm for indirect current controlled three-level inverter-based shunt active power filter under dynamic state conditions," Mathematical Problems in Engineering, Vol. 2016, p. 12, 2016. https://doi.org/10.1155/2016/968251

[72] M. Adel, S. Zaid, and O. Mahgoub, "Improved active power filter performance based on an indirect current control technique," Journal of Power Electronics, Vol. 11, No. 6, pp. 931-937, Nov. 2011. https://doi.org/10.6113/JPE.2011.11.6.931

[73] B. N. Singh, A. Chandra and K. Al-Haddad, "Performance comparison of two current control techniques applied to an active filter," *8th International Conference on Harmonics and Quality of Power. Proceedings (Cat. No.98EX227)*, 1998, pp. 133-138 vol.1, doi: 10.1109/ICHQP.1998.759859.

[74] Singh, B.N., Chandra, A., and Al-Haddad, K. (2000) DSP-based indirect-current-controlled STATCOM. II. Multifunctional capabilities. IEE Proceedings – Electric Power Applications, vol. 147, no. (2), pp. 113–118, 2000 10.1049/ip-epa:20000067

[75] S. Rahmani, K. Al-Haddad, and H. Y. Kanan, "Experimental design and simulation of a modified PWM with an indirect current control technique applied to a single-phase shunt active power filter," in Proceedings of the IEEE International Symposium on Industrial Electronics (ISIE), Vol. 2, pp. 519-524, Jun. 2005, doi: 10.1109/ISIE.2005.1528971.

[76] G. M. Babu, "Simulation study of indirect current control technique for shunt active filter," International Journal of Engineering Research and Applications, Vol. 3, No. 4, pp. 831-851, Jul./Aug. 2013.

[77] R. Panigrahi, P. C. Panda and B. D. Subudhi, "Comparison of performances of hysteresis and dead beat controllers in active power filtering," 2012 IEEE Third International Conference on Sustainable Energy Technologies (ICSET), Kathmandu, 2012, pp. 287- 292. doi: 10.1109/ICSET.2012.6357413.

[78] P. Karuppanan, S. K. Ram and K. Mahapatra, "Three level hysteresis current controller based active power filter for harmonic compensation," *2011 International Conference on Emerging Trends in Electrical and Computer Technology*, 2011, pp. 407-412, doi: 10.1109/ICETECT.2011.5760151.

[79] F. Ucar, R. Coteli, and B. Dandil, "Three level inverter-based shunt active power filter using multi-level hysteresis band current controller," Electrical Review, vol. 88, no. 11A, pp. 227– 231, 2012.

[80] L. A. Moran, J. W. Dixon and R. R. Wallace, "A three-phase active power filter operating with fixed switching frequency for reactive power and current harmonic compensation," in *IEEE Transactions on Industrial Electronics*, vol. 42, no. 4, pp. 402-408, Aug. 1995, doi: 10.1109/41.402480.

[81] V. Khadkikar, M. Singh, A. Chandra and B. Singh, "Implementation of single-phase synchronous d-q reference frame controller for shunt active filter under distorted voltage condition," *2010 Joint International Conference on Power Electronics, Drives and Energy Systems & 2010 Power India*, 2010, pp. 1-6, doi: 10.1109/PEDES.2010.5712526.

[82] M. Labeeb and B. S. Lathika, "Design and analysis of DSTATCOM using SRFT and ANN-fuzzy based control for power quality improvement," 2011 IEEE Recent Advances in Intelligent Computational Systems, Trivandrum, 2011, pp. 274-279,doi: 10.1109/RAICS.2011.6069317.

[83] H. Akagi, Y. Kanazawad and A. Nabae, "Instantaneous reactive power compensators comprising switching devices without energy storage components", IEEE Trans. Ind. Appl., vol. 20, no. 3, pp. 625-630, May/June 1984, doi: 10.1109/TIA.1984.4504460.

[84] V. Khadkikar, A. Chandra and B.N. Singh, "Generalized Single-Phase p-q Theory for Active Power Filtering: Simulation and DSP based Experimental Investigation", IET Power Electronics, vol. 2, no. 1, pp. 67-78, January 2009, doi:10.1049/iet-pel:20070375.

[85] B. Singh, D. T. Shahani and A. K. Verma, "Power balance theory based control of grid interfaced solar photovoltaic power generating system with improved power quality," *2012 IEEE International Conference on Power Electronics, Drives and Energy Systems (PEDES)*, 2012, pp. 1-7, doi: 10.1109/PEDES.2012.6484359.

[86] G. Bhuvaneswari and M. G. Nair, "Design, Simulation, and Analog Circuit Implementation of a Three-Phase Shunt Active Filter Using the I-cos ϕ Algorithm," in *IEEE Transactions on Power Delivery*, vol. 23, no. 2, pp. 1222-1235, April 2008, doi: 10.1109/TPWRD.2007.908789

[87] B. Singh and J. Solanki, "A Comparison of Control Algorithms for DSTATCOM," in *IEEE Transactions on Industrial Electronics*, vol. 56, no. 7, pp. 2738-2745, July 2009, doi: 10.1109/TIE.2009.2021596.

[88] U. Tahir, S. A. Ali, O. Azeem, O. Khan and R. Muzzammel, "THD improvement of phase voltages via injection of voltage in neutral conductor for three phase four wire distribution system," *2018 International Conference on Computing, Mathematics and Engineering Technologies (iCoMET)*, 2018, pp. 1-5, doi: 10.1109/ICOMET.2018.8346393.

[89] Bhim Singh, A. Adya, A. P. Mittal and J. R. P. Gupta, "Modeling and control of DSTATCOM for three-phase, four-wire distribution systems," *Fourtieth IAS Annual Meeting. Conference Record of the 2005 Industry Applications Conference, 2005.*, 2005, pp. 2428-2434 Vol. 4, doi: 10.1109/IAS.2005.1518801.

[90] Singh, B., Jayaprakash, P., and Kothari, D.P. (2008) A three-phase four-wire DSTATCOM for power quality improvement. Journal of Power Electronics, 8(3), 259–267.

[91] L. W. Dixon, J. Garcia C. and T. Luis Moran, "A control system for a three phase active power filter which simultaneously compensates power factor and unbalanced loads," *Proceedings of IECON '93 - 19th Annual Conference of IEEE Industrial Electronics*, 1993, pp. 1083-1087 vol.2, doi: 10.1109/IECON.1993.339124.

[92] B. Singh, K. Al-Haddad and A. Chandra, "A new control approach to three-phase active filter for harmonics and reactive power compensation," in *IEEE Transactions on Power Systems*, vol. 13, no. 1, pp. 133-138, Feb. 1998, doi: 10.1109/59.651624.

[93] S. Haykin, “Neural networks and learning machines”, Pearson Education, Inc., Upper Saddle River, New Jersey 07458, 2009.

[94] M. Qasim, P. Kanjiya and V. Khadkikar, "Artificial-Neural-Network-Based Phase-Locking Scheme for Active Power Filters," in *IEEE Transactions on Industrial Electronics*, vol. 61, no. 8, pp. 3857-3866, Aug. 2014, doi: 10.1109/TIE.2013.2284132.

[95] S. R. Das, P. K. Ray and A. Mohanty, "Improvement of Power Quality using Advanced Artificial Neural Network Algorithm," *2018 IEEE International Conference on Power Electronics, Drives and Energy Systems (PEDES)*, 2018, pp. 1-6, doi: 10.1109/PEDES.2018.8707591.

[96] L. Hua, W. Yuguo and Z. Wei, "Power Quality Disturbances Detection and Classification Using Complex Wavelet Transformation and Artificial Neural Network," 2007 Chinese Control Conference, 2007, pp. 208-212, doi: 10.1109/CHICC.2006.4347508.

[97] N. Gupta, S. P. Singh and S. P. Dubey, "Neural network-based shunt active filter for harmonic and reactive power compensation under non-ideal mains voltage," *2010 5th IEEE Conference on Industrial Electronics and Applications*, 2010, pp. 370-375, doi: 10.1109/ICIEA.2010.5516896.

[98] A. Kumar and P. Kumar, "Power Quality Improvement for Grid-connected PV System Based on Distribution Static Compensator with Fuzzy Logic Controller and UVT/ADALINE-based Least Mean Square Controller," in *Journal of Modern Power Systems and Clean Energy*, vol. 9, no. 6, pp. 1289-1299, November 2021, doi: 10.35833/MPCE.2021.000285.

[99] C. N. Bhende, S. Mishra and S. K. Jain, "TS-fuzzy-controlled active power filter for load compensation," in *IEEE Transactions on Power Delivery*, vol. 21, no. 3, pp. 1459-1465, July 2006, doi: 10.1109/TPWRD.2005.860263.

[100] C.T. Lin and Lee, C. S. G., Neural Fuzzy Systems, A Neuro–Fuzzy Synergism to Intelligent Systems. Englewood Cliffs, NJ: Prentice-Hall, pp. 533–607.

[101] T. D. Raheni and P. Thirumoorthi, "Intelligent control of shunt active power filter for minimization of current harmonics," *TENCON 2017 - 2017 IEEE Region 10 Conference*, 2017, pp. 2846-2851, doi: 10.1109/TENCON.2017.8228346.

[102] S. Sinha and A. Arora, "Comparison of IRPT, ANN and ANFIS based Control Algorithm for Shunt Compensation in Grid Connected Systems," *2021 Asian Conference on Innovation in Technology (ASIANCON)*, 2021, pp. 1-6, doi: 10.1109/ASIANCON51346.2021.9544740.

[103] M. A. A. M. Zainuri, M. A. M. Radzi, N. F. A. A. Rahman, A. C. Soh and N. A. Rahim, "Single phase shunt active power filter with simplified ADALINE neural network," *3rd IET International Conference on Clean Energy and Technology (CEAT) 2014*, 2014, pp. 1-6, doi: 10.1049/cp.2014.1489.

[104] S. Haykin and T. Kailath, “Adaptive Filter Theory”, Pearson education, New Delhi, India, 2003.

[105] T. Adalı and S. Haykin, Adaptive Signal Processing Next Generation Solutions, John Wiley & Sons, Hoboken, New Jersey, 2010.

[106] A. Singh, M. Badoni and B. Singh, "Application of least means square algorithm to shunt compensator: An experimental investigation," 2014 IEEE International Conference on Power Electronics, Drives and Energy Systems (PEDES), Mumbai, 2014, pp. 1-6. doi: 10.1109/PEDES.2014.7042044

[107] S. R. Arya and B. Singh, "Performance of DSTATCOM Using Leaky LMS Control Algorithm," in IEEE Journal of Emerging and Selected Topics in Power Electronics, vol. 1, no. 2, pp. 104-113, June 2013. doi: 10.1109/JESTPE.2013.2266372

[108] P. K. Ray, "Power quality improvement using VLLMS based adaptive shunt active filter," in *CPSS Transactions on Power Electronics and Applications*, vol. 3, no. 2, pp. 154-162, June 2018, doi: 10.24295/CPSSTPEA.2018.00015.

[109] Hongbing Li, Ningning Tong, Nannan Liu and Jun Jiang, "A new variable-step-size LMS adaptive filtering algorithm," *2008 9th International Conference on Signal Processing*, 2008, pp. 38-41, doi: 10.1109/ICOSP.2008.4697063.

[110] E. Walach and B. Widrow, "The least mean fourth (LMF) adaptive algorithm and its family," in *IEEE Transactions on Information Theory*, vol. 30, no. 2, pp. 275-283, March 1984, doi: 10.1109/TIT.1984.1056886.

[111] E. Eweda, "Global Stabilization of the Least Mean Fourth Algorithm," in *IEEE Transactions on Signal Processing*, vol. 60, no. 3, pp. 1473-1477, March 2012, doi: 10.1109/TSP.2011.2177976.

[112] R. K. Agarwal, I. Hussain and B. Singh, "Implementation of LLMF Control Algorithm for Three-Phase Grid-Tied SPV-DSTATCOM System," in *IEEE Transactions on Industrial Electronics*, vol. 64, no. 9, pp. 7414-7424, Sept. 2017, doi: 10.1109/TIE.2016.2630659.

[113] M. Srinivas, I. Hussain and B. Singh, "Combined LMS–LMF-Based Control Algorithm of DSTATCOM for Power Quality Enhancement in Distribution System," in *IEEE Transactions on Industrial Electronics*, vol. 63, no. 7, pp. 4160-4168, July 2016, doi: 10.1109/TIE.2016.2532278.

[114] G. Gui and F. Adachi, "Adaptive sparse system identification using normalized least-mean fourth algorithm," Int. J. Commun. Syst., vol. 28, no. 1, pp. 38–48, 2015. https://doi.org/10.1002/dac.2637.

[115] M. Badoni, A. Singh and B. Singh, "Comparative Performance of Wiener Filter and Adaptive Least Mean Square-Based Control for Power Quality Improvement," in IEEE Transactions on Industrial Electronics, vol. 63, no. 5, pp. 3028-3037, May 2016. doi: 10.1109/TIE.2016.2515558.

[116] M. Badoni, A. Singh and B. Singh, "Adaptive Neuro-fuzzy Inference System Least-Mean Square-Based Control Algorithm for DSTATCOM," in IEEE Transactions on Industrial Informatics, vol. 12, no. 2, pp. 483-492, April 2016. doi: 10.1109/TII.2016.2516823.

[117] Singh, Yashi; Hussain, Ikhlaq; Singh, Bhim; Mishra, Sukumar: 'Single-phase solar grid-interfaced system with active filtering using adaptive linear combiner filter-based control scheme', IET Generation, Transmission & Distribution, 2017, 11, (8), p. 1976-1984, DOI: 10.1049/iet-gtd.2016.1392.

[118] N. Kumar, I. Hussain, B. Singh and B. K. Panigrahi, "Implementation of Multilayer Fifth-Order Generalized Integrator-Based Adaptive Control for Grid-Tied Solar PV Energy Conversion System," in *IEEE Transactions on Industrial Informatics*, vol. 14, no. 7, pp. 2857-2868, July 2018, doi: 10.1109/TII.2017.2777882.

[119] N. Kumar, I. Hussain, B. Singh and B. K. Panigrahi, "Normal Harmonic Search Algorithm-Based MPPT for Solar PV System and Integrated With Grid Using Reduced Sensor Approach and PNKLMS Algorithm," in *IEEE Transactions on*

Industry Applications, vol. 54, no. 6, pp. 6343-6352, Nov.-Dec. 2018, doi: 10.1109/TIA.2018.2853744.

[120] H. Komurcugil, N. Altin, S. Ozdemir and I. Sefa, "Lyapunov-Function and Proportional-Resonant-Based Control Strategy for Single-Phase Grid-Connected VSI With LCL Filter," in *IEEE Transactions on Industrial Electronics*, vol. 63, no. 5, pp. 2838-2849, May 2016, doi: 10.1109/TIE.2015.2510984.

[121] C. Meza, D. Biel, D. Jeltsema and J. M. A. Scherpen, "Lyapunov-Based Control Scheme for Single-Phase Grid-Connected PV Central Inverters," in *IEEE Transactions on Control Systems Technology*, vol. 20, no. 2, pp. 520-529, March 2012, doi: 10.1109/TCST.2011.2114348.

[122] N. Arab, B. Kedjar, A. Javadi and K. Al-Haddad, "A Multifunctional Single-Phase Grid-Integrated Residential Solar PV Systems Based on LQR Control," in *IEEE Transactions on Industry Applications*, vol. 55, no. 2, pp. 2099-2109, March-April 2019, doi: 10.1109/TIA.2018.2883551.

[123] J.-H. Kim, S. -W. Lee, S. -R. Lee, T. -W. Lee and C. -Y. Won, "Power quality control using the Goertzel algorithm for grid-connected system," *INTELEC 2009 - 31st International Telecommunications Energy Conference*, 2009, pp. 1-3, doi: 10.1109/INTLEC.2009.5351931.

[124] Y. Singh, I. Hussain, S. Mishra, and B. Singh, "Adaptive neuron detection-based control of single-phase SPV grid integrated system with active filtering," IET Power Electronics, vol. 10, pp. 657-666, 2017, https://doi.org/10.1049/iet-pel.2016.0613.

[125] Tsai-Fu Wu, Hung-Shou Nien, Chih-Lung Shen and Tsung-Ming Chen, "A single-phase inverter system for PV power injection and active power filtering with nonlinear inductor consideration," in *IEEE Transactions on Industry Applications*, vol. 41, no. 4, pp. 1075-1083, July-Aug. 2005, doi: 10.1109/TIA.2005.851035.

[126] A. Chatterjee and K. B. Mohanty, "Control of single-phase power inverter using model predictive controller for grid integrated renewable energy systems," *2016 IEEE Region 10 Conference (TENCON)*, 2016, pp. 1678-1681, doi: 10.1109/TENCON.2016.7848303.

[127] G. A. Fogli, M. C. de Fernandes, J. A. T. de Faria, P. G. Barbosa and P. M. de Almeida, "A Single-phase Distributed Generation System with Load Power Compensation Capability using Linear Quadratic Regulator," *2018 13th IEEE International Conference on Industry Applications (INDUSCON)*, 2018, pp. 474-481, doi: 10.1109/INDUSCON.2018.8627284.

[128] H. Khalfalla, S. Ethni, M. Al-Greer, V. Pickert, M. Armstrong and V. T. Phan, "An adaptive proportional resonant controller for single phase PV grid connected inverter based on band-pass filter technique," 2017 11th IEEE International Conference on Compatibility, Power Electronics and Power Engineering (CPE-POWERENG), 2017, pp. 436-441, doi: 10.1109/CPE.2017.7915211.

[129] N. Kumar, B. Singh and B. K. Panigrahi, "ANOVA Kernel Kalman Filter for Multi-Objective Grid Integrated Solar Photovoltaic-Distribution Static Compensator," in *IEEE Transactions on Circuits and Systems I: Regular Papers*, vol. 66, no. 11, pp. 4256-4264, Nov. 2019, doi: 10.1109/TCSI.2019.2922405.

[130] M. Salimi, J. Soltani and A. Zakipour, "Experimental design of the adaptive backstepping control technique for single-phase shunt active power filters", IET Power Electron., vol. 10, no. 8, pp. 911-918, 2017. https://doi.org/10.1049/iet-pel.2016.0366

[131] V. N. Jayasankar and U. Vinatha, "Backstepping Controller With Dual Self-Tuning Filter for Single-Phase Shunt Active Power Filters Under Distorted Grid Voltage Condition," in IEEE Transactions on Industry Applications, vol. 56, no. 6, pp. 7176-7184, Nov.-Dec. 2020, doi: 10.1109/TIA.2020.3025520.

[132] M. Cirrincione, M. Pucci and G. Vitale, "A Single-Phase DG Generation Unit with Shunt Active Power Filter Capability by Adaptive Neural Filtering," in *IEEE Transactions on Industrial Electronics*, vol. 55, no. 5, pp. 2093-2110, May 2008, doi: 10.1109/TIE.2008.918642.

[133] P. Shah, I. Hussain, B. Singh, A. Chandra and K. Al-Haddad, "GI-Based Control Scheme for Single-Stage Grid Interfaced SECS for Power Quality Improvement," in *IEEE Transactions on Industry Applications*, vol. 55, no. 1, pp. 869-881, Jan.-Feb. 2019, doi: 10.1109/TIA.2018.2866375.

[134] P. Shah, I. Hussain, B. Singh, A. Chandra and K. Al-Haddad, "Optimal control scheme for single stage grid interfaced SECS for power quality improvement," *2017 IEEE Industry Applications Society Annual Meeting*, 2017, pp. 1-8, doi: 10.1109/IAS.2017.8101794.

[135]. S. Rahmani, K. Al-Haddad, and H. Y. Kanaan, "Two PWM techniques for single-phase shunt active power filters employing a direct current control strategy," IET Power Electronics, vol. 1, pp. 376-385, 2008. doi:10.1049/iet-pel:20070253

[136] Y. Singh, I. Hussain, B. Singh and S. Mishra, "Power quality improvement in single phase grid tied solar PV-APF based system using improved LTI-EPLL based control algorithm," *2017 7th International Conference on Power Systems (ICPS)*, 2017, pp. 289-295, doi: 10.1109/ICPES.2017.8387308.

[137] T. N. Gupta, S. Murshid and B. Singh, "Single-Phase Grid Interfaced WEGS using Frequency Adaptive Notch Filter for Power Quality Improvement," *2018 2nd IEEE International Conference on Power Electronics, Intelligent Control and Energy Systems (ICPEICES)*, 2018, pp. 630-635, doi: 10.1109/ICPEICES.2018.8897287.

[138] N. Kumar, B. Singh and B. K. Panigrahi, "PNKLMF-Based Neural Network Control and Learning-Based HC MPPT Technique for Multiobjective Grid Integrated Solar PV Based Distributed Generating System," in *IEEE Transactions on Industrial Informatics*, vol. 15, no. 6, pp. 3732-3742, June 2019, doi: 10.1109/TII.2019.2901516.

[139] H. Zhu and H. Fujimoto, "Suppression of Current Quantization Effects for Precise Current Control of SPMSM Using Dithering Techniques and Kalman Filter," in *IEEE Transactions on Industrial Informatics*, vol. 10, no. 2, pp. 1361-1371, May 2014, doi: 10.1109/TII.2014.2307195.

[140] S. Swain and B. Subudhi, "Grid Synchronization of a PV System With Power Quality Disturbances Using Unscented Kalman Filtering," in *IEEE Transactions on Sustainable Energy*, vol. 10, no. 3, pp. 1240-1247, July 2019, doi: 10.1109/TSTE.2018.2864822.

[141] M. A. Khanesar, E. Kayacan, M. Teshnehlab and O. Kaynak, "Extended Kalman Filter Based Learning Algorithm for Type-2 Fuzzy Logic Systems and Its Experimental Evaluation," in *IEEE Transactions on Industrial Electronics*, vol. 59, no. 11, pp. 4443-4455, Nov. 2012, doi: 10.1109/TIE.2011.2151822

[142] P. Shah, I. Hussain and B. Singh, "A Novel Fourth-Order Generalized Integrator Based Control Scheme for Multifunctional SECS in the Distribution System," in *IEEE Transactions on Energy Conversion*, vol. 33, no. 3, pp. 949-958, Sept. 2018, doi: 10.1109/TEC.2018.2806191.

[143] M. Badoni, A. Singh and B. Singh, "Power Quality Enhancement Using Euclidean Direction Search Based Control Technique," in *IEEE Transactions on Industrial Electronics*, vol. 67, no. 3, pp. 2231-2240, March 2020, doi: 10.1109/TIE.2019.2905835.

[144] P. Chittora, A. Singh and M. Singh, "Chebyshev Functional Expansion Based Artificial Neural Network Controller for Shunt Compensation," in *IEEE Transactions on Industrial Informatics*, vol. 14, no. 9, pp. 3792-3800, Sept. 2018, doi: 10.1109/TII.2018.2793347.

[145] B. Singh, N. Kumar and B. K. Panigrahi, "Steepest Descent Laplacian Regression Based Neural Network Approach for Optimal Operation of Grid Supportive Solar PV Generation," in *IEEE Transactions on Circuits and Systems II: Express Briefs*, vol. 68, no. 6, pp. 1947-1951, June 2021, doi: 10.1109/TCSII.2020.2967106.

[146] N. M. C. M., Y. Singh, S. B. Q. Naqvi, B. Singh and J. Pychadathil, "Multi-Objective Solar Power Conversion System With MGI Control for Grid Integration at Adverse Operating Conditions," in *IEEE Transactions on Sustainable Energy*, vol. 11, no. 4, pp. 2901-2910, Oct. 2020, doi: 10.1109/TSTE.2020.2981356.

[147] B. Singh, C. Jain and S. Goel, "ILST Control Algorithm of Single-Stage Dual Purpose Grid Connected Solar PV System," in IEEE Transactions on Power Electronics, vol. 29, no. 10, pp. 5347-5357, Oct. 2014, doi: 10.1109/TPEL.2013.2293656.

[148] P. Shukl and B. Singh, "Recursive Digital Filter Based Control for Power Quality Improvement of Grid Tied Solar PV System," in *IEEE Transactions on Industry Applications*, vol. 56, no. 4, pp. 3412-3421, July-Aug. 2020, doi: 10.1109/TIA.2020.2990369.

[149] Priyanka Chaudhary, M. Rizwan, "QNBP NN-based I cos ϕ algorithm for PV systems integrated with LV/MV grid", Soft Computing, vol.25, no.4, pp.2599, 2021, https://doi.org/10.1007/s00500-020-05295-8.

[150] V. Jain, I. Hussain and B. Singh, "A HTF-Based Higher-Order Adaptive Control of Single-Stage Grid-Interfaced PV System," in IEEE Transactions on Industry Applications, vol. 55, no. 2, pp. 1873-1881, March-April 2019, doi: 10.1109/TIA.2018.2878186.

[151] S. A. Verne and M. I. Valla, "Active power filter for medium voltage networks with predictive current control," Electric Power Systems Research, vol. 80, no. 12, pp. 1543– 1551, 2010. doi: 10.1016/j.epsr.2010.06.019.

[152] S. Rahmani, A. Hamadi and K. Al-Haddad, "A Lyapunov-Function-Based Control for a Three-Phase Shunt Hybrid Active Filter," in IEEE Transactions on Industrial Electronics, vol. 59, no. 3, pp. 1418-1429, March 2012. doi: 10.1109/TIE.2011.2163370.

[153] M. Mangaraj and A. K. Panda, "NBP-based I-cosϕ control strategy for DSTATCOM," in IET Power Electronics, vol. 10, no. 12, pp. 1617-1625, 10 6 2017. doi: 10.1049/iet.pel.2017.0129

[154] S. R. Arya, B. Singh, A. Chandra and K. Al-Haddad, "Learning-Based Anti-Hebbian Algorithm for Control of Distribution Static Compensator," in IEEE Transactions on Industrial Electronics, vol. 61, no. 11, pp. 6004-6012, Nov. 2014. doi: 10.1109/TIE.2014.2321341.

[155] M. Badoni, A. Singh and B. Singh, "Variable Forgetting Factor Recursive Least Square Control Algorithm for DSTATCOM," in IEEE Transactions on Power Delivery, vol. 30, no. 5, pp. 2353-2361, Oct. 2015. doi: 10.1109/TPWRD.2015.2422139.

[156] S. K. Kesharvani, A. Singh and M. Badoni, "Conductance based fryze algorithm for improving power quality for non-linear loads," 2014 International Conference on Signal Propagation and Computer Technology (ICSPCT 2014), Ajmer, 2014, pp. 703-708. doi: 10.1109/ICSPCT.2014.6884965.

[157] A. K. Singh, I. Hussain and B. Singh, "Double-Stage Three-Phase Grid-Integrated Solar PV System With Fast Zero Attracting Normalized Least Mean Fourth Based Adaptive Control," in IEEE Transactions on Industrial Electronics, vol. 65, no. 5, pp. 3921-3931, May 2018, doi: 10.1109/TIE.2017.2758750.

[158] S. Mishra and P. K. Ray, "Power Quality Improvement Using Photovoltaic Fed DSTATCOM Based on JAYA Optimization," in IEEE Transactions on Sustainable Energy, vol. 7, no. 4, pp. 1672-1680, Oct. 2016, doi: 10.1109/TSTE.2016.2570256.

[159] N. Kumar, B. Singh, B. K. Panigrahi and L. Xu, "Leaky-Least-Logarithmic-Absolute-Difference-Based Control Algorithm and Learning-Based InC MPPT Technique for Grid-Integrated PV System," in *IEEE Transactions on Industrial Electronics*, vol. 66, no. 11, pp. 9003-9012, Nov. 2019, doi: 10.1109/TIE.2018.2890497

[160] G. De Donato, G. Scelba, G. Borocci, F. Giulii Capponi and G. Scarcella, "Fault-Decoupled Instantaneous Frequency and Phase Angle Estimation for Three-Phase Grid-Connected Inverters," in *IEEE Transactions on Power Electronics*, vol. 31, no. 4, pp. 2880-2889, April 2016, doi: 10.1109/TPEL.2015.2445797.

[161] J. Svensson, "Synchronization methods for grid-connected voltage source converters", Proc. Inst. Elect. Eng. Generation Transmission Distribution, vol. 148, no. 3, pp. 229-235, 2001-May.doi:10.1049/ip-gtd:20010101

[162] M. Karimi-Ghartemani and M. R. Iravani, "A method for synchronization of power electronic converters in polluted and variable-frequency environments," in *IEEE Transactions on Power Systems*, vol. 19, no. 3, pp. 1263-1270, Aug. 2004, doi: 10.1109/TPWRS.2004.831280.

[163] V. Kaura and V. Blasko, "Operation of a phase locked loop system under distorted utility conditions," in *IEEE Transactions on Industry Applications*, vol. 33, no. 1, pp. 58-63, Jan.-Feb. 1997, doi: 10.1109/28.567077.

[164] C. Subramanian and R. Kanagaraj, "Single-Phase Grid Voltage Attributes Tracking for the Control of Grid Power Converters," in *IEEE Journal of Emerging and Selected Topics in Power Electronics*, vol. 2, no. 4, pp. 1041-1048, Dec. 2014, doi: 10.1109/JESTPE.2014.2341045.

[165] R. Weidenbrug, F. P. Dawson and R. Bonert, "New synchronization method for thyristor power converters to weak AC-systems," in *IEEE Transactions on Industrial Electronics*, vol. 40, no. 5, pp. 505-511, Oct. 1993, doi: 10.1109/41.238019.

[166] Cheng-Che Chen and Yuan-Yih Hsu, "A novel approach to the design of a shunt active filter for an unbalanced three-phase four-wire system under non sinusoidal conditions," in *IEEE Transactions on Power Delivery*, vol. 15, no. 4, pp. 1258-1264, Oct. 2000, doi: 10.1109/61.891512.

[167] Voltage Characteristics of Electricity Supplied by Public Distribution Systems, 1994.

[168] S. Golestan, M. Monfared, F. D. Freijedo and J. M. Guerrero, "Dynamics Assessment of Advanced Single-Phase PLL Structures," in *IEEE Transactions on Industrial Electronics*, vol. 60, no. 6, pp. 2167-2177, June 2013, doi: 10.1109/TIE.2012.2193863.

[169] N. Mohan, T. M. Undeland, and W. P. Robbins, Power Electronics-Converters, Applications, and Design. New York: Wiley, 1995.

[170] P. Kundur, N. J. Balu, and M. G. Lauby, Power System Stability and Control, vol. 7. New York, NY, USA: McGraw-hill, 1994.

[171] P. Krishayya et al., IEEE Guide for Planning DC Links Terminating at AC Locations Having Low Short-Circuit Capacities, Part I: AC/DC System Interaction Phenomena, IEEE Std. France: CIGRE, 1997.

[172] X. Chen, Y. Zhang, S. Wang, J. Chen and C. Gong, "Impedance-Phased Dynamic Control Method for Grid-Connected Inverters in a Weak Grid," in *IEEE Transactions on Power Electronics*, vol. 32, no. 1, pp. 274-283, Jan. 2017, doi: 10.1109/TPEL.2016.2533563.

[173] S. Golestan and J. M. Guerrero, "Conventional Synchronous Reference Frame Phase-Locked Loop is an Adaptive Complex Filter," in *IEEE Transactions on Industrial Electronics*, vol. 62, no. 3, pp. 1679-1682, March 2015, doi: 10.1109/TIE.2014.2341594.

[174] M. Reyes, P. Rodriguez, S. Vazquez, A. Luna, R. Teodorescu and J. M. Carrasco, "Enhanced Decoupled Double Synchronous Reference Frame Current Controller for Unbalanced Grid-Voltage Conditions," in *IEEE Transactions on Power Electronics*, vol. 27, no. 9, pp. 3934-3943, Sept. 2012, doi: 10.1109/TPEL.2012.2190147.

[175] F. Xiao, L. Dong, L. Li and X. Liao, "A Frequency-Fixed SOGI-Based PLL for Single-Phase Grid-Connected Converters," in *IEEE Transactions on Power Electronics*, vol. 32, no. 3, pp. 1713-1719, March 2017, doi: 10.1109/TPEL.2016.2606623.

[176] C. Zhang, X. Zhao, X. Wang, X. Chai, Z. Zhang and X. Guo, "A Grid Synchronization PLL Method Based on Mixed Second- and Third-Order Generalized Integrator for DC Offset Elimination and Frequency Adaptability," in IEEE Journal of Emerging and Selected Topics in Power Electronics, vol. 6, no. 3, pp. 1517-1526, Sept. 2018, doi: 10.1109/JESTPE.2018.2810499.

[177] A. Kulkarni and V. John, "Design of a fast response time single-phase PLL with DC offset rejection capability," *2016 IEEE Applied Power Electronics Conference and Exposition (APEC)*, 2016, pp. 2200-2206, doi: 10.1109/APEC.2016.7468172.

[178] Y. F. Wang and Y. W. Li, "Three-Phase Cascaded Delayed Signal Cancellation PLL for Fast Selective Harmonic Detection," in *IEEE Transactions on Industrial Electronics*, vol. 60, no. 4, pp. 1452-1463, April 2013, doi: 10.1109/TIE.2011.2162715.

[179] S. Golestan, M. Ramezani, J. M. Guerrero, F. D. Freijedo and M. Monfared, "Moving Average Filter Based Phase-Locked Loops: Performance Analysis and Design Guidelines," in *IEEE Transactions on Power Electronics*, vol. 29, no. 6, pp. 2750-2763, June 2014, doi: 10.1109/TPEL.2013.2273461.

[180] B. P. McGrath, D. G. Holmes and J. J. H. Galloway, "Power converter line synchronization using a discrete Fourier transform (DFT) based on a variable sample rate," in *IEEE Transactions on Power Electronics*, vol. 20, no. 4, pp. 877-884, July 2005, doi: 10.1109/TPEL.2005.850944.

[181] A. B. Shitole, H. M. Suryawanshi, S. Sathyan and M. M. Renge, "Adaptive notch filter based synchronization technique for integration of distributed generation systems to utility grid," *IECON 2014 - 40th Annual Conference of the IEEE Industrial Electronics Society*, 2014, pp. 5457-5461, doi: 10.1109/IECON.2014.7049334.

[182] P. Shah and B. Singh, "Kalman Filtering Technique for Rooftop-PV System Under Abnormal Grid Conditions," in *IEEE Transactions on Sustainable Energy*, vol. 11, no. 1, pp. 282-293, Jan. 2020, doi: 10.1109/TSTE.2018.2890600.

[183] Saxena, H., Singh, A. & Rai, J.N., "Enhanced Third-Order Generalized Integrator-Based Grid Synchronization Technique for DC-Offset Rejection and Precise Frequency Estimation". Arab J Sci Eng 46, 9753–9762 (2021). https://doi.org/10.1007/s13369-021-05559-x

[184] Saxena, H., Singh, A., Rai, J. N., & Badoni, M, "PV integrated grid synchronization technique using modified SOGI-FLL and zero-crossing detector. Electrical Engineering", Electr Eng 104, 1361–1372 (2022). https://doi.org/10.1007/s00202-021-01394-3

[185] Saxena, H., Singh, A. and Rai, J.N. (2020, Adaptive spline-based PLL for synchronisation and power quality improvement in distribution system. IET Gener. Transm. Distrib., 14: 1311-1319. https://doi.org/10.1049/iet-gtd.2019.0662

[186] Q. Zhang, X. Sun, Y. Zhong, M. Matsui and B. Ren, "Analysis and Design of a Digital Phase-Locked Loop for Single-Phase Grid-Connected Power Conversion Systems," in IEEE Transactions on Industrial Electronics, vol. 58, no. 8, pp. 3581-3592, Aug. 2011, doi: 10.1109/TIE.2010.2087295.

[187] N. Kumar, B. Singh and B. K. Panigrahi, "Framework of Gradient Descent Least Squares Regression-Based NN Structure for Power Quality Improvement in PV-Integrated Low-Voltage Weak Grid System," in *IEEE Transactions on Industrial Electronics*, vol. 66, no. 12, pp. 9724-9733, Dec. 2019, doi: 10.1109/TIE.2018.2886765.

[188] T. K. Chau, S. S. Yu, T. Fernando and H. H. -C. Iu, "Demand-Side Regulation Provision From Industrial Loads Integrated With Solar PV Panels and Energy Storage System for Ancillary Services," in *IEEE Transactions on Industrial Informatics*, vol. 14, no. 11, pp. 5038-5049, Nov. 2018, doi: 10.1109/TII.2017.2782244.

[189] V. Rallabandi, O. M. Akeyo, N. Jewell and D. M. Ionel, "Incorporating Battery Energy Storage Systems Into Multi-MW Grid Connected PV Systems," in *IEEE Transactions on Industry Applications*, vol. 55, no. 1, pp. 638-647, Jan.-Feb. 2019, doi: 10.1109/TIA.2018.2864696.

[190] M. Pulcherio, M. S. Illindala, J. Choi and R. K. Yedavalli, "Robust Microgrid Clustering in a Distribution System With Inverter-Based DERs," in *IEEE Transactions on Industry Applications*, vol. 54, no. 5, pp. 5152-5162, Sept.-Oct. 2018, doi: 10.1109/TIA.2018.2853039.

[191] P. C. Loh, D. Li, Y. K. Chai and F. Blaabjerg, "Autonomous Operation of Hybrid Microgrid With AC and DC Subgrids," in *IEEE Transactions on Power Electronics*, vol. 28, no. 5, pp. 2214-2223, May 2013, doi: 10.1109/TPEL.2012.2214792.

[192] H. Kanchev, D. Lu, F. Colas, V. Lazarov and B. Francois, "Energy Management and Operational Planning of a Microgrid With a PV-Based Active Generator for Smart Grid Applications," in *IEEE Transactions on Industrial Electronics*, vol. 58, no. 10, pp. 4583-4592, Oct. 2011, doi: 10.1109/TIE.2011.2119451.

[193] S. Kumar, B. Singh, B. C. Pal, L. Xu and A. Al-Durra, "Energy Efficient Three-Phase Utility Interactive Residential Microgrid With Mode Transfer

Capabilities at Weak Grid Conditions," in IEEE Transactions on Industry Applications, vol. 55, no. 6, pp. 7082-7091, Nov.-Dec. 2019, doi: 10.1109/TIA.2019.2937861.

[194] Z. Yao, L. Xiao and Y. Yan, "Seamless Transfer of Single-Phase Grid-Interactive Inverters Between Grid-Connected and Stand-Alone Modes," in *IEEE Transactions on Power Electronics*, vol. 25, no. 6, pp. 1597-1603, June 2010, doi: 10.1109/TPEL.2009.2039357.

[195] Z. Yi, W. Dong and A. H. Etemadi, "A Unified Control and Power Management Scheme for PV-Battery-Based Hybrid Microgrids for Both Grid-Connected and Islanded Modes," in *IEEE Transactions on Smart Grid*, vol. 9, no. 6, pp. 5975-5985, Nov. 2018, doi: 10.1109/TSG.2017.2700332.

[196] A. Mondal and M. S. Illindala, "Improved Frequency Regulation in an Islanded Mixed Source Microgrid Through Coordinated Operation of DERs and Smart Loads," in *IEEE Transactions on Industry Applications*, vol. 54, no. 1, pp. 112-120, Jan.-Feb. 2018, doi: 10.1109/TIA.2017.2761825.

[197] F. Chishti, S. Murshid and B. Singh, "Frequency Adaptive Multistage Harmonic Oscillator for Renewable-Based Microgrid Under Nonideal Grid Conditions," in IEEE Transactions on Industrial Electronics, vol. 68, no. 1, pp. 358-369, Jan. 2021, doi: 10.1109/TIE.2020.2965474.

[198] S. Shubhra and B. Singh, "Three-Phase Grid-Interactive Solar PV-Battery Microgrid Control Based on Normalized Gradient Adaptive Regularization Factor Neural Filter," in IEEE Transactions on Industrial Informatics, vol. 16, no. 4, pp. 2301-2314, April 2020, doi: 10.1109/TII.2019.2937561.

[199] S. Singh, S. Kewat, B. Singh, B. K. Panigrahi and M. K. Kushwaha, "Seamless Control of Solar PV Grid Interfaced System With Islanding Operation," in *IEEE Power and Energy Technology Systems Journal*, vol. 6, no. 3, pp. 162-171, Sept. 2019, doi: 10.1109/JPETS.2019.2929300.

[200] S. Kumar, B. Singh, B. C. Pal, L. Xu and A. Al-Durra, "Energy Efficient Three-Phase Utility Interactive Residential Microgrid With Mode Transfer Capabilities at Weak Grid Conditions," in IEEE Transactions on Industry Applications, vol. 55, no. 6, pp. 7082-7091, Nov.-Dec. 2019, doi: 10.1109/TIA.2019.2937861.

[201] Karthikeyan, V. and Gupta, R. (2017), Varying phase angle control in isolated bidirectional DC–DC converter for integrating battery storage and solar PV system in standalone mode. IET Power Electronics, 10: 471-479. https://doi.org/10.1049/iet-pel.2016.0162

[202] Beniwal, N., Hussain, I. and Singh, B. (2018), Control and operation of a solar PV-battery-grid-tied system in fixed and variable power mode. IET Gener. Transm. Distrib., 12: 2633-2641. https://doi.org/10.1049/iet-gtd.2017.1095

[203] S. Kumar and B. Singh, "Seamless operation and control of hybrid PV-BES-utility synchronized system," 2018 IEEMA Engineer Infinite Conference (eTechNxT), 2018, pp. 1-6, doi: 10.1109/ETECHNXT.2018.8385329.

[204] S. Kumar and B. Singh, "Seamless transition of three phase microgrid with load compensation capabilities," 2017 IEEE Industry Applications Society Annual Meeting, 2017, pp. 1-9, doi: 10.1109/IAS.2017.8101757.

[205] G. L. Sicuranza and A. Carini, "On the BIBO Stability Condition of Adaptive Recursive FLANN Filters With Application to Nonlinear Active Noise Control," in *IEEE Transactions on Audio, Speech, and Language Processing*, vol. 20, no. 1, pp. 234-245, Jan. 2012, doi: 10.1109/TASL.2011.2159788.

[206] G. L. Sicuranza and A. Carini, "A Generalized FLANN Filter for Nonlinear Active Noise Control," in IEEE Transactions on Audio, Speech, and Language Processing, vol. 19, no. 8, pp. 2412-2417, Nov. 2011, doi: 10.1109/TASL.2011.2136336.

[207] Kumar, V., Prabhu, K.M.M., Das, D.P.: 'Block filtered-s least mean square algorithm for active control of non-linear noise systems active mitigation of non-linear noise process', IET Signal Process., 2010, 4, (2), pp. 68–180 ,doi: 10.1049/iet-spr.2008.0157

[208] J. C. Patra, W. C. Chin, P. K. Meher and G. Chakraborty, "Legendre-FLANN-based nonlinear channel equalization in wireless communication system," *2008 IEEE International Conference on Systems, Man and Cybernetics*, 2008, pp. 1826-1831, doi: 10.1109/ICSMC.2008.4811554.

[209] H. H. Ali and M. T. Haweel, "Legendre neural networks with multi input multi output system equations," *2012 Seventh International Conference on Computer Engineering & Systems (ICCES)*, 2012, pp. 92-97, doi: 10.1109/ICCES.2012.6408490.

[210] Bayin, S.S., "Mathematical methods in science and engineering", Wiley, Hoboken, New Jersey, USA, 2nd Edn , 2006.

[211] Rasala, R.: 'The rodrgues formulae and polynomial differential operators', J. Math. Anal. Appl., 1981, 84, (2), pp. 443–482, https://doi.org/10.1016/0022-247X(81)90180-3.

[212] G. L. Sicuranza and A. Carini, "On the Accuracy of Generalized Hammerstein Models for Nonlinear Active Noise Control," *2006 IEEE Instrumentation and Measurement Technology Conference Proceedings*, 2006, pp. 1411-1416, doi: 10.1109/IMTC.2006.328598.

[213] Scarpiniti M, Comminiello D, Parisi R, Unicini A, "Nonlinear spline adaptive filtering, Digital Signal Processing, Volume 93, no. 4, pp. 772-783, 2016. https://doi.org/10.1016/j.sigpro.2012.09.021.

[214] M. Scarpiniti, D. Comminiello, G. Scarano, R. Parisi and A. Uncini, "Steady-State Performance of Spline Adaptive Filters," in *IEEE Transactions on Signal Processing*, vol. 64, no. 4, pp. 816-828, Feb.15, 2016, doi: 10.1109/TSP.2015.2493986.

[215] Carl de boor, "Practical Guide to Splines," Applied Mathematical Sciences 27. USA: Springer-Verlag; 2001.

[216] Salomon D., “Beizer approximation. In: Curves and surfaces for computer graphics,” 1st edn. Springer, NY, pp 176–248,2006.

[217] Racine JS,“A primer on regression splines, “CRAN R-Project 1990,pp. 1–11,2018.

[218] A. Candan, "An Efficient Filtering Structure for Lagrange Interpolation," in IEEE Signal Processing Letters, vol. 14, no. 1, pp. 17-19, Jan. 2007, doi: 10.1109/LSP.2006.881528.

[219] V. Valimaki, "A new filter implementation strategy for Lagrange interpolation," *Proceedings of ISCAS'95 - International Symposium on Circuits and Systems*, 1995, pp. 361-364 vol.1, doi: 10.1109/ISCAS.1995.521525.

[220] A. Franck, "Efficient Algorithms and Structures for Fractional Delay Filtering Based on Lagrange Interpolation," J. Audio Eng. Soc., vol. 56, no. 12, pp. 1036-1056, 2008

APPENDIX

Appendix I

Design Parameters of Single-Phase Grid Connected System

Simulation Parameters

Grid supply voltage: 110 V (rms), 1-phase, 50 Hz, interfacing inductor: 3 mH, reference DC bus voltage = 200 V, non-linear load rating: 1-phase 2-leg diode bridge rectifier connected to R_{NL1}= 7.5 Ω, L_{NL1}= 40 mH, R_{NL2}= 15 Ω, linear load rating: R_L = 15 Ω, L_L= 80 mH, R=15 Ω, Mixed Loading: R_L = 7.5 Ω, L_L = 40 mH, supply side inductor L_s : 1×10^{-6}, DC bus capacitance: 3000 µF, PV panel specifications: Kyocera Solar KD250GX-LFB2, maximum power P_{mp} = 250.022 W, open circuit voltage V_{oc} = 36.9 V, short circuit current I_{sc} = 9.09 A, maximum voltage, V_{mp} = 29.8 V, maximum current I_{mp} = 8.39 A, series connected module per string = 3, cells per module = 60, parallel solar strings = 1, temperature coefficient of voltage (%/°C) = −0.32, temperature coefficient of current (%/°C) = 0.06, sampling time: 5 µs.

Experimental parameters

Grid supply voltage: 110 V (rms), 1-phase, 50 Hz, SAPF rating: 1.5 kVA, interfacing inductor: 3 mH, non-linear load rating: 1- phase 2-leg diode bridge rectifier connected to resistive load : 250 V, 24 A, inductive load: 80 mH, 15 mA, reference DC bus voltage = 200 V, DC bus capacitance: 3000 µF, PV panel specifications: EN50530, irradiation: 1000 W/m2 , Pmp = 500 W (3-phase), 166 W (per-phase), temperature coefficient of voltage (%/°C) = − 0.38, sampling time = 50 µs.

APPENDIX II

Design Parameters of Three-Phase Grid Connected System

Simulation Parameters

Grid supply voltage: 110 V (rms), 1-phase, 50 Hz, interfacing inductor (L_f): 1 mH, reference DC bus voltage (V_{dc}^*) = 200 V, non-linear load rating: 3-phase 3-leg diode bridge rectifier connected to R_{NL1}= 7.5 Ω, L_{NL1}= 40 mH, R_{NL2}= 15 Ω, linear load rating: P=1000 W, Q_L= 500 VAR, Mixed Load Rating: P=1000 W, Q_L= 500 VAR, supply side inductor Ls : $1 \times 10{-}6$, DC bus capacitance: 3000 µF, PV panel specifications: Kyocera Solar KD250GX-LFB2, maximum power P_{mp} = 250.022 W, open circuit voltage V_{oc} = 36.9 V, short circuit current I_{sc} = 9.09 A, maximum voltage, V_{mp} = 29.8 V, maximum current I_{mp} = 8.39 A, series connected module per string = 3, cells per module = 60, parallel solar strings = 1, temperature coefficient of voltage (%/°C) = −0.32, temperature coefficient of current (%/°C) = 0.06, sampling time: 5 µs.

Experimental Parameters

Grid Supply voltage (v_s) : 110 V (rms) 3-ϕ, 50 Hz, SAPF rating: 10 kVA, Interfacing Inductor (L_f): 1 mH, Reference DC Voltage (V_{dc}^*)=200 V, Non-Linear Load Rating: Diode-bridge rectifier feeding Resistive Load: 6 kW, 24 A, Inductive Load: 80mH, 15mA, Linear Load Rating:15 kVA, pf: 0.7 to 1, DC bus Capacitance: 1640μF, Chroma PV Simulator: PV panel Specifications: EN50530, Solar Irradiation:1000 W/m^2,P_{mp}=300W, Temperature Coefficient of Voltage (%/℃)=-0.38.

Appendix III

Design Parameters of Battery Interfaced PV integrated Grid Connected System

Simulation Parameters

Grid supply voltage: 110 V (rms), 1-phase, 50 Hz, Interfacing inductor: (L_f): 3 mH, reference DC bus voltage (V_{dc}^*)= 200 V, non-linear load rating: 1-phase 2-leg

diode bridge rectifier connected to R_{NL1}= 7.5 Ω, L_{NL1}= 40 mH, R_{NL2}= 15 Ω, Supply side inductor L_s : 1 × 10−6, DC bus capacitance: 3000 µF, PV panel specifications: Kyocera Solar KD250GX-LFB2, maximum power P_{mp} = 250.022 W, open circuit voltage V_{oc} = 36.9 V, short circuit current I_{sc} = 9.09 A, maximum voltage, V_{mp} = 29.8 V, maximum current I_{mp} = 8.39 A, series connected module per string = 3, cells per module = 60, parallel solar strings = 1, temperature coefficient of voltage (%/°C) = −0.32, temperature coefficient of current (%/°C) = 0.06, sampling time: 5 µs. Battery specifications: Lead Acid Battery 120 V, 20 Ah, Initial State of charge=90%, Battery response time=0.1s, L_b= 3 mH